Femtosecond X-Ray Scattering in Condensed Matter

DISSERTATION

zur Erlangung des akademischen Grades
doctor rerum naturalium
(Dr. rer. nat.)
im Fach Physik

eingereicht an der
Mathematisch-Naturwissenschaftlichen Fakultät I
Humboldt-Universität zu Berlin

von
Herr Dipl.-Phys. Clemens von Korff Schmising
geboren am 20.07.1977 in Bonn

Präsident der Humboldt-Universität zu Berlin:
Prof. Dr. Dr. h.c. Christoph Markschies

Dekan der Mathematisch-Naturwissenschaftlichen Fakultät I:
Prof. Dr. Lutz-Helmut Schön

Gutachter:

1. Prof. Dr. Thomas Elsässer
2. Prof. Dr. Oliver Benson
3. Prof. Dr. Martin Wolf

eingereicht am:	7. Juli 2008
Tag der mündlichen Prüfung:	24. November 2008

Abstract

This thesis investigates the manifold couplings between electronic and structural properties in crystalline Perovskite oxides and a polar molecular crystal. Ultrashort optical excitation changes the electronic structure and the dynamics of the connected reversible lattice rearrangement is imaged in real time by femtosecond X-ray scattering experiments.

An epitaxially grown superlattice consisting of alternating nanolayers of metallic and ferromagnetic strontium ruthenate (SRO) and dielectric strontium titanate serves as a model system to study optically generated stress. In the ferromagnetic phase, phonon-mediated and magnetostrictive stress in SRO display similar sub-picosecond dynamics, similar strengths but opposite sign and different excitation spectra. The amplitude of the magnetic component follows the temperature dependent magnetization square, whereas the strength of phononic stress is determined by the amount of deposited energy only.

The ultrafast, phonon-mediated stress in SRO compresses ferroelectric nanolayers of lead zirconate titanate in a further superlattice system. This change of tetragonal distortion of the ferroelectric layer reaches up to 2 percent within 1.5 picoseconds and couples to the ferroelectric soft mode, or ion displacement within the unit cell. As a result, the macroscopic polarization is reduced by up to 100 percent with a 500 femtosecond delay that is due to final elongation time of the two anharmonically coupled modes.

Femtosecond photoexcitation of organic chromophores in a molecular, polar crystal induces strong changes of the electronic dipole moment via intramolecular charge transfer. Ultrafast changes of transmitted X-ray intensity evidence an angular rotation of molecules around excited dipoles following the 10 picosecond kinetics of the charge transfer reaction. Transient X-ray scattering is governed by solvation, masking changes of the chromophore's molecular structure.

Keywords:
X-ray Diffraction, Femtosecond, Ferroelectricity, Ferromagnetism

Zusammenfassung

Diese Arbeit untersucht die vielfältigen Wechselwirkungen zwischen elektronischen und strukturellen Eigenschaften in Perovskit-Oxiden und in einem molekularen Kristall. Optische Anregung mit ultrakurzen Lichtimpulsen verändert die elektronische Struktur und die Dynamik der damit verbundenen reversiblen Gitterveränderung wird mit zeitaufgelöster Femtosekunden Röntgenbeugung direkt aufgezeichnet.

Eine Nanostruktur aus metallischen und ferromagnetischen Strontium Ruthenat (SRO) und dielektrischen Strontium Titanat Schichten dient als Modellsystem, um optisch induzierten Druck auf einer subpikosekunden Zeitskala zu untersuchen. In der ferromagnetischen Phase zeigen phononischer und magnetostriktiver Druck eine vergleichbare ultraschnelle Dynamik und eine ähnliche Größe unterschiedlichen Vorzeichens. Die Amplitude des magnetischen Drucks folgt dem Quadrat der temperaturabhängigen Magnetisierung.

In einem weiteren Doppelschichtsystem komprimiert der sich ultraschnell aufbauende phononische Druck in SRO benachbarte ferroelektrische Blei Zirkonat Titanat Schichten. Dies reduziert die tetragonale Verzerrung von bis zu 2 Prozent innerhalb 1.5 Pikosekunden und koppelt an die ferroelektrische „weiche Mode“, beziehungsweise an die Ionenverschiebung innerhalb der Einheitszelle. Damit verbunden wird die makroskopische Polarisation bis zu 100 Prozent reduziert; aufgrund der Anharmonizität der Kopplung mit einer Verzögerung von 500 Femtosekunden.

Femtosekunden Photoanregung von Chromophoren in einem molekularen Kristall induziert eine Änderung des Diopolmomentes durch intramolekularen Ladungstransfer. Die Änderung der gestreuten Röntgenintensität weist auf eine Molekül-Rotationsbewegung in der Umgebung angeregte Dipole hin, welche der 10 Pikosekunden Dynamik des Ladungstransfer folgt. Die transienten Röntgenstreusignale werden vollständig von der kollektiven Solvatation bestimmt und verdecken lokale, intramolekulare Strukturänderungen.

Schlagwörter:
Röntgenbeugung, Femtosekunden, Ferroelektriztät, Ferromagnetismus

Contents

Chapter 1

Introduction

'If you want to understand function, study structure', exhorted Francis Crick when he resolved the molecular structure of DNA. However, knowledge of a *static* structure is often only a first step towards unraveling how microscopic systems work. In particular, elementary processes in condensed matter are frequently governed by nuclear rearrangements, which take place on a femtosecond[1] time scale, and are ultimately set by the translational, rotational or vibrational motions on an atomic length scale. Hence, function is intrinsically coupled to *dynamic* structure.

While ultrafast optical spectroscopy has become a well established tool to follow such microscopic processes in real time [1], the information on structural changes is, at most, indirect and changes in geometry triggered by elementary excitations and interactions have mostly remained elusive. X-ray scattering, on the other hand, gives direct access to structure in condensed media. Since the wavelength of X-ray photons is comparable to interatomic distances, diffraction patterns determine atomic positions with high precision. During the last decade great progress has been made to combine the temporal resolution of ultrafast technologies with the spatial resolution of X-rays, that is, developing X-ray sources with ever shorter pulse duration [2]. Yet, ultrafast X-ray scattering is still a nascent field of science with not insignificant technical constraints, and only a limited number of successful femtosecond X-ray diffraction [3–21] and absorption [22] experiments have been carried out. In this thesis, I present ultrafast X-ray diffraction experiments, contributing both to new insight into electronic correlations and their interaction with reversible, structural degrees of freedom and to a deeper understanding of X-ray scattering effects related to the transient character of the structure.

[1] 1 f (femto)=10^{-15} = one billionth of a millionth

Electronic phase transitions are associated with ultrafast changes of structure and have received increasing interest in solid state physics, for example, the metal-insulator transition in VO_2, where a structural rearrangement on a sub-picosecond time scale occurs [5]. A recent study presented experimental results on the direct manipulation of the electronic phase of manganites (manifesting the huge resistivity changes) by directly driving metal-oxygen phonons by mid-infrared radiation; hence, exploiting the pronounced interplay between electronic and nuclear structure [23]. Ferroelectricity and ferromagnetism are two further prominent examples where electronic correlations are connected with atomic rearrangements. Time-resolved optical second-harmonic generation on gadolinium/terbium surfaces established the quasi-instantaneous interactions of coherent optical phonons and magnetic order via modulation of the exchange coupling [24, 25]. Apart from this, the relevant time scales of elementary interactions between structural and electronic degrees of freedom connected with ferroelectricity and ferromagnetism have remained mostly unexplored and, hence, little is known about the underlying microscopic processes. The work presented here addresses this question twofold: first, how fast is the macroscopic polarization altered by launching lattice excitation in ferroelectric media, and secondly, how fast is the response of a ferromagnetic crystal structure to ultrafast demagnetization. A further example includes a molecular crystal belonging to the larger class of systems where the optically modified electronic structure results in an ultrafast structural response. Here, an optically induced charge transfer reaction connected with a large dipole change triggers solvation related, structural changes in a polar molecular crystal.

X-ray scattering will attenuate a primary X-ray beam, a process known to occur in perfect and, less well known, also in imperfect crystal structures. In general, crystal distortions change the fraction of coherently scattered photons and result in a modified integrated Bragg diffracted intensity. In time-resolved X-ray experiments photo-excitation may result in ultrafast changes of lattice geometries, requiring a sound description of transient scattering effects. The most obvious example which has been studied by time-resolved X-ray techniques is ultrafast laser-induced melting in semiconductor samples [4, 7, 8, 13, 14, 17], causing a complete loss of order on an ultrafast time-scale and a corresponding reduction of coherently scattered X-rays. More subtle types of optically induced atomic motion, such as ultrafast laser heating [3, 12], are well known processes described by the Debye-Waller factor. A number of experiments studied laser induced acoustic deformations in crystalline material by observing line-shifts of Bragg reflections or the evolution of sidebands [8, 26–30]. The consequences for the angle integrated Bragg

reflectivity due to a disturbance of the crystal in form of a shock wave was studied in indium antimonide [31]. The reflectivity was shown to increase, however, no quantitative analysis was presented. In chapter 4, it is shown that lattice distortions in form of an optically launched strain wave in a highly perfect crystal results in a nonlinear increase of integrated coherently scattered X-rays. The complicated shape of the transient X-ray reflectivity curves is fully explained by dynamical X-ray diffraction theory and allows to quantitatively determine minute structural changes with an unprecedent accuracy.

Dynamics in complex molecular or protein crystals have been studied by static diffuse scattering and revealed pronounced, correlated, intermolecular motion of molecules within the lattice [32–34]. Several time-resolved liquid phase X-ray scattering experiments with 100 picosecond temporal resolution reported on the light induced structural changes in molecules and their interaction with the surrounding solution [35–37]. In chapter 7, it is discussed how photoinduced charge transfer reactions lead to solvation-driven molecular dynamics in a crystalline environment on a ten picosecond time-scale. The collective response of the crystal lattice after an ultrafast dipole change of diluted chromopores results in a modification of the number and anisotropy of the coherently scattered X-ray photons.

Outline

The thesis is organized as follows:

Chapter 2 introduces the general formula for X-ray scattering by electrons, and discusses the most common approximations that lead to the kinematic and dynamical X-ray diffraction theory. A brief introduction into lattice dynamics is presented and the consequences for X-ray diffraction pattern are discussed.

Chapter 3 introduces the experimental techniques, including the setup for the generation of ultrashort hard X-ray pulses and briefly discusses the relevant underlying physical concepts.

Chapter 4 focuses on propagating strain waves in a perfect crystal substrate after photoinduced stress in an epitaxial ferroelectric nanolayer. Analysis with dynamical X-ray diffraction theory reveals complicated interference effects due to coherently scattered X-rays. Its quantitative description allows an exact determination of minute dynamical structural changes down to approximately 10 fm.

Chapter 5 investigates stress generation mechanisms in the itinerant ferromagnetic Perovskite $SrRuO_3$ experimentally. Femtosecond X-ray diffraction experiments provide direct evidence of phonon mediated stress and subpi-

cosecond magnetostriction.

Chapter 6 begins with an introduction of ferroelectricity, which is discussed with emphasis on its connection to structural degrees of freedom, that is, how it is governed by elongation of certain phonon modes. Additionally, mechanical and electric boundary effects in thin films and their coupling to the macroscopic polarization are mentioned.

A time-resolved X-ray structure analysis of ferroelectric nano-layers exposed to an ultrafast optically induced uniaxial stress is presented. Launching such lattice excitation results in an ultrafast reduction of the macroscopic polarization. This is shown by directly measuring the relevant atomic amplitudes.

Chapter 7 reports another type of a polar solid: a molecular crystal shows ultrafast solvation-related structural rearrangement after a photoinduced charge transfer process. This is revealed by studying the ultrafast changes in X-ray transmission which are dominated by diffuse scattering. X-ray reflectivity/transmission changes due to local changes of the diluted chromophores are masked by the collective response of the crystal.

Chapter 2

X-Ray Scattering in Condensed Matter

In the following the general formula for X-ray scattering of a distribution of free and non-relativistic electrons is presented and it is shown how appropriate approximations lead to the kinematic and dynamical X-ray diffraction theory for crystalline materials. Within the general description of X-ray scattering the effect of extinction is elucidated, that is, the attenuation of the incoming X-ray beam due to scattering. Such effects due to multiple scattering events play an important role, both, in a highly perfect crystal and in a material with significant deviations from a perfect crystal structure, when attenuation due to diffuse or incoherent scattering dominates.

The detailed derivation of the diffraction theory establishes the basis to link the observables, namely the time-dependent intensities and positions of X-ray diffraction peaks, and changes of atomic positions. With a sound understanding of the diffraction theory and the manageable number of degrees of freedom of the investigated samples, the connection between measurement and its physical significance is accomplished. Also, since time-resolved X-ray diffraction is still a developing field of science, with not insignificant technical constraints, to investigate an intelligent choice of Bragg reflections is an inevitable prerequisite for successful experiments.

In the last part of this chapter the family of Oxide with a Perovskite crystal structure is introduced and the manifold couplings between electronic and structural degrees of freedom is discussed. This is followed by a section on the the dynamics of crystal lattices and their transient character influences X-ray scattering. In this context the most important milestones in ultrafast X-ray science are presented.

2.1 Classical Scattering from Free Non-Relativistic Electrons

Single Electron

It is well-known that accelerated charges emit electromagnetic radiation and that in condensed matter electrons make the strongest contribution to the scattering of X-rays[1]. Hence, the response of a single free, non-relativistic electron subject to the electric field of an incident X-ray beam is the natural starting point for the discussion of X-rays and their interaction with matter.

Let us assume that at position $\vec{x}_1$ an electron is accelerated by an electric field E_1^{loc} as depicted in figure 2.1 a). Then, the radiated field at some position $\vec{x}_\mathrm{i}$ is given by [38]:

$$\vec{E}_\mathrm{i}^{\mathrm{rad}}(\vec{x}_\mathrm{i}) = r_0 \cdot \vec{n}_{1\mathrm{i}} \times (\vec{n}_{1\mathrm{i}} \times \vec{E}_1^{\mathrm{loc}}) \frac{e^{i|\vec{k}_0||\vec{x}_1 - \vec{x}_\mathrm{i}|}}{|\vec{x}_1 - \vec{x}_\mathrm{i}|} \tag{2.1}$$

where r_0 is the Thomson scattering length, or classical electron radius

$$r_0 = \frac{e^2}{4\pi\epsilon_0 mc^2} = 2.82 \times 10^{-5} \mathring{A}. \tag{2.2}$$

$\vec{n}_{1\mathrm{i}}$ denotes a unit vector pointing along $(\vec{x}_\mathrm{i} - \vec{x}_1)$. In elastic scattering the wavelength, λ, remains constant and $|\vec{k}_0| = 2\pi/\lambda$ denotes the magnitude of the wave vector of the radiated wave, which points along the propagation direction of the wave.

Random Distribution of Electrons

Let us now consider a situation as depicted in figure 2.1 b), where an incident plane (X-ray) wave $\vec{E}_{\mathrm{ext}} e^{i\vec{k}_0\vec{x}_\mathrm{i}}$ is scattered at a distribution of N free, non-relativistic electrons. The total electric field at position x_i is:

$$\vec{E}_\mathrm{i}^{\mathrm{loc}}(\vec{x}_\mathrm{i}) = E_{\mathrm{ext}} e^{i\vec{k}_0\vec{x}_\mathrm{i}} + r_0 \cdot \sum_{\mathrm{j}\neq\mathrm{i}}^{N} \vec{n}_{\mathrm{ij}} \times (\vec{n}_{\mathrm{ij}} \times \vec{E}_\mathrm{j}^{\mathrm{loc}}) \frac{e^{i|\vec{k}_0||\vec{x}_\mathrm{i} - \vec{x}_\mathrm{j}|}}{|\vec{x}_\mathrm{i} - \vec{x}_\mathrm{j}|}. \tag{2.3}$$

In addition to the incoming plane wave, each electron is subject to the scattered wave of all surrounding electrons, which, in turn, influence the driving field of the neighboring electrons. The apparent difficulty is solving this formula to self-consistently evaluate the local fields at the positions of every

[1] Due to the much larger mass of the nuclei, their contribution to X-ray scattering is negligible.

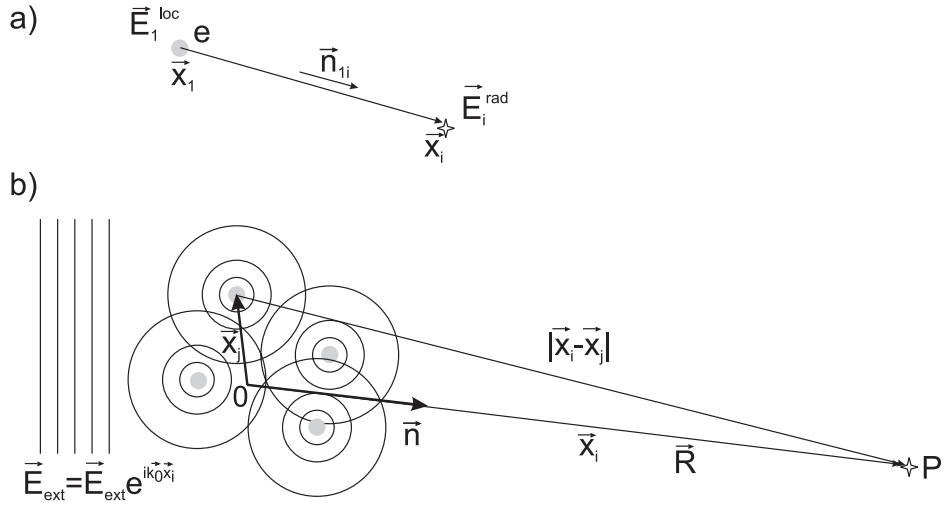

Figure 2.1: **a)** Schematic for the scattering field of a single electron. **b)** Scattering from a distribution of electrons, observed at point P.

scattering electron. In other words, the problem arises from the fact that equation 2.3 contains the local fields on both sides of the equation. Hence, finding a solution requires diagonalizing a matrix of the order N. However, with the typical electron density of condensed matter in the order of 10^{23} cm^{-3}, this is impossible.

If the driving fields $E_{\mathrm{j}}^{\mathrm{loc}}$ at positions x_{j} are known, the scattered wave at any position P is calculated as:

$$\vec{E}_{\mathrm{P}}^{\mathrm{scatt}}(\vec{x}_{\mathrm{P}}) = r_0 \cdot \sum_{\mathrm{j}\neq\mathrm{i}}^{N} \vec{n}_{\mathrm{ij}} \times (\vec{n}_{\mathrm{ij}} \times \vec{E}_{\mathrm{j}}^{\mathrm{loc}}) \frac{e^{i|\vec{k}_0||\vec{x}_{\mathrm{i}}-\vec{x}_{\mathrm{j}}|}}{|\vec{x}_{\mathrm{i}}-\vec{x}_{\mathrm{j}}|}. \tag{2.4}$$

This expression represents the most general formula for the radiated field from a random distribution of free and non-relativistic electrons. Significant simplifications which need to reflect the properties of the scattering material need to be found to approximate equation 2.4. First of all, let us consider a crystalline material described by a basis structure, usually referred to as a unit cell, which is repeated periodically in space. The unit cell itself consists of some spatial arrangement of (different) atoms and its size is determined by the lattice constants a, b and c. This symmetry permits to describe the electron distribution as (infinitely) extended planes of constant electron density and allows to deduce a manageable approximation of equation 2.3. It is known as the two wave approximation in the dynamical X-ray diffraction theory. This is presented in section 2.7. However, there exists an even simpler approximation, which mostly gives a good agreement with experimental

data. It is known as the kinematic X-ray theory and neglects all multiple scattering events. This is discussed in section 2.3.

However, first of all it must be remembered that the smallest scattering unit in crystals are atoms, made up of bound electrons.

2.2 Scattering from an Atom

Let us consider the scattering from an atom with Z electrons. To continue with the classical approach we consider that each electron is spread out into a diffuse cloud of negative charge, characterized by a charge density, ρ. The quantity $\rho\delta V$ is the ratio of the charge in volume δV to the charge of one electron, such that for each electron $\int \rho\delta V = 1$. The wave mechanical treatment then tells us that the amplitude of elastic scattering from the element $\rho\delta V$ is equal to $\rho\delta V$ times the amplitude of classical elastic scattering from a single electron. To calculate the radiated field at position $\vec{x}$ of this charge density, one has to integrate the contributions of the different volume elements and keep track of their relative phase differences. If we denote the wave vector of the scattered wave with $\vec{k}_{\mathrm{S}}$, with $|\vec{k}_0| = |\vec{k}_{\mathrm{S}}|$ the phase difference is $\Delta\phi(\vec{r}) = (\vec{k}_0 - \vec{k}_{\mathrm{S}})\vec{r} = \vec{Q}\vec{r}$, where $\vec{Q}$ is the wave vector transfer. This leads to the definition of the atomic form factor

$$f_0(\vec{Q}) = \int \rho(\vec{x}) e^{i\vec{Q}\vec{x}} d\vec{x}, \tag{2.5}$$

which is the Fourier transform of the charge density, ρ. In the limit of a point-like charge or $Q \to 0$, the volume elements scatter in phase and $f_0(\vec{Q} = 0) = Z$. On the other hand, with increasing $\vec{Q}$, more elements scatter out of phase and the atomic form factor decreases and consequently $f_0(\vec{Q} \to \infty) = 0$. This simple treatment relies on two assumptions: first of all, that the charge distribution for each electron in the atom has a spherical symmetry and secondly, the wavelength of the X-ray beam is much smaller than any of the absorption edge wavelengths of the atom. Deviations from spherical symmetry are accounted for by the quantum mechanical description, where the electron density is described by the atomic wave functions. These have been calculated and for computational convenience are fitted to the following analytical approximation:

$$f_0(Q) = \sum_{j=1}^{4} a_j e^{-b_j(\frac{Q}{4\pi})^2} + c \tag{2.6}$$

where the fitting parameters a_j, b_j and c are tabulated in the International Tables of Crystallography [39].

If the X-ray frequency is smaller than an atomic transition energy and we allow for photoabsorption, a dispersion correction is necessary and the atomic scattering factors are described in the form

$$f_0(\vec{Q}, E) = f_0(\vec{Q}) + f'(E) + if''(E) \tag{2.7}$$

where the term $f'(E)$ corrects for the fact that the electrons are bound and are not able to fully follow the driving field. The term $if''(E)$ allows the response of the electrons to have a phase lag with respect to the X-ray field and represents the dissipation in the system (absorption). The imaginary part is derived from the atomic photoabsorption cross-section and the real part is calculated with the Kramers-Kronig relation. The values are tabulated for atomic numbers up to Uranium, and in an energy range between 50-30,0000 eV [40]. Since these corrections are mainly due to the inner-shell electrons they have no appreciable dependence on $\vec{Q}$.

2.3 Kinematic X-ray Diffraction Theory

Discarding the second term of equation 2.3, that is, neglecting all multiple scattering events leads to the kinematic X-ray diffraction theory. It is well-suited to describe scattering from very thin crystals or powder-samples consisting of small crystallites. This approximation also presents an adequate description of weak Bragg reflection and, in particular, of imperfect crystals (please compare section 2.4). In general, multiple scattering is only of significance if very many electrons contribute coherently to diffraction peaks. This is simply because the scattered field of a single electron is only proportional to r_0, hence it is very small.

The configuration as depicted in figure 2.1 b) allows a further simplification of equation 2.3. Let the point of observation, P, at position, $\vec{x}_\mathrm{i}$, be far away from the charge distribution. Further, we denote the distance between P and the origin 0 with R along direction $\vec{n}$ and the position of some electron, j, with $\vec{x}_\mathrm{j}$. Hence, it is sufficient to approximate $|\vec{x}_\mathrm{i} - \vec{x}_\mathrm{j}| \approx R - \vec{n}\vec{x}_\mathrm{j}$ in the exponent. This, together with the kinematic approximation, that the local fields $E_\mathrm{j}^\mathrm{loc}$ are solely determined by the incident plane wave $E_\mathrm{ext}\vec{\epsilon}_0 e^{i\vec{k}_0\vec{x}_\mathrm{i}}$, one finds for the scattered field at P:

$$\vec{E}_\mathrm{j}^\mathrm{scatt}(P) = r_0 E_\mathrm{ext} \frac{e^{i|\vec{k}_0|R}}{R} \cdot \vec{n} \times (\vec{n} \times \vec{\epsilon}_0) \sum_\mathrm{j} e^{i\vec{Q}\vec{x}_\mathrm{j}} \tag{2.8}$$

where the polarization vector $\vec{\epsilon}_0$ of the incoming wave has been introduced. The vectorial change in the wave number has been introduced in the previous

section as $\vec{Q} = \vec{k}_0 - |\vec{k}_0|\vec{n} = \vec{k}_0 - \vec{k}_\mathrm{S}$. One notes that the radiation is polarized in the plane containing $\vec{\epsilon}_0$ and $\vec{n}$. More specifically, the vector product can be evaluated and yields:

$$\vec{n} \times (\vec{n} \times \vec{\epsilon}_0) = -\sin(\angle(\vec{n}\vec{\epsilon})) = -p, \tag{2.9}$$

where p denotes the polarization factor. In X-ray scattering it is usually more convenient to specify the angle between the incoming and scattered directions. It is denoted by 2θ. Then one writes

$$p = \begin{cases} 1 & \text{if } P \text{ is in the plane of } \vec{k}_0 \text{ and } \vec{\epsilon} \\ \cos(2\theta) & \text{if } P \text{ is out of plane of } \vec{k}_0 \text{ and } \vec{\epsilon} \end{cases} \tag{2.10}$$

The polarization factor $\cos(2\theta)$ is simply due to the fact that an observer in the plane of the polarization of the incident wave sees a reduced acceleration with increasing 2θ, which is exactly zero for $2\theta = \pi$. Or in other words: a dipole does not radiate along its axis.

We now turn to (perfect) crystalline materials, where we have to take into account the basis $\vec{R}_\mathrm{n}$ forming the crystal, the relative positions of the different atoms within the basis or unit cell and their atomic form factors. This yields the well known result (for example Warren [41], Jens Als-Nielsen [42]):

$$E^{\mathrm{crystal}}(\vec{Q}) = -p \cdot r_0 \cdot E_{\mathrm{ext}} \frac{e^{i|\vec{k}_0|R}}{R} \cdot F_{\mathrm{hkl}} \sum_\mathrm{n} e^{i\vec{Q}\vec{R}_\mathrm{n}} \tag{2.11}$$

with the following definition for the structure factor for one unit cell

$$F_{\mathrm{hkl}} = \sum_j f_0^\mathrm{j}(\vec{Q}, E) e^{i\vec{Q}\vec{r}_\mathrm{j}}. \tag{2.12}$$

Here $\vec{r}_\mathrm{j}$ is the position of the jth atom/molecule in the unit cell. The unit cell structure factor F_{hkl} depends on the kind of atoms and their relative positions. Constructive or destructive interference from the scattered waves of the individual atoms within a unit cell results in a modulated X-ray reflectivity. In particular, if the waves scattered from similar atoms are exactly out of phase, one speaks of forbidden reflections.

The set of vectors $\vec{R}_\mathrm{n}$ builds the lattice and can be written in the form:

$$\vec{R}_\mathrm{n} = n_1\vec{a}_1 + n_2\vec{a}_2 + n_3\vec{a}_3 \tag{2.13}$$

where n_1, n_2 and n_3 are integer numbers and $a_1 = a$, $a_2 = b$ and $a_3 = c$ are the lattice constants of a unit cell. Equation 2.11 can be replaced by a geometric sum, and after multiplication of the resultant product with its

complex conjugate one obtains the so-called interference function, sinc^2. In the limit of large crystals this only yields a nonzero diffracted intensity if $\vec{Q}\vec{R}_\mathrm{n} = 2\pi \times integer$. Very often it is easier to describe the scattering process in reciprocal space, spanned by the reciprocal basis vectors (a_1^*, a_2^*, a_3^*), which fulfill $a_\mathrm{i} \cdot a_\mathrm{j}^* = 2\pi\delta_\mathrm{i,j}$. The points on this reciprocal lattice are specified by vectors of the type $\vec{G} = h\vec{a}_1^* + k\vec{a}_2^* + l\vec{a}_3^*$, where h, k, l are integers and are usually referred to as Miller Indices. Accordingly, lattice planes are denoted by (h,k,l), directions in the unit cell by [h,k,l]. We can now re-express the condition for a non-vanishing scattered amplitude by the Laue condition:

$$\vec{Q} = \vec{G}. \tag{2.14}$$

It is easily shown that the Laue condition is equivalent to the Bragg law, which reads as follows:

$$k \cdot d \cdot \sin(\theta) = \pi \times integer \tag{2.15}$$

where d is a lattice constant or, more generally, the distance between two scattering atomic planes $\mathrm{d_{hkl}}$.

Attenuation of the incoming X-ray beam due to absorption is readily included by multiplying the total diffracted energy per volume block δV of the crystal by the absorption factor $\exp(-\mu z/\sin(\theta))$ and integrating over the penetration depth, z. Here μ denotes the linear absorption coefficient.

2.4 Diffuse Scattering

Diffraction patterns of 'real' materials contain, in addition to sharp Bragg peaks, a continuous background known as diffuse scattering. This scattering necessarily arises whenever there are departures from a perfectly periodic structure. Such deviations can exist on different length scales and may have different physical origins, but all of these effects may be brought together under a common name: disorder.

Generally, diffuse scattering is defined as the difference between the total and the coherently scattered (Bragg peaks) light:

The total differential scattering cross-section for electrons in the kinematic approximation [38] is calculated with the absolute square of equation 2.3:

$$\left(\frac{d\sigma}{d\Omega}\right)_\mathrm{total} = \left\langle \left| \sum_\mathrm{j} r_0 e^{i\vec{Q}\vec{x}_\mathrm{j}} \right|^2 \right\rangle |\vec{n} \times (\vec{n} \times \vec{\epsilon})|^2 \tag{2.16}$$

where the symbol $\langle\rangle$ means average over time, that is, the average over the movements of atoms taking different values of $\vec{x}_\mathrm{j}$. In an experiment the

observation time is always large with respect to the time scale of atomic motions[2], hence, one always averages over many 'instantaneous' realizations of the structure [43]. The last factor $|\vec{n}\times(\vec{n}\times\vec{\epsilon})|^2 = 1/2\cdot[1+\cos^2(2\theta)]$ allows for polarization averaging for an unpolarized incident X-ray beam.

However, the differential scattering cross-section of the coherently scattered light (Bragg peaks) corresponds to the absolute square of the average structure

$$\left(\frac{d\sigma}{d\Omega}\right)_{\text{Bragg}} = \left|\left\langle\sum_{\text{j}} r_0 e^{i\vec{Q}\vec{x}_{\text{j}}}\right\rangle\right|^2 |\vec{n}\times(\vec{n}\times\vec{\epsilon})|^2. \tag{2.17}$$

The diffuse scattering is then simply the difference of the two, namely,

$$\left(\frac{d\sigma}{d\Omega}\right)_{\text{diffuse}} = \left(\frac{d\sigma}{d\Omega}\right)_{\text{total}} - \left(\frac{d\sigma}{d\Omega}\right)_{\text{Bragg}} \tag{2.18}$$

In the limit of a perfect crystal structure the coherently scattered light is identical to the total scattered light. However, in the other limit, when $\vec{Q}\vec{x} \gg 1$ all summands in equation 2.17 vanish in the averaging (as the mean of quickly oscillating functions) and the coherent scattering is equal to zero.

One can easily show (for example Warren [41]) that equation 2.18 does not produce sharp Bragg-like structures if random deviations only are allowed from the strictly periodic structure. Hence, it describes a broadly distributed, smoothly varying intensity component. Note that diffuse scattering contains complementary information to the conventional analysis of Bragg peaks as it is sensitive on how *pairs* of atoms behave and is, potentially, a rich source of information on how atoms and molecules interact [44, 45].

Certainly the most well known and prominent disorder stems from thermal motion. Since the frequency of X-rays is extremely high (ν(Cu K_α)= 1.2×10^{18} Hz), a scattering event always takes place with a quasi-static structure. In a classical picture this is even (mostly) true for the position of the scattering electrons, and certainly always true for much slower thermal vibrations. X-ray scattering, therefore, takes place with a static structure where the individual scatterers are statistically displaced from their average position, described by the mean deviation $\langle\delta_{\text{j}}\rangle = 0$. The angle bracket $\langle\rangle$ again denotes temporal averaging. Evaluating the average of the e-function,

[2] In femtosecond X-ray diffraction this is not strictly true, however, one always measures the average over many events.

one finds two terms for the total cross-section:

$$\left(\frac{d\sigma}{d\Omega}\right)_{\text{total}} = r_0^2 \sum_{\text{i,j}} e^{-\frac{1}{2}Q^2\langle\delta_\text{j}^2\rangle} e^{i\vec{Q}\vec{x}_\text{j}} e^{-\frac{1}{2}Q^2\langle\delta_\text{i}^2\rangle} e^{i\vec{Q}\vec{x}_\text{i}} + \tag{2.19}$$

$$r_0^2 \sum_{\text{i,j}} e^{i\vec{Q}(\vec{x}_\text{j}-\vec{x}_\text{i})} \left(e^{Q^2\langle\delta_\text{i}\delta_\text{j}\rangle} - 1\right) \tag{2.20}$$

The first part of this equation leads to Bragg peaks which are attenuated by the Debye-Waller factor, $\exp(-M)$, where $M = -\frac{1}{2}Q^2\langle\delta^2\rangle$ is the mean temperature factor. It increases for larger scattering vector $\vec{Q}$, or for reflections with a high index. Typically, the average displacements of atoms $\sqrt{\langle\delta^2\rangle}$ at room temperature are in the range between 0.05 and 0.3 Å, which translates into a few to more than 10% of the bond length. The second term describes diffuse scattering. For a completely uncorrelated motion, all cross-terms in the sum vanish and only an isotropic, homogeneous, diffuse background remains. More generally, the width of diffuse scattering depends on what length scale movement of thermally excited atoms are correlated. Note again that in crystalline materials the smallest unit of correlated electrons is an atom. However, bonded molecules or larger fractions of the latter may also exhibit correlated motion, which manifests the diffuse scattering. This will be important in chapter 7, when discussing transient X-ray signals from molecular crystals.

2.5 X-Ray Reflectivity of a Superlattice

The expression superlattice refers to an artificial structure which consists of thin layers of different materials which are repeated periodically along one direction. Even though we calculate the X-ray reflectivity of such structures with the dynamical Darwin equation 2.33 (derived in the following section), it is very helpful to comprehend how the X-ray reflectivity pattern of a superlattice is influenced by its structural properties.

Figure 2.2 depicts a perfect superlattice structure in one-dimensional real space. It consists of N double layers with a periodicity $D = d_\text{A} + d_\text{B}$ along the z direction. The layers A and B have a lattice constant in growth direction of a_A and a_B and a scattering amplitude f_A and f_B, respectively. A rectangular, that is, abrupt profile of the layer sequence along the growth direction is assumed. To illustrate the diffraction pattern in a simple way, we recall that the real and reciprocal space are connected by Fourier transform, and to calculate the intensity we use the kinematic approximation. The structure can be decomposed along the z-axis into the sum of both materials.

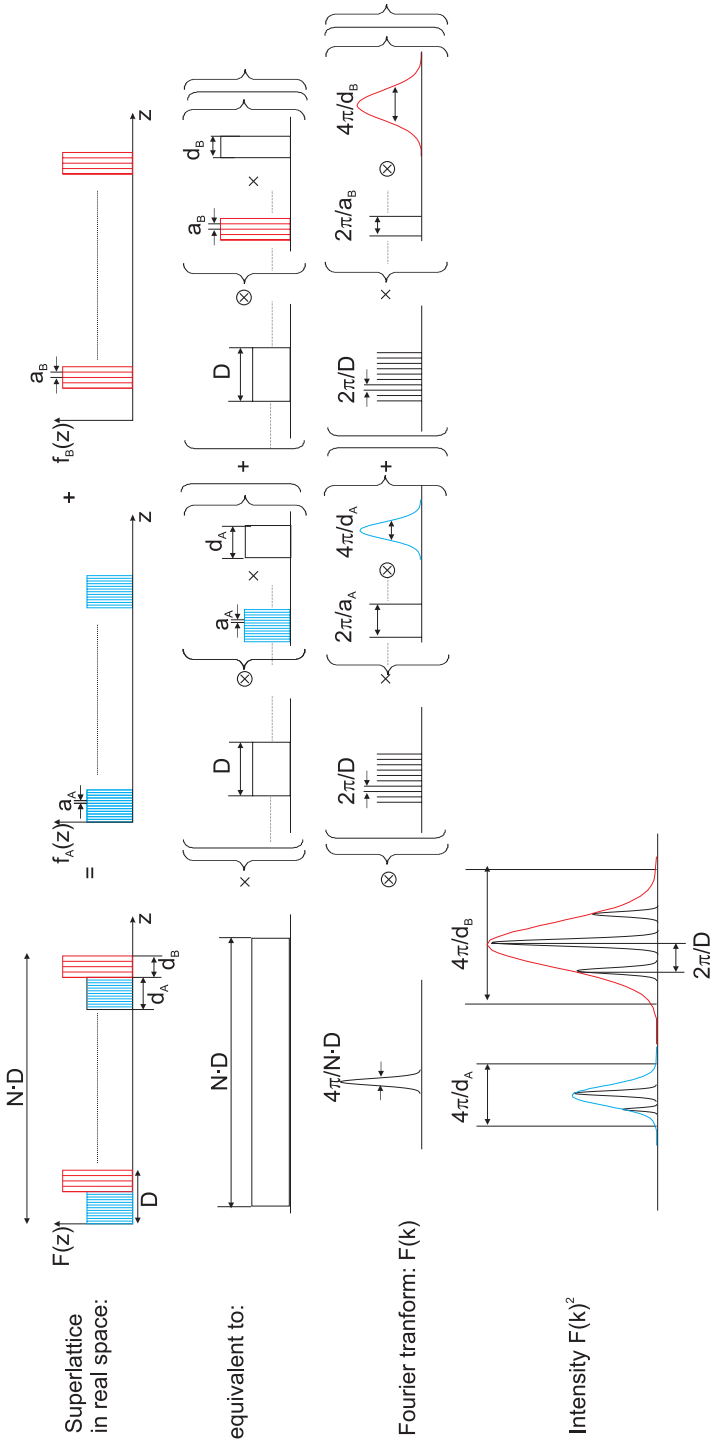

Figure 2.2: X-Ray analysis of a superlattice structure. Schematic based on [46]

Further, the two materials can be considered to consist of repeating atomic planes with distance $a_{\mathrm{A/B}}$ each multiplied with their actual thickness $d_{\mathrm{A/B}}$. Convoluting these objects with the periodicity D and adding them yields the equivalent superlattice as depicted at the top left corner in figure 2.2. Finally, one has to take into account that the superlattice is not infinitely extended in space, but consists only of N alternating layers. The X-ray pattern is obtained by taking the Fourier transform of this decomposed structure: the finite extension of the superlattice structure corresponds to a broadening of the superlattice peaks to a width of $4\pi/ND$. The additional periodicity D of the structure is equivalent to equally spaced peaks with distance $2\pi/D$ in Fourier space. The lattice planes of the layers A and B give rise to envelope functions with distance $2\pi/a_{\mathrm{A/B}}$ and a width determined by their respective thickness $d_{\mathrm{A/B}}$. Their amplitude is proportional to the structure factor $f_{\mathrm{A/B}}$. For sufficiently large differences between a_{A} and a_{B}, and no interference between their scattering amplitudes, this yields the final X-ray pattern, which is shown in the bottom of figure 2.2. It is made up of the equally distanced superlattice peaks with finite width, multiplied with the envelope functions of the individual layers.

Experiments in chapter 5 and 6 are performed on nano-layered superlattice structures. The advantages of this sample geometry are manifold: the additional periodicity exhibits favorable properties for X-ray scattering, namely an increased reflectivity compared to single layers, and strong amplification of reflectivity changes despite only subtle changes in lattice structure. Such amplification of intensity changes will be particularly pronounced if superlattice peaks are positioned at the steep slope of the envelope function and structural changes modulate the layer thicknesses $\mathrm{d_{A,B}}$, that is, shift the envelope functions. Also in the performed experiments the time-scale of lattice excitations are governed by strain propagation, that is, by the sample thickness and the velocity of sound, which makes the use of thin layers a prerequisite to resolve ultrafast processes. Finally structural changes which mainly involve rearrangement of light elements like oxygen, are very difficult to observe by X-rays scattering, whereas their subsequent coupling to volume expansion is readily detected. Then the resolved time-scale is again ultimately limited by the layer thicknesses.

2.6 Reciprocal Space Mapping

X-ray reflections (0 0 l) of atomic planes parallel to the surface contain no information about the in-plane lattice constants. To fully characterize the structure of a superlattice, it is crucial to know whether the layers are grown

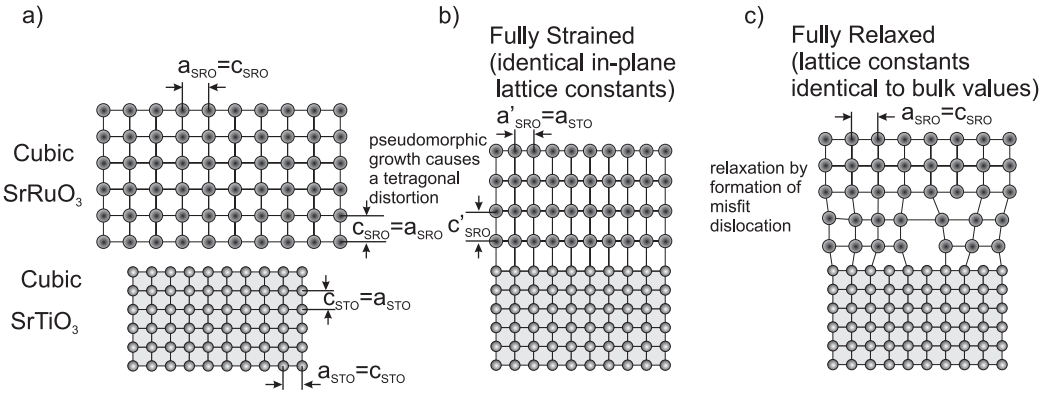

Figure 2.3: **a**) Two materials (for example, $SrTiO_3$ and $SrRuO_3$) with different in plane lattice constants. **b**) Pseudomorphic growth causes a tetragonal distortion. **c**) The layers relax by formation of misfit dislocations.

pseudomorphically on the substrate, that is, the in-plane lattice constant a is dictated by the substrate and is identical for the entire structure, or whether the layers are relaxed and have lattice constants identical to their bulk values. Usually, it is a delicate balance of layer thickness and misfit strain that decides whether a superlattice is pseudomorphic or relaxed. Thick layers with large differences in lattice constants tend to relax through the formation of dislocations. Furthermore, strain may significantly alter the physical properties of the thin layers, something which is particularly pronounced in strained ferroelectric layers because of the strong strain-polarization coupling (compare chapter 6.1.3). The two extreme cases are schematically shown in figure 2.3 for the materials $SrTiO_3$ and $SrRuO_3$.

Reciprocal space mapping is performed such that the Bragg reflection under investigation is fully mapped in a confined area in Q space. One chooses an asymmetric reflection, such that the diffracting atomic planes ($h\ k\ l$) contain information on both the in- and out-of-plane lattice constant. This is depicted schematically in figure 2.4 a) for real space: the incoming X-ray beam, $\vec{k}_0$, is Bragg matched with respect to the diffracting plane and makes an angle, ω, with the surface of the crystal. The included angle between the outgoing X-ray beam, k_S, and k_0 is $(\pi - 2\theta)$. In reciprocal space the diffracting condition may be understood with help of the Ewald sphere: a circle with radius $|\vec{k}|$ is drawn around the starting point of the incoming vector $\vec{k}_0$ and for every reciprocal lattice point which intersects the circle one gets a Bragg reflection. This is shown for the Bragg peak (1 0 3) in figure 2.4 b). To map Q-space around the reciprocal lattice point one has to perform successive $(\omega - 2\theta)$ scans for different starting values of ω. Note that that

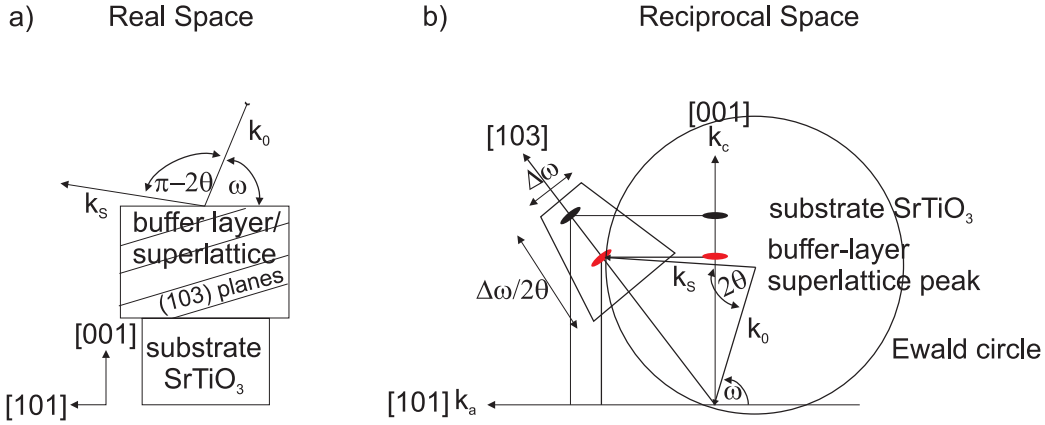

Figure 2.4: **a**) Asymmetric Bragg reflection in real space **b**) An ω-scan in combination with a $\omega - 2\theta$-scan spans reciprocal space around a reciprocal lattice point.

in an ω-scan the reciprocal space perpendicular to the [h k l] direction is scanned, while an $(\omega - 2\theta)$-scan measures along the [h k l] direction, spanning Q-space. The experimental realization is straightforward: an ω-scan is performed by rotating the crystal, keeping the position of the detector fixed, while an $(\omega - 2\theta)$-scan involves rotating both crystal and detector with a ratio 1:2. From the geometry of the reciprocal lattice and the Ewald construction, it is easily found that [compare figure 2.4]:

$$k_{\mathrm{c}} = \frac{2}{\lambda} \sin\theta \cos(\omega - \theta) \tag{2.21}$$

$$k_{\mathrm{a}} = \frac{2}{\lambda} \sin\theta \sin(\omega - \theta) \tag{2.22}$$

where λ is the X-ray wavelength and θ equals $2\theta/2$. The projection of the measured reciprocal points to k_{a} and k_{c} yields the respective lattice constants a and c directly. In the schematically depicted case in figure 2.4 for a (103) reflection one calculates $c = 3 \cdot 2\pi/k_{\mathrm{c}}$ and $a = 1 \cdot 2\pi/k_{\mathrm{a}}$. Elongations of the reciprocal points along the ω directions give information about the mosaic spread of the sample (its degree of imperfection) and elongation along k_{c} is a measure of the fluctuation in thickness of the superlattice layers. For more details on high resolution X-ray scattering and reciprocal space mapping refer to [47–49] or to the textbook 'Thin Film Analysis by X-Ray Scattering' by Birkholz [50].

2.7 Dynamical X-ray Diffraction Theory

In the following we will discuss the two-wave approximation for dynamical X-ray diffraction theory. We consider a translation symmetry with respect to atomic planes d_{hkl} with homogeneous electron density. In this configuration equation 2.3 is greatly simplified since only two electric fields interact, namely, the reflected and transmitted wave.

The Darwin formalism leads to the correct description of X-ray diffraction from highly perfect crystals and turns out to be particularly adequate to account for scattering of crystalline (strained) nano-layers. Furthermore, it allows to calculate the primary extinction, the attenuation of the transmitted beam due to coherent scattering losses.

2.7.1 Scattering from a Single Layer of Atoms

Let us consider the reflection of a single layer of atoms, with M atoms per unit area in the XY plane. The incident plane emanates from a distant point, S, and we want to calculate the scattered radiation at point, P, and the transmitted radiation at P' (compare figure 2.5). Let the rays $\overline{S0}$ and

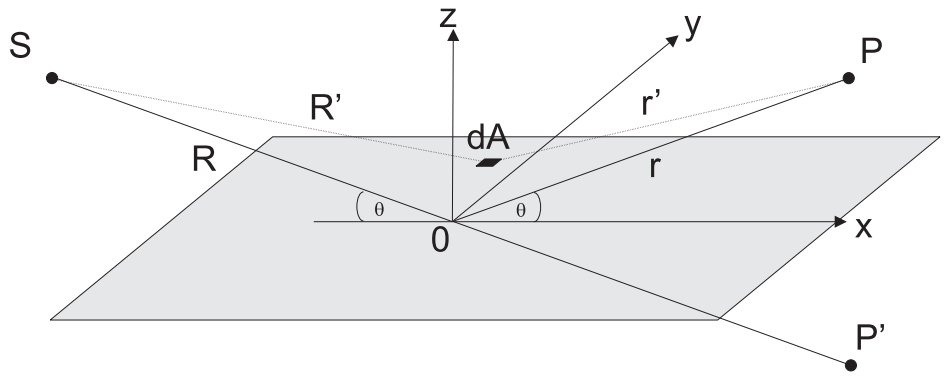

Figure 2.5: Representation of an X-ray beam coming from point S incident on a single layer of atoms in the XY-plane. The scattered radiation is observed at point P and the transmitted radiation at P'.

$\overline{0P}$ make equal angles θ with the XY plane and let the origin 0 be chosen such that $\overline{S0} + \overline{0P}$ is minimum. The amplitude of the primary beam at the origin is E_{ext}. For simplicity we assume the beam $\vec{E}_{\mathrm{ext}}$ to be polarized parallel to the Y-axis. First, we determine the value of the electric field due to radiation scattered by atoms in the element of area dA with the total path

length $R' + r'$.

$$dE_P = \frac{-E_{\text{ext}} r_0 f_0(\vec{Q}, E)}{r'} e^{ik_0(R'+r')} M dA$$

In comparison with equation 2.3 this represents the local field due to scattering of electrons homogenously distributed in the area, dA. Then the total scattered field E_{P} is given by summarizing over contributions from all atoms in the plane. We replace the sum by an integral because the phase varies only slowly. Only atoms close to the origin 0 contribute to the integral such that it is possible to replace r' by the average value r and one calculates (for example Warren [41]):

$$E_{\text{P}} = E_{\text{ext}}(-iq) e^{ik_0(R+r)} \tag{2.23}$$

with the abbreviation

$$q = r_0 \frac{2\pi M f_0(\vec{Q}, E) p}{\sin(\theta) k} \tag{2.24}$$

where we have reintroduced the polarization factor, p. For all atoms other than the ones at the origin 0, the path length is longer than the minimum distance $R + r$ and the weighted average of the contributions corresponds to an effective increase in path length of $\lambda/4$. This is the significance of the additional 90° phase shift. The transmitted field $E_{\text{P}'}$ is the sum of the primary and the scattered waves, except that we replace q with q_0:

$$q_0 = r_0 \frac{2\pi M f_0(0, E)}{\sin(\theta) k}. \tag{2.25}$$

yielding:

$$E_{\text{P}'} = E_0(1 - iq_0) e^{ik_0(R+r)} \approx E_0 e^{ik_0(R+r)} e^{-iq_0}. \tag{2.26}$$

2.7.2 Refractive Index

If the X-ray beam with incidence angle, θ, travels a distance, r, within a crystal with layers spacing, d, the number of traversed layers is given by $s = r \sin\theta / d$. Using this expression, we can write for the total field at point P':

$$E_{\text{P}'} = E_0 e^{ik_0(R+r)} e^{-isq_0} = E_0 e^{ik_0(R + r(1 - \frac{q_0 \sin\theta}{kd}))} \tag{2.27}$$

Comparing this expression with a wave which travels a distance R through empty space with wavelength $\lambda = 2\pi/k_0$ and a distance r in a medium with wavelength $\lambda' = 2\pi/k_{\text{S}}$, the electric field is determined to be:

$$E_{\text{P}'} = E_0 e^{ik_0 R + ik_{\text{S}} r} \tag{2.28}$$

The index of refraction in the medium is defined as $n = k_0/k_S$. Comparison of equations 2.27 and 2.28 yields:

$$n = 1 - \frac{q_0 \sin(\theta)}{kd} = 1 - r_0 \frac{2\pi N f(0,E)}{k^2}. \tag{2.29}$$

This predicts an index of refraction which is smaller than unity, in agreement with the experimentally measured value. The negative sign in equation 2.29 is a direct result of the cross product in equation 2.1. Whereas in expressions for the intensity of a diffracted beam, the negative sign always drops out when squaring the amplitude, the index of refraction is a phenomena, where the negative sign can be measured directly. This result may also be compared with the simple Lorentz oscillator model, where the real part of the dielectric function drops below zero at resonances and approaches unity for large frequencies.

2.7.3 Darwin Formalism

To formulate the dynamical diffraction theory allowing for multiple scattering events, we follow essentially the same approach as first developed by Darwin [51] in 1914. The perfect crystalline structure is treated as an infinite stack of atomic planes, each of which scatters a small wave, which may be subsequently re-scattered in the direction of the incident beam. As depicted in figure 2.6 a) each layer labeled with the index r, starting with the surface layer $r = 0$, transmits and reflects the incident field. Let the angle contained between the incident field and the atomic layers be denoted by θ and the distance between neighboring planes by d. The objective is to calculate the transmission T_0 and, more importantly, the reflectivity R_0, which is the ratio between the total reflected wavefield S_0 and incident field T_0. The field T propagates in the direction of the incident beam, while the S field travels in the direction of the reflected beam. Both experience attenuation and a phase shift due to absorption and scattering at each plane r. From Bragg's law it is immediately evident that get only an appreciable reflected wave, when the field S scattered at plane r is in phase with the reflected field from layer r+1. In figure 2.6 b), this corresponds to the requirement that the distance AMA' is equal to an integer number of π or expressed in terms of a phase factor ϕ:

$$\phi = kd \sin(\theta). \tag{2.30}$$

To derive the fundamental difference equations for the matrix Darwin formalism let us denote the field above layer r on the z-axis with T_r and S_r. The reflected S field just above the r+1 layer at point M is S_{r+1} and after

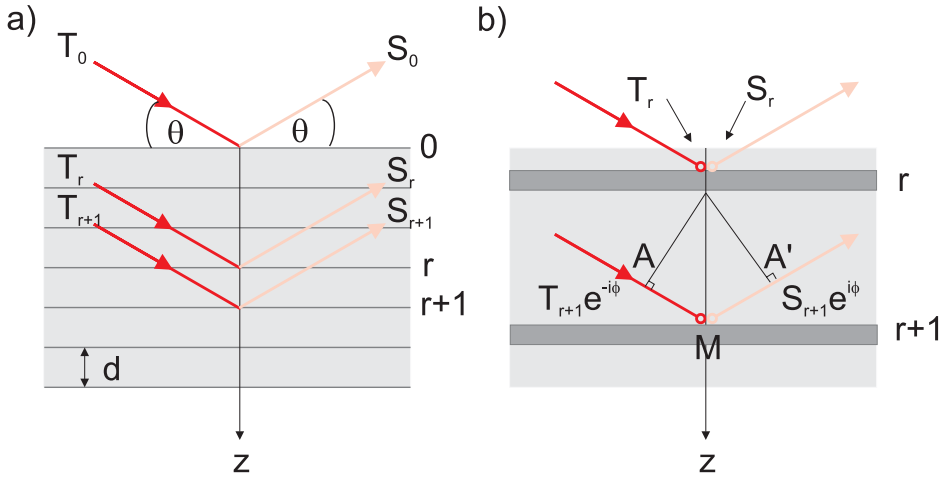

Figure 2.6: **a**) Transmission T_r and Scattering S_r of a perfect crystal with the atomic layers labeled r. The amplitude reflectivity is defined as the ratio between the total reflected field S_0 and the total incident field T_0. **b**) Schematic to derive the fundamental difference equation.

propagating to position A' it is $S_{r+1}e^{i\phi}$. Transmission through the r'th layer changes the field by a factor $(1-iq_0)$ as calculated in equation 2.26. Addition of the reflected part $-iqT_r$ (compare equation 2.23) yields the total field:

$$S_r = (1 - iq_0)S_{r+1}e^{i\phi} + (-iq)T_r \tag{2.31}$$

Similarly we can construct the field T just below the r'th layer. Its wavefront is shifted by the distance $\overline{AM}$, that is, $T_{r+1}e^{-i\phi}$. It consists of the transmitted and attenuated field $(1-iq_0)T_r$ and the wave $S_{r+1}e^{i\phi}$, which is reflected from the bottom of the r'th layer:

$$T_{r+1}e^{-i\phi} = (1 - iq_0)T_r + (-iq)S_{r+1}e^{i\phi} \tag{2.32}$$

In the derivation of these two equations we have assumed that the reflectivity per layer is small and the higher order reflections proportional to q^3, q^5, et cetera, are ignored. The above derivation also becomes invalid when the scattering angle θ approaches zero, as in the range of total reflection. Simple algebraic rearrangement connects the transmitted and scattered field of layer

r with the layer r+1:

$$\begin{pmatrix} S_{\mathrm{r}} \\ T_{\mathrm{r}} \end{pmatrix} = \underbrace{\frac{1}{1-iq_0}\begin{pmatrix} (1-iq_0)^2-(-iq)^2 & (-iq) \\ -(-iq) & 1 \end{pmatrix}}_{H}\underbrace{\begin{pmatrix} e^{i\phi} & 0 \\ 0 & e^{-i\phi} \end{pmatrix}}_{L}\begin{pmatrix} S_{\mathrm{r+1}} \\ T_{\mathrm{r+1}} \end{pmatrix}$$
$$= H \cdot L \begin{pmatrix} S_{\mathrm{r+1}} \\ T_{\mathrm{r+1}} \end{pmatrix} \tag{2.33}$$

In this expression we have separated effects due to scattering and absorption, which is described by the matrix H, and propagation effects described by the matrix L. To calculate the absolute reflectivity of a structure consisting of one layer, the reflected/transmitted amplitude is equal to $(S_1, T_1) = (0, T_1)$, which yields a reflectivity $R_{\mathrm{N}} = |-iqe^{-2i\phi}|^2$ (compare equation 2.23). This is equivalent to $|(HL)_{12}/(HL)_{22}|^2$, where the two indices mark the entry of the (2×2) matrix HL. For a structure consisting of N layers, we set the amplitudes below layer N to be equal to $(S_{\mathrm{N+1}}, T_{\mathrm{N+1}}) = (0, T_{\mathrm{N+1}})$. Adding more layers is equivalent to a multiplication of the matrices $H_{\mathrm{N}}L_{\mathrm{N}} \cdot H_{\mathrm{N-1}}L_{\mathrm{N-1}} \cdots H_1L_1$ for the respective atomic layers $N, N-1, \cdots, 1$. Along the same lines, we can determine the absolute transmission T_0. The total reflectivity R_0 and transmission T_0 for a structure with N layers is then given by

$$R_0 = \left| \frac{\prod_{r=1}^{N} (H_r L_r)_{12}}{\prod_{r=1}^{N} (H_r L_r)_{22}} \right|^2 \qquad T_0 = \left| \frac{1}{\prod_{r=1}^{N} (H_r L_r)_{22}} \right|^2 \tag{2.34}$$

It is straightforward to extend this matrix formalism to more complex unit cells and heterostructures consisting of layers composed of different atoms and with different interatomic spacings. Note that uniaxial strain can easily be accounted for by adjusting the k dependent phase factor ϕ in the propagator matrix L. Please take note of further details summarized in Appendix A.

2.7.4 Extinction

When an X-ray beam traverses a crystalline solid, it is attenuated. One can differentiate two mechanisms, absorption and scattering. For moderate X-ray photon energies (that is $h\nu < m_{\mathrm{e}}c^2$=1.022 MeV) absorption is dominated by the photo-effect and is described by the imaginary part of the atomic form factor (see equation 2.7). The effect of extinction due to scattering may already be appreciated for a single electron. Using equation 2.1 as the local

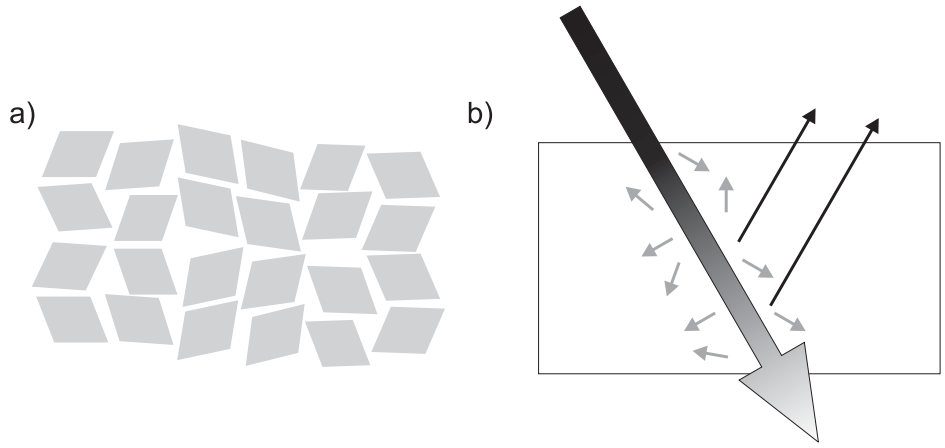

Figure 2.7: **a**) Schematic of a mosaic crystal. **b**) Extinction due to coherent Bragg-scattering (black arrows) and incoherent scattering (grey arrows).

field for a single electron in equation 2.4 for the radiated field at the position of the electron shows that the radiated wave acts on the electron itself. This is known as radiation damping, and implies that the radiated field is directed against the local field and slows the movement of the electron. The energy of the radiated wave is lost for the incident plane wave and results in an attenuation in the forward scattering direction. In the framework of scattering in crystalline materials, attenuation due to elastic X-ray scattering is usually denoted by primary and secondary extinction. (In what follows Compton-scattering, that is, inelastic scattering, is also neglected.) The underlying (oversimplified) picture is due to Darwin and schematically depicted in figure 2.7 a). The crystal is considered to be an assembly of mosaic blocks, where each little block can have a high degree of perfection. The orientations of the individual blocks have a slight variation, which can be caused by small grain boundaries or some other kind of dislocations. Primary extinction describes the attenuation of the primary beam due to coherent scattering into a Bragg peak for one (large) block and follows directly with equation 2.34 for T_0 [black arrows in figure 2.7 b)]. For a strong Bragg reflection in highly perfect crystals, the extinction length may be as short as a few micrometers, easily an order of magnitude smaller than the absorption length of the material. If the individual blocks are small and their orientational disorder is small, secondary extinction plays a role as well, since the scattering of each block cannot be considered as incoherent with respect to diffraction from other blocks. In other words the primary beam is reduced in intensity because it has been diffracted by several blocks with identical orientation. Note that what is usually referred to as 'blocks' may have very different physical ori-

gins. For example, such correlations of atomic positions may also be caused by rigid molecules, or a well ordered fraction of the latter. Such 'blocks' may then be responsible for an appreciable extinction. The scattered light is radiated in many different directions leading to a pronounced anisotropy of the extinction [grey arrows in figure 2.7 b)].

Historically, the word extinction refers to the fact that the *integrated* intensity is reduced in an experiment where extinction effects play a role and where the sample is rotated through the reflecting position or, equivalently, when the incident beam is divergent. However, it is important to keep in mind that for a monochromatic, highly parallel beam the reflection of a perfect crystal is nearly one and, of course, larger than for a mosaic crystal.

In chapter 4 primary extinction in a highly perfect crystal plays a decisive role to interpret the time-resolved X-ray data.

In chapter 7 experimental results are discussed, where the transmitted beam is modulated by strong anisotropic incoherent scattering, whereas coherent Bragg-scattering plays a minor role. This may be classified as secondary extinction.

2.8 Perovskite Oxides

2.8.1 Elementary Interactions

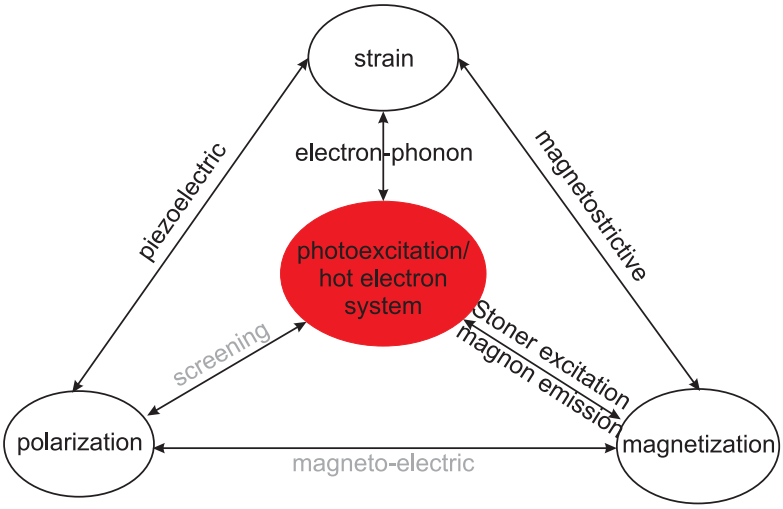

Figure 2.8: Elementary interactions in multiferroics. The black labeled interactions are discussed in detail in chapter 5 and 6.

The physical properties of Perovskite oxides are extremely diverse, rang-

ing from metallic and ferromagnetic ($SrRuO_3$), insulating and ferroelectric ($PbTiO_3$) to anti-ferroelectric and dielectric ($SrTiO_3$). Of particular interest for this work are the manifold interactions between these many different types of electronic ordering and structural degrees of freedom. A schematic overview is given in figure 2.8 and listed below:

- A photoexcited electron system at an elevated temperature cools down by electron-phonon coupling and induces strain in the material (section 5.3).
- Optical induced demagnetization by Stoner excitations, i.e. spin flips, will couple to strain via the magneto-volume effect (section 5.4).
- Strain couples to the macroscopic polarization by the piezoelectric effect (chapter 6).
- Excited electrons in a ferroelectric material can screen electric fields and modify the macroscopic polarization.
- Materials that display simultaneous electric and magnetic order have received considerable interest in recent years [52]. If magnetization can be induced by an electric field and electrical polarization by a magnetic field one speaks of the the magneto-electric effect.

The first three types of interactions will be discussed in detail in chapter 5 and 6.

2.8.2 Static Structures

In the following, we will briefly introduce the structural properties of the three different kinds of Perovskite oxides which are the building blocks of the superlattices studied in this work. The present work deals exclusively with Perosvkite crystal structures ABO_3 with A=Sr,Pb and B=Ti,Ru,Zr.

Properties of $\mathbf{Pb(Zr_{1-x}Ti_x)O_3}$

Figure 2.9 shows a schematic of the ABO_3 crystal structure in the paraelectric phase and for $PbTiO_3$ in the ferroelectric phase. Ferroelectric $PbTiO_3$ has a tetragonal unit cell with lattice constant $a = b = 3.904$ Å and $c = 4.152$ Å. The undistorted diamond shape of the oxygen octahedra together with its absolute displacement with respect to Ti ($\xi_{Ti-O} = 0.30$ Å) and Pb ($\xi_{Pb-O} = 0.47$ Å) was determined in a combination of X-ray and neutron diffraction experiments [53]. Note, that due to the small atomic scattering

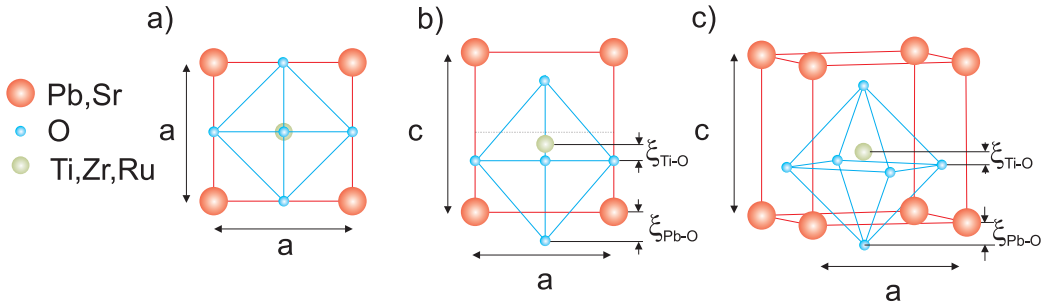

Figure 2.9: **a**) Cubic, non-polar structure of an ABO_3 Perovskite crystal. **b**) Crystal structure of $PbTiO_3$ in the ferroelectric phase. The phase transition is accompanied by a tetragonal distortion, that is, an elongation along the polarization direction c and an ion displacement ξ_{Pb-O} and ξ_{Ti-O}. **c**) 3-dimensional view of the ferroelectric structure showing the oxygen octahedron.

amplitude of oxygen, it is a formidable task to determine its atomic positions. In particular, this is true in the present work, where we are mainly sensitive to the heavy atoms, namely, Ti/Zr and Pb. The growth of solid solutions of type $Pb(Zr_{1-x}Ti_x)O_3$ allows the tuning of the lattice constants and phase transition temperatures with changing composition, x. In the present work, we used a sample with a composition $x = 0.8$, which corresponds to a lattice constant $c = 3.93$ Å: perfectly matching the pseudocubic $SrRuO_3$.

Properties of $SrRuO_3$

$SrRuO_3$ crystallizes in an orthorhombically distorted Perovskite structure with lattice constants $a = 5.53, b = 5.57, c = 7.85$ [54]. Since the lattice distortion is small (0.4° degree), one can consider it to be *pseudocubic* with $a' = 3.93 = d_{110}$ [55]. Figure 2.10 depicts the orthorhombic and pseudocubic unit cell. If grown epitaxially on a $SrTiO_3$ substrate, the [110] direction is usually referred to as the [001] direction, pointing along the stacking direction. $SrRuO_3$ shows ferromagnetic ordering below its Curie temperature of $T_C = 160$ K.

Properties of $SrTiO_3$

$SrTiO_3$ is dielectric and crystallizes in a cubic Perovskite structure with a lattice constant $a = b = c = 3.905$. It is not ferroelectric at any temperature, but shows a tendency to a polar instability, with a polar phonon that strongly decreases in frequency as the temperature is lowered. However, at low temperatures, the phonon stabilizes and the transition does not occur, leading to

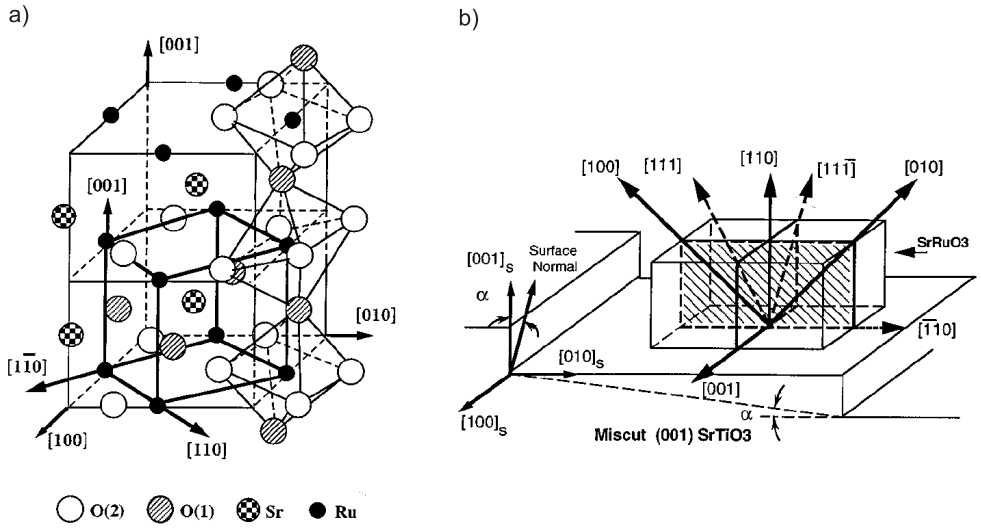

Figure 2.10: **a**) Schematic diagram of $SrRuO_3$ crystal structure in orthorhombic unit cell. The inner cube constructed by thick solid lines is the pseudocubic unit cell. **b**) The epitaxial arrangement of single domain epitaxial SrRuO3 [110] films on miscut [001] $SrTiO_3$ substrates. Usually the [110] direction of the pseudocubic structure is referred to the c-axis or [001] direction [56].

the term 'incipient ferroelectric' [57]. There is a structural phase transition at 110 Kelvin where the oxygen octahedra rotate around the z-axis to lower the symmetry to a tetragonal phase, called an antiferrodistortive transition [58]. However, the tetragonal distortion is very small $c/a = 1.00056$.

2.9 Transient Crystal Structures

In the following chapter, we present a very brief introduction to lattice dynamics, show how the dispersion relations for superlattice structures are modified and briefly discuss its relevance for time-resolved X-ray diffraction; more details are found in various textbooks, for example Kittel [59], Ashcroft and Mermin [60].

2.9.1 Lattice Dynamics in Superlattice Structures

If one assumes a restoring force which is proportional to the (small) displacement of atoms from their original equilibrium positions, a set of differential harmonic oscillator equations describe the lattice dynamics. For an n-atomic crystal, we have 3n equations: 3 describe the acoustic modes where atoms

within a unit cell oscillate in phase. The remaining 3(n-1) eigenmodes are called optical phonons. Here, neighboring atoms oscillate out of phase. One may also describe optical phonons as local distortions (within the unit cell) and acoustic phonons as global lattice distortions. If the displacement of the atoms is along the wavevector $\vec{k}$, the lattice vibrations are denoted as longitudinal, when they are perpendicular to $\vec{k}$, they are called transversal.

To simulate the lattice distortion we use a simple linear chain model [61]. It is valid for phonons propagating along the [001] direction, where planes of atoms move as a whole, and the longitudinal and transverse vibrations are decoupled. For longitudinal modes, we only consider a single nearest neighbor spring constant, while they are allowed to be different in different materials. The spring constants κ are fitted to the corresponding velocity of sound v and mass densities ρ of the material, according to the relation $\kappa = \rho v^2$. Only distortions of whole unit cells are taken into account, hence, optical phonons are not considered. For our purpose this simplified description is adequate, but note that optical-distortions may be readily incorporated as well [62]. The underlying concept is depicted in figure 2.11. Along one direction atoms with mass m_i (in our case unit cells) are connected by springs κ_i which are displaced from their equilibrium position by x_i. We consider N unit cells and the index i counts the unit cells. After optical excitation of one material (SRO, blue dots) stress builds up within time t_stress. This is equivalent to a compression of the corresponding springs with the atoms still at their equilibrium position, that is, no strain. At the interfaces where the stress is not balanced, propagating strain waves originate and modify the interatomic distances. For details about the calculation please refer to appendix B.

A superlattice structure gives rise to a new periodicity along its stacking direction z and defines a new structure unit cell. This is the origin of its distinct dispersion relation. If one superlattice period d_SL consists of several unit cell layers of the constituent materials, the new unit cell is large. The large unit cell in real-space corresponds to a folded Brillouin zone in k-space extending between $\mathrm{k_z}$=0 and π/d_SL. Acoustic phonon excitations of bulk materials that extend over many unit cells are modified in the superlattice. In k-space, such a modification manifests the back-folding of the bulk acoustic phonon dispersion into the folded Brillouin zone of the superlattice in z-direction. Backfolding results in additional phonon branches, which are, in fact, optical phonons in the superlattice zone scheme, separated by energy gaps at $\mathrm{k_z}$=0 and π/d_SL. This is shown in figure 2.12.

To be more specific we show a calculation for a superlattice structure containing 12 unit cells of $Pb(Zr_{0.8}Ti_{0.2})O_3$ and 16 unit cells $SrRuO_3$. This sample was used in a series of experiments, in particular in chapter 6. In

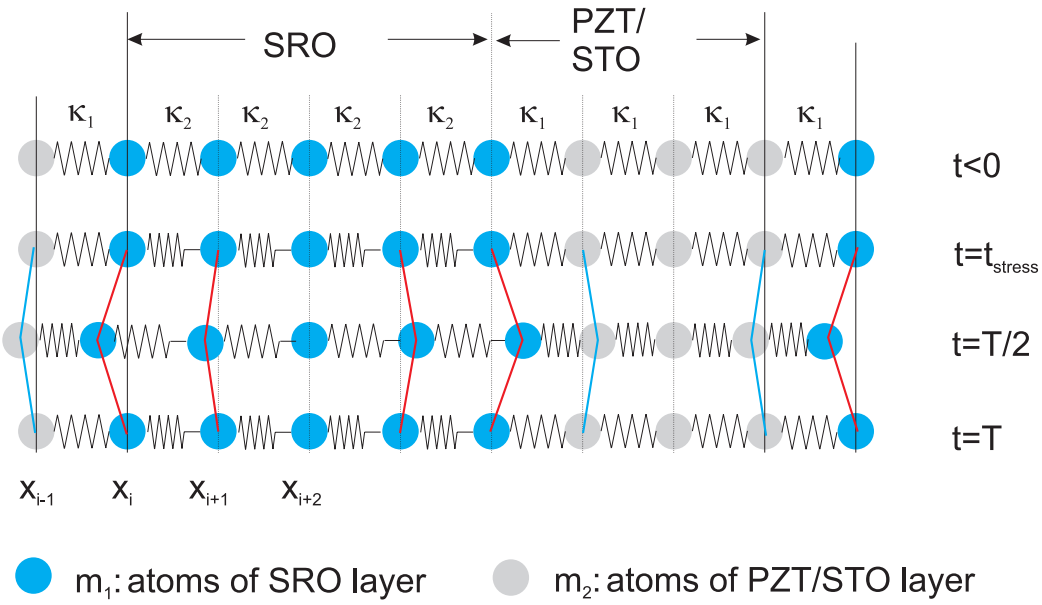

Figure 2.11: Schematic of linear chain model. Stress in the SRO layers is produced within t_{stress}, equivalent to a compression of the springs, with the atoms still at their equilibrium position (that is, no strain). Propagating strain fronts originate from interfaces where the stress is not balanced. Lower rows show a snapshot of a ZFLAP oscillation for $t = T/2$ and $t = T$.

the folded Brillouin zone these longitudinal acoustic phonons are referred to as zone folded acoustic phonons or ZFLAP. They are former bulk acoustic phonons with wave vector $k = g_{\text{SL}}$, which are transformed into an optical phonon of the SL at $k = 0$. In figure 2.12 b), there exist two phonon modes at $k = 0$ and $\nu \approx 0.5$ THz, which correspond to a symmetric A_1 and anti-symmetric B_2 ZFLAP [red and blue dot in Figure 2.12 b)]. The A_1 mode has maximal atomic displacements and thus a node of the lattice strain $\Delta a/a_0$ at the center of the PZT and SRO layers, whereas the B_2 mode (blue dot) has maximal strain and no atomic displacement at these symmetry centers [compare figure 2.12 c)]. The fact that the symmetric A_1 mode has higher frequency than the asymmetric B_2 mode is determined by the masses and force constants in the linear chain model. X-ray diffraction is most sensitive on the $A1$ mode.

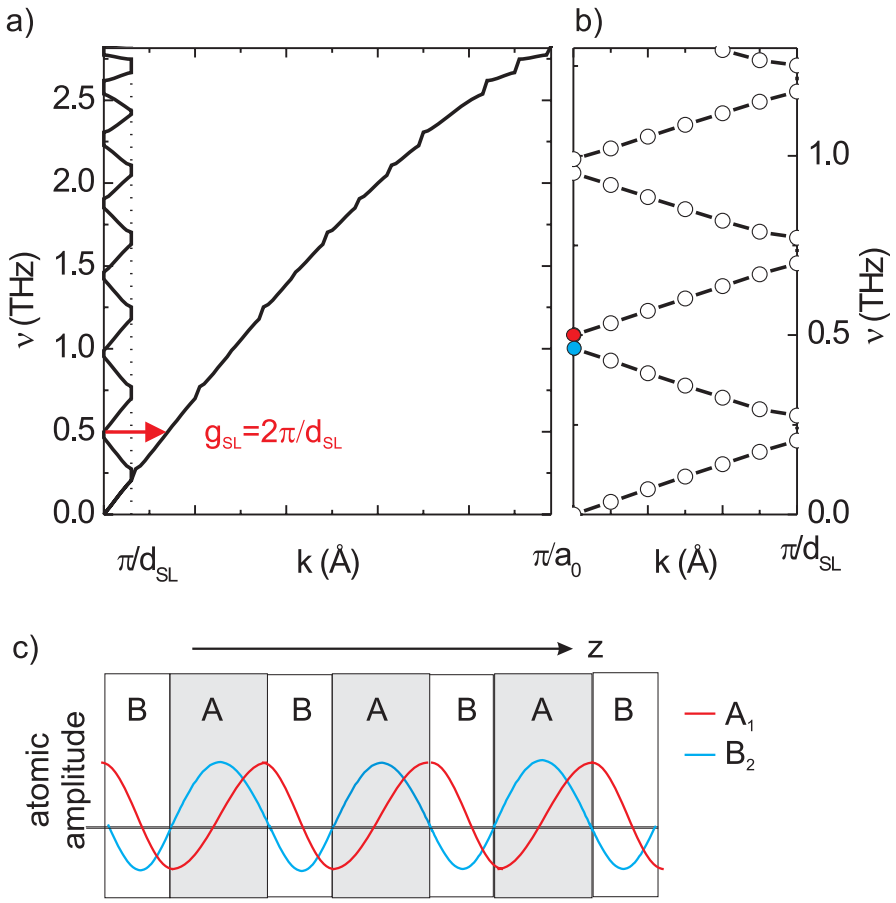

Figure 2.12: **a**) Superlattice longitudinal acoustic phonon dispersion, both in the Brillouin zone of the average lattice constant a_0 and in the folded Brillouin zone determined by the superlattice periodicity d_{SL}. The reciprocal SL vector g_{SL} indicates the experimentally excited ZFLAP. **b**) A more detailed view of the zone folded Brillouin zone. The symmetric ZFLAP A_1 is marked with a red dot, the asymmetric ZFLAP B_2 with a blue dot. **c**) Strain distribution for the A_1 and B_2 mode in a superlattice structure.

2.9.2 Time Resolved X-Ray Diffraction of Transient Structures

Time dependent deviations from an equilibrium crystal structure may happen on a very fast time-scale, determined by the microscopic interactions. Such lattice dynamics or phonon modes generally evade direct investigation since established ultrafast optical spectroscopy only gives indirect access to

structural information and conventional (static) X-ray diffraction measures the time- and space-averaged crystal structure and cannot resolve the momentary position of the individual atoms. Time-resolved X-ray techniques offer the potential to overcome these limitations.

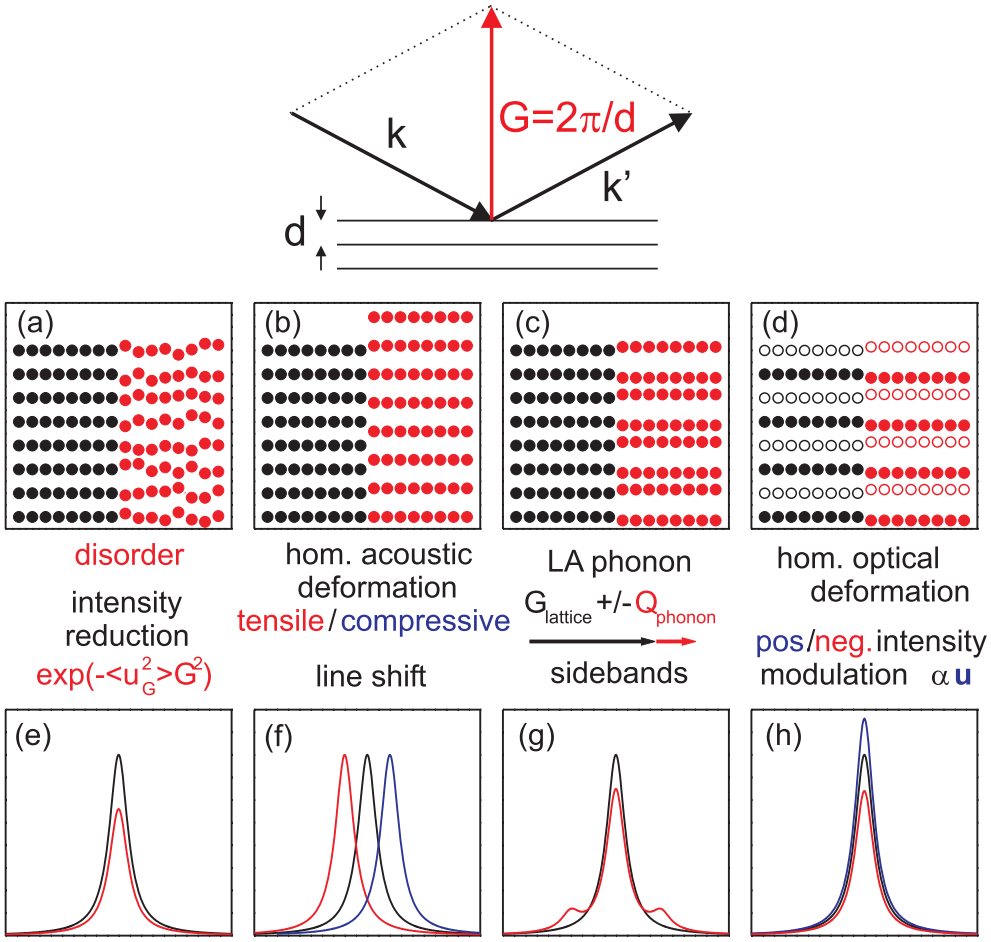

Figure 2.13: We consider a symmetric X-ray diffraction geometry with a scattering wave vector $\Delta k = G$ parallel to the vertical direction along which different kinds of lattice distortions (upper panel **a-d**) occur. In each case, the dynamically strained crystal (red •) is compared with the undistorted lattice (black •). The lower panel **e-h**) shows the influence of these distortions on the angular pattern of a Bragg peak [63].

In general, changes in the crystal lattice affect both the position and strength of the Bragg peaks. In figure 2.13, different types of lattice changes are illustrated in a schematic way [63, 64]. One can differentiate the following kinds of excitations of phonons and their impact on the X-ray diffraction

pattern:

- One of the very first experiments with ultrashort X-ray pulses studied the structural changes due to laser heating in an organic film [3]. A strong decrease of a Bragg reflection on a sub-picosecond time-scale was attributed to laser-induced disorder, followed by slower thermal expansion [figure 2.13 a) and e)]. Further prominent examples are photoinduced melting, a transition from an ordered solid to a disordered liquid phase, which is connected with a randomization and fluctuation of atomic positions. Several papers focused on the onset of melting on an ultrafast time-scale in InSb and Ge samples [4, 7, 8, 13, 14]. In particular, the experimental results of the last two listed publications point to an initial isotropic disordering process, independent of the reciprocal lattice vector, which only eventually leads to the transition from crystalline solid to disordered liquid. The conclusion is that the inter-atomic potentials are softened and the atoms initially move freely with large amplitude along an effectively barrier-less potential energy surface with initial conditions set by room temperature thermodynamic velocities. This loss of the long-range order suppresses all Bragg peaks.

  The Debye-Waller effect is a well known example where excitation of phonons due to an elevated temperature modify the X-ray pattern. The incoherent, statistical atomic motions lead to a reduction of all X-ray reflection, while the effect is larger for reflections with a high index. This was studied on an ultrafast time scale on a germanium sample [12].

- If the energy of the optical excitation is transferred to the lattice it leads to a spatial expansion and to a compression of adjacent (unexcited) parts of the sample. Acoustic phonon and shock wave propagation in crystalline solids was investigated inter alia by [8, 26–29, 31, 65–70]. The relevant time-scales are set by the velocity of sound and, depending on the particular length scale ($1 - 100$ nm), range between a few picoseconds and hundreds of picoseconds. Homogeneous longitudinal acoustic strain is connected with a change in the crystal volume, and leads to an angular shift of the Bragg peaks [figure 2.13 b) and f)]. If the wave vector of the acoustic phonon is larger than the studied length scale, the phonons lead to sidebands, because the phonon spatially modulates the lattice planes. For insufficient angular resolution, an effective broadening of the Bragg peak is observed while keeping its integrated intensity [figure 2.13 c) and g)]. Note that this is only true if it is adequate to apply the kinematic description. Quite different and

astonishing effects may result for perfect crystals in the framework of dynamical X-ray diffraction theory (compare chapter 4).

- Finally homogenous optical phonon excitations are structural changes within the unit cell and can lead to both an increase or a decrease in the strength of individual Bragg peaks via changes in the structure factor [figure 2.13 d) and h)]. The most prominent example is the direct observation of the totally symmetric A_{1g} optical mode in Bismuth [9]. For the first time, the atomic displacement within the unit cell was measured, as well as its relationship with the stability limit of a structural phase. Strong excitation corresponding to atomic displacements of more than 10 per cent of the nearest-neighbor distance – near the Lindemann limit – leads to a subsequent loss of long-range order, which was attributed to the melting of the material. This experiment triggered a number of further time-resolved X-ray diffraction experiment on Bismuth [16, 19, 20]. In particular, the controversy whether the observed amplitude-dependent frequency of optical phonons in Bismuth was caused by anharmonicity or softening of the interatomic potential was addressed. Direct observation of the atomic amplitudes decided this in favor of the latter [16]. Also excitations of zone folded longitudinal acoustic phonons (ZFLAP) may be counted as optical phonons, with the superlattice periodicity as unit-cell. For the first time, X-ray diffraction experiments on a GaAs/AlGaAs superlattice system unambiguously unraveled the excitation mechanism as being of a displacive kind [11].

  Conformational changes of molecules in a crystalline environment also belong to this class of structural changes. Beautiful experiments carried out in Grenoble in the group of Michael Wulff include a time-resolved Laue X-ray experiment, where about 3000 diffraction peaks where analyzed to literally 'watch' a protein as it executes its function [71]. Another example is the observation of a paramagnetic/ferromagnetic phase transition in an organic crystal [10].

In general, the observed dynamics consist of both structural changes within the unit cell connected with optical phonon excitations and variations of the unit cell size related to acoustic phonons with a wavelength larger than the dimensions of a unit cell. Optical phonon excitations modify local geometries and thus the structure factor, whereas acoustic phonons result in long-range changes of geometry. Note that changes within the unit cell happen on a time scale set by the phonon period, whereas changes of the size of the unit cell are determined by the dimension of the entire structure and the velocity

of sound and are generally much slower.

Chapter 3

Experiment

Science and technology has accepted the immense challenge to extend ultrafast techniques to an ever increasing photon energy, paving the way to ultrafast X-ray science. Two approaches have proven to be most successful, namely laboratory-based sources, such as laser-driven plasmas and high harmonic generation, and large scale accelerator based installations, in particular with additional electron bunch compression or electron slicing schemes. In the near future the free electron laser (FEL) promises a great leap forward in ultrafast X-ray technology. Each method has its specific advantages and limitations, and whether they can meet the expectations of scientists will depend on the investigated problem. The following gives a brief introduction of the available light sources for high energetic photons which paved the way for ultrafast X-ray science.

Synchrotrons are a well established source of highly brilliant and tunable X-ray light. Relativistic electron bunches are accelerated and cycled in a storage ring and used to emit X-ray pulses from bend magnets or insertion devices. However, the pulse width of the radiated X-rays is limited to the 20-100 ps range, determined by the equilibrium length of a stored electron bunch. Pioneering techniques have been developed at the bending magnet beamline of the Advanced Light Source in Berkeley to overcome the inherent limitations of the time-resolution of synchrotron light. In a first step subpicosecond X-ray pulses were generated by 90° Thomson scattering [72], however only low flux densities could be achieved. A few years later it was replaced by the much more successful slicing scheme: an optical femtosecond laser pulse scatters from a relativistic electron bunch and cuts out a slice of the $\approx$ 100 ps long synchrotron pulse [73]. While the X-ray pulse duration is indeed very short ($\approx$ 100 fs), its apparent disadvantage is that it discards most photons and, as a result, also only delivers a moderate X-ray flux. Furthermore, its extraction from the large pedestal due to the picosecond X-ray

pulse is still problematic. Nonetheless this scheme has also been successfully implemented at the Swiss Light Source [74] extending to the hard X-ray range and at BESSY for the soft X-ray regime [75, 76]. In a different approach to produce femtosecond X-ray bursts, electron bunches at the Stanford Linear Accelerator Center (SLAC) are chirped and then sent through a series of energy-dispersive magnetic chicanes to create 80-fs electron pulses. These are then transported through an undulator (periodic, transverse magnetic fields) to create sub 100-femtosecond X-ray pulses. The SPPS (Sub-Picosecond-Pulse-Source) operated at a fixed wavelength at a rather small repetition rate of $\approx$ 10 Hz. The SPPS was shut down in 2006 to make way for the Stanford Coherent Light Source (LCLS), a free electron laser extending into the hard X-ray regime, which is planned to be operational in 2009. A second FEL is being built in Hamburg and is expected to be commissioned at the end of 2013. The principle of FELs is self-amplified-stimulated-emission (SASE). A relativistic electron bunch traverses a long undulator, where it emits synchrotron radiation. The radiated light interacts with the electrons and leads to micro-bunching of the electrons, separated by a distance equal to one wavelength of the radiation. Since the emitted light is in phase with the motion of the electrons, coherent constructive superposition stimulates further emission and result in a very intense X-ray laser beam. The wavelength may be readily tuned by adjusting the energy of the electron beam or the magnetic field strength of the undulators. The LCLS will deliver monochromatic, sub 100 fs pulses in an energy range between 800 eV and 8 KeV and deliver the enormous brilliance of up to 10^{33} photons/(s mm^2 mrad^2 0.1% bandwidth) or about 10^{12} photons/pulse. One disadvantage is shared by all accelerator based X-ray sources, namely the lack of inherent synchronization with the excitation laser pulse (not to mention that they come with a hefty price tag). Despite significant progress (in particular [19, 77]), pump/probe path length fluctuations, arising from the large spatial dimensions, have remained detrimental to a femtosecond time resolution.

Laboratory based sources include high harmonic generation, which are based on focusing an ultrashort optical pulse in a gas yet, which then generates harmonics of the fundamental frequency up to the XUV [78–81]. These sources are (currently) limited to pulse energies of up to about 400 eV. Yet, these pulses are extremely short and have sparked the field of attosecond physics. For studies of structural dynamics in condensed phase media, however, higher photon energies in the keV range are required. Indeed first experiments seem to indicate that the production of hard X-rays with high harmonic generation may be a viable route [82].

In this work a laser-driven plasma source is used to produce ultrashort hard X-rays and a detailed characterization and a brief introduction of the

source	availability	photons/pulse/ 0.1%bandwidth	pulse width	energy range	repetition rate
higher-harmonic-generation	since ca. 1988	e.g. carbon K edge ≈100	$\geq$ 100as	$\leq$ 400 eV	1-10 kHz
laser-generated plasmas	since ca. 1991	$10^3 - 10^5$	$\approx 100 - 300$ fs	$\leq$ 30 keV	1-2 kHz
3^{rd} generation synchrotron	since ca. 1994	$10^4 - 10^6$	$\approx 20 - 200$ ps	0-100 keV	$\leq$ 500 MHz
slicing scheme at bending magnet	since 2000	$10^1 - 10^3$	$\approx$ 100 fs	0-100 keV	1-10 kHz
short pulse photon source (SPPS)	2003-2006	10^8	$\approx$ 100 fs	8 keV	10 Hz
X-ray free electron laser	from 2009/2013	10^{12}	$\approx$ 100 fs	$\approx$ 0.8-8 keV	100-500 Hz

Table 3.1: Main parameters of of ultrashort X-ray sources

underlying physical processes are given in the following section. Early realizations of laser-generated plasma sources have mostly focused on the characteristic line emissions [83–85], whereas only a few attempts have been made to optimize the broadband background radiation [86–88].

Finally an exciting new development must be mentioned in which synchrotron radiation is produced by accelerating electrons in a laser-plasma wakefield [89]. The generated electron bunches with 64 MeV energy and an estimated length of only 10 fs are sent through an undulator to produce synchrotron radiation in the visible to infrared range. The demonstrated scaling of wavelength with energy promises future potential of such novel laser-based light sources to generate radiation from the infrared to X-ray wavelengths.

Table 3.1 summarizes the current and future parameters of the different sources capable of producing ultrashort X-ray pulses.

The following section will introduce the main components of the experimental setup, consisting of a Ti-Sapphire laser system, the copper band target for the production of the ultrashort X-ray pulses, optics for different wavelength and pump geometries, X-ray optics to manipulate the probe beam, a cryostat to control the temperature of the sample and finally CCD-cameras for X-ray detection. It includes a summary of the important characteristics of the laser-based X-ray source with special emphasis on time resolution and time-delay zero determination.

3.1 Ti-Sapphire Laser System

For the generation of ultrashort K_α radiation we use a Ti:sapphire laser system, operated at a 1-kHz repetition rate. A Kerr-lens mode-locked Ti:sapphire oscillator with a prism-free chirped mirror design generates pulses of 22-fs duration. These pulses are stretched to the duration of 230 ps and amplified by a regenerative amplifier. The output pulses of an energy of 1.7mJ are passed through a $\lambda/2$ Pockels cell and a calcite polarizer for additional suppression of prepulses. The final amplification is performed in a 20-mm-long Ti:sapphire rod cooled to 213 K and placed in a small evacuated chamber to prevent condensation. The rod is pumped with two Q-switched, intracavity frequency-doubled Nd:YLF lasers, each producing up to 20-W average power at 527 nm. After amplification to a pulse energy of 9.6mJ, the pulses are compressed by a two grating (1200 lines/mm) compressor. Output pulses with an energy up to 6.2mJ and a pulse duration of 45 fs are generated. The temporal structure of the pulses was measured by a third-order autocorrelator with a dynamic range of eight orders of magnitude. The contrast of the main pulse to amplified spontaneous emission (ASE) was 10^7. The energy

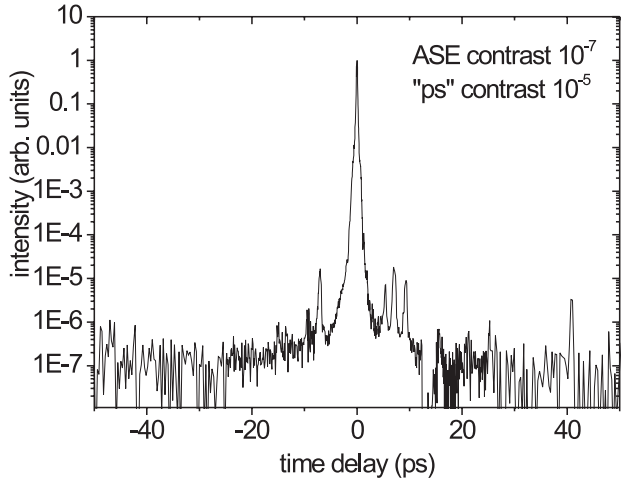

Figure 3.1: Third order correlation measurement. The contrast of the main pulse to amplified spontaneous emission (ASE) is 10^7. The energy contrast of the main pulse to the pre-pulse located at 6.5 ps before the main pulse is as high as 10^5

contrast of the main pulse to the pre-pulse located at 6.5 ps before the main pulse was as high as 10^5 [compare figure 3.1]. The laser-beam quality analyzed with a Shack-Hartmann wavefront sensor showed a Strehl ratio [1] of 0.973 (RMS=0.025 waves). The pulse-to-pulse energy fluctuation was 0.3% (RMS) [90, 91].

3.1.1 Pump Probe Setup

The pump-probe technique employs a strong pump pulse, which optically induces a non-equilibrium state in the sample that is monitored by a delayed X-ray pulse, called the probe pulse. By changing the time-delay between pump and probe pulses one samples the evolution of the excited state as a function of time, or, takes snapshots of a moving structure. The temporal resolution is ultimately limited by the duration of the pulses, however, non-collinearity or chromatic dispersion of pump and probe beams may reduce the temporal resolution. The timing between the two pulses is controlled

[1] Strehl ratio is the ratio of the observed peak intensity at the detection plane of a telescope or other imaging system from a point source compared to the theoretical maximum peak intensity of a perfect imaging system working at the diffraction limit.

by a mechanical delay stage, which can be moved with μm-precision. For example an additional path length of 3μm for the probe pulse corresponds to an observation only 10 fs after the excitation has taken place, determined by the velocity of light. The important condition that the probe pulse only weakly interacts with the sample and does not alter the state, which it is observing, is well fulfilled for our low intensity X-ray flux.

A schematic of the experimental setup is shown in figure 3.2 a). The main beam is divided by a beam splitter with the ratio 5:95. The intense part is sent into the vacuum chamber to generate X-rays, while the weak part with approximately 300 μJ energy is used as pump-pulse. Its beam waist is reduced by a telescope, subsequently passes the delay stage and is collimated onto the sample. Additionally the wavelength of the pump beam can be tuned, either by second harmonic generation in a BBO crystal or with an optical parametric amplifier (OPA). In the OPA a strong pump wave (k_1, ω_1) and a collinear weak seed wave (k_2,ω_2) generates a third light wave (k_3, ω_3) at their difference frequency. Simultaneously, the wave at the lower frequency ω_2 is amplified to fulfill energy and momentum conservation:

$$\omega_1 = \omega_2 + \omega_3 \text{ with } \omega_2 > \omega_3 \tag{3.1}$$

$$\vec{k}_1 = \vec{k}_2 + \vec{k}_3 \tag{3.2}$$

Equation 3.2 describes the phase-matching condition, where identical phases of the three light fields are involved such that constructive interference between the pump wave and the converted waves occurs during propagation through the nonlinear crystal. The light wave at frequency ω_1 is called the fundamental whereas ω_2 and ω_3 are termed signal and idler, respectively. Phase-matching is achieved by exploiting the birefringence of the crystal. This allows to tune the wavelength between 1.2 μm (signal) and 2.2 μm (idler) with pulse energies of typically $E_{\text{idler}} = 20$ μJ and $E_{\text{signal}} = 35$ μJ. For more details please refer to [92], where the exact same setup is characterized and explained in more detail.

3.2 X-Ray Source

A picture of the vacuum chamber for X-ray production is shown in figure 3.3 a). The key element of the X-ray source consists of a copper-foil transportation system. A 20 mm wide and 20 μm thick foil is spooled onto two coils and can be moved back and forth. The speed of the coils is adjusted such that each laser pulse hits a fresh surface. Since the laser pulse induces a damaged spot of about 20 μm diameter [compare figure 3.3 b)] with a 1 kHz

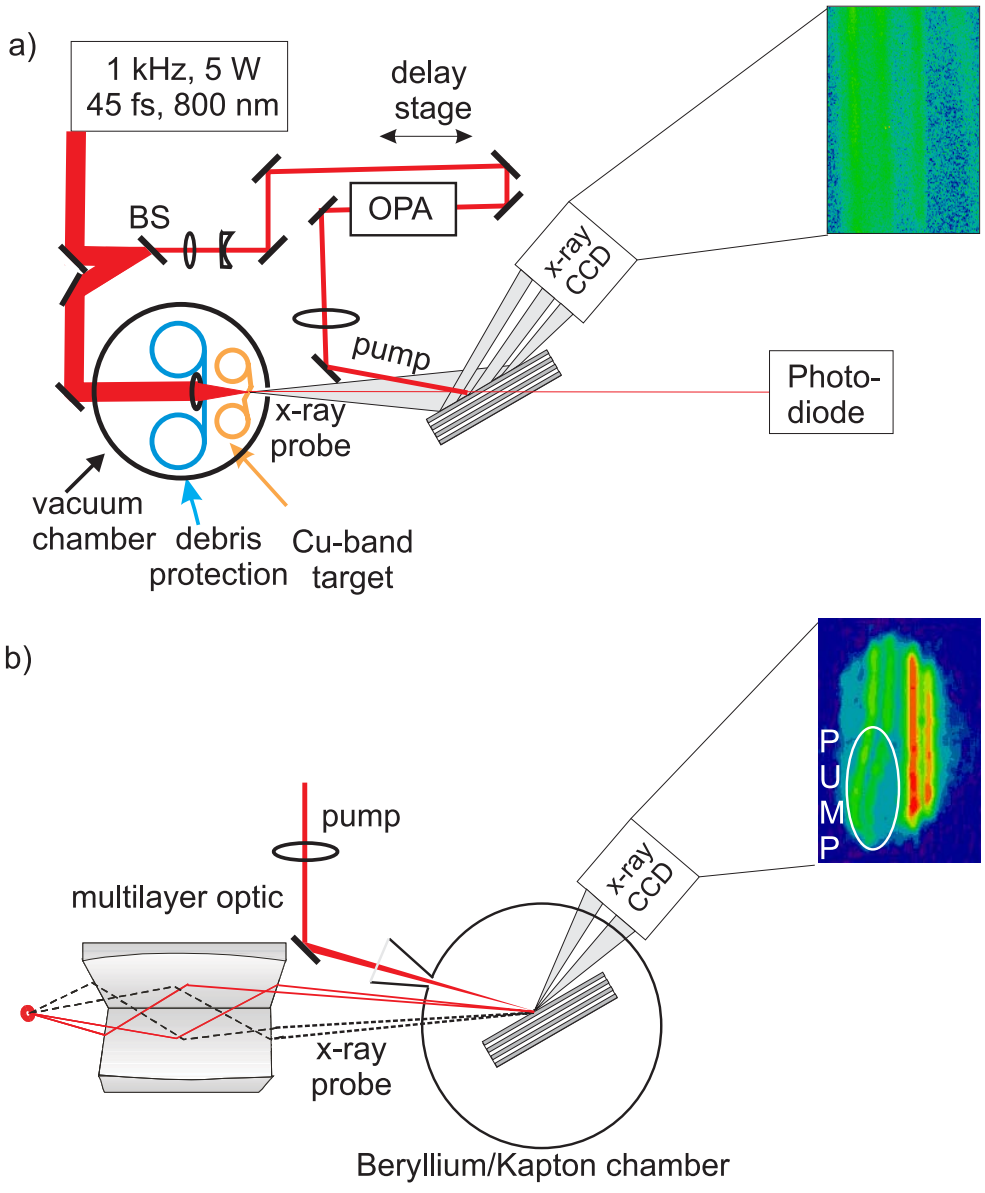

Figure 3.2: **a**) Schematic of the experimental setup. In a geometry with no X-ray mirror one can perform optical pump/optical probe experiments in the same setup to determine time-delay zero. **b**) Extension of the setup with a multilayer mirror and a cryostat. The contrast of the X-ray diffraction pattern is enhanced when using a mirror.

repetition rate the minimal speed is 2 cm/s. As soon as the end of the band is reached, the band shifts vertically by about 0.5 mm and starts to move in

the other direction. The p-polarized laser beam is focused by a lens of 100 mm focal length into a spot with a diameter of 6.7 μm FWHM, producing an on-axis peak intensity of more than 10^{17} W/cm^2. The rapid heating of the copper target by the focused laser beam causes a shock wave, which leads to the ejection of molecular clusters and small target fragments. To protect the focusing lens from the copper debris, a 175 μm thick and 200 m long plastic band is placed in front of the lens and is continuously moved during the experiment at approximately 20 mm/min. The protective band also changes its direction once it has reached its end. It is sufficient to replace the band after about 10 hours of operation, when the laser transmission decreases due to a copper coating. The whole setup is placed into a vacuum chamber which is evacuated to pressures below 10^{-4} mbar. This is necessary to avoid ionization of air, which takes place at much lower intensities of about 5×10^{14} W/cm^2 under ambient pressure.

3.2.1 Physical Origin of Characteristic X-Ray Pulses

When an ultrashort, intense laser beam is incident on a solid target the electrons and ions in a thin layer at the air/target interface experience the electric field of the laser, which greatly exceeds the typical atomic fields. For intensities above 10^{15} W/cm^2 one usually identifies two dominant processes for energy transfer, *resonance absorption* and *vacuum heating*. Resonant absorption relies on an efficient coupling between the electromagnetic wave and the electron plasma in the target. In the standard picture [93], a p-polarized light wave tunnels through to the critical surface ($N_\mathrm{e} = N_\mathrm{c}$), where it excites a plasma wave. This wave grows over a number of laser periods and is eventually damped by collisions [94, 95]. The critical density for a laser frequency $\omega_\mathrm{Laser} = 2.4 \times 10^{15} 1/\mathrm{s}$ is given by $N_\mathrm{c} = \omega_\mathrm{Laser} m_\mathrm{e}/(4\pi e) = 2.5 \times 10^{18}$ cm^{-3}. For an approximate plasma expansion velocity of 0.1 nm/fs and for a laser pulses with a duration of only 45 fs, the interaction basically takes place with a solid target (for example: $\mathrm{N_{Cu}} = 8.5 \times 10^{22}$ cm^{-3}e). For this condition of an overdense plasma resonance absorption ceases to work. It has been shown though, that by applying a pre-pulse, which is intense enough to ionize the target, the efficiency of the energy transfer via resonance absorption may be enhanced [96, 97]. However, this approach has not been followed.

The alternative model of *vacuum heating* was proposed by Brunel [98] in which the electrons are directly heated by the p-polarized laser beam. According to this model, the electric field of the laser drags the electrons away from the target surface, turns them around and accelerates them back into the solid, all within one half laser cycle. The electrons can gain very high kinetic energies and enter the target to produce X-ray radiation by K-shell

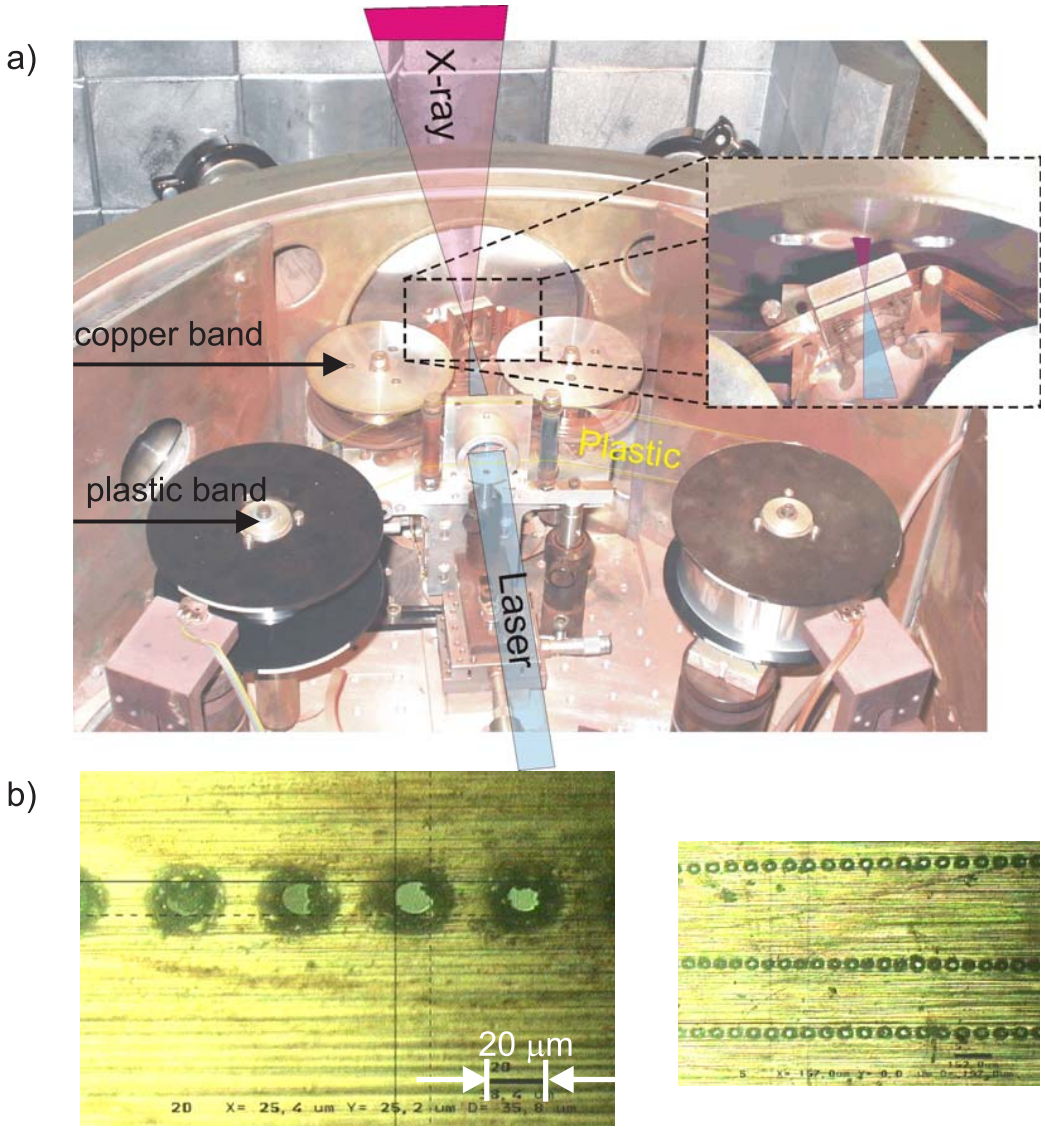

Figure 3.3: **a**) Photograph of the vacuum chamber. The laser beam enters through the middle and is focused onto the copper foil. The lens is protected by a moving plastic band. **b**) Photograph of the used copper foil. The laser drills holes of ≈ 20 μm diameter in to the copper foil.

ionization and bremsstrahlung [84], similar to a conventional X-ray tube. Brunel-like vacuum heating is assumed to be the dominant mechanism in the X-ray source described in this chapter.

Assuming a Maxwellian distribution of hot electrons $E \propto c \cdot \exp(-E/T_e)$ [99, 100], the high energetic bremsstrahlung has been associated with the

average energies of the hot electrons [101, 102]. Usually the electron temperature is determined by the ponderomotive scaling law and the electron temperature as a function of laser irradiance ranges between $T_e \propto (I\lambda^2)^{0.3...0.5}$ [103–105].

3.2.2 Characterization of the X-Ray Source

The following section discusses the most important properties of the laser-based X-ray source [106, 107]. The most relevant parameters for time-resolved X-ray diffraction experiments include the number of produced X-ray photons, the duration of the X-ray pulses and the source size. A study on the flux dependence as a function of copper-foil thicknesses is mentioned [108].

X-Ray Yield

The incoherent X-rays are assumed to be emitted homogeneously in 4 π and are detected in transmission and reflection geometry. In all measurements the angle between the p-polarized laser and the copper foil is chosen to be 20°, for which the X-ray flux showed a pronounced maximum. The low energy part between 2.5 -20 keV is detected with Si based photodiode (XR-100CR Amptek Inc.) with a resolution of 250 eV, the high energetic background is measured with a scintillation photomultiplier detector (Scionix Inc. with a detection range up to 150 keV with 3-10 keV resolution). Both detectors are placed 1.3 m away from the source and the use of an additional lead pinhole assures a single photon counting mode.

Figure 3.4 a) shows the spectrum of the characteristic Cu K_α (the doublet line Cu $K_{\alpha1}$ = 8048 eV and $K_{\alpha2}$ = 8028 eV is not resolved) and the K_β = 8905 eV line. The inset of figure 3.4 a) plots the higher energetic X-ray radiation on a logarithmic scale. The high energetic X-ray photons yield an electron energy of $E_e = 28$ keV, assuming the relation given in the previous section. The total X-ray flux as well as the number of only K_α photons are measured in transmission geometry as a function of pulse energy. The pulse energy is reduced by different beam splitters, whereas the beam diameter and pulse duration is kept constant. As shown in figure 3.4 the X-ray yield increases with higher pulse energy and reaches the highest measured value of 6.8×10^{10} photons/second for 5 mJ pulses, corresponding to an intensity of $\approx 10^{17}$ W/cm^2. The conversion efficiency of laser energy into the K_α emission reaches a maximal value of 2×10^{-5}.

The increasing X-ray yield with higher laser intensities is consistent with the steep increase of the electron cross-section for the K-shell ionization with increasing electron energies. Both a calculation based on the Bethe formula as

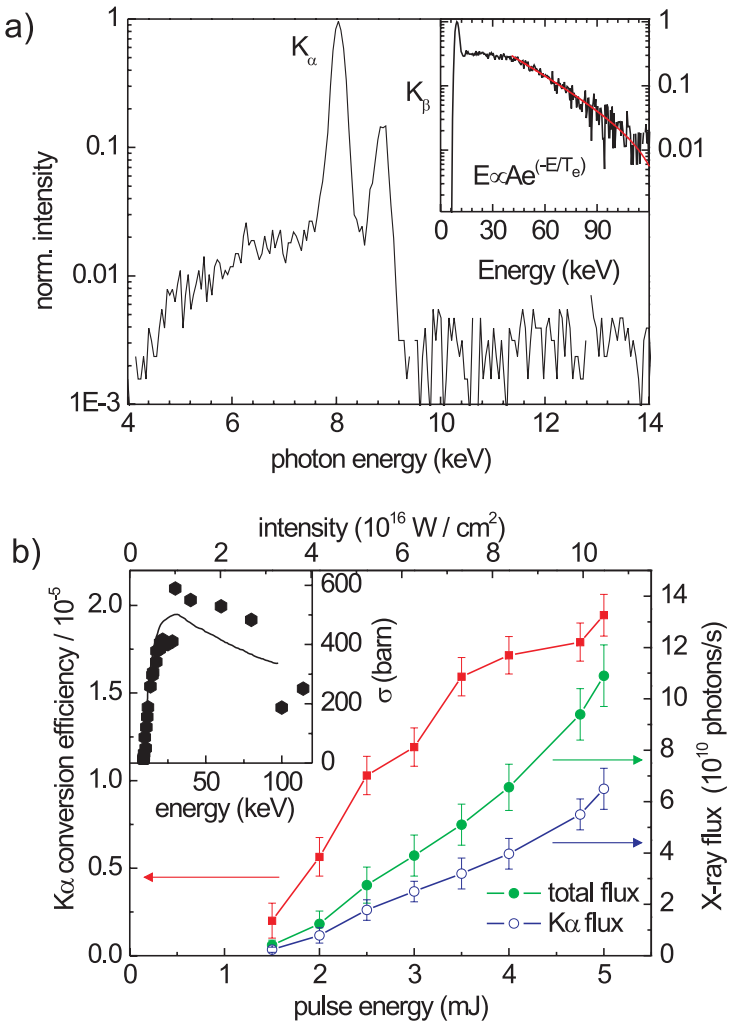

Figure 3.4: **a**) Characteristic K-shell radiation of the laser based X-ray source in transmission geometry. Inset: High energetic Bremsstrahlung with a fit to yield an electron temperature T_e=28 keV. **b**) X-ray flux and K_α conversion efficiency as a function of pulse energy. Inset: Calculated and experimental cross-section for K-shell ionization Rez [109], Liu et al. [110]

well as experimental data for the cross-section for K-shell ionization of copper as a function of electron energies is shown in the inset of figure 3.4 b) [109, 110]. It shows a maximum around $\approx$ 27 keV, which in our case corresponds to the highest laser intensity of $\approx 10^{17}$ W/cm^2. Note that for Titanium, an alternative material commonly used in laser based X-ray sources, the maximal cross-section is at $\approx 5 \times 10^{15}$ W/cm^2, roughly an order of magnitude

lower compared to copper [97, 104]. Accordingly a saturation of the X-ray flux with increasing laser intensity has been shown experimentally [111]. In our setup no saturation of the X-ray flux has yet been observed. This suggests that with higher pulse energy or tighter focusing the X-ray flux should increase.

Additionally it has to be taken into account that for moderate electron energies, the stopping length for electrons is shorter than the thickness of the used copper foils. Thus, fast electrons (100 keV) will slow down within the target to energies around the optimal $T_e \approx 27$ keV and efficient K shell ionization will still take place. Calculated CSDA values (continuous stopping down approximation), that is, a very close approximation to the average path length traveled by a charged particle as it slows down to rest, can be accessed from the ESTAR sever of the National Institute for Standards and Technology. For copper, values of 3.5 μm for approximately 30 keV electrons and 20 μm for 90 keV electrons are given. Note that ionization of the K-shell of copper seizes to work below an electron energy of approximately 8 keV, however such low energetic electrons have an almost negligible path length in Cu. More importantly, multiple scattering events change the direction of the electrons such that not all electrons reach the maximal penetration depth.

X-Ray Source Size

The size of the X-ray emitting area has been measured in the horizontal plane by using a knife-edge technique and detecting a 23-fold magnified X-ray image with a CCD. Integration of the shadow image yields a source size of only 10μm [figure 3.5].

This is only insignificantly larger than the laser spot size. This has been observed previously for a similar laser/X-ray spot ratio of $8\mu m/11\mu$m [84]. The small size of the source suggests that the electrons are stopped in the copper foil within a few micrometers.

Study for Different Foil Thicknesses

The X-ray yield for different foil thicknesses was studied experimentally both in forward (transmission) and backward (reflection) geometry and the results are shown in figure 3.5. The data points for the same foil thickness were measured simultaneously. In reflection geometry we observe a constant photon flux, with a mean value of 8.7×10^{10} photons/s. In transmission geometry the x-ray flux decreases with increasing foil thickness and is reduced by more than 50% for the 40 μm thick target.

The most straightforward explanation for the constant flux in reflection

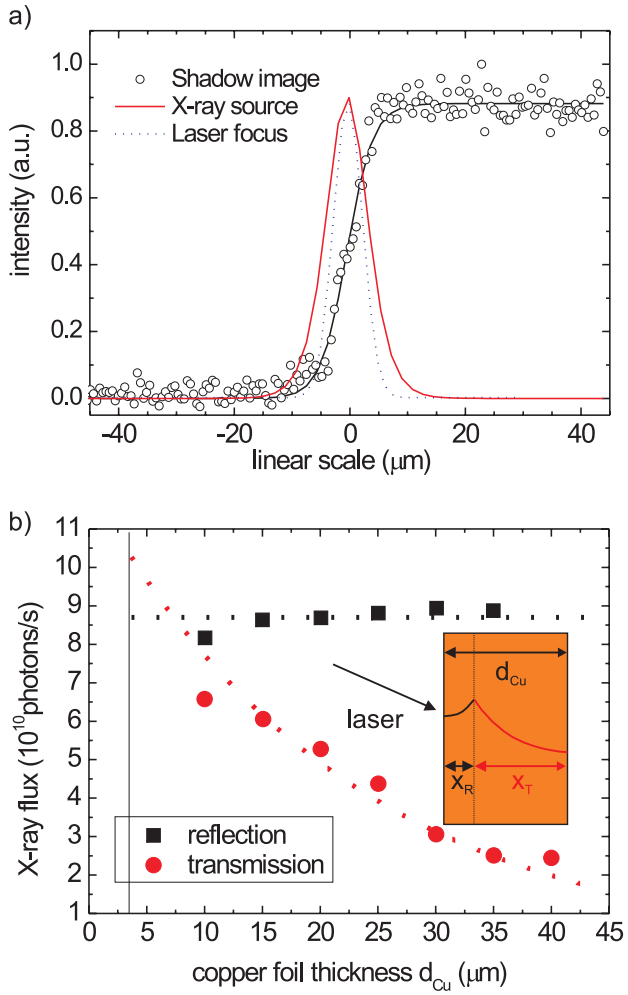

Figure 3.5: **a**) Experimental shadow image for a knife edge measurement (hollow circles) and the corresponding Gaussian profile of the x-ray emitting area (solid curve). The focal spot of the laser is shown for comparison. **b**) X-ray flux for different copper foil thicknesses for transmission and reflection geometry. The red dotted line shows the calculated transmitted X-ray intensity for a mean electron penetration depth of 3.7 μm. Inset: Schematic showing the attenuation for the reflection and transmission geometry.

and a simultaneous decreasing flux for transmission is schematically shown in the inset of the figure 3.5. The electrons are stopped within a few micrometers (x_{R}<10μm) where they act as a source for the X-ray flux. The transmitted

X-ray beam suffers attenuation as it traverses the increasing distance x_{T} of the copper foil, while the reflected X-rays always cross the same distance x_{R}. For a qualitative analysis we compare the measured data points for reflection and transmission for each foil thickness and calculate an average depth for the source of the X-rays. We use Lambert Beer's law and an attenuation coefficient of copper $\mu_{\mathrm{CuK}_\alpha} \approx 0.045\ \mu\mathrm{m}^{-1}$ [40] and extract a mean penetration depth of

$$x_{\mathrm{e}} = x_{\mathrm{R}} = 3.7 \pm 0.7 \mu\mathrm{m}. \tag{3.3}$$

For a copper foil exceeding this thickness the X-ray flux in backward-direction is constant [compare dotted line in figure 3.5], at $2x_{\mathrm{R}}$ the flux for transmitted and reflected X-rays are equal. The transmitted X-ray flux decreases with increasing foil thickness as depicted by the calculated red, dotted line in figure 3.5. For copper foils thinner than 3.6 μm one would expect a decreasing X-ray flux, as the electrons are too energetic to fully deposit their energy within the target. This is apparently not the case for the foil thicknesses studied in this work, such that the target may be treated as being essentially a bulk material. This analysis is certainly an oversimplification of the very complicated underlying plasma physics. The electron energy distribution may be non-gaussian, multiple scattering events may take place and so forth. Nonetheless it gives a simple approximation of the electron stopping length, which is also in very good agreement with the value estimated for an electron temperature of 28 keV.

Defiant of the somewhat lower X-ray yield we favor the transmission geometry for the time-resolved experiments. First, the group velocities of the X-ray and the laser pulses are similar, and thus the timing of the optical pump and the X-ray probe can be determined by using a part of the laser beam, which passes through the target on the same path as the X-ray beam for adjustment in an all-optical cross correlation. Secondly, the temporal jitter, which is caused by microscopic fluctuations of the target position and exists for the reflection configuration, is eliminated for the transmission configuration. In the time-resolved experiments discussed in this work we used exclusively 20 μm thick targets, mainly because of their better long-term mechanical stability.

3.3 Time-Resolved X-Ray Diffraction Setup

3.3.1 X-Ray Pulse Duration and Accurate Time Delay Zero Determination

The temporal durations of the pump and probe pulses are important parameters because they limit the temporal resolution of the measurement systems. Pulse characterization in the visible and near-infrared is well established, and also for shorter wavelength in the XUV and soft X-ray regime new sensitive methods have been developed. For hard X-rays with multi keV-energies and sub-picosecond pulse duration, pulse characterization is still an unsolved problem. Two methods have been reported for measuring the ultrashort pulse duration in the XUV-to X-ray region. One uses an X-ray streak camera, with a temporal resolution of only a few picoseconds, and the other is based on the correlation method. The correlation method can be classified into two types: auto-correlation and cross-correlation. The auto-correlation method records the signal resulting from the temporal overlap of a master pulse and a replica of it in a non-linear medium as a function of the time delay between the two pulses. In the XUV region, this has been demonstrated by using two-photon ionization of He or Ar and Xe gas [112, 113]. This has only been successfully applied for wavelength of up to 88 nm (9th harmonic of the Ti:Sa laser pulse) mainly because it is difficult to produce pulses which are intense enough to induce measurable nonlinearities of atomic media. Cross-correlation may have an enhanced sensitivity because it replaces one of the two weak photon beams by an intense laser pulse. A widely used cross-correlation method in the XUV to soft-X-ray region is based on the laser-assisted photoelectric effect (LAPE) [80, 114–119] The LAPE induces changes in the photoelectron energy spectrum, that is, appearance of sidebands, peak energy shift, and broadening of the peaks, and these changes are recorded as a function of the time delay between the intense laser pulse and the weak short-wavelength pulse. Going to larger photon energies these methods eventually fail also as the photo absorption cross-section starts to decrease exponentially. Additionally to identify the spectral shift of the resulting side-bands, the X-ray spectral width must be kept well below the laser photon energy $\hbar\omega \approx 1.6$ eV to avoid overlap of the sidebands with the main peak. For Cu $K_{\alpha 1}$ and $K_{\alpha 2}$ with a line width of 2.4 eV and 2.9 eV, respectively, [120] this is not fulfilled. At the FEL in Hamburg (FLASH) it was recently demonstrated that soft high-flux X-ray pulses ($\approx$ 40 eV) can induce a sub-picosecond transient optical reflectivity change in GaAs [121]. The authors expect this method to be applicable for higher X-ray energies up to keV, in particular, for the very high flux of future FELs. They propose this method as a tool to determine

the X-ray/optical cross-correlation for time-resolved FEL experiments.

So far only upper limits for the temporal duration of hard X-ray pulses have been inferred in ultrafast X-ray diffraction experiments: changes of X-ray diffraction signals due to non-thermal melting [4, 8, 14, 122] and/or strain generation in semiconductors [11, 26] have been analyzed and give lower limits between 300 and 500 fs. Also by X-ray diffraction observation of laser-induced coherent optical phonons in bulk bismuth, determined the X-ray pulses of the Swiss Light Source with a slicing scheme to have a duration of 140 ± 30 fs FWHM [19, 20]. The majority of time-resolved X-ray diffraction experiments have measured X-ray intensity changes due to atomic movements, which due to their finite inertia, set an upper limit to the temporal resolution. In laser-based X-ray sources with moderate photon fluxes, it remains a challenge to find a measurable, instantaneous X-ray response due to solely electronic contributions.[2]

The difficulty to determine the X-ray pulse duration impedes measurements of absolute time-delay zero between optical pump and X-ray probe beam in a cross-correlation measurement. Experiments with accelerator based X-ray sources require a synchronized femtosecond laser providing the pump pulses. The jitter between the X-ray pulses and an external pump laser pulse has been measured indirectly by an electro-optical sampling technique that records the arrival time of electron bunches with subpicosecond accuracy [77], but does not provide the timing of the X-ray pulse at the location of the sample. For experiments with laser driven plasma sources, where optical pump and X-ray probe pulses are intrinsically synchronized, one may use a sample showing a fast X-ray response upon excitation to infer time-delay zero. This method may be hampered by the irreversible character of the pump-induced structural changes, requiring a fresh sample volume for each pump pulse and, thus, limiting the maximum possible pulse repetition rate. Again the assumption of an instantaneous sample response may be invalid.

Our Experimental Approach

In the following a novel technique is presented to determine time-delay zero by comparing the very pronounced X-ray reflectivity change of a superlattice sample (compare section 5.2 for a detailed description of the sample) to its instantaneous optical response. This is achieved in a setup without X-ray optic as shown in figure 3.6. The optically induced X-ray transient is measured first. For the comparative measurement of the transient *o*ptical reflectivity

[2] One promising approach is the investigation of the forbidden (222) reflection of diamond, which exclusively stems from bonding electrons. Preliminary time-resolved experiments have been carried out, however, no conclusive results presently exist.

of the sample, the Cu target and the 10 μm thick Aluminum/Kapton seal of the vacuum chamber are removed and the probe pulse that normally generates the X-rays, is attenuated by closing an iris. Otherwise, the pathway of the probe pulse and the sample position are left unchanged. The attenuated 800 nm probe beam hits the sample at the same position as the X-ray pulses and the reflected or transmitted intensity is measured as a function of pump-probe delay, t, with a photodiode. To enhance the signal to noise ratio the optical pump beam is chopped with 500 Hz and the signals with and without pump pulse are compared. The form of temporal response is independent of the excitation energy. The comparison between optical and X-ray response calibrates the superlattice sample, which can than be used to infer time-delay zero with an accuracy of $\pm$ 100 fs [123]. Additionally to confirm that the steep signal change in the all-optical experiment corresponds to an instantaneous response, time delay zero was measured by cross-correlation of the optical pump and optical probe pulse in a BBO crystal. Hence, the ultrafast X-ray response is calibrated: the first minimum of the oscillatory signal change occurs at $t = 2.0$ ps (see graph in figure 3.6). For comparison of the temporal response of a SL for different excitation wavelength a three beam setup was implemented as schematically indicated in figure 3.6. This seems to be the only possible solution since, due to the low pulse energies of the near-infrared pulses, these experiments had to be performed with a focused X-ray beam, that is, with an X-ray mirror. The X-ray mirror was sealed with Beryllium windows and therefore did not transmit optical wavelengths. The beam path (b1) for the fundamental pump pulses (λ = 800 nm) was calibrated as mentioned above, that is, the first minimum of the X-ray oscillation was set to be at $t = 2.0$ ps. The third beam (b3) was split off by a second beam splitter (BS2) and its path length was controlled by a second delay stage. It was set to an equal length compared to the λ = 800 nm pulses (b1) by second harmonic generation in a BBO crystal. Finally time delay zero between the X-ray pulses and the near infrared pump pulses (b2) (signal or idler output of an OPA) was determined by again measuring the respective frequency mixing in a BBO crystal with the third beam (b3). The BBO crystal was mounted on a pinhole with 100 μm diameter and was fixed on the sample itself. For this method we estimate an accuracy of $\pm$100 fs.

Target Geometry and X-ray Pulse Duration

Finally it is worthwhile to discuss the physical constraints of the X-ray pulse duration in laser-driven plasma sources. In particular, we will address a possible dependence of the temporal length of X-ray pulses on the thickness of

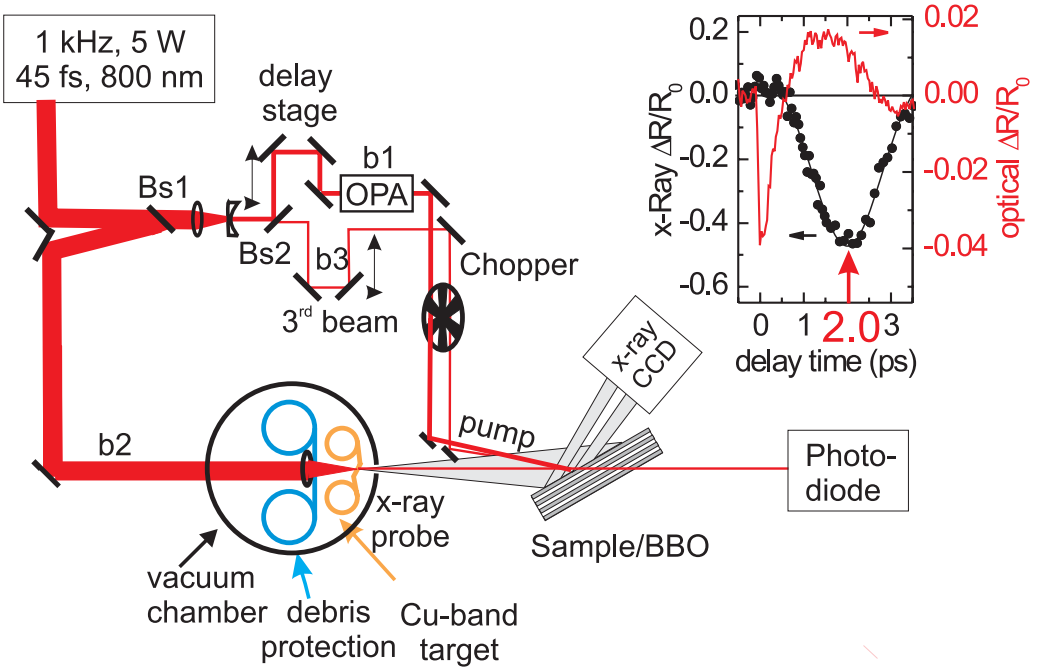

Figure 3.6: Schematic of the experimental setup to determine time delay zero. Without X-ray mirror the optical response determines time delay zero with an accuracy of ±100 fs. The ultrafast X-ray and optical transients are shown in the upper right hand corner. For experiments with an X-ray optic a third beam is set to equal length with the calibrated $\lambda = 800$ nm beam path.

the target. For bulk targets we expect an increase in pulse duration with increasing laser intensity. As the higher energetic electrons penetrate deeper into the material and continue to produce K_α photons, their velocity mismatch broadens the X-ray pulse. In very thin foils this can be minimized, even though possibly at the cost of reducing the total X-ray flux. The hot electrons traverses the foil before depositing their entire energy and thus limiting the interaction length. For very thin foils Monte Carlo calculations predict a 90 fs long X-ray pulse in a 1.7 μm Cu foil for an intensity of 7 $\times 10^{15}$ W/cm^2 [104]. Simulations also point to an asymmetric temporal pulse shape with a long tail. The inferred electron temperature in our setup of $T \approx 28$ keV corresponds to a velocity of $v_e \approx 0.32$ c, thus an X-ray photon generated at the front surface of the foil leaves the target earlier than a photon generated at a position deeper inside the target. With the approximate stopping length for 28 keV electrons in copper of approximately 3.5 μm, the velocity dispersion should only amount to a time smearing of ≈ 30 fs. If these

simple considerations hold and vacuum heating is the dominant mechanism, we may expect to produce X-ray pulses, which are not considerably longer than the driving laser pulse.

3.3.2 Detecting X-Ray Pulses

CCD-cameras compared to photon counting detectors not only greatly ease the alignment, but may also provide two pieces of information simultaneously, namely the intensity of reflections as well as their angular position. Furthermore two or more closely spaced reflections can be recorded at the same time. We have used two different X-ray CCD cameras, a deep depletion directly detecting CCD camera and a indirectly detecting scintillation based X-ray camera. The direct detecting camera is extremely sensitive as a single K_α photons results in $\approx$ 2000 electrons against a dark charge of only one electron per hour per pixel. This allows also to differentiate between K_α and higher energetic bremsstrahlung or even K_β radiation. The main disadvantage is its lower quantum efficiency of $\approx 50\%$ and the fact that the CCD chip is damaged by the X-ray flux: First, the dark current increases at locations where exposure has been high. Test measurements at 8 keV indicate that this increase becomes noticeable when the lifetime exposure exceeds about 1 million X-ray photons detected per pixel. The dark current continues to rise as the accumulated dose grows. For even higher exposures, the second stage of failure occurs: the formation of a charge trap. The charge trap prevents efficient charge transfer through the affected pixels and looks like a partial bad column. Again, in test measurements at 8 keV, a trap forms when the lifetime exposure reaches about 50 million detected photons per pixel. The indirectly detecting CCD camera uses a phosphor scintillator and a taper fibre bundle to image secondary photons onto the CCD chip. The scintillation material is Gadolinium oxysulfide (with terbium) polycrystalline phosphor (Gd_2O_2S:Tb) with a very high quantum efficiency of nearly 100%. For our camera with a 2.5:1 fiberoptic taper, this phosphor generates approximately 7 electrons for each 8-keV x-ray photon. Obviously single photon counting does not work with this camera. Since the CCD chip itself is not exposed to the hard X-ray radiation no degradation occurs. Therefore this camera is well suited to characterize the X-ray source and may be used to align the X-ray mirrors. The readout speed of both cameras is identical, 1 kHz readout of a full frame takes about 2 seconds, whereas with 100 Hz it takes 18 seconds. Restricting the readout to small regions of interest together with binning several pixels the readout time may be reduced to a few hundred Milliseconds. The most important parameters of the two cameras are summarized in Table 3.2.

	Ropers Scientific Scintillation Detector	Ropers Scientific Deep Depletion
Chip Size	1340× 1300	1340×1300
Pixel Size	20×20 μm	20×20 μm
Quantum Efficiency (Cu-K_α)	$\approx$ 95 %	$\approx$ 50 %
Working temperature	-35° Celsius	-100° Celsius
Type of cooling	Peltier	liquid Nitrogen
Number of electrons per K_α	7	2190
Dark charge	0.054 e/s	1.44 e/hr
Readout noise 100 kHz	3.32 e	2.81 e
Readout noise 1 MHz	7.41 e	5.26 e
Readout time 100 kHz	18 s	18 s
Readout time 1 MHz	1.8 s	1.8 s

Table 3.2: Main parameters of the two different CCD cameras used in the time-resolved x-ray diffraction experiments.

3.3.3 Source Stability and Normalization Schemes

Intensity fluctuations of the X-ray source are the dominant origin for noise in the time-resolved X-ray diffraction experiments, when changes of the structure factor (number of reflected photons), rather than line-shifts are of interest. We can differentiate between long time drifts of the X-ray flux, which can amount to a decrease of up to 50 % over a whole day and fluctuations on a shorter time-scale. For the slowly decreasing X-ray flux over the course of several hours one can identify two main contributions: first, the debris caused by the explosions in the copper target coat the protective plastic band in front of the lens and reduce its transmission for the main laser beam. Secondly, the microscopic holes which are formed after the explosions impair the mechanical stability of the copper foil and tend to bend it along the horizontal direction. This moves it out of the laser focus as well as increase its fluctuations. Note that instabilities of the target only in the range of the Rayleigh length ($\approx 50\mu m$) can already half the impinging laser intensity and thus have dramatic consequences on the X-ray emission. Microscopic band fluctuations also happen on shorter time scales. Also on shorter time scales, the instability of the driving laser pulse leads to fluctuations. As the electron acceleration in the laser plasma, and thus the K_α production is a highly non-linear process, small variations in the laser energy result in large fluctuations of X-ray photon numbers. However, the laser generally had very small pulse to pulse fluctuations. Finally the X-ray mirrors are very sensitive to the position of the X-ray source, which makes pointing instabilities of the

laser another source of X-ray fluctuations.

The detrimental influence of long time drifts may easily be avoided by reducing the integration time per time-delay point and averaging over many temporal scans. In other words the fluctuations need to be on a longer time scale than the time it takes to measure one temporal scan, which is determined by the number of data points, the integration time and readout time of the CCD-camera. This time can be further reduced by measuring alternatively delay points before and after time-delay zero, of course with the disadvantage to greatly lengthen the total measuring time. The most accurate and robust normalization scheme is to directly compare the X-ray signal diffracted from an un-pumped and a close by pumped region of the crystal [compare figure 3.2 b)]. This makes almost no assumption about the isotropy of the source. This is only possible if the X-ray probe diameter is larger than the optically excited region.

In the present work the investigated thin layers or superlattices where grown on top of a substrate with similar lattice constants. This implies that for an X-ray beam with finite divergence the substrate reflection can be measured simultaneously and may be used for normalization. Care has to be taken for larger delay times when the assumptions that the substrate material is not affected by the excitation loses its validity. In particular, strain waves in the substrate can significantly alter the reflected intensity (compare chapter 4). It is advisable to be cautious when using the transmitted X-ray beam for normalization. Mainly because for crystals made out of light elements, which is of course a prerequisite to measure an appreciable amount of transmitted photons, optical excitation may change the diffuse scattering and thus modulate the transmitted beam [124]. For normalization one may also use a second crystal which remains un-pumped and is mounted on an individual rotation stage to diffract the X-ray flux ideally on the same or on a separate X-ray camera.

An exemplary measurement of the X-ray fluctuations is shown in figure 3.7. It shows the diffracted photons of the (002) planes of a bulk $SrTiO_3$ crystal which is unaffected by optical pump light. In the time-resolved experiments it was used as a normalization signal. The integration time per point was 15 seconds and the different images were acquired in direct succession. The number of photons fluctuates by about 100.000, the overall standard deviation amounts to approximately 10%. Note, that noise due to the counting statistic ($1/\sqrt{N}$, N number of photons) plays a negligible role.

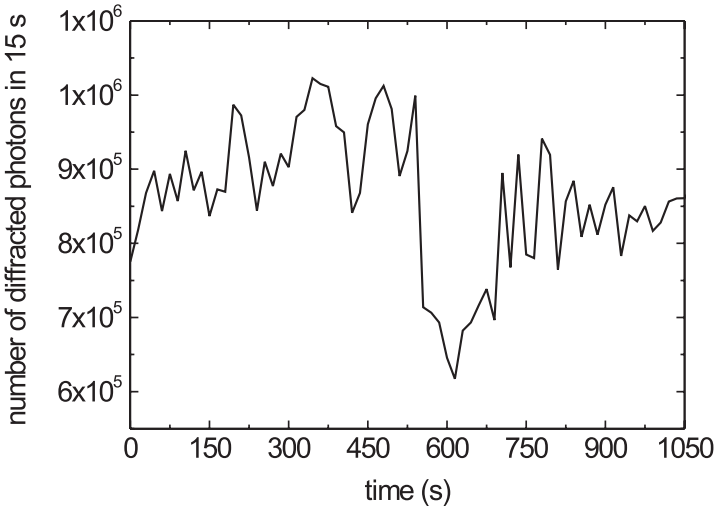

Figure 3.7: Total amount of diffracted X-ray photons of the (002) STO substrate Bragg reflection unaffected by the pump pulse. The graph shows a continuous scan with 15 seconds integration time.

3.3.4 X-Ray Optics

The main advantages of X-ray optics in time-resolved X-ray diffraction experiments are an intensity gain by focusing, the suppression of the Bremsstrahlung background and of the characteristic K_β radiation as well as a convenient control over the divergence of the X-ray beam. Since for X-rays the real part of the refractive index n is nearly 1, X-rays cannot be shaped by lenses. Instead we use the possibility of controlled X-ray beam shaping by Bragg diffraction. In the present work three different multilayer optics in a Montell geometry were used as summarized in Tab. 3.3. Their advantage in comparison with other designs are their exceptionally high transmission between 0.3 and 0.8, their large collecting solid angle Ω_0 and their small focus size of down to d=32 μm [125]. The number of photons per second incident on the sample amounted to maximal 2×10^6. For the very small source size and an approximate penetration depth into the multilayer of 1 μm, no appreciable temporal broadening is expected. Their large convergence angle allows to measure several of the closely spaced superlattice SL Bragg peaks and the substrate peak simultaneously. Even though the suppression of K_β is very good (for optic 3 the ratio K_α/K_β was measured to be 0.0005), both $K_{\alpha 1}$ and $K_{\alpha 1}$ are transmitted. Obviously this increases the total photon flux, but it may be detrimental once Bragg peaks start to overlap. In particular it makes the static characterization of the samples more difficult.

	1	2	3
Manufacturer	Incoatec	Incoatec	Osmic
X-ray source-focus distance (mm)	500	500	297
X-ray source-optic distance (mm)	50	20	43
length of optic (mm)	150	80	124
Magnification	3	7.333	2
Solid Angle Ω_0 (sr)	2×10^{-3}	$9.3{\times}10^{-4}$	8.8×10^{-4}
Transmission	0.6	0.5	0.2
1-D convergence $\Delta\theta_{\mathrm{mirror}}(deg)$	0.688	0.183	0.45
Focus size (μm)	80	150	32
Beryllium windows	no	no	yes
photons/s on sample	$\approx 2 \times 10^6$	$\approx 5 \times 10^5$	$\approx 5 \times 10^5$
Experiment	Cryostat SL	DIABN	SL

Table 3.3: Main design parameters of the three different multilayer mirrors employed in the time-resolved x-ray experiments.

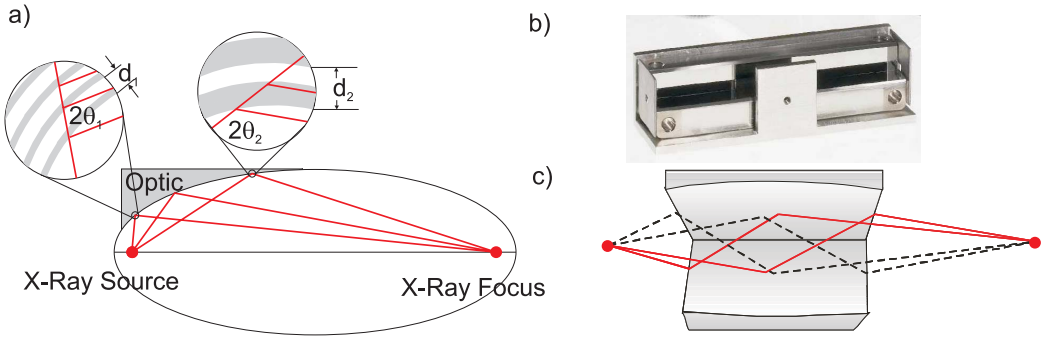

Figure 3.8: **a**) Schematic of an elliptically shaped, focusing multilayer. **b**) Photograph and **c**) schematic of the multilayer mirror in the Kirkpatrick-Baez scheme.

Focusing optics work by curving the optics surfaces into elliptical shapes. The d-spacing (thickness of a single bilayer) of the multilayer coating is controlled along the optic´s surface to satisfy Bragg´s law at every point, as schematically shown in figure 3.8 a). The typical values for the thickness of the bilayers are between 3-5 nm. There are two possible optical paths [figure 3.8 c)] to focus in two dimensions by the Kirkpatrick-Baez scheme [126]. Changing the size of the ellipse allows to tailor the distance between source and optic and between optic and focus. This flexibility is important for time-resolved experiments, since the focus of a laser-driven-plasma-source has a restricted accessibility and to achieve a source-optic distance below 2

Centimeters is usually impossible. Geometrical constraints are also determined by the type of goniometer and, for low temperature experiments, by a cryostat.

3.3.5 X-Ray Cryostat

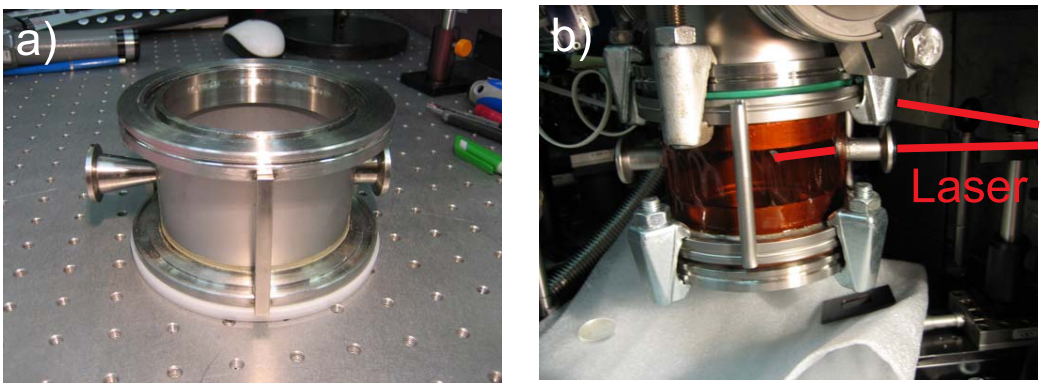

Figure 3.9: Photograph of the vacuum chamber for the cryostat. The optical excitation light is coupled in via a glass window attached to the conical tube. The X-rays enter and leave the chamber through **a**) the grey Beryllium wall and **b**) through a the orange Kapton foil.

For low temperature experiments we used a Helium/Nitrogen-flow-cryostat manufactured by CRYOVAC. The lowest accessible temperature was 20 Kelvin for liquid Helium and 85 Kelvin for liquid Nitrogen, two heaters with 5 and 50 Watts were used to stabilize the temperature to a relative accuracy of 0.4 Kelvin. The heater is also designed to heat the sample to up to 600 Kelvin. The sample plate was on an manually controlled x-y-z stage and additionally the angle θ and ϕ could be controlled, albeit fairly coarsely. Ideally one chooses a constant Helium flow to cool the sample to a temperature slightly below the desired value and uses the electric heaters to set a constant temperature. To have a maximum flexibility and to avoid to place the entire setup including the CCD-camera in vacuum, a small Beryllium vacuum chamber was constructed, which only enclosed the sample. A photograph is shown in figure 3.9 a). The walls of the chamber were chosen to have a thickness of 500 μm which ensured a sufficient stability. They amount to a total attenuation of about 15 %. The optical pump light was coupled into the chamber through a glass window, attached to a conical tube. This sets a minimum value for the angle between X-ray probe and pump light of about 15 degrees, which - at least for small beam diameters - does not significantly

impair the temporal resolution. Since Beryllium is an extremely toxic material, in a new design the Beryllium wall was replaced by a 125 μm thick, non-toxic and inexpensive Kapton foil [compare photograph in figure 3.9 b)]. It can withstand atmospheric pressure and amounts to a similar X-ray attenuation. It has the additional advantage of being transparent for visible light, such that the sample can be monitored during the experiment.

Chapter 4

Strain Propagation in Nanolayered Perovskites

Strain is the geometrical expression of deformation caused by the action of stress on a physical body. More specifically, for thin epitaxially grown films one-dimensional strain may be defined as the ratio between the (strained) out-of-plane and in-plane lattice constant, c and a, respectively. It is denoted as tetragonal distortion $\eta = c/a$. Note that for structures in equilibrium this value is exactly one only for perfectly cubic structures.

Physical properties of Perovskite oxides depend very sensitively on strain [127] and may lead to preferable properties like enhanced remanent polarizations and larger electro-optic coefficients [128]. Beyond static *strain engineering*, electron-phonon coupling after photo-excitation can result in dynamic transient strain that propagates through a Perovskite film and its substrate, directly affecting their mechanical and electronic behavior. In particular, propagation of optically induced acoustic strain waves allows for a spatial modulation of electronic properties in a well-defined way. As strain propagates at the speed of sound ($v_{ph} \approx 8000$ m/s), the relevant time scale of strain transients in nanostructured Perovskites (thickness d $\leq$100 nm) is in the order of tens of picoseconds. Ultrafast time-resolved X-ray diffraction offers the possibility to measure absolute strain amplitudes on the relevant time scales.

In the following quantitative measurements of photoinduced transient strain in a Perovskite thin film heterostructure are presented. A peculiar two-step time evolution of diffracted X-ray intensity is identified which originates from the interference of X-rays diffracted from strained and unstrained parts of the sample. An analysis of such behavior by dynamical diffraction theory allows for an absolute calibration of the change in tetragonal distortion in a range down to $\Delta c/c_0 = 2 \times 10^{-5}$.

4.1 Characterization of PZT/SRO Heterostructure

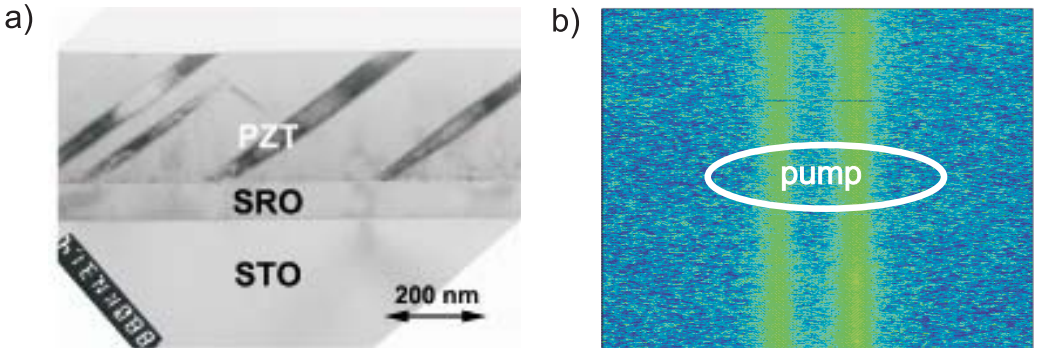

Figure 4.1: **a**) Transmission Electron Microscope image of the PZT/SRO heterostructure grown on a STO substrate. **b**) CCD image of the (004) Bragg reflection of the STO substrate. The two reflections are due to the diffraction of $K_{\alpha 1}$ and $K_{\alpha 2}$. The excited region is indicated as projected on the CCD-camera.

The heterostructure was fabricated at the Max Planck Institute of Microstructure Physics, Halle, by pulsed-laser deposition, employing a KrF excimer laser (λ=248 nm). The $SrRuO_3$ (SRO) layer was deposited on single crystalline $SrTiO_3$ (100) (STO) substrates (miscut angle 0.25°, $c = a = b =$ 0.3905 nm) at a temperature of T=980 K in a background atmosphere of 100 mTorr oxygen. The subsequent $PbZr_{0.2}Ti_{0.8}O_3$ (PZT) layer was grown at T=850 K in 200 mTorr oxygen, and the ratio of Zr vs Ti ions was chosen to match the in-plane lattice constant of PZT with $SrRuO_3$. Macroscopic ferroelectric hysteresis curves, dielectric measurements, and local piezoresponse scanning force microscopy investigations confirmed the ferroelectric behavior of the PZT film, including a remanent polarization of the order of P_r=80 $\mu C/cm^2$ [129]. Transmission Electron Microscope (TEM) and electron diffraction investigations performed on a thinned cross-section sample revealed the entire heterostructure to be epitaxial and the interfaces to be plane and sharp. The films contain ferroelectric domain boundaries of 90° a-c type [figure 4.1]. A 90° tilt of the a and c axis results in a considerable strain in PZT and, hence, results in a pronounced contrast in the TEM image [130]. The layer thicknesses of 100 nm for the SRO and 250 nm for the PZT layer are read from the TEM image.

4.2 Time Resolved X-Ray Data

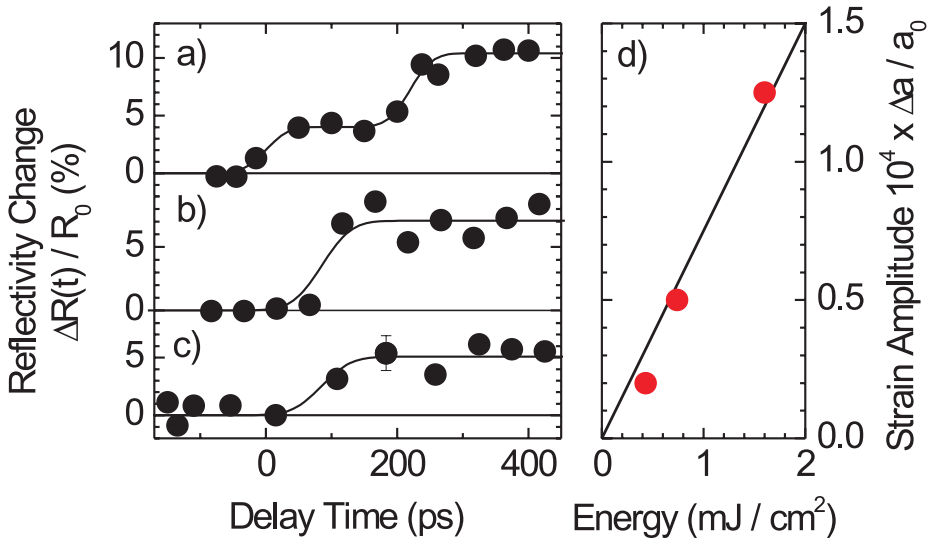

Figure 4.2: **a**) Measured angle-integrated diffraction intensity of the (004) reflection of STO for different pump fluences of **a**) 1.6 mJ/cm^2, **b**) 0.74 mJ/cm^2 and **c**) 0.43 mJ/cm^2. Black dots represent the measured data points and the lines are guides to the eye. The reflectivity change $\Delta R/R_0$ is plotted as a function of the delay time between 400 nm pump and X-ray probe pulses. **d**) Measured strain amplitude (red dots) versus excitation fluence together with a linear fit.

In the experiment, PZT and SRO layers of the sample are excited by a pump pulse with λ_{ex} = 400 nm (second harmonic of the fundamental wavelength), an energy up to 100 μJ and a duration of 50 fs. The spot size on the sample is 6 mm^2. Optical excitation creates stress in the excited layers and the resultant strain and its subsequent propagation into the $SrTiO_3$ substrate is probed by diffracting X-ray pulses off the (004) atomic planes of $SrTiO_3$ for different time delays. For each time delay the diffracted intensity of the substrate is integrated for 120 seconds and at least two scans in the temporal forward and backward direction are averaged. The influence of X-ray intensity fluctuations on the signal is minimized by normalizing to the reflection unaffected by the pump light [compare figure. 4.1 b)]. To monitor unwanted effects like thermally induced angular misalignment of the crystal,

every fourth measurement point is taken at negative delay, that is, before the pump pulse excites the sample.

In figure 4.2, the transient change of the angle-integrated reflectivity $\Delta R/R_0 = (\Delta R - R_0)/R_0$ of the (004) reflection of the STO substrate is plotted as a function of the delay time between 400 nm pump and X-ray probe pulses (dots, R, R_0: reflectivity with and without excitation). The transients measured with pump fluences of a) 1.6 mJ/cm^2, b) 0.74 mJ/cm^2, and c) 0.43 mJ/cm^2 display an increase of the angle integrated reflectivity which occurs in the picosecond time domain, that is, much slower than our time resolution. The time evolution changes significantly with pump fluence. For the strongest excitation [figure 4.2 a)], the signal clearly grows in two steps, whereas only one step is found for weaker excitation. Moreover, the maximum reflectivity change $\Delta R/R_0$ does not scale linearly with the excitation fluence.

4.3 Strain Propagation and X-Ray Interference

4.3.1 Strain Propagation

The pulses centered at $\lambda_{ex} = 400$ nm are exclusively absorbed in the PZT and SRO layers, as the STO substrate is transparent at this wavelength [131–133]. The pump pulse produces stress on a fast time-scale, which leads to the formation of propagating strain fronts, modifying the separation of lattice planes c [134]. In the experiment the diameter of the laser spot exciting the crystal is very large compared to the laser penetration depth, therefore the strain pulse launched into the crystal is one-dimensional, and strain occurs only along the surface normal c. The resulting lattice dynamics is described by a linear chain model, as explained in section 2.9.1 and appendix B. Such transient changes of lattice geometry give rise to changes in the time-resolved X-ray diffraction pattern.

Parameters of Strain Propagation Calculation

To calculate the propagating strain pattern $\Delta c(t)/c_0$ after photoexcitation, we need the corresponding masses and elastic constants or values for the velocity of sound in PZT, SRO and STO. For bulk STO these values are known, for the longitudinal propagation in [001] direction, we have $v_{STO} = 7876 m/s$ [135]. For the thin top layers of crystalline PZT and SRO the values taken from literature may be less reliable. Most publications measure the velocity

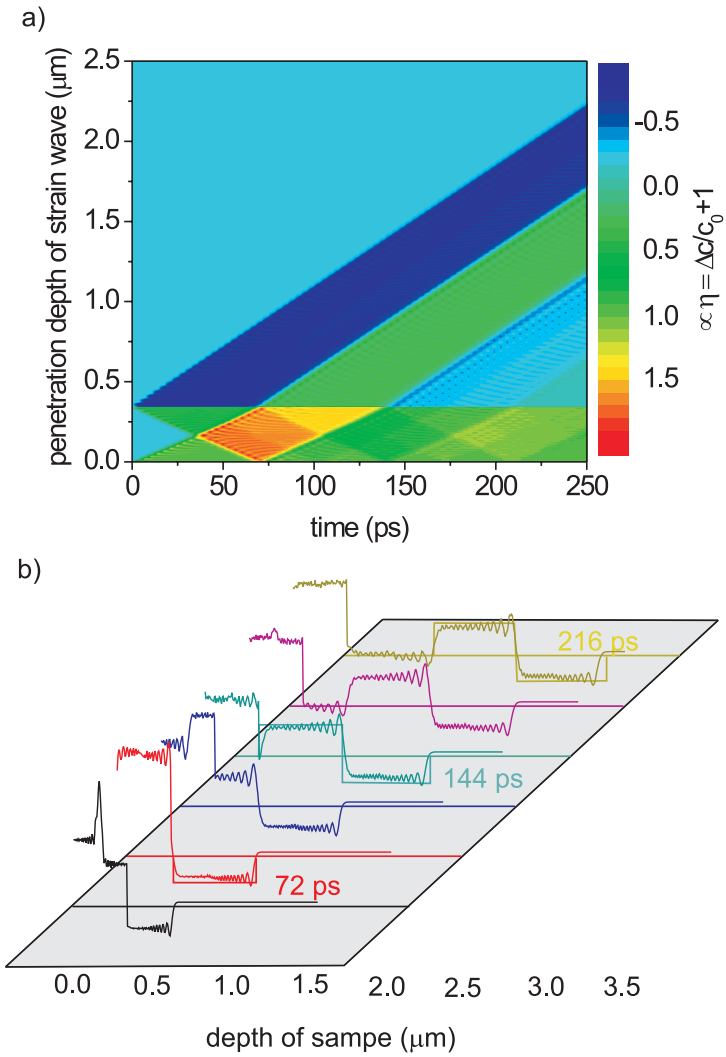

Figure 4.3: **a**) Calculated strain pattern as a function of penetration depth and time delays. **b**) Cross sections for different time delays. For simplicity the strain front entering the STO substrate is assumed to be of rectangular shape.

of sound in poly-crystalline SRO samples as v_{SRO}=6312 m/s [54] or ceramic PZT $v_{\mathrm{PZT}} \approx 4500$ m/s [136]. Here, one expects an average piezo-electric contribution. Unfortunately, for the solid solution $PbZr_{0.2}Ti_{0.8}O_3$ experimental data on elastic properties is limited. The velocity of sound in a single crystal $PbTiO_3$ crystal was measured by Brioullin scattering [137] and the corresponding elastic constant along the [001] direction was determined to be 150

GPa, yielding a similar sound velocity as mentioned above. Similar results for single crystal $PbTiO_3$ were also obtained in a related work [138]. Lower values have been reported in a comparison of elastic constants of sol-gel and epitaxial films [139]. Changes of the velocity of sound due to mechanical boundary conditions of the substrate resulting in biaxial strain in the thin layers should also be considered; albeit they are small in $BaTiO_3$ [140], they are expected to be more pronounced in PZT. Finally the presence of a-domains, as seen in the TEM picture [figure 4.1 a)], additionally alters the average sound velocity. The phonon calculation is performed with an average velocity of sound for the top layer of $v_{\mathrm{PZT/SRO}} \approx 3100$ m/s, despite the fact that the values published in literature give evidence of a larger velocity of sound. This procedure is supported by our experimental data, as discussed later, but admittedly represents a source of uncertainty. As discussed in section 2.9.1 on lattice dynamics only an average relative mass density for each individual unit cell is used to determine the corresponding spring constants. The induced stress is normalized to one and the resulting strain only later quantitatively determined by the experimental data (compare details in appendix B). The relevant parameters used in the simulation for the strain propagation are summarized in table 4.1.

	$PbZr_{0.2}Ti_{0.8}O_3$	$SrRuO_3$	$SrTiO_3$
velocity of sound v	3100 m/s	3100 m/s	7876 m/s
layer thickness d	250 nm	100 nm	$>$ 3500 nm
relative mass densities $\Delta\rho/\rho_0$	1	0.797	0.618

Table 4.1: Parameters used in the strain front propagation simulation of the heterostructure PZT/SRO on a STO substrate

Strain Pattern

The simulation according to section 2.9.1 then yields a) the 2-dimensional strain pattern $\propto \Delta c/c_0$ as a function of penetration depth and time and b) cross-sections for various time delays as shown in figure 4.3. In the following discussion of the strain pattern several simplifications are introduced, first of all, one assumes that the the strain fronts have a symmetric, rectangular shape, as depicted schematically in figure 4.3 b). Later it is shown that this is a valid approximation, since the measured X-ray reflectivity change only depends on the accumulated strain and not on the exact form of the strain pattern. Secondly, one also neglects secondary weaker compression and expansion waves which enter the substrate after two and three round trips,

respectively. For the analysis of the experimental data, only consider three different strain fronts are considered, one generated at the air-PZT interface and two at the SRO/STO interface[1], where the stress in the material is not balanced. At t=0, an expansion front with an amplitude $2\Delta c/c_0$ starts from the sample surface and enters the STO substrate after

$$\Delta t = d_{\mathrm{PZT}}/v_{\mathrm{PZT}} + d_{\mathrm{SRO}}/v_{\mathrm{SRO}} \approx 113 \text{ ps}. \tag{4.1}$$

At the SRO/STO interface, two strain fronts of amplitude $\Delta c/c_0$ start at t=0, a compressive one into the optically unexcited STO substrate, and due to conservation of momentum an expansive one into the SRO and PZT layers. The latter strain front is reflected at Δt from the sample surface and is converted into a compression front that enters the STO substrate at $2\Delta t$. The maximum strain in the top layers is reached after Δt when the strain fronts from both interfaces constructively overlap [cross-section plotted in red in figure 4.3 b)]. The time it takes the strain wave to cross the front layer and the sound velocity in STO, v_{STO}, determines the width of the compressive and expansive strain wave entering the STO substrate. Accordingly, the width of the compressive and expansive strain front is

$$d = d_{\mathrm{exp}} = d_{\mathrm{compr}} = \Delta t \cdot v_{\mathrm{STO}} \approx 890 \text{ nm}. \tag{4.2}$$

After 2 $\Delta t \approx 226$ ps the strain front has completely entered the substrate.

4.3.2 X-Ray Interference

For a quantitative analysis of the measured angle-integrated transients of figure 4.2 and, in particular, to understand the origin of the double step behavior, dynamical X-ray diffraction theory must be applied. The matrix formalism introduced in chapter 2.7.3 is used to model the changes in X-ray reflectivity. The rectangular strain profiles as discussed above change the distance c between atomic planes and modify the phase factor ϕ according to equation 2.30. Hence, the effect of strain is fully described by modified propagation matrices L in equation 2.33. Appendix A contains further details of the calculation.

Phonon Induced Sidebands

The strain wave changes the lattice-plane distances c that determine the phase shift of the X-ray waves scattered from each lattice plane. According

[1] We further neglect the strain wave originating from the discontinuity at the PZT/SRO interface.

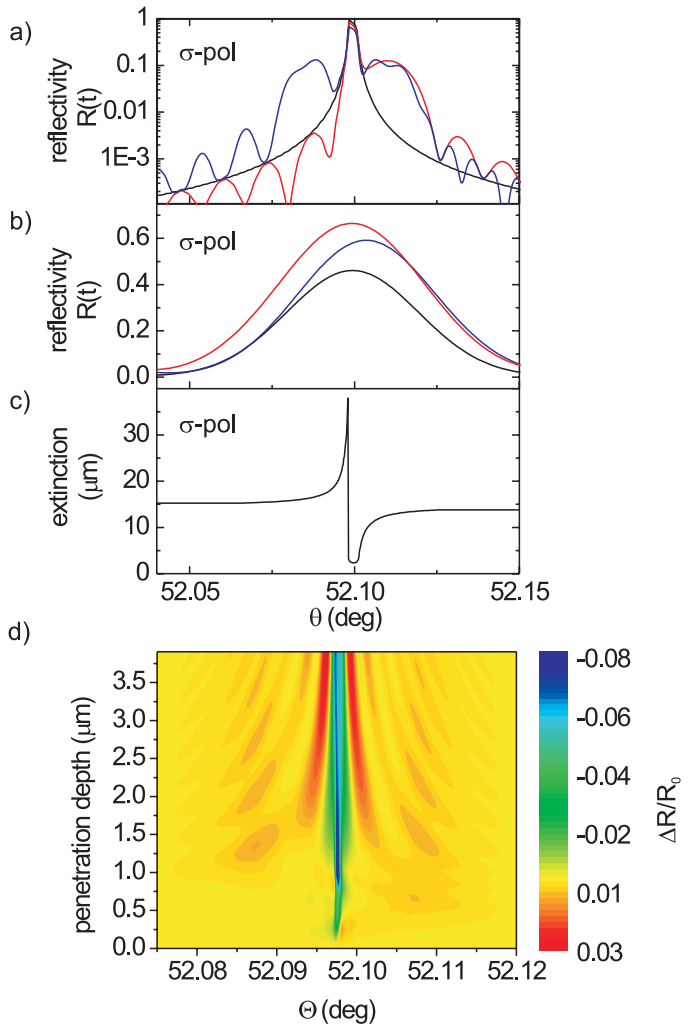

Figure 4.4: **a**) Reflectivity of the (004) reflection for σ polarized X-rays of the STO substrate as a function of the diffraction angle θ calculated without strain (solid black), with a compression (red dotted) and a compression and an expansion wave (blue line). **b**) Convolution of the curves shown in the upper panel with the angular resolution of the experiment. **c**) Calculated extinction length of the (004) reflection as a function of θ for σ polarized X-rays. **d**) Calculated reflectivity change as a function of diffracting angle and penetration depth of the strain wave for a strain amplitude of $\Delta c/c_0 = 1.25 \times 10^{-4}$.

to Bragg's law, the compressed part of the sound wave reflects at larger angle, θ, while the expansion wave reflects at smaller θ. The resulting calculated sidebands around the central peak are shown in the angle resolved pattern in figure 4.4 a) for the case of σ polarized X-rays: the red line shows the sideband only due to the compression wave, which enters the substrate first. The blue line is the result of the same calculation, only now for later times when the total strain wave has entered the bulk: sidebands appear at both larger and smaller angles.

This may be fully appreciated by inspection of the calculated contour plot 4.4 d). It displays the change of reflectivity as a function of diffraction angle, θ, and penetration depth of the strain wave in micrometers. The calculation includes σ and π polarization as required for the unpolarized X-ray source. Also the (small) reduction of the form factors due to the Debye Waller factor [141] of $SrTiO_3$ is taken into account. One clearly sees the build-up of sidebands as the strain wave enters the substrate, first at larger angles and subsequently at smaller angles. The sidebands result in an increase of reflectivity (red color code), while the center of the Bragg peak is (slightly) attenuated (blue color code).

Line-Shift of Bragg Diffraction Peak

Figure 4.4 b) shows the calculated convolution of the theoretical X-ray reflectivity curves to yield the angular resolution of the measured $K_{\alpha 1}$ and $K_{\alpha 1}$ lines. Unfortunately, details of the evolution of the sidebands generated by the strain wave cannot be resolved. In particular, the intensity oscillations at an offset angle, $\Delta\theta$, cannot be detected. Figure 4.5 shows the calculated shift of the center of gravity of the diffraction line as a function of the penetration depth of the strain wave with an amplitude of $\Delta c/c_0 = 1.25 \times 10^{-4}$. Under the experimental conditions described above this amounts only to 5 arc seconds. One can easily measure the angular range which is imaged onto a single CCD pixel that gives the absolute lower limit of the experimental angular resolution. This is plotted in the same graph as the grey shaded area and amounts to, approximately, 4 arc seconds. Admittedly, this experimental setup is not optimized for angular resolution, but note that for the lowest measured strain, the expected angular shift is below one arc second, but results in a pronounced reflectivity change of 5 %.

X-Ray Extinction

In the high-quality STO crystal, the X-ray penetration depth at Bragg peaks is determined by extinction, that is, by the constructive interference of all

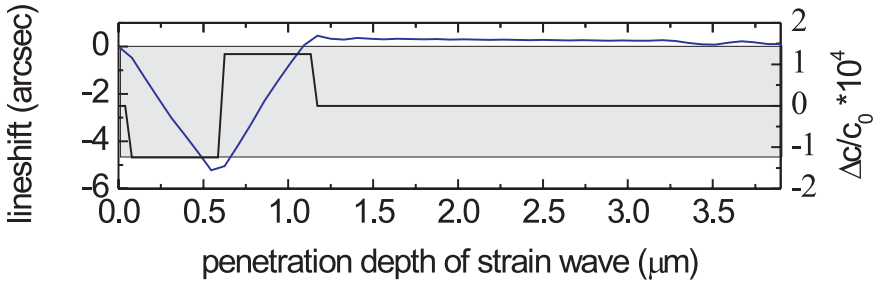

Figure 4.5: Calculated line-shift for a strain amplitude of $\Delta c/c_0 = 1.25\times10^{-4}$. When the complete strain wave has entered the crystal the center of gravity of the diffracted signal has relaxed to its original value. The shaded area marks the angles imaged on one single CCD-pixel and gives a lower limit of the angular resolution of the experiment.

waves scattered from lattice planes that scatter in phase. For the (004) peak of the STO substrate studied here, the X-ray extinction length depends strongly on the diffraction angle θ. For sigma (σ) polarized X-ray light the calculation yields an extinction length at the center of the Bragg peak of only $\approx$ 3 μm [figure 4.4 c)] [2]. As schematically depicted in figures 4.6 a) and b), the presence of the strain wave leads to an increase of the X-ray penetration depth at the center of the Bragg peak because the strained part of the sample does not contribute to extinction. While the central peak is only moderately reduced in intensity by absorption over the enhanced penetration depth, in the angle-integrated signal, the additional intensity of the sidebands overcompensates the loss in the center and results in an overall increase of diffracted intensity.

Reflectivity Calculations

In figure 4.7, the calculated angle-integrated reflectivity change, $\Delta R/R_0$, normalized to the strain amplitude $\Delta c/c_0$ is plotted as a function of the propagation distance of the strain wave into the STO substrate for different *accumulated* strain amplitudes $d \cdot \Delta c/c_0$ of the compressive/expansive strain waves. These are simply obtained by performing an angle integration of the reflectivity curves, two of which are exemplarily shown in figure 4.4 a). Note that the curves are plotted with an offset of 500, 1000, 1500, 2000, 4000 and

[2]The asymmetry of the extinction curve and, in particular, the increase of penetration depth for smaller angles is due to the Borrmann effect, which describes a decrease in absorption when the minima of the X-ray wave coincide with the maxima of the electron distribution.

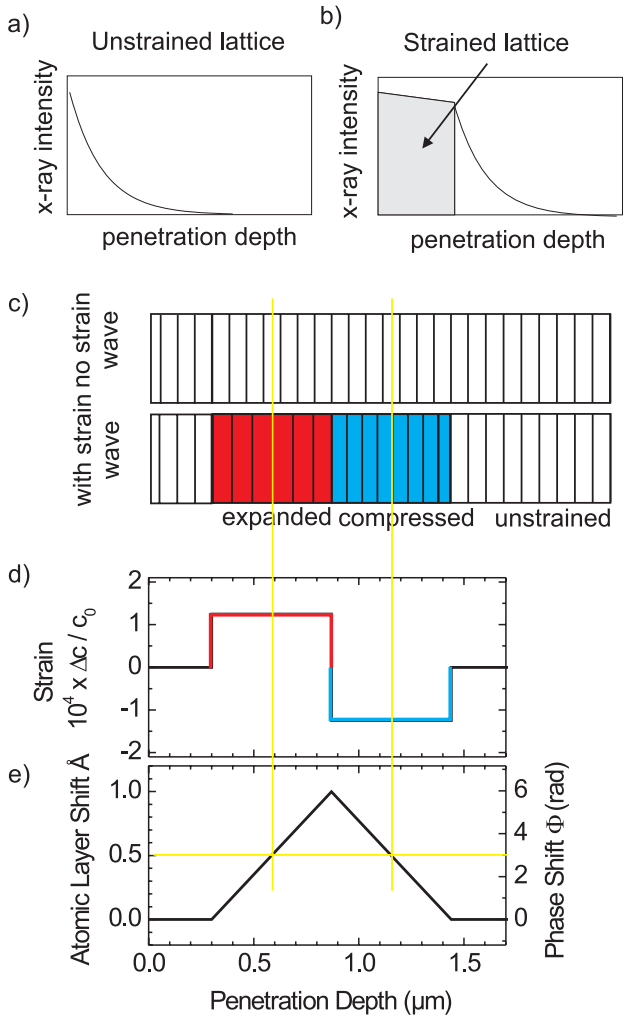

Figure 4.6: **a**) Decreasing X-ray intensity as a function of penetration depth. **b**) The strained part of the lattice does not contribute to the extinction length, therefore the X-rays penetrate deeper into the crystal. **c**) Schematic of lattice planes in the unstrained and strained STO crystal. The yellow line marks the position where the central part of the compressive and expansive part are out of phase with respect to the unstrained sample. **f**) Compressive and expansive part of the strain wave with $\Delta c/c_0 = 1.25\times10^{-4}$ **g**) Integration of the strain fronts shows an accumulated lattice displacement of one full lattice-plane distance, that is, 1/4 of the lattice constant $c_0 = 0.3905$ nm, corresponding to a π phase shift for the central parts of the compressive and expansive strain waves.

5000 for increasing strain amplitudes. The shape of the curves changes above a certain threshold (for $d \cdot \Delta c/c_0 < 0.004$ nm the shape remains constant), indicating a nonlinear dependence of the integrated X-ray reflectivity on the strain amplitude. While for extremely low strain amplitudes the reflectivity change, $\Delta R/R_0$, shows a pronounced maximum within the first micrometer of penetration, the curves of the experimentally accessible strain amplitudes $d \cdot \Delta c/c_0 > 0.025$ nm show a single, step-like reflectivity increase up to a plateau extending over several micrometers of penetration depth. For $d \cdot \Delta c/c_0 = 0.1$ nm [thick red curve in figure 4.7] the reflectivity change $\Delta R/R_0$ grows in two distinct steps as a function of the penetration depth as observed in our time-resolved experiment shown in figure 4.2 c). This feature occurs

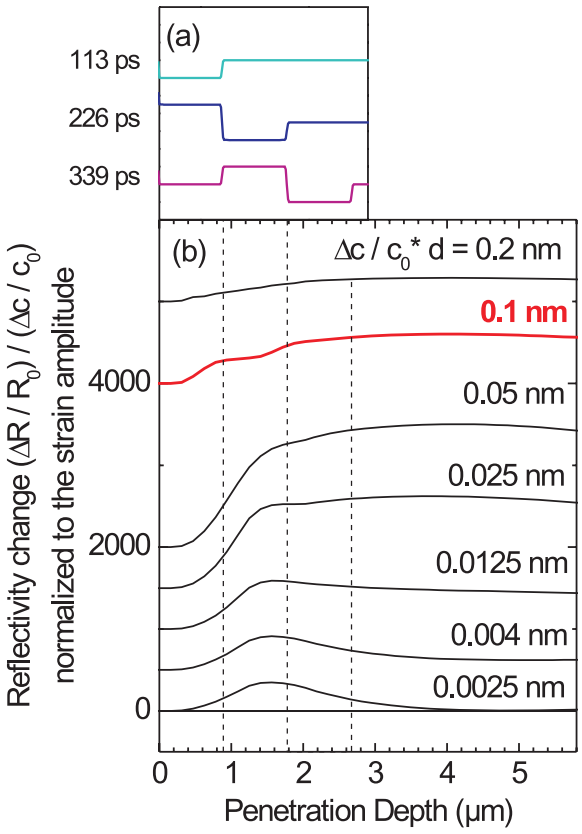

Figure 4.7: Calculated reflectivity change $\Delta R/R_0$ of the (004) reflection of STO normalized to the strain amplitude $\Delta a/a_0$ as a function of the position of the strain wave (leading edges of the wave in upper inset indicated by dashed lines) for different strain amplitudes as indicated. For $\Delta c/c_0 = 1.25 \times 10^{-4}$ the signal grows in two steps (thick red line).

when the accumulated lattice displacement on both the STO compression and expansion waves approaches $\Delta c/c_0 \cdot d = 0.1$ nm. This is equivalent to 1/4 of the lattice constant $c_0 = 0.3905$ nm and corresponds to the distance of the scattering planes $d_{\mathrm{hkl}} = d_{004}$. The signal reaches the plateau after the entire strain wave has entered the substrate. Careful analysis reveals that the calculated double-step trace reaches the plateau approximately at the same time as the experimental data. This time is given by $2\Delta t = 2d \cdot v_{\mathrm{STO}} = 226$ ps. This supports the assumed value for the velocity of sound in the top layer of $v_{\mathrm{SRO/PZT}}$, which determines the width of the strain wave of $d = 890$ nm.

X-Ray Interference

The figures 4.6 c)-e) schematically depict how the interference of X-ray leads to the measured double step in the time dependent X-ray reflectivity change. In the upper part of panel c) the equidistant lines symbolize the scattering planes (004) of the undisturbed crystal. In the lower part, the compression (blue) and expansion (red) waves have entered the sample and lead to a smaller and bigger distance between the atomic layers, respectively. If the total accumulated strain amounts to the distance of the scattering planes ($1/4\ c_0 = 1/4 \cdot 0.3905$ nm), the central parts of the compression and expansion wave are exactly out of phase with the unstrained sample. This position is marked with a thick yellow line. In figure 4.6 d), the strain wave is plotted with its absolute value as a function of penetration depth and, finally, the integrated strain is shown in figure 4.6 e). A π phase shift between strained and unstrained parts of the sample leads to destructive interference and, thus, a saturation of the reflectivity. In fact, the destructive interference interrupts the monotonous increase due to the build-up of sidebands, observed for weaker strain amplitudes.

Absolute Calibration of Strain Amplitudes

The two-step relation between $\Delta R/R_0$ and $\Delta c/c_0$ is only observed in a narrow range of strain amplitudes in the simulation around $d \cdot \Delta c/c_0 = 0.1$ nm. Together with the value for the width of the strain wave, $d \approx 890$ nm, this allows for a comparison with the experimental data and for an absolute calibration of the strain amplitudes underlying the measured transients. The double-step measured with a pump fluence of 1.6 mJ/cm^2 [figure 4.2 a)] is in good agreement with the calculated signal for a strain amplitude $\Delta c/c_0 = 1.25 \times 10^{-4}$ [compare red line in figure 4.7]. The reflectivity changes observed with lower pump fluences [figures 4.2 b) and c)] are also in good agreement with the simulated traces and yield $\Delta c/c_0 = 5 \times 10^{-5}$ and $\Delta c/c_0 = 2 \times 10^{-5}$,

respectively. This allows for deriving the strain amplitude as a function of fluence, as shown in figure 4.3 d) together with a linear fit to the data. The evaluation shows that within the experimental accuracy, the response is linear and the smallest measured amplitude of the strain wave has a value of only $\Delta c = 2 \times 10^{-5} \cdot c_0$, or in absolute numbers 10 femtometer.

Even though the absolute value of the reflectivity change is well reproduced by the simulation, it depends very sensitively on the scattering amplitude of the crystal. This inevitably also depends on the crystalline perfection of the sample, which is usually unknown or difficult to quantify. Also ambiguities and uncertainties in the data analysis may have a slight influence on the absolute reflectivity change. However, the double-step increase represents a robust condition to set the absolute strain amplitude.

The results obtained here can be compared to experiments in germanium on a silicon substrate [28], where the strain transients in the silicon substrate were determined from the observed line-shift. In these experiments a larger peak strain of 5×10^{-4} induced by the weakest pulses (15 mJ/cm^2) was detected via the line-shift of 3 arc s. Earlier work detected large strain of milliångström in GaAs by a line-shift of about 100 arc seconds [26]. In experiments with an almost monochromatic, parallel X-ray beam from a synchrotron facility the intensity oscillations were observed at an offset angle with respect to the Bragg angle [compare figure 4.4 d)], but also induced much larger strain amplitudes [14, 66]. An increase of integrated reflectivity of a polychromatic X-ray beam diffracted off a strained indium antimonide sample was interpreted in a similar way as presented here [31]. Strained parts of the sample diffract additional X-rays of different wavelength and add to the total diffracted intensity. However, extinction effects due to coherent scattering were not discussed, nor did they present a quantitative analysis.

In conclusion, femtosecond time-resolved X-ray diffraction gives direct insight into strain propagation in Perovskite nanostructures. The intensity of the (004) Bragg peak of the STO substrate displays a time evolution strongly depending on the strain-inducing optical pump fluence. For a narrow range of strain amplitudes, interference of different diffracted X-ray components results in a characteristic two-step increase of Bragg intensity with time. This behavior is fully reproduced by dynamical X-ray diffraction theory and allows for an absolute calibration of strain amplitudes. The shape and size of the induced strain profile can be customized by tailoring the excited top layer. Our results demonstrate the potential of ultrafast X-ray diffraction for a nondestructive analysis of short-lived strain phenomena down to $\Delta c = 2 \times 10^{-5} c_0 \approx 10$ femtometer in technologically relevant Perovskite nanostructures.

Chapter 5

Ultrafast Stress Generation in $SrRuO_3$

The following chapter discusses time-resolved X-ray diffraction experiments on superlattice structures to unravel the mechanism of optically induced stress in the metallic and ferromagnetic oxide $SrRuO_3$. The X-ray response after optical excitation of a ferroelectric/metallic (PZT/SRO) and two dielectric/metallic (STO/SRO) heterostructures are investigated. Direct comparison of X-ray and optical data reveal a delayed rise of the expansive phonon mediated stress. The influence of the optical excitation wavelength both with respect to the induced phonon amplitude and its temporal response is studied. Measurements below the Curie temperature, T_C=160 K, of $SrRuO_3$ reveal an ultrafast magnetostrictive component of stress after a photoinduced reduction of the macroscopic magnetization.

5.1 Stress Generation in Metals

The absorption of an ultrashort optical pulse produces a hot electron population. On a timescale typically in the order of 10 femtoseconds electron-electron scattering leads to a thermal distribution of electrons such that the electrons are characterized by a Fermi-Dirac distribution at a temperature T_e. Consecutive electron-phonon scattering takes place within a few hundreds of femtoseconds and leads to an elevated lattice temperature T_l and a cooling of the electron gas. Anharmonic incoherent phonon-phonon scattering results in an expansion of the solid.

In thermodynamics the build-up of stress is described by the Grüneisen concept and has two components according to the two temperature model. A temperature is attributed to the lattice T_l and to the electronic system T_e. It

was first introduced to explain experimental results which showed deviations from Ohm's law for large current densities [142]. The two contributions to stress may be described as follows [143]:

$$\sigma = \sigma_\mathrm{e} + \sigma_\mathrm{l} = \gamma_\mathrm{e} C_\mathrm{e} T_\mathrm{e} + \gamma_\mathrm{l} C_\mathrm{l} T_\mathrm{l} \tag{5.1}$$

where $\gamma_{\mathrm{e,l}}$ and $C_{\mathrm{e,l}}$ are the Grüneisen parameter and specific heat for electrons and the lattice, respectively.

The lattice Grüneisen parameter for a phonon mode k is defined as the negative logarithmic derivative of the frequency of the mode, ω_k, with respect to volume (see for example M. Born [144]):

$$\gamma_{\mathrm{l,k}} = -\frac{\partial \ln(\omega_\mathrm{k})}{\partial \ln(V)} \tag{5.2}$$

The overall Grüneisen parameter is the weighted average of the γ_k, in which the contribution of each normal mode is weighted by its contribution to the specific heat C_k:

$$\gamma_\mathrm{l} = -\frac{\sum_\mathrm{k} \gamma_\mathrm{k} C_\mathrm{k}}{\sum_\mathrm{k} C_\mathrm{k}} = \frac{V}{C_\mathrm{k} \beta} 3\alpha, \tag{5.3}$$

where β is the compressibility and α the linear thermal expansion. Since the compressibility has a weak dependence on temperature the above definition of a *constant* γ implies that specific heat and the thermal expansion have an identical dependence on temperature. In the simplest approximation the frequency dependence of the Grüneisen parameter can be expressed by a single Debye or Einstein frequency/temperature. Then the Grüneisen parameter is equivalent for all modes of lattice vibrations. Note that this is strictly true for a diatomic chain. The notion that the thermal properties are not sensitive to the frequency distribution except at low temperatures is also supported by the close agreement between the Debye and Einstein curves for the specific heat despite the radically different frequencies assumed. In real crystals γ_l does have a (slight) dependence on the mode specific frequencies and therefore on temperature, while the deviations are generally most pronounced at low temperatures (for example, compare a pressure dependent study on GaAs [145]).

It is very important to keep in mind that the Grüneisen concept is only valid in thermodynamic equilibrium, such that its application to non-equilibrated systems after impulsive optical excitation seems – at least – problematic. Nonetheless, it is extensively used in ultrafast science (for example [27, 146, 147]) and indeed may remain a valuable concept, if all phonon-modes have an identical or similar Grüneisen parameter. Then phonon mediated

stress will only depend on the total population of excited phonons and redistribution within or cooling of such a non-equilibrium phonon gas will leave stress unchanged. When discussing the experimental results, the strength and limitations of this concept is further discussed.

An estimation of the lattice Grüneisen parameter for $SrRuO_3$ with help of equation 5.3 and the values listed in table 5.1 [54] yields $\gamma_{\mathrm{l,SRO}} \approx 1.7$.

Linear thermal expansion coefficient α (K^{-1})	Compressibility β (GPa^{-1})	Heat capacity C ($JK^{-1}mol^{-1}$)
1.05×10^{-5}	5.83×10^{-3}	109.9

Table 5.1: Thermodynamic Parameters of $SrRuO_3$ at 300 Kelvin [54]

In complete analogy an electronic Grüneisen parameter γ_{e} is introduced, which describes the thermal expansion caused by electrons at elevated temperatures. In the simplest approximation the electrons are described as a free Fermi gas with $E_{\mathrm{F}}/kT \gg 1$, where E_{F} is the Fermi energy. Here γ_{e} reduces to the constant 2/3. For interacting electrons in a lattice potential γ_{e} is modified, and it takes a range of values and can be negative and positive. For an equilibrated system ($T_{\mathrm{l}} = T_{\mathrm{e}}$) one readily appreciates that only for very small temperatures the electronic contribution to stress becomes dominant, because the specific heat of the electronic system scales linearly with temperature, whereas the specific heat of the lattice scales with T^3. At room temperature, however, the specific heat of electrons is about two orders of magnitude smaller than the specific heat of the lattice. This implies that the electronic contribution to the total stress is only of significance for $T_{\mathrm{e}} \gg T_{\mathrm{l}} \gg 1$.

With the advent of lasers delivering ultra short optical pulses, it became possible to study the electronic contribution to the total stress, before the electronic energy is transferred to the crystal lattice, which usually happens within a few ps or faster. Early work [148–151] investigated the thermal relaxation in metals by optical spectroscopy. The observed transient thermomodulation was attributed to electron-phonon scattering and electron diffusion. A simple formula for the electron relaxation rate was derived from the original two temperature model [152]. Later studies also included finite times for electron-electron scattering [134, 153, 154]. Note that the two temperature model is based on fast electron-electron interaction with respect to electron-phonon interaction; a prerequisite to define a temperature to the lattice and electron subsystems. While for noble metals this is usually a good approximation, slower electron thermalization must be expected for very pronounced athermal electron distributions [155, 156].

Very recent work directly measured the electronic contribution to stress after optical excitation of Aluminum by time-resolved electron diffraction [146, 147]. Due to the different temporal evolutions of electronic and lattice stress, namely, quasi-instantaneous and delayed, respectively, the two contributions were extracted from the ultrafast decrease of a Bragg reflection and a small phase shift of the oscillating Bragg peak position. Note that the electronic contribution to the expansion in metals is quasi-instantaneous and decays with the electron-phonon equilibration time of typically only a few hundred femtoseconds. In our experiment it will play a negligible role for stress generation.

In semiconductors the situation is quite different and the electronic stress induced by optical excitation is usually described by a deformation potential, which can be positive or negative. Here, the contribution of the electrons to stress may greatly exceed the phonon contribution [11]; for a detailed discussion of the excitation mechanism of coherent phonons please refer to [157].

5.2 Characterization of the STO/SRO Superlattice Sample

5.2.1 Equilibrium Structure at Room Temperature

The $SrTiO_3$(STO)/$SrRuO_3$(SRO) superlattice was fabricated at the Max-Planck-Institute for the Physics of Microstructures, Halle, by pulsed-laser deposition, employing a KrF excimer laser ($\lambda = 248$ nm). A 50 nm thick SRO electrode was deposited on a single crystalline $SrTiO_3$ (001) substrate (miscut angle of 0.25°) at a temperature of T = 700°C in a background atmosphere of 100 mTorr oxygen. The subsequent 10 layers of STO and SRO were grown at T = 575°C in 200 mTorr oxygen and T = 980 K in 100 mTorr oxygen, respectively. The surface morphology of the layers was investigated by atomic force microscopy (AFM), indicating step-flow growth with step-bunching for the SRO layer and layer-by-layer growth for the SRO layer [158]. TEM and electron diffraction investigations performed on a thinned [159] cross-section sample revealed the entire heterostructure to be epitaxial[1] and the interfaces to be plane and sharp [figure 5.1 b)]. For an accurate determination of the static structure additional high resolution X-ray diffraction measurements were performed at the Leibniz Institut für Kristallzüchtung, Berlin.

[1]The term epitaxy (Greek; epi 'above' and taxis 'in ordered manner') describes an ordered crystalline growth on a monocrystalline substrate.

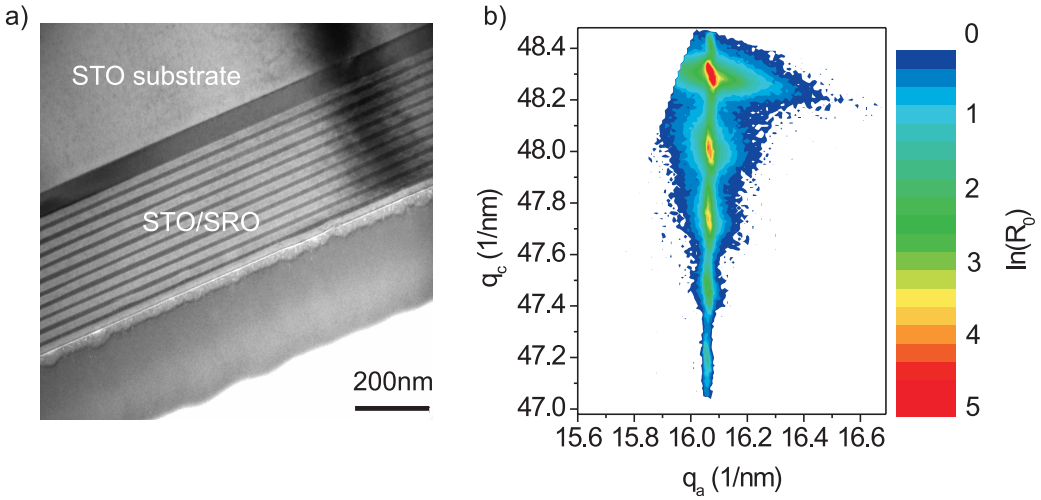

Figure 5.1: **a**) TEM image of the STO/SRO superlattice. **b**) High resolution reciprocal space map around the asymmetric (1 0 3) Bragg reflection of the STO substrate. Clearly visible are the identical in plane lattice constants, indicating a pseudomorphic growth.

Figure 5.1 b) shows a high resolution reciprocal space map around the asymmetric STO Bragg reflection (1 0 3). It shows the X-ray reflectivity on a logarithmic scale as a function of the reciprocal lattice vectors q_c and q_a. The lattice constants of the STO substrate can be read off directly with the relation:

$$c_{\mathrm{STO}} = 3 \cdot \frac{2\pi}{q_c} \quad a_{\mathrm{STO}} = 1 \cdot \frac{2\pi}{q_a}. \tag{5.4}$$

For lower values of q_c we see 5 superlattice reflections. All of them yield approximately the same value for q_a corresponding to the same in plane lattice constant a. This is very valuable information, since it is a priori not clear whether the 50 nm SRO buffer layer has relaxed to its bulk value and dictates the in-plane lattice constants for the superlattice. Apparently this is not the case and the whole structure is pseudomorphically grown on top of the STO substrate. The elongation of the SL peaks in the reciprocal space map along the q_c direction are due to thickness fluctuations in the layer period, which are also visible in the TEM image. In absolute numbers the mean of these thickness fluctuations amount to approximately 0.7 nm; relative to the layer period d_{SL} these fluctuations remain well below 1%. The elongation along the q_a direction are due to the mosaicity (imperfection) of the substrate/superlattice structure. They correspond to an angular width in the ω scan, and reflect the fact that parts of the sample remain Bragg-

matched for a finite angular range.

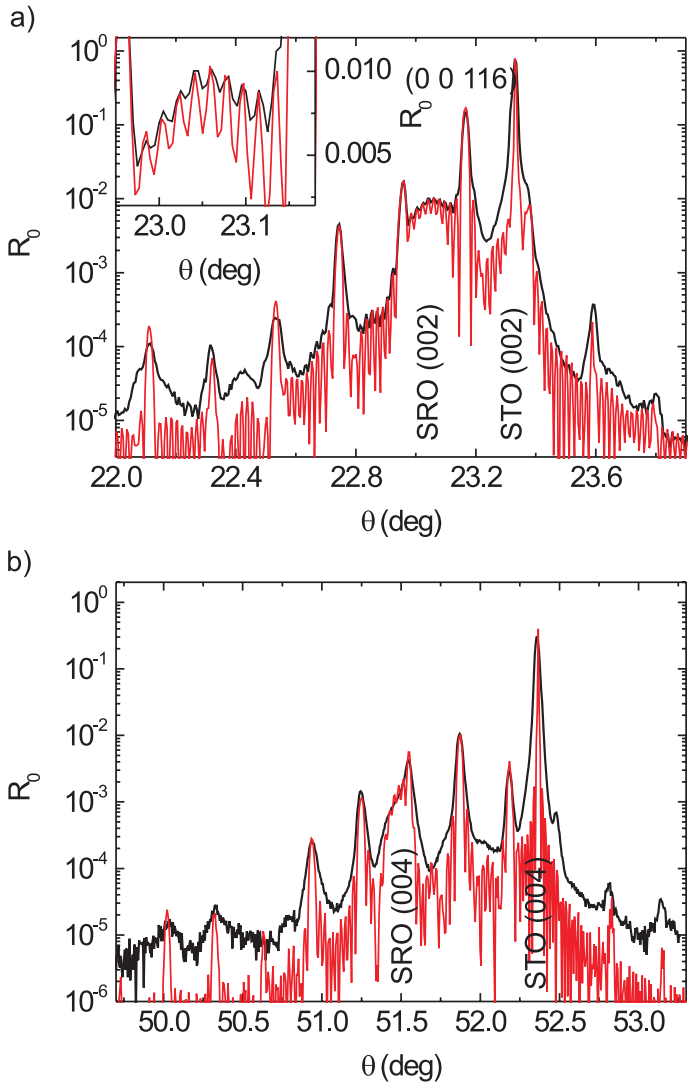

Figure 5.2: **a**) High resolution X-ray reflectivity curve around the (0 0 2) STO substrate reflection, together with a simulation with dynamical diffraction theory (red line). **b**) Measurement and simulation around the (0 0 4) STO Bragg reflection.

$\omega/2\theta$ scans around the (002) and (004) STO Bragg peak in a commercial X-ray diffractometer with a monochromatic and highly parallel beam (2-crystal geometry) are shown in figure 5.2 a) and b). The high dynamic range of approximately 10^6 is achieved by an automated attenuation scheme, the angular resolution is in the order of the natural linewidth of the $SrTiO_3$

substrate peak. We can easily identify the STO (0 0 2) and (0 0 4) substrate peak at 23.3° and 52.3°, respectively (note that the substrate has a miscut angle). Also the broad reflection due to the SRO buffer layer is easily identified at 23.05° and 51.5°. In both scans one can identify about 9 equidistant superlattice peaks, with intensities characteristic for the superlattice structure. The most intense SL peak (0 0 116) at 23°, between the peak of the SRO buffer layer and the STO substrate reflection, is investigated in the time-resolved experiments. The inset of figure 5.2 a) is a magnification of the buffer layer reflection where one can clearly see the (N-2) sidemaxima, with N=10 being the number of double layers. The best simulation based on dynamical X-ray diffraction theory (red curves) yields the structural parameters averaged over the whole structure as summarized in Table 5.2. The

parameter	value (nm)
d^0_{SL}	22.72
d_{SRO}	7.48
d_{STO}	15.24
c_{SRO}	0.3938
c_{STO}	0.3907
no unit cells STO	39
no unit cells SRO	19

Table 5.2: Parameters describing the equilibrium structure of the STO/SRO superlattice

same parameter values which are listed in table 5.2 are used to calculate the reflectivity curve around the (0 0 4) substrate reflection and one finds a remarkably good agreement between experiment and theory. One may pause here for a moment to appreciate the quality of the sample as well as the accuracy with which one can describe it. The good sample quality also yields a high X-ray reflectivity with a narrow linewidth. Within a short integration time of only 5-10 seconds one collects approximately 10,000 reflected photons of the SL planes (0 0 116) in the plasma source setup. This makes this sample ideal to study more details about the stress generation in $SrRuO_3$.

5.2.2 Reflectivity-Strain Mapping

In the following the relation between the measured X-ray reflectivity change of the superlattice peak (0 0 116) and the strain in SRO layer is established. We will see that for early times ($t < 10$ ps) this relation is linear and that only for long delay times, when the entire superlattice starts to expand,

the connection between reflectivity and strain becomes more complicated. Importantly, the reflectivity-strain mapping shows a negligible dependence on the sample temperature.

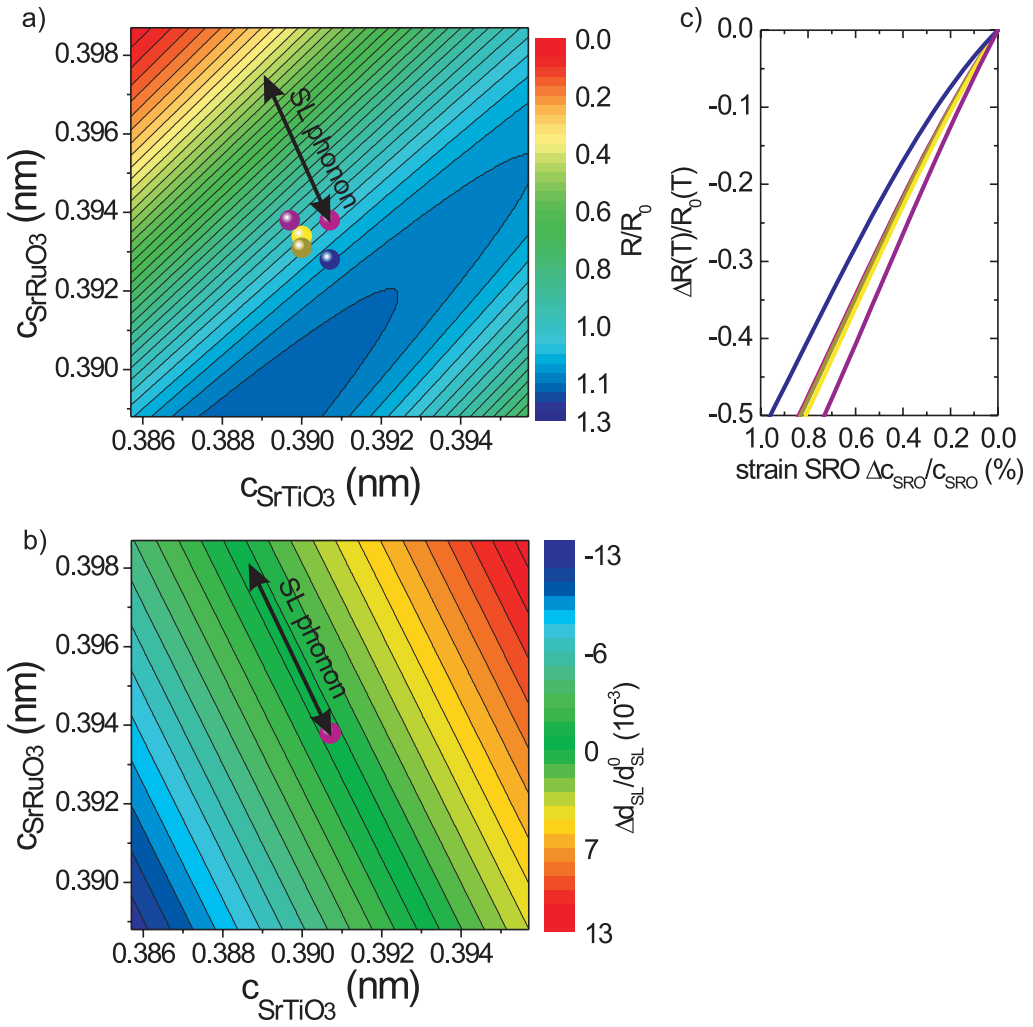

Figure 5.3: **a**) Calculated reflectivity change of the (0 0 116) SL peak as a function of the c-lattice constants of SRO and STO. The magenta colored dot marks the equilibrium structure at room temperature. The arrow points along the direction of expansive strain in SRO and compressive strain in STO, corresponding to the A1 SL-phonon. **b**) Calculated change of the superlattice periodicity $\Delta d_{SL}/d^0_{SL}$ as a function of the c-lattice constants of SRO and STO. **c**) Calculated normalized reflectivity change as a function of SRO strain for different starting lattice constants.

The contour plot in figure 5.3 a) shows the calculated reflectivity change of the (0 0 116) SL peak as a function of the c-axis of STO c_{STO} and SRO c_{SRO}, normalized to the reflectivity for the known c-axis parameters at room temperature. It was calculated with equation 2.33 in the framework of dynamical X-ray diffraction theory. In the upper left hand corner the contour lines are equidistant and run diagonally along increasing lattice constants of STO and SRO. For larger values of c_{STO} and smaller values of c_{SRO} the reflectivity change increases, reaches a maximum and decreases again. Contour plot 5.3 b) shows the relative change of the superlattice periodicity $\Delta d_{\mathrm{SL}}/d^0_{\mathrm{SL}}$ as a function of c_{STO} and c_{SRO}. This function is given by:

$$d_{\mathrm{SL}}(x,y) = 39(3.875 + x \cdot 0.0005) + 19(3.888 + y \cdot 0.0005) \tag{5.5}$$

$$\text{with } (x,y) = (0 \ldots 199, 0 \ldots 199) \tag{5.6}$$

$$d_{\mathrm{SL}}(100,100) = d^0_{\mathrm{SL}} = 39 \cdot c_{\mathrm{STO}} + 19 \cdot c_{\mathrm{SRO}} = 22.72 \text{ nm} \tag{5.7}$$

Excitation of an A1 ZFLAP corresponds to an expansion of the SRO layers and a concomitant compression of the STO layers, leaving the superlattice period d_{SL} constant. On the contour plot 5.3 b) these structural changes of oscillating layer thickness run along the diagonal contour lines, marked with a black arrow. The slope of the arrow is determined by the relative thicknesses of the two layers, which implies that the relative strain in the SRO layers is approximately twice as large as in the STO layers. Measurements of the line-shift of the superlattice peaks are proportional to the superlattice periodicity

$$\frac{\Delta d_{\mathrm{SL}}}{d^0_{\mathrm{SL}}} = \left(\frac{\cos(\theta)}{\sin(\theta)}\right) \theta_0 \frac{\Delta\theta}{\theta_0} \tag{5.8}$$

Hence, simultaneous time-resolved measurements of the line-shift and of the reflectivity change determine an intersection of the contour lines of plots 5.3 a) and b) allowing to identify the time dependent c-axis of STO c_{STO} and of SRO c_{SRO}.

Different lattice temperatures result in changed c-axis constants and, hence, different starting points for the superlattice phonon motion on the contour plots. The magenta colored dot exactly in the center of the contour plots marks the equilibrium structure at room temperature with $\mathrm{d_{STO}} = 0.3907$ nm and $\mathrm{d_{SRO}} = 0.3938$ nm. The position of the yellow dot was calculated by taking into account the thermal expansion of STO [160–162] and SRO [163]. The olive colored dot was gained from the measured relative temperature dependent line-shift of the (0 0 116) SL peak with respect to the STO substrate peak, together with the tabulated thermal expansion of STO (see references above). We additionally picked two extreme cases where the STO c-axis remained constant, while the SRO c-axis contracted by twice the amount as

expected (blue dot) and vice versa (violet dot). These five cases are compared in figure 5.3 c), where we plotted the reflectivity change as a function of strain in the SRO layer. These curves are gained from the contour plot by moving from the 5 respective dots in direction of the SL phonon, along the black arrow towards the upper left hand corner. Since solely reflectivity changes are of interest, the curves in figure 5.3 c) are normalized to the room temperature measurement. To keep track of the different scenarios the same color-code as in the contour plot is used. It is obvious that for the two realistic cases there is basically no change at all and even for the two extreme (and unrealistic) cases the reflectivity changes remain moderate. Here, for a 50 percent decrease in reflectivity at room temperature the maximum deviations amount to less than 7%. Please note that this would not be true for c-axis lattice parameters in the lower right hand side of contour plot figure 5.3 a). Here, the contour lines are no longer equidistant and the reflectivity-strain mapping becomes highly nonlinear.

5.3 Ultrafast Phonon Mediated Stress in $SrRuO_3$

5.3.1 Time Resolved X-Ray Data

Superlattice Phonon Mode

Figure 5.4 displays the X-ray reflectivity change as a function of time delay between the excitation pump pulse ($\lambda = 800$ nm, fluence of 7.5 mJ/cm^2) and the X-ray probe pulse. It shows oscillatory signal changes around a decreased reflectivity of approximately 20%. The oscillation period is 3 ps. For later time delays one observes smaller amplitudes and after 30 ps the reflectivity has dropped by 40 %.

Ultrafast Rise Time of Stress in $SrRuO_3$

A combination of optical and X-ray data is presented that sets zero time-delay to an accuracy of approximately 100 fs. This allows to describe the build-up of stress in the SRO layers with unprecedented temporal resolution. For three different superlattice structures the X-ray response is compared to optical transmission and reflectivity changes under identical pump conditions. The geometry of the experimental setup remained unchanged and the comparative optical/X-ray experiments were performed in direct succession. In addition to the superlattice characterized in the preceding section,

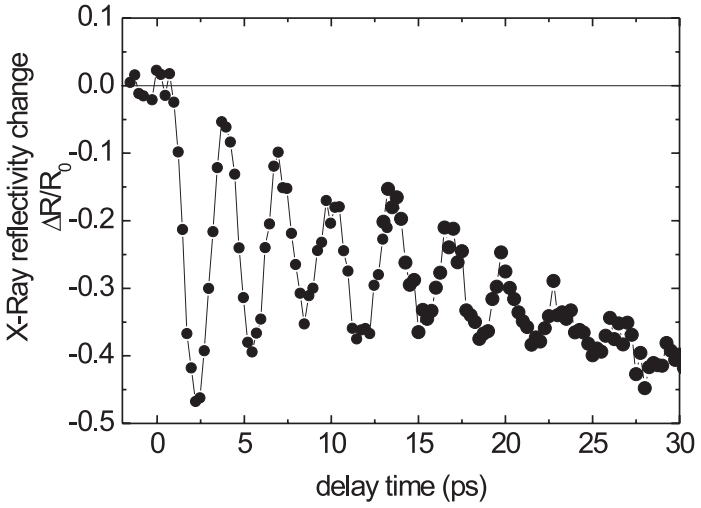

Figure 5.4: **a**) Reflectivity change of the superlattice peak (0 0 116) of the $(STO/SRO)_{10}$ structure as a function of delay time.

$(STO/SRO)_{10}$, we included another STO/SRO superlattice with 30 double layers and a shorter period of the SL phonon of 2 ps, $(STO/SRO)_{30}$, and a superlattice structure $(PZT/SRO)_{15}$, whose properties will be discussed in detail in chapter 6. Here similar SL peaks were chosen, situated next to the (0 0 2) substrate STO peak and sensitive to the layer thickness modulation, that is, with a linear relationship between reflectivity change and strain. For the superlattice $(PZT/SRO)_{15}$ this corresponds to the Bragg reflection (0 0 56).

The experimental results are shown in figure 5.5 a) for time delays between -1 and 3.5 ps. One observers the first part of the SL phonon oscillation. An intensity increase of about 50% at a time delay 1.5 ps for the $(PZT/SRO)_{10}$ superlattice (blue squares), a decrease of reflected intensity of approximately 30% at 2 ps for the $(STO/SRO)_{10}$ superlattice (red dots) and a significantly lower decrease of intensity of 15% at 1.5 ps for the $(STO/SRO)_{30}$ superlattice. The measurement of the $(PZT/SRO)_{10}$ SL was done with an excitation fluence of 3 mJ/cm^2, the non-ferroelectric superlattices with a higher fluence of 6 mJ/cm^2.

Only one optical reflectivity measurement is shown (black line), but all traces for the three SL are identical. A narrow pulse-limited decrease of reflectivity occurs around time delay zero. The pump-induced electronic polarization decays with a de-phasing time short compared to the pulse duration, resulting in an 'instantaneous' nonlinear response of the sample. The

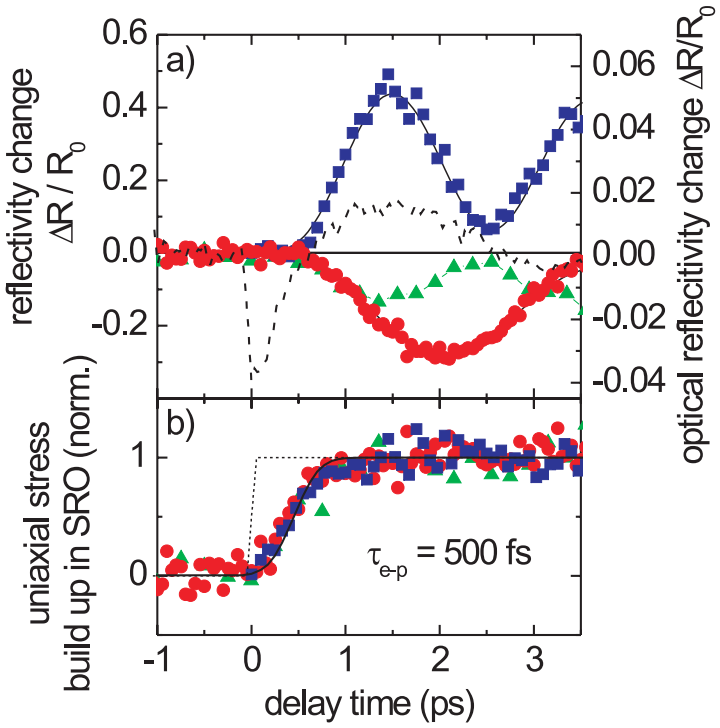

Figure 5.5: **a**) Reflectivity change of the $(PZT/SRO)_{10}$ (blue squares), $(STO/SRO)_{10}$ (red dots) and $(STO/SRO)_{30}$ (green triangles) superlattices. The optical reflectivity change is plotted as the dashed black line. **b**) Time evolution of the uniaxial stress build-up in the SRO layers derived from the curves in **a**) according to the differential equation of a forced oscillator. The dotted line is a guide to the eye.

initial reflectivity change is followed by a fast reflectivity increase with a characteristic time constant of $\tau_{opt} \approx 300$ fs and phonon oscillations.

Wavelength Dependence of Stress in $SrRuO_3$ at Room Temperature

Whether the rise time of the stress generating force in SRO depends on the excitation wavelength was experimentally tested in a series of experiments. An optical parametric amplifier (OPA) was setup to convert the fundamental wavelength of the Ti:Saphire laser to near infrared wavelengths between 1100 nm and 2250 nm. Either the signal or the idler of the OPA with pulse energies between 25 (signal) and 15 (idler) μJ energy was focused onto the sample. The spatial overlap of optical and X-ray light was ensured by a 100 μm pinhole, the temporal equivalence of the respective beam path was

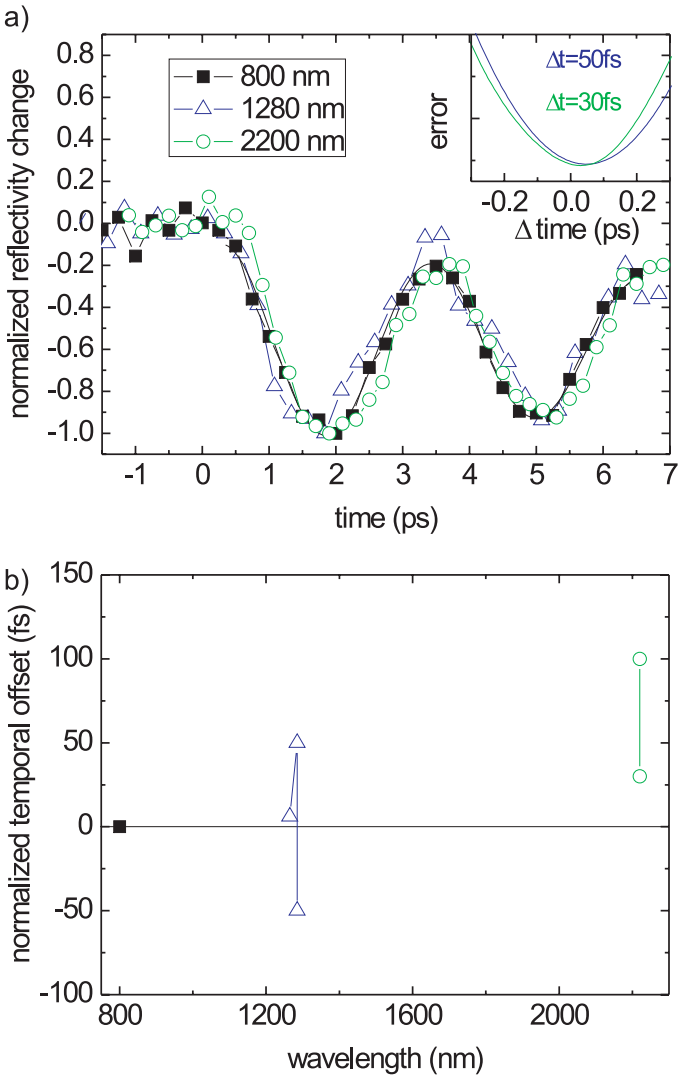

Figure 5.6: **a**) Normalized reflectivity change of the (0 0 116) Bragg reflection of the STO/SRO SL as a function of time. The black squares show the reference measurement at 800 nm and the blue triangle and the green circle show measurements for 1280 nm and 2200 nm, respectively. The inset shows the temporal offset of the two near-infrared measurements with respect to the 800 nm pump wavelength. **b**) Temporal offset of the oscillations normalized to the measurement at $\lambda = 800$ nm for different wavelengths. Within the experimental accuracy it remains constant.

determined by a third beam and frequency mixing in a BBO crystal mounted directly on a second pinhole with 100 μm diameter. The thin metal foil with

both pinholes was fixed on the sample surface at exactly the same height. This allows a temporal resolution on the order of 100 fs.

Figure 5.6 a) shows the normalized reflectivity change as a function of time for three different excitation wavelengths. The black dots show the response after 800 nm excitation, the blue triangles and the green circle show the response after excitation with 1280 nm and 2200 nm, respectively. The inset shows the temporal error function, which determines the optimal temporal overlap between the reference curve measured at 800 nm and the respective measurements with the near infrared pump beams. The data points $A_{800\ \mathrm{nm}}(t)$ for the reflectivity change for 800 nm excitation is linearly interpolated with a function of the form

$$f(a, b, c) = a + b \cdot A_{800\ \mathrm{nm}}(t - c). \tag{5.9}$$

The data points measured for the near infrared excitation are then fitted to the function $f(a, b, c)$. This yields the parameters a, b and c, while different values for c are shown in the inset of figure 5.6 a). The minimum determines the temporal offset of the measured curves with respect to the 800 nm measurement. Note that this does not assume any particular functional relationship. For the curves shown one determines a value of 50 fs and 30 fs for 1280 nm an 2200 nm, respectively. Figure 5.6 b) summarizes the results for different experimental runs. It shows the temporal offset normalized to the measurement at $\lambda = 800$ nm as a function of excitation wavelength. Within the accuracy of the experiment one cannot infer any dependence of the rise time on the excitation wavelength.

The X-ray reflectivity measurements for different excitation wavelengths also allow to compare the amplitude of the superlattice phonon for identical incident pump fluence. This analysis is shown in figure 5.7 a), where the amplitude of the phonon oscillation normalized to the incident excitation fluence is plotted as a function of excitation wavelength. One observes an increase of approximately a factor of two. However, the absorption of $SrRuO_3$ also increases by a factor of two between 800 and 2200 nm [figure 5.7 b)]. This suggests that the higher absorption for near infrared light is the reason for the larger induced strain in the $SrRuO_3$ layer. We conclude, that at room temperature the optically induced stress is independent of the excitation wavelength and only depends on the total amount of deposited energy.

Stress in $SrRuO_3$ on Longer Time Scales

Measurements of single SL-Bragg reflections on longer time scales ($t \leq 200$ ps) yield two complementary information, the reflectivity change of the SL

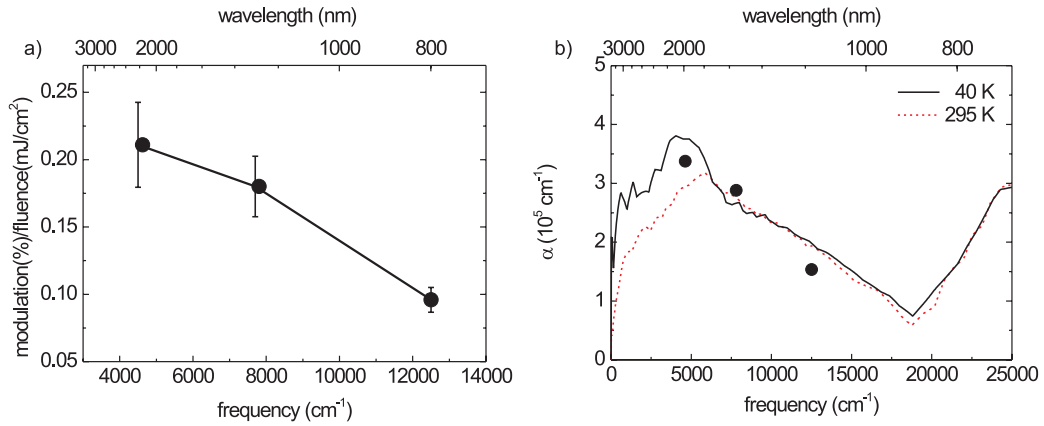

Figure 5.7: **a**) The phonon amplitude normalized to the excitation fluence as a function of excitation wavelength. Error bars show the reproducibility of the experiment. Lines are guides to the eye. **b**) Absorption coefficient taken from [132] for 40 and 295 Kelvin together with linearly scaled data from **a**).

peak and its line-shift due to an expansion of the whole SL structure. We performed measurements on the reflectivity change of the (0 0 56) and (0 0 116) Bragg peaks on a longer time scale for two samples, the $(PZT/SRO)_{15}$ and $(STO/SRO)_{10}$ superlattice, respectively. The results are shown in figure 5.8 and figure 5.9. The first few ps are plotted on a linear time scale and one can make out an reflectivity change due to the first part of the SL-oscillation. The position of the Bragg reflection remains unchanged during this time. For longer times the data is shown on a logarithmic time-scale: we see a line-shift due to the expansion of the whole superlattice structure and a remaining intensity change of the corresponding SL peaks.

5.3.2 Discussion

Origin of Superlattice Phonon Oscillation

The 800 nm and near infrared pump pulses exclusively interact with the metallic SRO layers and cause a uniaxial stress with the superlattice periodicity. Stress is generated on a time scale short compared to the vibrational period $T = 3$ ps of the SL phonon mode and thus launches a coherent superposition of acoustic phonon states corresponding to a standing wave in the SL. The period of 3 ps is given by the layer thicknesses and the respective velocity of sounds for SRO and STO. For a constant thickness of the entire SL structure (for times $t < 10$ ps, compare figure 5.9), this implies an expansion of the SRO layer and a concomitant compression of the adjacent

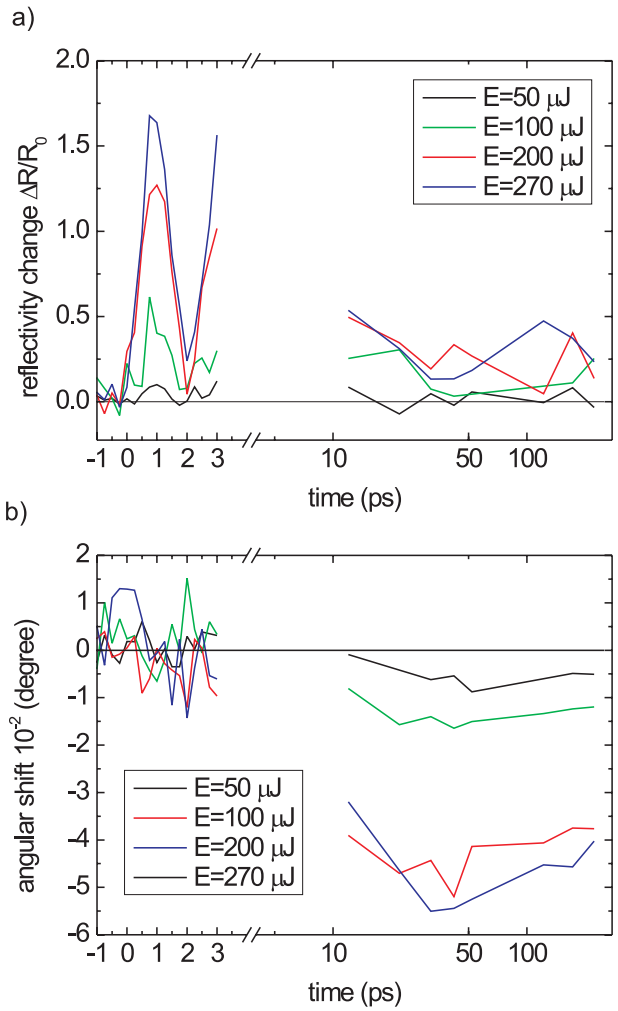

Figure 5.8: **a)** Reflectivity change and **b)** angular shift of the (0 0 56) Bragg peak of the PZT/SRO SL structure. The time axis is shown in two parts, up to 4 ps it is linear and then it is plotted on a logarithmic length scale. The measurements are shown for 4 different excitation fluences.

STO layers, equivalent to a change in their respective lattice constants. In agreement with the presented discussion of the X-ray pattern of a SL structure (compare chapter 2.5 and an explanatory schematic 6.9 presented in the following chapter) the induced changes of the respective c lattice constants result in a shift of the envelope functions, which in turn modulate the intensity of the SL peaks and cause the observed time-dependent reflectivity changes. The quantitative calculation is shown in figure 5.3 and for the

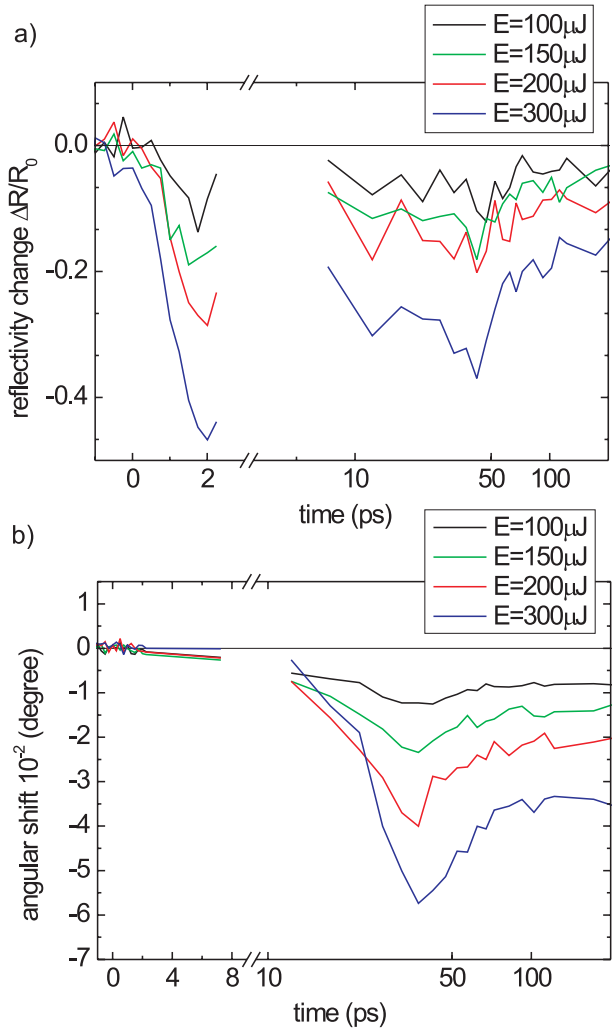

Figure 5.9: **a)** Reflectivity change and **b)** angular shift of the (0 0 116) Bragg peak of the $(STO/SRO)_{10}$ SL structure. The time axis is shown in two parts, up to 3/9 ps it is linear and then it is plotted on a logarithmic length scale. The measurements are shown for 4 different excitation fluences.

range of strains considered here reveal an almost perfectly linear relationship between reflectivity change and strain in the SRO layers.

Rise Time of Uniaxial Stress

With the established linear relationship between the reflectivity change of the chosen SL-Bragg peaks and the tetragonal distortion of the SRO layers Δd_{SRO} we can derive the driving force F(t) (uniaxial stress) acting on the SL phonon by the following differential equation:

$$\frac{d^2\Delta d_{\mathrm{SRO}}}{dt^2} + \left(2\Gamma \frac{d\Delta d_{\mathrm{SRO}}}{dt}\right) + \omega_0^2 \Delta d_{\mathrm{SRO}} = F(t) \tag{5.10}$$

with the frequency ω_0 of the experimentally observed superlattice oscillation of the different superlattices. An additional damping constant Γ improves the agreement between measurements and calculated values and is motivated by the fact that the superlattice structure consists of only 10 periods and is coupled to the STO substrate or SRO buffer layer. For every round-trip of the strain wave within the tenth layer a compression or expansion wave is efficiently coupled into the substrate. Differentiating d_{SRO} and plugging it into the above equation, yields the resulting normalized force shown in figure 5.5 b). The second derivative introduces a fair amount of noise, such that the exact form, especially the curvature of the force around time delay zero is difficult to determine. Nonetheless, we find good agreement for the following function:

$$F(t) = const. \cdot (1 - \exp(-t/\tau_{\mathrm{phonon}})) \tag{5.11}$$

This function describes the induced stress for all three superlattices with an identical rise time of $\tau_{\mathrm{phonon}} = 500$ fs. As a crosscheck we calculated the amplitude of the oscillations using equation 5.11. The result is plotted as the thin black lines in figure 5.5 a). The function $F(t) = 1 - \mathrm{erf}(t - \tau_{\mathrm{phonon}})$ gives a somewhat better agreement for early time delays, possibly because of a finite temporal resolution. However, the differences are subtle and the experimental data does not allow a clear discrimination.

Temporal Evolution of Strain and Dependence on Excitation Fluence

While the measured line-shift only yields the expansion of the whole superlattice structure, the additionally measured intensity change allows us to calculate the strain for the two layers individually (compare section 5.2.2). The result for the reflectivity curve shown in figure 5.4 and its corresponding line-shift is displayed in figure 5.10. One clearly sees the oscillatory expansion of the SRO layers and the simultaneous compression of the STO layers. Their relative amplitude is determined by their respective thicknesses and

amounts to approximately 2:1. Around 40 ps the expansion of the SRO layers reaches a maximum of about 1%. This is due to the expansion of the entire superlattice. The STO layers have already relaxed to their original thickness. For later times the amplitude of the thickness variation for SRO has dropped to about 50% of its first maximum at 2 ps. Finally one observes a slight expansion of the STO layers at 200 ps. The same temporal behavior is visualized in figure 5.10 as a trajectory in $c_{\mathrm{SRO}} - c_{\mathrm{STO}}$ space.

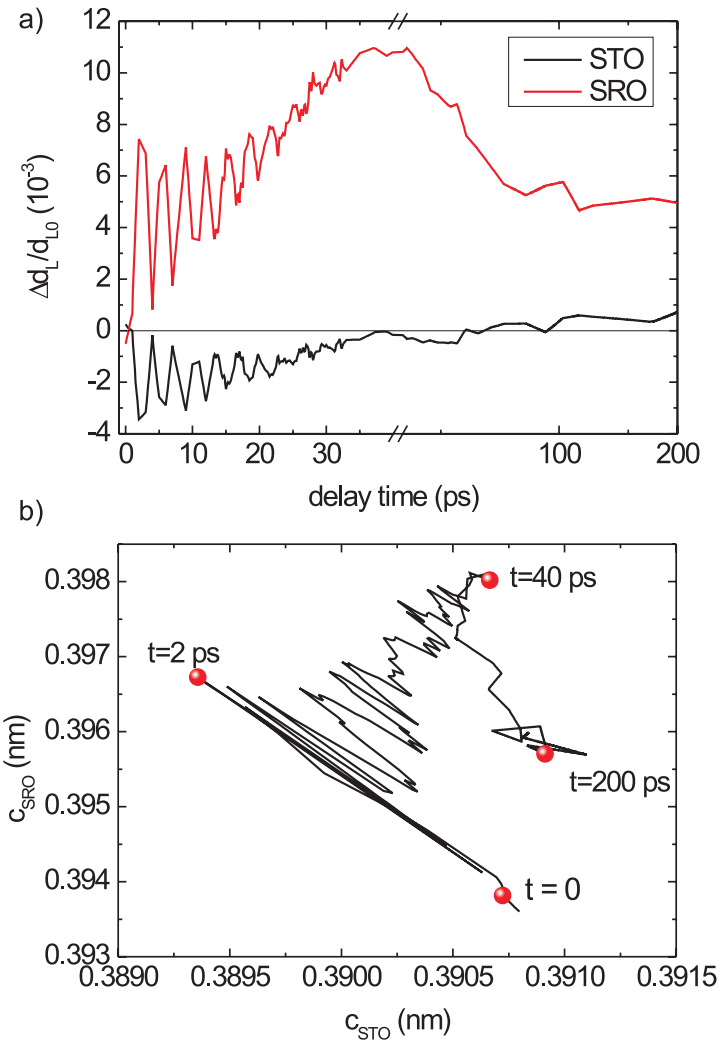

Figure 5.10: **a**) Change of the layer thickness of d_{SrRuO_3} (red line) and d_{SrTiO_3} (black line) as a function of time delay for an excitation fluence of 7.5 mJ/cm^2. **b**) Time dependent trajectory in $c_{\mathrm{SRO}} - c_{\mathrm{STO}}$ space.

Such an evaluation for different excitation fluence is presented in fig-

ure 5.11 for the data shown in figure 5.8 and 5.9. We plotted the change in the tetragonal distortion $\Delta\eta/\eta_0$ ($\eta = c/a$) for the two prominent time points t=2 ps (hollow symbols) and t=200 ps (filled symbols). First of all one notices a linear relation between the excitation fluence and the induced strain. After 200 ps the SRO layers remain expanded by approximately half their value compared to t=2 ps, while the STO layers have relaxed to their equilibrium tetragonal distortion. The situation for the PZT/SRO superlattice shows an identical behavior.

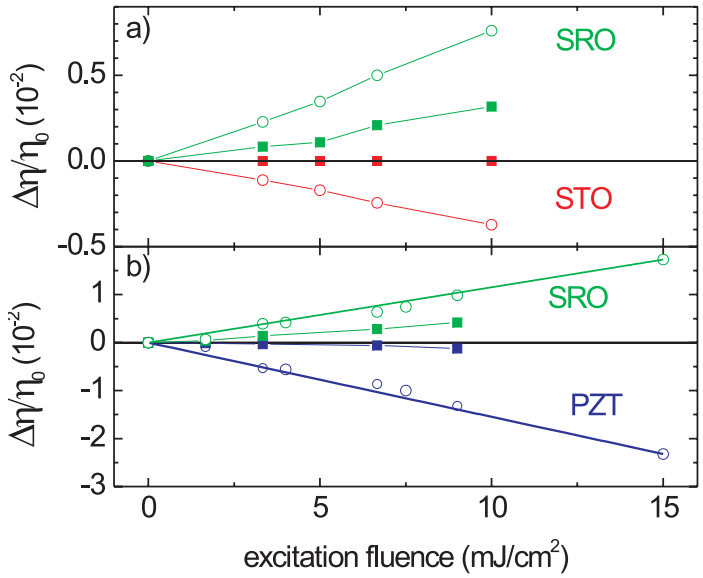

Figure 5.11: **a**) Tetragonal distortion of STO and SRO as a function of excitation fluence. The hollow symbols represent the maximal distortion at 2ps and the filled symbols the remaining distortion after 200ps. **b**) Same analysis for the PZT/SRO superlattice. Here the maximal distortion is reached after 1.5 ps.

Phonon Mediated Stress

The linear dependence of the induced strain as a function of the absorbed energy, the finite rise of stress and its independence on the excitation wavelength, points to an indirect generation of mechanical stress via coupling of the excited electronic system to lattice degrees of freedom. Since we have not observed any signs for an appreciable instantaneous contribution to stress, electronic contributions to stress, σ_e, are assumed to play no role.

We calculate the expected temperature increase of the excited SRO layers after optical excitation. For an excitation fluence of $E_{ex} = 6.5$ mJ/cm^2 and corrections with measured values for reflection and transmission, one can approximate the deposited energy within the thin SRO layers. A certain inaccuracy is difficult to avoid, because the transmitted light is additionally attenuated by the SRO buffer layers. Also corrections due to the nano-layered arrangement of SRO is neglected. Together with the specific heat of SRO [54] we determine an approximate temperature rise of 110 Kelvin. The volume expansion of SRO as a function of temperature yields $V(290K + 110K)/V(290K) = 4.5 \times 10^{-3}$ [54]. With the in-plane lattice constants fixed, the temperature induced volume change occurs along the c-axis, while the amplitude depends on the Poisson ratio. The expansion after 2 ps for a fluence of $E_{ex} = 6.5$ mJ/cm^2 was measured to amount to $\Delta\eta(2\text{ ps})/\eta_0 = 5 \times 10^{-3}$ and after 200 ps to $\Delta\eta(200\text{ ps})/\eta_0 = 2 \times 10^{-3}$, thus in the right order of magnitude for an expansion driven by anharmonic phonon-phonon interaction and in agreement with an average Grüneisen parameter of $\gamma_l \approx 2$.

The simplest model for the anharmonic coupling between the phonon system and the SL phonon may be written as $\sum_i q_i^2 \eta$ with q and η denoting the coordinates of the phonon system and specific SL phonon, respectively. The coupling to the tetragonal distortion is proportional to the elongation of the modes of the phonon system. Hence, changes in the force driving the SL phonon depend on the total population of phonons as well as the Grüneisen parameter of each specific phonon mode. Optical phonon modes between 100 and 400 cm^{-1} describing the rotation and tilts of oxygen octahedra have been identified to play an important role in changes of the volume in Perovskite oxides [164, 165]. This would imply that the Grüneisen parameter is in fact mode-specific and larger of this class of optical phonons.

Optical reflectivity measurements revealed a characteristic decay time of approximately $\tau_{optical} \approx 300$ fs (also compare section 5.4.4), which is attributed to the equilibration of the electronic system [150]. Accordingly, we interpret the rise time of stress of $\tau_{phonon} = 500$ fs (mainly) to the electron-phonon coupling time. The small discrepancy between $\tau_{optical}$ and τ_{phonon} maybe due to further redistribution of the non-thermal optical phonon gas. Occupation of new phonon modes with stronger coupling to thermal expansion, that is, for a mode dependent Grüneisen parameter, stress can evolve even after the electronic system has thermalized. This may include oxygen octahedra modes and also the decay of optical phonons into acoustic phonons, which usually happens within a few picoseconds or less.

Hence, the following scenario is proposed: the optical excitation of SRO creates a hot electron population, which thermalizes by electron-electron and electron-phonon scattering within 300-500 femtoseconds leading to an ele-

vated lattice temperature. The build-up of a non-equilibrated optical phonon population produces stress and results in the strong superlattice phonon amplitudes by anharmonic phonon-phonon interaction.

Finally, the result that no appreciable energy transfer into the neighboring layers has taken place within the first 200 ps requires further discussion (see $\Delta\eta(200\text{ps})/\eta_0$ for STO and PZT in figure 5.11). This is most likely due to the modified phonon dispersion in the superlattice structure, resulting in a very slow thermal conductivity. Optical phonons may be confined to the SRO layers, because at their material specific eigenfrequency no eigenmode exist in the neighboring layer. However, optical phonons have only a typical lifetime in the order of several picoseconds before they decay into acoustic modes. This is significantly shorter than the time of observation at $t = 200$ ps. Note that even acoustic phonons may be essentially non-propagating along the stacking direction of the superlattice, because back-folding into the mini-Brillouin results in a flat dispersion relation. Note that this is not true in the $a-b$ plane, where the properties of the phonons is governed by a bulk dispersion relation. Furthermore, the finite size of the superlattice results in a limited number of phonon modes [compare figure 2.12 b)]. An energy transfer via the superlattice phonon mode is negligible. The total energy of the superlattice phonon, driven by the excitation with the same periodicity is not very large. We estimate the optical induced stress to amount to 1 GPa for the highest excitation fluence, such that the ratio between the total deposited energy (≈ 1 GJ/m^3) and the energy of the superlattice phonon is roughly 1/100.

5.4 Ultrafast Magnetostriction in the Ferromagnet $SrRuO_3$

$SrRuO_3$ becomes ferromagnetic below the Curie Temperature of T_C=160 K and a magnetic component of stress contributes to structural changes after photo excitation. Time-resolved X-ray diffraction experiments reveal ultrafast magnetostriction after laser-induced changes of the electronic system, partly compensating the phonon-mediated stress. A specific excitation spectrum is observed, which is attributed to the shape of the electronic band structure in the magnetically ordered electron system.

5.4.1 Ultrafast Laser-Induced Demagnetization

Ultrafast laser-induced magnetization dynamics were first demonstrated by Beaurepaire et al. [166] in 1996 and triggered ongoing experimental and the-

oretical work [167, 168]. Beyond the technological interest in fast switching speeds for magnetic recording, significant interest in this fields originates form pure scientific curiosity, that is, exploring the ultimate limits for magnetization dynamics and the underlying microscopic interactions.

While the early results of ultrafast demagnetization were confirmed by several groups [169, 170], microscopic modeling has been restricted to few attempts [171] and the fs scale magnetization in itinerant ferromagnets have remained a major theoretical challenge. Even the characteristic time-scales and corresponding elementary processes have not been doubtlessly identified. On a fs to several 100 fs timescale, electron-electron and spin-orbit interactions dominate, in the subpicosecond to ps time scale electron-phonon coupling may be the responsible process and demagnetization due to direct spin-lattice are usually assumed to be even slower. Nonetheless a full consensus about a typical demagnetization time of $\tau_{\mathrm{mag}} \approx$ 100-300 fs for elementary ferromagnetic transition metals has been achieved [168]. Except for recent experiments of ultrafast demagnetization ($\tau_{\mathrm{mag}} \approx$ 200fs)) [172], little is known about the underlying microscopic processes in SRO. The interplay of strong spin-orbit coupling, which manifests itself in the strong magnetic anisotropy and pronounced magneto-volume effect in SRO, coulomb exchange energy and strong hybridization of the Ru 4d and O 2 p orbitals, leaves room for various scenarios for demagnetization, including a direct spin-flipping optical transition, or intraband scattering processes of non-thermal electrons involving magnon emission.

5.4.2 Magnetic Properties of $SrRuO_3$ and their Interplay with Structure

Itinerant Ferromagnetism of $SrRuO_3$

$SrRuO_3$ is a 4d transition metal itinerant ferromagnet with a Curie temperature T_c=160 Kelvin.

The term itinerant refers to magnetic systems where the unpaired electrons responsible for the magnetic moment are no longer localized at a specific atom (for example Ru^{4+}), but are delocalized with their original energy levels broadened into energy bands. On a simplest level the emergence of ferromagnetism can be qualitatively understood in the frame work of the Hubbard model [173]. For a single-band-model every atomic site has only two states, corresponding to a spin up and spin down state. Only electrons with opposite spin are allowed to interact. Then, the additional coulomb energy which is required to occupy a single state with two electrons is denoted by Δ_{ex}. This electron-electron interaction leads to a $\vec{k}$ independent shift of

the electron bands. It is proportional to the density of electrons, which have a spin opposite to the one of the electron under consideration. The splitting is proportional to the relative magnetization ($n\uparrow - n\downarrow$) and to Δ_{ex}. For a single parabolic band this is schematically depicted in figure 5.12 a). For a Fermi energy ε_F as shown, an unequal number of electrons in the spin up (blue shaded area) compared to the spin down state (red shaded area) results. This implies that such a splitting in majority and minority electrons is likely to occur if $\Delta_{ex}/2$ is large and the density of states at the Fermi surface ε_F is high. This is known as the Stoner criterion for ferromagnetism $\Delta_{ex}/2 \cdot N(\varepsilon_F) > 1$ [174, 175].

The main experimental evidence for itinerant or band magnetism in $SrRuO_3$ is the lack of saturation to the full magnetic moment in high electric fields and its non-integer number. This may be understood as follows: The octahedral crystalline electric field of O atoms [176] splits the fivefold degeneracy of the Ru $4d^4$ configuration into a triplet (t_{2g}) ground state, two-thirds occupied, and a doublet (e_g) excited state, unoccupied (compare figure 5.12). Hund's rule predicts a low spin alignment ($\uparrow\uparrow\uparrow\downarrow$) (S=1), a magnetic moment $\mu_{eff} = 2\mu_B\sqrt{S(S+1)} \approx 2.8\mu_B$ and a saturation magnetization for high magnetic fields of $2\mu_B$. This scenario, where the magnetism is mostly carried by the spin is often a fair approximation, because for solids the orbital momentum, present in the atomic ground state for an individual atom, is largely quenched due to crystal field effects. However, one may already suspect that in 4d orbitals of such heavy elements spin-orbit coupling is large, and may be in the same order as the crystal field splitting.

A number of experimental papers have focused on determining the magnetic moment of $SrRuO_3$: the earliest work on the ferromagnetic properties of $SrRuO_3$ revealed a surprisingly low saturation moment of 0.85 μ_B [177], only a little later a low-temperature magnetic moment of $1.4\mu_B$/Ru was determined by neutron diffraction [178]. A more recent study also by neutron diffraction at T=10 K determined the ferromagnetic ordered Ru moment to amount to $1.63\pm0.06\mu_B$ [179]. In both cases the low values were explained by collective-electron magnetism. A saturation magnetization of $\approx 1.4\mu_B$ at 30 Tesla was found by [180].

These low values for μ_B were confirmed by theoretical work, in particular by first principle calculations [181], corroborating the possibility of the band ferromagnetism in $SrRuO_3$ with a reduced ordered moment of 1.45 μ_B/Ru. Another theoretical approach [182, 183] leads to the ferromagnetic state with a moment of 1.59 μ_B/Ru for the real orthorhombic symmetry.

One reason for the difficulties of measuring the magnetic moment of $SrRuO_3$, resulting in the large variety of reported values, is the large magneto-

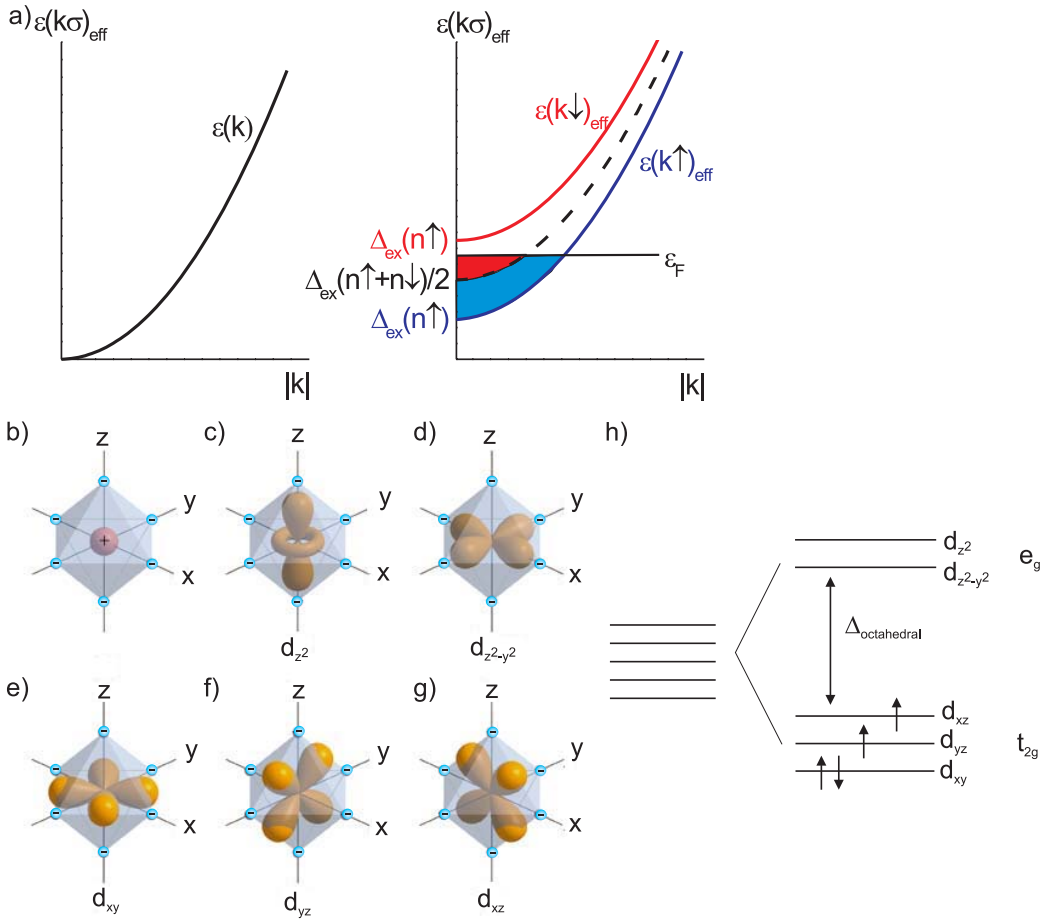

Figure 5.12: **a**) Stoner model of the band splitting leading to a ferromagnetic state. **b**) An octahedral array of negative charges (oxygens, blue dots) approaching a metal ion. The orientations of the d-orbitals relative to the negatively charged ligands. Notice that the lobes of the d_{z^2} and $d_{x^2-y^2}$ orbitals [**c**) and **d**)] point towards the charges. The lobes of the d_{xy}, d_{yz}, and d_{xz} orbitals [**e**)-**g**)] point between the charges. **h**) Energy splitting results in a low spin configuration with S=1.

crystalline anisotropy [184]. This describes the quite unusual and surprising effect that both the shape of hysteresis curves and the saturation magnetization strongly depends on the direction of the applied magnetic field. It is attributed to the strong spin-orbit coupling in SRO.

Experimentally, the temperature dependence of the magnetization $M(T)$

of $SrRuO_3$ is described by the empirical formula [179]:

$$M = M_0(1 - (T/T_C)^\delta)^\beta \tag{5.12}$$
$$\delta = 1 \tag{5.13}$$
$$\beta = 0.25 \tag{5.14}$$

The simplest motivation for the functional relation $\sqrt[4]{1 - T/T_C}$ is a Taylor expansion of the free energy F up to sixth power in M and minimizing F with respect to M. The quadratic coefficient is taken to be proportional to $(1 - T/T_C)$ (compare section 6.1.2 on the Landau theory of ferroelectricity).

Another argument for a tendency towards greater electron itineracy are the more extended d orbitals of 4 d ions, compared with 3 d ferromagnets. For 4d oxides this results in the hybridization between the transition metals and O 2p orbitals. For the so called p-d hybridization in $SrRuO_3$ one can find strong experimental [185, 186] and theoretical [182, 183] evidence. Accordingly one has to conclude additionally that a substantial fraction of the spin moment is O p like.

Invar Effect

The above mentioned p-d hybridization also leads to the pronounced interplay between structural degrees of freedom and the magnetic and electronic properties. In the present work they are of main interest and will be discussed in the following: While the crystal structure of $SrRuO_3$ remains practically invariable in the temperature range of 1.5-290 K [179, 187], there is a strong dependence of volume on the magnitude of the magnetic moment, known as the 'Invar effect'. The itinerant electron magnetic substance has a negative contribution to thermal expansion and compensates the normal lattice expansion due to incoherent phonon motion: the volume of a $SrRuO_3$ unit cell remains constant below the critical temperature. Figure 5.13 a) shows measurements of the unit cell volume by X-ray diffraction as a function of temperature. The difference in volume ΔV_M between the thermal expansion as determined by the Debye model and the measured values was attributed to the additional magnetic contributions below the Curie temperature [163, 187, 188]. Note that this assumes that in the ferromagnetic phase the anharmonic phonon phonon interaction remains unaltered. The volume is affected by the magnitude of the magnetic moment through the magneto-volume effect. If ω_m denotes the thermal expansion due to magnetic effects, C is the magneto-volume coupling constant and B the bulk modulus we can

write [189][2]:

$$\omega_{\mathrm{m}} = C/B \cdot M^2. \tag{5.15}$$

Experimentally this relation is well reproduced [163] and yields $\omega_{\mathrm{m}}(T = 0\ \mathrm{K}) \approx 1 \times 10^{-3}$. This is also supported by theoretical studies, where the magnetic moment was calculated to increase with increasing volume with a slope of 0.06 $\mu_{\mathrm{B}}/\mathrm{\AA}^3$ about the experimental volume [183].

With the approximate relation $M \propto \sqrt[4]{1 - T/T_{\mathrm{C}}}$ [179] and equation 5.15, one gets $\omega_{\mathrm{m}} \propto \sqrt{1 - T/T_{\mathrm{C}}}$, that is, an approximate square root dependence of the magneto volume effect as a function of temperature. This is in good experimental agreement with [163, 187].

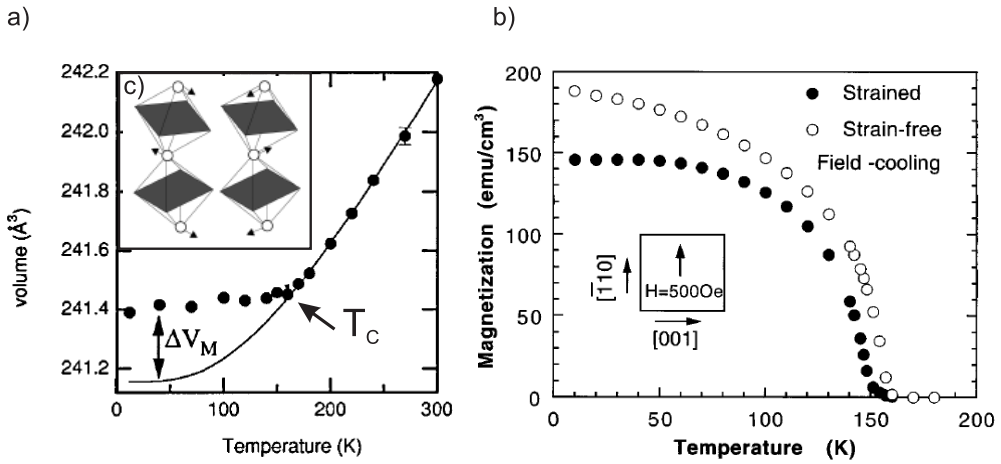

Figure 5.13: **a**) Volume of the SRO unit cell as a function of temperature. Below 160 Kelvin the thermal expansion is compensated by magnetostrictive components resulting in a zero thermal expansion coefficient [163]. **b**) The magnetization versus temperature curves for both a strained and a strain-relaxed $SrRuO_3$ thin film [190]. **c**) Oxygen octahedra phonons (mainly) responsible for stabilizing the ferromagnetically ordered state [165].

For a thin film with a pseudocubic structure the magneto-volume effect is even more pronounced. Figure 5.13 b) reproduces the experimental results of a magnetization measurement of a strained and strain-relaxed SRO thin film [190]. The strain was induced by growing the SRO film epitaxially on a STO substrate which amounts to 0.67 % in plane strain. Note that this is the situation in our sample. One then calculates $\omega_{\mathrm{m}} = 3.5 \times 10^{-3}$ for $T = 0$ K.

[2]Again, the derivation is based on a Taylor expansion of the free energy, assuming only even terms in M and a lowest coupling term $\omega_{\mathrm{m}} M^2$. This is discussed in detail for the electric polarization in section 6.1.2.

This is confirmed by similar results [191], which report on the magnetization of SRO grown on different substrates, and thus with different compressive and tensile strains. The easy axis of magnetization lies in the (001) plane, its direction is between the [110] and [010] direction; along the growth direction it is approximately a factor of two smaller [56, 192] (compare figure 2.10).

Microscopically the zero thermal expansion coefficient was found to be stipulated by freezing of the mutual rotations/tilts of the oxygen octahedra below the phase transition into the ferromagnetic phase [compare figure 5.13 c)]. This was revealed in a series of neutron diffraction experiments [179, 187]. The Ru-O bond length remains constant between 1.5 and 300 Kelvin, while the angle Ru-O drops with decreasing temperature and stays constant below T_C. The importance of the orthorhombic distortion (that is, the tilted oxygen octahedra) for stabilizing the magnetic state is also discussed in theoretical work: calculations for a perfectly cubic SRO unit cell yields much lower magnetic moments, while the rotation of the RuO_3 octahedra by 8° in SRO was found to be close to the value of maximum magnetization [182].

Magnetic Grüneisen Parameter of $SrRuO_3$

The thermodynamic model of stress generation is extended further to incorporate magnetic contributions: one defines a magnetic specific heat and magnetic thermal expansion coefficient, which, along the same lines as above, are linked by a magnetic Grüneisen parameter. If E_m is the magnetic interaction energy, we can write:

$$\gamma_m = \left(-\frac{\partial ln(E_m)}{\partial ln(V)} \right)_T . \tag{5.16}$$

Experimentally it is difficult to separated magnetic and electronic contributions at low temperatures, such that one often defines a common Grüneisen parameter γ_{em}. Note that values of γ_{em} may have large values and may be of either sign.

A simple approximation for the magnetic Grüneisen parameter for $SrRuO_3$ is given in the following. The total specific heat of $SrRuO_3$ at its Curie temperature of $T = 160$ K amounts to approximately $C_{total} = 90$ J/K/mol, while its magnetic contribution is given by only $C_{mag} = 4.4$ J/K/mol [193]. The total thermal expansion coefficient drops to zero at $T = 160$ K [194], that is, the volume change due to anharmonic phonon-phonon interaction and magnetic contributions exactly cancel each other. Hence, with equation 5.16 or 5.3 the ratio between the lattice and magnetic Grüneisen parameter is determined to $\gamma_l/\gamma_m \approx -0.05$. With the approximation made in section 5.1 for the lattice Grüneisen parameter one finds

$\gamma_m \approx -33$. Hence, moderate energy changes in the magnetic system result in a huge compression of the lattice.

Again caution is necessary when applying this thermodynamic picture to non-equilibrium physics. In fact, we have already mentioned specific optical phonon-modes, which play a dominant role in the coupling between ferromagnetism and structural degrees of freedom. This is apparently in conflict with the mode-independent Grüneisen-concept.

A number of papers have investigated the dependence of the critical temperature on the applied pressure. Resistance and A.C. susceptibility measurements for $SrRuO_3$ under a hydrostatic pressure revealed a decrease in T_C at a rate of -6.3 to -7.9 K/GPa [194–197]. In a thin film of $SrRuO_3$ a smaller value of -5.9 K/GPa was found [198]. Note, that the values of $\partial T_C/\partial P$ are fairly moderate, pointing to a very stable magnetic state and also imply that the strain caused by the pseudomorphic growth has only a minor impact on the transition temperature T_C. Figure 5.13 b) shows very small changes of the Curie temperature for different strains, in line with the numbers for $\partial T_C/\partial P$, however, one observes very large differences in saturation magnetization at T=0 for different strains. This is the component which for ultrafast changes in magnetization (with $\Delta S = 0$) is believed to lead to correspondingly sub-picosecond and very pronounced changes in the lattice structure.

Despite the growing number of publications on $SrRuO_3$, evincing the large progress explaining its electronic and magnetic properties and their *static* interaction with structural degrees of freedom, the dynamics and relevant time-scales of such couplings have remained unknown. In particular, how fast is the structural response, that is, reduction of the unit-cell volume, after an optically induced demagnetization? This unresolved question is addressed experimentally by the structurally sensitive method of X-ray diffraction. The results are presented in the the following.

5.4.3 Time Resolved X-ray Data

With the Curie temperature $T_C = 160$ K of $SrRuO_3$ it is necessary to cool the sample and perform the measurements with a cryostat. As excitation wavelength we chose the fundamental beam with $\lambda = 800$ nm and the idler output of the OPA with $\lambda = 2250$ nm. This necessitated a rather laborious modification of the experimental setup. The implementation of the cryostat set additional geometric constraints and required a change of the X-ray optic together with the focusing conditions. Only optic No. 1 (see Tab. 3.3) has an adequate divergence to measure two neighboring Bragg reflections simultaneously as well as a sufficient distance between source and focus.

Again the X-ray response turned out to be extremely sensitive on the focal spot size as well as the spatial overlap of X-ray probe and pump beam. In the experiment we investigated the dependence of the phonon amplitude and temporal shape as a function of excitation wavelength and temperature.

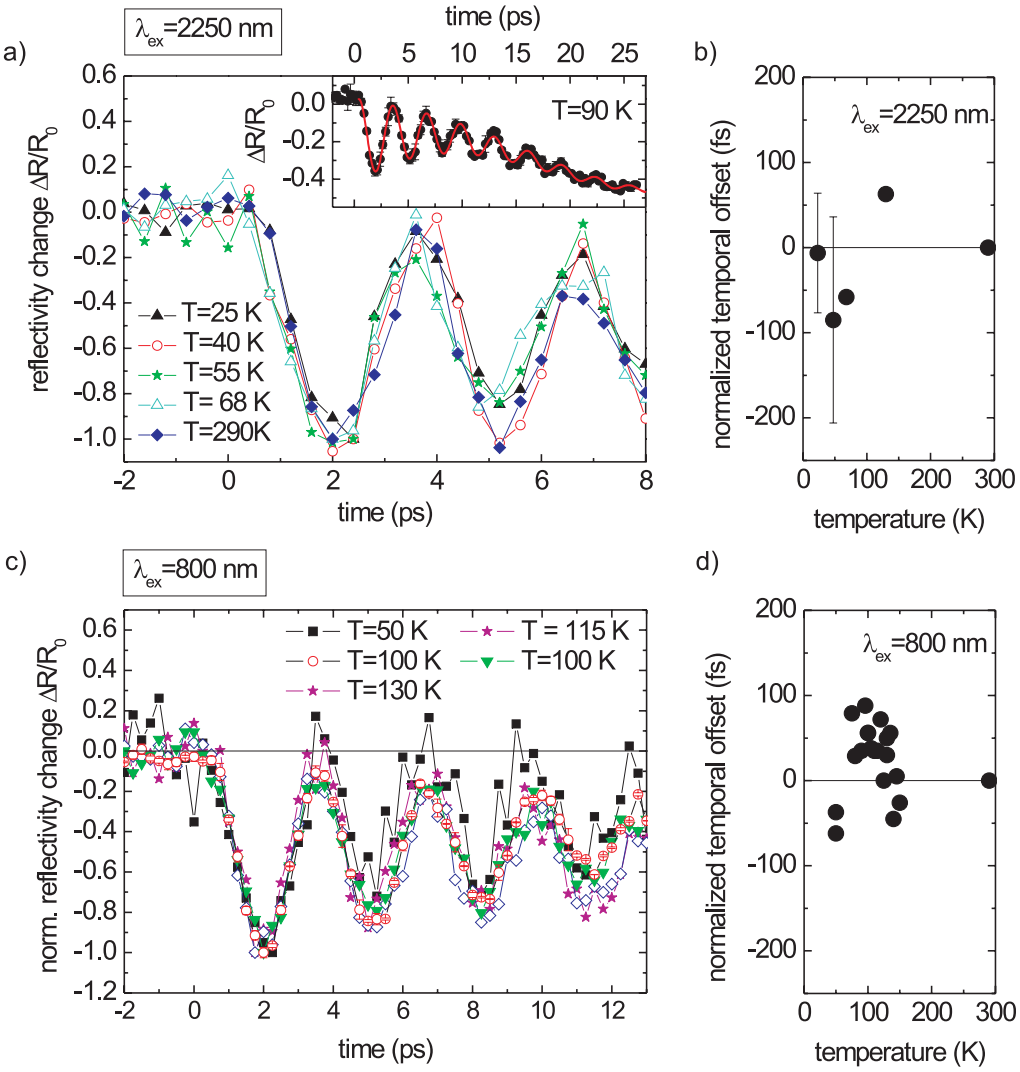

Figure 5.14: Normalized reflectivity change for different temperatures as a function of time. The excitation wavelength is **a**) $\lambda = 2250$ nm and **c**) $\lambda = 800$ nm. Inset: Time dependent reflectivity change on a longer time scale at $T = 90$ K. Temporal offset of the phonon oscillations as a function of temperature for **b**) $\lambda = 2250$ nm and **d**) $\lambda = 800$ nm.

Figure 5.14 a) shows the normalized reflectivity change as a function of

time for temperatures between 290 Kelvin and 25 Kelvin. The inset shows the reflectivity change on a longer time scale for T=90 K. Here one may appreciate how for longer times the phonon oscillations are superimposed by an oscillation of longer period (approximately 30 ps), which is apparently due to the expansion of the entire SL structure. We again calculated the temporal error function describing the temporal offset of the oscillations to deduce a possible temporal offset for different temperatures. This time is plotted in figure 5.14 b) as a function of temperature. The values scatter around the time of the room temperature measurement with an rms value of approximately 100 fs. One cannot make out a trend, which suggests that within the accuracy of the experiment, the time remains constant. For repeated measurements at the same temperature the mean time delay is plotted together with an error bar reflecting the rms value.

In figure 5.14 c) the corresponding measurement carried out with an excitation wavelength of $\lambda = 800$ nm is shown. The normalized X-ray reflectivity change is plotted as a function of temperature. For better clarity only measurements taken at 4 different temperatures are shown. Again one observes well overlapping curves, the only slight deviations can be observed for the lowest temperature of 50 K, here the X-ray reflectivity seems to indicate stronger modulation and even reaches positive values for minimal elongations. Figure 5.14 d) shows the deduced temporal offset normalized to the room temperature measurement as a function of temperature; here all measurements have been included. Again, there seems to be no recognizable dependence on temperature.

More rewarding information can be deduced from the phonon amplitudes, both as a function of time and excitation wavelength. The experimental results are plotted in figure 5.15. Graph a) shows three exemplary curves measured with an excitation wavelength of $\lambda = 2.2$ μm for $T = 20$ K (red filled dots), $T = 160$ K (black stars) and $T = 290$ K (green circles). Figure 5.15 b) compares the phonon amplitude normalized to the room temperature measurement as a function of temperature. The whole data set consists of 7 different experimental runs, carried out on different days, but with comparable excitation fluence. Identical temperatures have been averaged, the reproducibility determines the error of approximately $\pm$ 7 %. The green, filled dots show the data recorded with the infrared excitation pulses ($\lambda = 2.2\mu$m): for temperatures above $T_C \approx 160$ K the phonon amplitude remains constant and drops considerably for temperatures below T_C. For the lowest temperature the amplitude has dropped to nearly 50 %. For excitation with 800 nm, the effect is much less pronounced, and the amplitude is reduced by approximately 20 %. The phonon amplitudes show an approximate square root dependence on temperature.

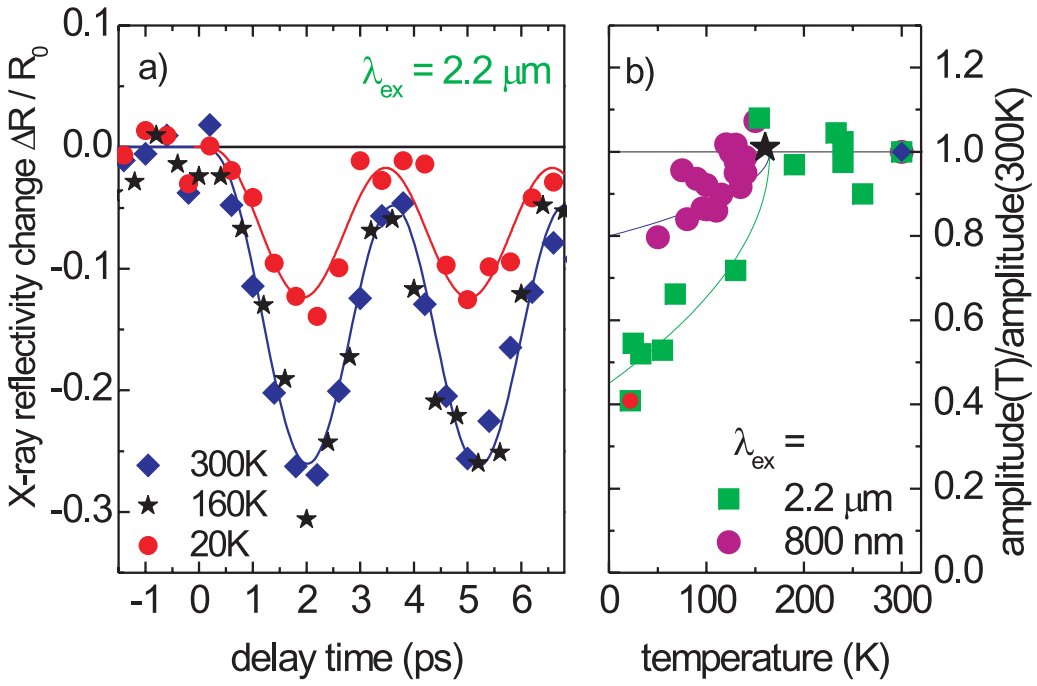

Figure 5.15: **a**) $\lambda = 2.2$ μm pump X-ray reflectivity of the superlattice peak (0 0 116) for 300 K (blue triangle), 160 K (black stars) and 20 K (red dots). The solid lines are calculations with equation 5.10) and a rise time of $\tau_{\text{phonon}} = \tau_{\text{mag}} = 500$ fs. **b**) Lattice temperature dependence of the amplitude(T) of the SL phonon oscillation normalized to its value at room temperature for excitation wavelengths as indicated. The contribution of magnetic contractive stress follows approximately the temperature dependent magnetization squared $M(T)^2$ (solid lines).

5.4.4 Time Resolved Optical Data

To learn more about the electronic system in $SrRuO_3$, in particular, with regard to the temporal evolution of the demagnetization after optical excitation, temperature dependent all optical reflectivity measurements have been carried out. Figures 5.16 show the time-resolved reflectivity change probed with $\lambda = 2.2$ μm after excitation with a) $\lambda = 2.2$ μm and b) $\lambda = 800$ nm. The data is shown for an early time scale, up to 2 ps, and for three exemplarily temperatures of 300, 160 and 20 Kelvin. Only for early delay times $t < 2$ ps the time-resolved curves are discussed. One finds satisfactory agreement with the experimental data for a fit function containing a fast and slow

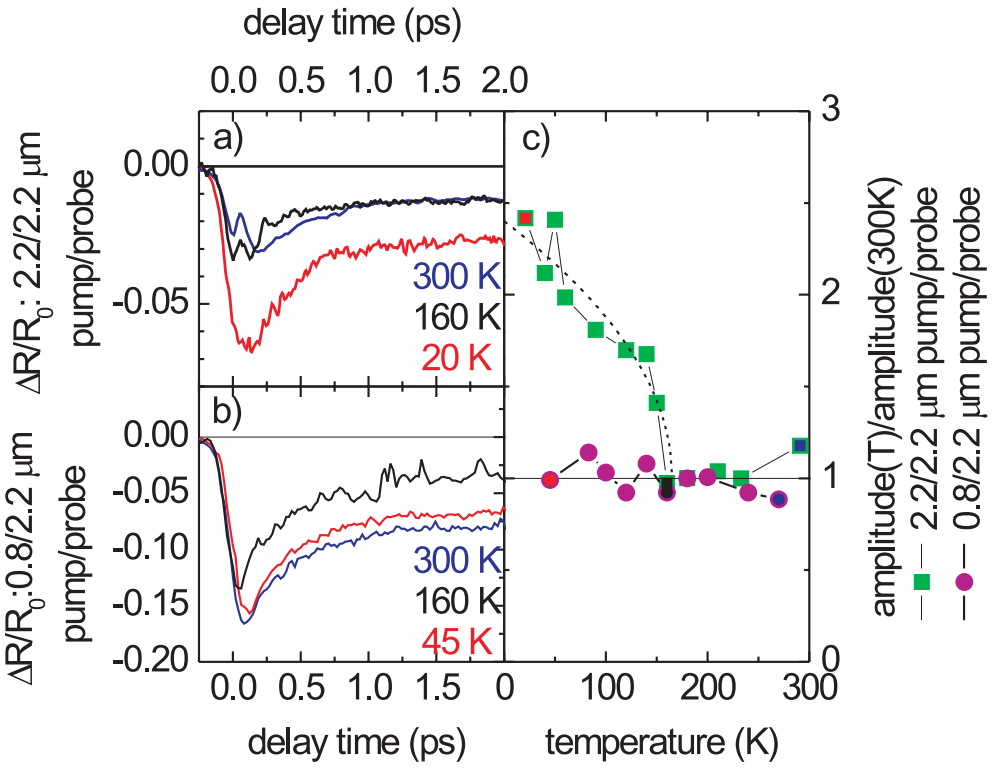

Figure 5.16: **a**) $\lambda = 2.2/2.2$ μm pump probe transient reflectivity for 300 K (blue curve), 160 K (black curve) and 20 K (red curve). **b**) $\lambda = 0.8/2.2$ μm pump probe transient reflectivity. **c**) Amplitude of the fast component of the optical reflectivity as a function of temperature. For excitation with $\lambda = 2.2$ μm one observes a behavior mimicking the magnetization square behavior.

exponential component:

$$R(t,a,b,c,d,e,f) = \frac{1}{2}\left(1 + \mathrm{erf}(\frac{t-a}{b}) + c\exp(-\tau_{\mathrm{optical}}t) + e\exp(-ft)\right) \tag{5.17}$$

The time constant of the fast exponential decay yields values of approximately $\tau_{\mathrm{optical}} = 250 - 300$ fs. Only for measurements at the Curie temperature the decay time is slightly lower. Integration over the fast component (that is $\sum R(t,a,b,c,d)$ and normalization to its mean value above T_C yields the points shown in figure 5.16 c). While for the data pumped with $\lambda = 800$ nm there is no observable dependence on temperature, the integrated fast component for an excitation wavelength of 2.2 μm clearly follows an approximate square root dependence.

5.4.5 Discussion

For a constant amount of absorbed pump energy, a temperature independent Grüneisen constant and unchanged anharmonic phonon phonon interaction, one expects the SL phonon driving stress amplitude to be independent of the lattice temperature. Thus, the observed temperature dependent behavior of the phonon amplitudes gives evidence of additional contributions to the photo-generated stress below $T_C = 160$ K. The data points in figure 5.15 b) approximately follow the temperature dependent magnetization $M^2(T)$ (solid line) [163], suggesting a contractive magnetic contribution to stress driving the SL phonon.

Ultrafast Demagnetization

Let us first address the question of ultrafast demagnetization, certainly the prerequisite of magnetostrictive effects. The ultrafast time scale of the magnetostrictive component and the distinct excitation spectrum, that is, the more pronounced effects observed for an excitation wavelength of $\lambda = 2.2$ μm, give the most valuable information about the underlying mechanism. The most likely scenario seems to be either demagnetization by direct optical spin-flip transitions, or electron-magnon scattering during the fast thermalization of the hot electron gas.

In literature there is experimental and theoretical evidence strongly supporting these scenarios: Figure 5.7 b) shows the frequency dependent absorption coefficient $\alpha(\omega)$ of metallic $SrRuO_3$ as calculated from experimental reflectivity data and its dielectric function [132]. One clearly sees an absorption maximum around 5000 cm^{-1}, which grows for lower temperatures. This gap is attributed to electronic correlation effects and, hence, can be associated with the magnetically ordered electron system. Secondly, band structure calculation [181, 183] show a large pile up of the density of states (DOS) of the majority spins about 2500 cm^{-1} below the fermi-energy E_F, while unoccupied states of the minority spins are about 2500 cm^{-1} above E_F. The calculated density of states is shown for the ferromagnetic case in figure 5.17 a) and schematically for the paramagnetic case b).

For allowed optical transitions between these two density of state peaks one expects a strongly enhanced demagnetization for photon energies around 5000 cm^{-1}. Note that due to the strong spin-orbit coupling of Ru d orbitals and the hybridization of Ru d and O p orbitals such transitions are not necessarily forbidden. This is well known from atomic physics: for heavy elements the spin-orbit coupling for each individual electron increases and the interaction is described by jj coupling. The forbidden intercombination,

that is, transitions between states with different multiplicity or $\Delta S \neq 0$, take place. The most prominent example is the strongest line in the spectrum of mercury with $\lambda = 253.7$ nm. In this scenario the additional absorption peak around 5000 cm^{-1} [figure 5.7 b)] in the ferromagnetic phase would stem from spin-flipping (demagnetizing) optical transitions, so called intercombination transitions. An approximation of the excitation density of SRO yields several tens of percent of free electrons, with $n(e)_{SRO} = 1.22 \times 10^{22}$ cm^{-3}, an excitation fluence of 6.6 mJ/cm^2 [compare figure 5.11 and figure 5.3 b)] and the wavelength $\lambda = 2.2$ μm. This very high value of the excitation density supports the assumption of a considerable reduction of the macroscopic magnetization, even in direct optical intercombination transitions. For higher photon energies ($\lambda = 800$ nm) the process of demagnetization is less efficient, because here the DOS for majority and minority spins is more symmetric and the number of photons is lower by about a factor of 3. This scenario implies an instantaneous demagnetization, such that the finite rise time of the magnetostrictive stress must be due to secondary processes, that is, phonon-phonon interaction. This will be discussed in the following section.

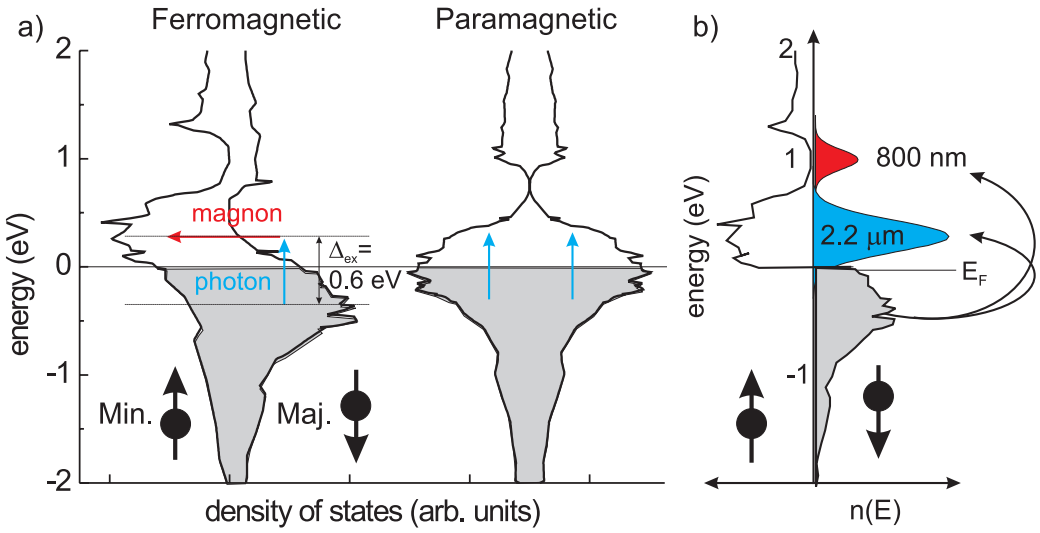

Figure 5.17: **a**) Calculation of the density of states (DOS) of SRO for the ferromagnetic case [183] and a schematic DOS in the paramagnetic case. Δ_{ex} corresponds to 5000 $cm^{-1} = 2$ μm≈ 0.6 eV in SRO. **a**) Electron distribution after optical excitation with 800 nm and 2.2 μm for identical total energy.

Alternatively, a slightly modified picture would also explain the wavelength dependence of the demagnetization; it is depicted in schematic 5.17 b). Optical excitation from filled (majority) electron states at approximately -0.3 eV (grey area) results in an non-thermal electron distribution around 0.3 eV

(blue area) and around 1.2 eV (red area) for wavelength of 2.2 μm and 800 nm, respectively. Again, recall that for an identical total deposited energy the number of excited electrons for 800 nm excitation is smaller by about a factor of three. Low energy magnetic excitations (magnons) are emitted during the thermalization of the hot electron gas; the reservoir for angular momentum is attributed to electron orbits (compare for example [199]). This process is expected to be most efficient for high energetic electrons and around 0.3 eV, where the unoccupied minority spins have a maximum. Successive spin flips during carrier thermalization result in a randomization of a certain fraction of the magnetic order. Hence, the demagnetization depends on the number of *photoexcited* electrons and, for identical excitation energy, will be larger for 2.2 μm excitation. A finite time for demagnetization is now permitted and an upper limit is given by the electron equilibration time. Importantly, in this model spin flips of thermalized electrons must be assumed to be very slow. This is in agreement with band structure calculation including spin-orbit interaction showing that the band-electron wavefunctions consist of different orbit and spin components, while the contribution of such spin-mixed states grows for increasing energy [200]. At the band minimum (thermal electrons) they play a negligible role and so do spin-flipping processes. Note, that the photoexcited electrons with 800 nm or 2.2 μm have a temperature of approximately 4000 K or 16000 K, respectively, that is, much higher than the temperature of the equilibrated electron system. The earlier mentioned optical Kerr experiments [172] also revealed that thermal contribution to the demagnetization around T_C are considerably slower ($\approx$ 10 ps).

Since the processes of phonon generation and demagnetization are both linked to the thermalization of hot electrons, a similar rise time of phonon mediated and magnetostrictive stress follows.

This described scenario of optical, wavelength dependent, ultrafast demagnetization is further corroborated by the optical pump probe data presented in section 5.4.4. Here the fast component of the reflectivity change after $\lambda = 2.2$ μm excitation shows the characteristic behavior of a demagnetization curve. It remains constant above the Curie temperature and then follows an approximate $M^2(T)$ dependence for lower temperatures. This can be compared to the recent systematic study on various ferromagnetic compounds including SRO by femtosecond magneto-optical Kerr experiments [172]. The fast component ($t < 200$ fs) of the time-resolved ellipticity as a function of temperature exhibits a very similar behavior as shown in figure 5.16. This close agreement suggests that the all optical data can be interpreted as a probe for magnetization. The temporal resolution of the all optical data is in the order of 100 fs, such that it is in agreement with both demagnetization scenarios described above. The results for the 800 nm

pump/2.2 μm probe optical data show no appreciable dependence on temperature. This may be due to a nonlinear (or in general more complicated and unknown) relationship between the optical response and magnetization, or that indeed some fraction of electrons are spin-flipped in direct optical transitions for 2.2 μm excitation. A more conclusive interpretation of the all optical data certainly requires further experimental efforts.

Ultrafast Magnetostriction

Accordingly, after optical excitation the SRO layers are assumed to be (partially) demagnetized, and one expects consequences for the crystal structure. This is maintained by the overwhelming experimental and theoretical evidence of the strong magneto-volume effect in SRO [163, 179, 182, 183, 188]. Therefore, the reduction of phonon amplitude below T_C is assigned to the contractive stress induced by magnetostriction. The effect is large and for the lowest temperature we measure approximately $\eta_{mag} = 2.5 \times 10^{-3}$. The magnitude of the ultrafast magneto-volume effect is in quantitative agreement with previously reported values in thin films: the magnetization of thin film SRO was compared with different in-plane strain and revealed huge magneto-volume effect at $T = 0$ Kelvin of up to 3.5×10^{-3} [190, 191].

While the *static* connection between magnetization and decreasing volume is well established, the corresponding dynamics of such interactions have remained unknown. The presented time-resolved X-ray experiments allow to determine the relevant time-scales with a sub-picosecond resolution. Careful analysis of the measured transient reflectivity curves point to no appreciable temperature dependent temporal offset between the oscillations. This suggests that the processes leading to magnetostriction happen on a similar time-scale as the expansive phonon mediated stress. For a quantitative analysis the differential equation 5.10 is solved for a phonon and magnetic stress contribution:

$$F(t) = A[1 - \exp(-t/\tau_{phonon})] - B[1 - \exp(-t/\tau_{mag})] \tag{5.18}$$

where the parameter A only depends (linearly) on the incident pump fluence and the parameter B on M^2, the excitation wavelength λ_{ex} (and presumably on the incident pump fluence). The calculation is presented in figure 5.18 and compared to two exemplary curves at 300 and 20 Kelvin. For a constant rise-time of the phonon induced force of $\tau_{phonon} = 500$ fs we find best agreement for traces with $\tau_{mag} \approx 500$ fs. The calculation for an instantly produced stress ($\tau_{mag} = 50$ fs) after demagnetization shows significant deviations, in particular a large phase shift of nearly 500 fs [compare green dashed line in figure 5.18 a)]. Also for much slower build-up of the magnetic component

(τ_{mag} = 1250 fs) the calculated oscillation shows poor agreement. However, care has to be taken not to overrate the temporal resolution of the experiment. With slight changes in τ_{phonon} = 500 of ± 100 fs – certainly within the experimental error – magnetostriction between 200 fs< τ_{mag} < 750 fs still gives a fair agreement with the measured phonon oscillations. Additionally, note that the curves shown in figure 5.18 a) are exemplary results for T = 20 K, while the set of repeated measurements show a relative noise in amplitude of up to 10%. However, it is justified to exclude an instantaneous as well as slow (>800 fs) magnetic contribution to stress.

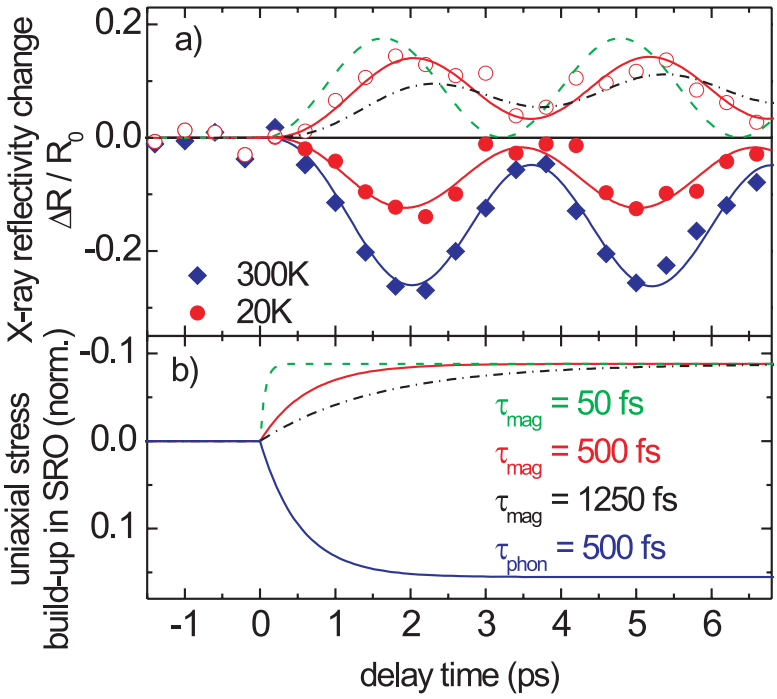

Figure 5.18: **a**) X-ray reflectivity for T=300 K and 20 K (solid symbols). Extracted magnetostrictive component together with calculated traces for different transient stress according to lower panel. Best agreement is found for τ_{mag} = 500 fs. **b**) Build-up of phonon mediated and magnetostrictive stress for different time constants τ_{mag}

If the process of demagnetization is assumed to be quasi instantaneous (τ_{mag} < 100 fs), the observed delay of the onset of the magnetostrictive stress is attributed to successive phonon-phonon interaction, that is, interaction between excited phonons and the tetragonal distortion. Optical phonons have been found to play an important role for the spin exchange coupling and

have been identified as the oxygen vibrations $A_g(5)$ and $B_{2g}(4)$ [compare figure 5.13 a)], which modulate the Ru-O-Ru bond angle [179, 187]. In Raman measurements they have been found at 391 cm^{-1} and 393 cm^{-1} [165]. Further contributions stem from phonons between 94 cm^{-1} and 250 cm^{-1} [164]. We may assume that the ultrafast optical demagnetization changes the potential for these phonon modes, that is, they are displacively excited. Therefore, the build-up of the magnetic contribution to stress happens on a time scale set by their specific frequencies, corresponding to up to several hundred femtoseconds. Even though this notion is in agreement with our experimental data and supported by literature, it is important to remember that the presented X-ray experiments are not sensitive to oxygen atoms displacements. Thus a direct verification of the role of the oxygen octahedra on an ultrafast time scales has yet to be demonstrated.

Summarizing, the scenario of magnetostriction may happen as follows: the strong spin-orbit interaction in the itinerant ferromagnet $SrRuO_3$ allows for spin-flipping intraband scattering processes, involving the absorption of a photon and emission of a magnon. The resulting reduction of magnetization couples to the tetragonal distortion via the magneto-volume effect and reduces the amplitude of the superlattice phonon oscillation. The finite rise time of the magnetostrictive stress component is attributed to intraband spin-flipping scattering processes during carrier thermalization and/or to the elongation of specific optical phonon modes and their subsequent coupling to the crystal volume.

In conclusion, we have identified different mechanisms of ultrafast stress generation in the itinerant ferromagnet SRO. Measurements of photoinduced structural dynamics in real-time by ultrafast X-ray diffraction provides the first direct evidence for a subpicosecond build-up of magnetostrictive stress in nanolayered SRO. The amplitude of the magnetostrictive component of transient stress decreases with increasing temperature, mimicking the temperature dependent magnetization. The magnetostrictive stress compensates a major fraction of the crystal expansion driven by non-equilibrium phonons.

Chapter 6

Coupled Ultrafast Lattice and Polarization Dynamics in Ferroelectric Nanolayers

The ferroelectric properties of $PbTiO_3$ (PTO) and its derivatives like $Pb(Zr_{0.2}Ti_{0.8})O_3$(PZT) solid solutions are essentially determined and controlled by two prominent phonon modes of the crystal lattice: (i) The tetragonal distortion along the c axis is characterized by η=c/a of the unit cell where a and c are the in-plane and out-of-plane lattice constants. (ii) The ferroelectric soft mode is connected with the displacement $\xi_{\mathrm{Pb-Ti}} = \xi_{\mathrm{Pb-O}} - \xi_{\mathrm{Ti/Zr-O}}$ of the Pb and Ti cations given by the difference of the displacements between the respective cation and the oxygen anions. The ferroelectric polarization P is proportional to the soft mode displacement, that is, $P \propto \xi_{\mathrm{Pb-Ti}}$. At room temperature, the underdamped soft mode displays a frequency somewhat below 100 cm^{-1}, corresponding to a subpicosecond oscillation period [201]. The *dynamics* of ferroelectricity is intrinsically coupled to lattice dynamics, that is, atomic motions along the two modes η and $\xi_{\mathrm{Pb-Ti}}$. This raises the question if and how fast the macroscopic polarization of Perovskite nanolayers can be manipulated by launching lattice excitations. So far, experimental work on this issue has remained limited. All-optical measurements of the ultrafast polarization dynamics lack the exact determination of atomic amplitudes, and the fastest switching times observed so far for epitaxial ferroelectric materials are in the 100 ps range [202].

This chapter presents a time-resolved X-ray diffraction experiment to study polarization dynamics in a $Pb(Zr_{0.2}Ti_{0.8})O_3/SrRuO_3$ superlattice (SL) under optically induced uniaxial stress. Two Bragg reflections provide sufficient information to derive the coupled dynamics of the two modes that are relevant for ferroelectricity. The uniaxial stress compresses the PZT layers

by up to $(\eta/\eta_0) - 1 = 0.022$ without destroying the sample. We demonstrate that such transient stress can reversibly switch off the ferroelectric polarization of PZT within less than 2 ps.

6.1 Ferroelectricity

The ferroelectric phase transition is a *structural* phase transition, as a result of which a spontaneous polarization occurs in the crystal, that is, a component of the electric polarization vector, which is caused by relative displacements of atoms in each of the unit cells of the crystal and which results in the appearance of the pyroelectric effect.

Ferroelectrics are in thermal equilibrium in each polarization state $+P$ and $-P$ and their basic properties are determined by the characteristic double well potential (compare figure 6.2). At sufficiently low temperatures neighboring ions sit on the same side of the potential forming *domains* leading to a net polarization per unit volume. Usually a crystal consists of many domains with random polarization such that the total macroscopic polarization averages to zero. If an external electric field can pole the crystal resulting in one single domain with a macroscopic polarization the crystal is called ferroelectric.

As the temperature is increased the ions in the double wells obtain enough kinetic energy to hop rapidly back and forth between the two minima of the potential, such that their mean displacement corresponds to a non-ferroelectric or paraelectric state. This phenomena is called a *order-disorder phase transition*. The ion positions are ordered below a phase transition temperature and are disordered above T_0. Alternatively, in a *displacive transition*, the potential barrier of the double well is reduced with increasing temperature and the minima move to their initial midpoint. This can happen over a small temperature range for which the ion kinetic energy $k_\mathrm{B}T$ changes very little.

In the following the very intuitive microscopic theory of Cochran is discussed, which explains a ferroelectric phase transition as a result of an instability for a certain normal mode of vibration, that is, nuclear motion. This is followed by an introduction of the thermodynamic approach developed by Landau and Devonshire. This gives a good macroscopic description of ferroelectric phase transitions and allows us to include electrical and mechanical boundary condition, which play an important role in ferroelectric thin films.

6.1.1 Soft Mode or Cochran Theory of Ferroelectricity

A very elegant and intuitive model for ferroelectricity was formulated by Cochran [203] in 1960. The main thesis of this work is that ferroelectricity can be treated as a problem of lattice dynamics and that the lower-symmetry ferroelectric phase corresponds to an eigenvector of a transverse optical mode. The phase transition is described as a result of a mechanical instability of a crystal lattice with respect to a normal mode. At the transition point the unstable crystal lattice is restructured such that it is stable for all Eigenmodes. The following discussion is restricted to a simple ionic crystal of sodium chloride type, although the same work also considers the problem of $BaTiO_3$.

Because at low frequencies the polarization of ionic crystals are mainly due to a displacement of the atomic cores (ionic polarization), which are accompanied by a displacement of the electrons with respect to the core (electronic polarization), the polarization must be directly linked to lattice dynamics. This leads to the assumption that we can express the polarization P as a superposition of plane waves, just like one decomposes the displacement of atoms into eigenmodes. We can write:

$$P \sim \exp i\{\vec{k}\vec{r} - \omega t\} \tag{6.1}$$

and also for the electric field which is caused by the polarization:

$$E \sim \exp i\{\vec{k}\vec{r} - \omega t\} \tag{6.2}$$

With help of the Maxwell equations we can readily prove that the electric local field E_{loc} acting on the atoms for transversal (t) and longitudinal (l) lattice vibrations are as follows (see for example [204]):

$$\vec{E}^{\mathrm{t}}_{\mathrm{loc}} = \vec{E}_{\mathrm{Lorentz}} = \frac{1}{3\varepsilon_0}\vec{P} \tag{6.3}$$

$$\vec{E}^{\mathrm{l}}_{\mathrm{loc}} = \vec{E}_{\mathrm{Lorentz}} - \frac{1}{\varepsilon_0}\vec{P} = -\frac{2}{3\varepsilon_0}\vec{P} \tag{6.4}$$

where $\vec{P}/3\varepsilon_0$ is the Lorentz field. E_{loc} is the electric field at the site of the displaced atom that is produced by the dipoles throughout the rest of the solid [compare figure 6.1 a)]. The problem is greatly simplified by only considering $\vec{k}$ along the symmetry direction [100], because then the force constants can be considered to only act between planes of atoms, and the problem becomes similar to that of a linear chain. Further simplification is possible when $k = 0$. For any such mode all atoms of the same type have the same displacement and the only force constant involved, for a diatomic

crystal, is that between the two Bravais arrays of atoms such as sodium and chlorine. For simplicity only the negative ion are taken to be polarizable. We use the shell model for a polarizable atom in the following way: one considers 3 Bravais lattices: the positive ions, and the core and shell of the negative ions. The shell (representing the outer electrons) is coupled to the core of the negative ion by an isotropic and short-range force, specified with the force constant κ. The short-range force between the shell and the core of the positive ion is described by the force constant κ_0. Finally we have to consider the long-range Coulomb forces, which depend on the polarization P. If we denote u_1, u_2 and v_2 as the displacements from their equilibrium positions of positive ions and the core and shells of negative ions, respectively, we may write for the equation of motion for the transverse mode:

$$\begin{aligned} m_1\ddot{u}_1 &= \kappa_0(v_2 - u_1) + \frac{1}{3\varepsilon_0}PZe; \\ m_2\ddot{u}_2 &= \kappa(v_2 - u_2) + \frac{1}{3\varepsilon_0}PXe; \\ 0 &= \kappa(u_2 - v_2) + \kappa_0(u_1 - v_2) + \frac{1}{3\varepsilon_0}PYe. \end{aligned} \tag{6.5}$$

Ze, Xe, Ye are the charges of the positive ions, the cores and shells of the negative ions, respectively. For a neutral crystal we have $X + Y + Z = 0$, e denotes the elementary charge. The third equation specifies that the shells always occupy positions of equilibrium corresponding to the instantaneous configuration of the nuclei. This situation is depicted schematically in figure 6.1 b).

We choose $\vec{q}$ along [100] with the atoms displaced parallel to [001] and make the ansatz $u_{1,2} = U_{1,2}\exp(-iwt), v_2 = V_2\exp(-iwt)$, etc. and $P = \mathfrak{P}\exp(-iwt)$. Simple algebraic rearrangement, introducing the effective value $Z' = Z + Y\kappa_0/(\kappa + \kappa_0)$ and noting that $\mathfrak{P} = e(ZU_1 + XU_2 + YV_2)/V$ (where V=unit cell volume) yield the following:

$$\mathfrak{P}\left(1 - \frac{(Ye)^2}{3V\varepsilon_0(\kappa + \kappa_0)}\right) = \frac{Z'e}{V}\xi. \tag{6.6}$$

Here we have also introduced the abbreviation $\xi = |U_1 - U_2|$, which describes the relative displacement of the core ions. Note that this is directly proportional to the polarization $\mathfrak{P}$. Let us now additionally consider the situation when an effective field $E = \mathfrak{E}\exp(-i\Omega t)$ exists inside the crystal, with a frequency Ω such that the cores do not move appreciably. The equilibrium is then given by $\mathfrak{E}Ye = (\kappa + \kappa_0)V_2$ and the polarization due to displacement of the shells is $\mathfrak{P} = YeV_2/V$. One calculates the electronic polarizability of

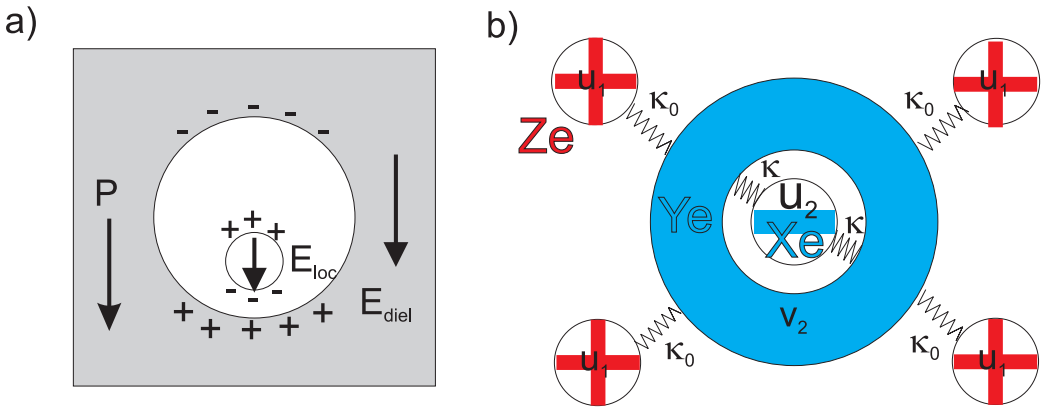

Figure 6.1: **a**) 'Cavity method' to calculate the local field E_{loc} induced by the field E_{diel}, as the sum of all dipolar fields throughout the solid. **b**) Cochran Shell model for short range forces: the core of the negative ion is coupled to its shell with force constant κ, the core of the positive ion is coupled to the shell with force constant κ_0.

the negative ion to be:

$$\alpha_e = \frac{\mathfrak{P}V}{\mathfrak{E}} = \frac{(Ye)^2}{\kappa + \kappa_0}. \tag{6.7}$$

The electric polarizability α_e is, however, related to the optical-frequency dielectric constant ε_e by the Clausius-Mossotti formula

$$\frac{\alpha_e}{3V\varepsilon_0} = \frac{\varepsilon_e - 1}{\varepsilon_e + 2}. \tag{6.8}$$

With this formula and the ansatz for equation 6.5 one gets

$$\mu w_T^2 = \kappa_0' - \frac{(\varepsilon_e + 2)(Z'e)^2}{9V\varepsilon_0} \tag{6.9}$$

with $\kappa_0' = \kappa\kappa_0/(\kappa+\kappa_0)$ and the reduced mass $\mu = m_1 m_2/(m_1+m_2)$. We have added a suffix T to emphasize that we are dealing with a transverse optical mode. For the longitudinal optical mode we can repeat the above derivation except we have to use the the electric field as specified in equation 6.4:

$$\mu w_L^2 = \kappa_0' + \frac{2(\varepsilon_e + 2)(Z'e)^2}{9V\varepsilon_0\varepsilon_e} \tag{6.10}$$

With the well known Lyddane-Sachs-Teller-relation between the frequencies ω_L and ω_T and the static and optical-frequency dielectric constant ε_s and ε_e,

respectively (for a simple derivation for ionic crystals see [205]):

$$\frac{\omega_{\mathrm{L}}^2}{\omega_{\mathrm{T}}^2} = \frac{\varepsilon_{\mathrm{s}}}{\varepsilon_{\mathrm{e}}} \tag{6.11}$$

we can appreciate the significance for ferroelectricity. As we will discuss in the following chapter a condition for the transition to the polar phase is that the static dielectric constant goes to infinity. Such an anomalously large dielectric constant stems from the fact that a very small applied field will alter substantially the displacement polarization near the ferroelectric transition. According to equation 6.11 this happens when the transverse optical mode ω_{T} approaches zero or when it 'softens':

$$\kappa_0' = \frac{(\varepsilon_{\mathrm{e}} + 2)(Z'e)^2}{9V\varepsilon_0}. \tag{6.12}$$

This condition implies that the crystal becomes instable with respect to the transverse optical mode. The phonon mode softens exactly when the short-range forces (κ_0', which favor the nonpolar paraelectric phase) are compensated by the long-range Coulomb forces (right-hand side of equation 6.12, which favor the ferroelectric phase). Note that the crystal does not necessarily lose its stability for other eigenmodes. In particular we can see that the longitudinal mode (equation 6.10) never causes a crystal instability. Even though for alkali-halogenide the two forces are of the same order of magnitude, κ_0' is about twice as large as the Coulomb part, such that a complete compensation is impossible, however for $BaTiO_3$ one can show that such a compensation is feasible.

All above considerations have been based on a harmonic approximation. Anharmonicity, however, makes quantities like the volume of the unit cell V and Z', κ_0' linear dependent on temperature. Only for simplicity we take κ_0' to be independent of temperature and only the last term of equation 6.9 is responsible for the temperature variation. Accordingly we write:

$$1 - \frac{(\varepsilon_{\mathrm{e}} + 2)(Z'e)^2}{9V\kappa_0'\varepsilon_0} = \frac{\mu\omega_{\mathrm{T}}^2}{\kappa_0'} = \gamma(T - T_{\mathrm{C}}), \tag{6.13}$$

where γ is a temperature coefficient of the same order of magnitude as the volume coefficient of expansion, and T_{C} is the temperature where the crystal just becomes unstable. Curie-Weiss law follows with equation 6.9 and equation 6.11:

$$\varepsilon_{\mathrm{s}} = \varepsilon_{\mathrm{e}} + \frac{(\varepsilon_{\mathrm{e}} + 2)^2(Z'e)^2}{9Vk_0'\gamma(T - T_{\mathrm{C}})}. \tag{6.14}$$

From these relations the connection to thermodynamic theory may easily be established, however, this will not be pursued here. The thermodynamic theory of ferroelectricity will be introduced in the next section.

It may be helpful to reexpress the above considerations with the following microscopic mean field theory: the diatomic solid in the paraelectric phase has the ions equally spaced, such that a small displacement of the ions with charge $\pm eZ'$ relative to each other by the amount ξ induces a polarization P (chapter V, M. Born [144]):

$$P = \frac{1}{V}(Z'e\xi + \alpha_{\mathrm{e}} E_{\mathrm{loc}}) \tag{6.15}$$

where α_{e} is the electronic polarizability of the ion and again only the negative ions are considered to be polarizable. Substituting the local field for a transverse mode of vibration as given in equation 6.3 and solving for P, we get:

$$P = \frac{Z'e\xi/V}{1 - \alpha_{\mathrm{e}}/(3\varepsilon_0 V)} = \frac{1}{V}\xi Z^*. \tag{6.16}$$

Here we introduced the transverse effective charge, or Born effective charge Z^*, which measures the average electric dipole moment per unit cell V generated by the corresponding relative ion displacement ξ . If such a phonon goes 'soft' and acquires a finite frozen amplitude ξ_0, then $\xi_0 Z^*/V$ is the approximate (to linear order $O(\xi)$) macroscopic ferroelectric polarization. Because of the polarizability of the ion, the Born charge Z^* is larger than the bare charge, and if

$$\frac{\alpha_{\mathrm{e}}}{3\varepsilon_0 V} = 1 \tag{6.17}$$

the denominator vanishes and the induced polarization diverges. This is called the polarization catastrophe and marks the onset of the ferroelectric instability. Rewriting equation 6.6 with equation 6.7 in terms of α_{e} we find that the identical condition as given in equation 6.17 leads to the crystal instability for the transverse optical mode. In other words for a diatomic crystal the term 'instability' and 'polarization catastrophe' are synonymous.

6.1.2 Landau-Devonshire Theory

Based on symmetry considerations Landau Theory [206–208] can provide a reliable description of a system's equilibrium behavior near a phase transition. To ferroelectricity it was first applied by Devonshire [209–211]. Landau characterizes a phase transition in terms of an order parameter, a physical quantity that is zero in the high symmetry (disordered) phase and changes

to a finite value if the symmetry is lowered. For the case of a paraelectric-ferroelectric transition this order parameter is the polarization P. The free Energy $\mathcal{F}$ is then expanded as a power series around the transition point and the state of the system is found by minimizing the free energy $\mathcal{F}(P)$ with respect to P. This somewhat surprising ansatz, namely that a singular behavior associated with a transition can be described by a regular expansion, works also because the value of the order parameter itself is temperature dependent and a singular function of the expansion coefficients. Nonetheless we may expect that the powerlaw breaks down close to the transition and that its validity needs to be checked experimentally. The variables which describe the equilibrium state of the bulk ferroelectric includes temperature (T), polarization (P), the electric field (E), strain (η), and stress (σ). For simplicity we restrain the discussion to one-axial ferroelectric materials. If we also postpone the influence of strain and stress on ferroelectricity to section (6.1.4), we can write for the free energy $\mathcal{F}$:

$$\mathcal{F}_{\mathrm{P}} = \frac{1}{2}aP^2 + \frac{1}{4}bP^4 + \frac{1}{6}cP^6 - EP \tag{6.18}$$

where the power series is truncated at the sixth term. The coefficients a_0 and c are always positive and the parameter a is proportional to T and can be written as $a = a_0(T - T_{\mathrm{C}})$ with the transition temperature T_{C}. Due to symmetry (the free energy should not depend whether we have $+P$ or $-P$) we only consider even terms. Below the transition point the value of P is adjusted such that $\mathcal{F}$ has the smallest possible value. With the order parameter having a macroscopic physical interpretation, equally the derivatives of the thermodynamical potentials ($\mathcal{F}$) with respect to the order parameter P correspond to macroscopic physical quantities, namely:

$$\frac{\partial \mathcal{F}_{\mathrm{P}}}{\partial P} = E \qquad \text{electric field} \tag{6.19}$$

$$\frac{\partial^2 \mathcal{F}_{\mathrm{P}}}{\partial P^2} = \frac{1}{\chi} \qquad \text{reciprocal dielectric susceptibility} \tag{6.20}$$

The nature of the transition is now determined by the sign of the parameter b. If $b > 0$ then a second order transition occurs at the Curie temperature $T = T_0 = T_{\mathrm{c}}$ and the free energy evolves continuously as a function of temperature from the first schematic ($P = 0$) in figure 6.2 a) to the second, that has a minima at the finite polarizations $P = \pm P_0$. Minimizing F ($\partial F_{\mathrm{P}}/\partial P = 0$), setting $E = 0$ and retaining only the highest order terms we can estimate the spontaneous polarization to be:

$$P_0 = \pm\sqrt{\frac{a_0}{b}(T_{\mathrm{C}} - T)}. \tag{6.21}$$

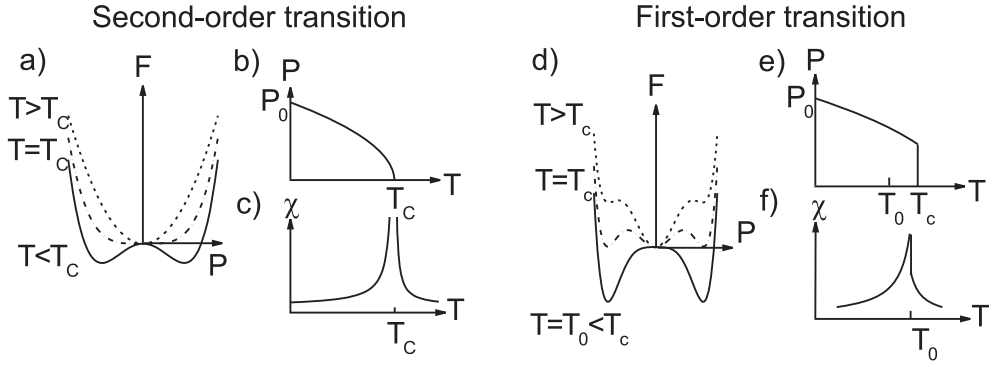

Figure 6.2: **a**) Free energy as function of polarization below at and above the phase transition. **b**) Order parameter P for a second order phase transition as a function of temperature **c**) Typical ferroelectric behavior of the dielectric susceptibility as a function of temperature. **d**) Free energy for a discontinuous transition. **e**) The order parameter changes abruptly at $T = T_c$ for a first order transition. **f**) The dielectric susceptibility remains finite at $T = T_c$, even theoretically. Compare [127].

The spontaneous polarization P_s decreases with a square root dependence with increasing temperature [compare figure 6.2 b)]. The negative and positive sign correspond to the energetically degenerate cases of an up and down orientation of P_s. This allows the build-up of anti-parallel domains.

The dielectric function ε or dielectric susceptibility χ usually shows a very pronounced maximum at the phase-transition temperature. This may serve as an evidence for a ferroelectric transition, which can be conveniently probed with optical means. The theoretical behavior of the dielectric susceptibility is shown in figure 6.2 c). For example in $SrTiO_3$, the real part of the dielectric function ε reaches very high values of almost 24000 below 10 K, and serves as a sign for its polar instability [57].

If the quartic coefficient b in the expansion 6.18 is negative the transition is called *first-order* or discontinuous. Now the free energy may have a subsidiary minimum even for $T > T_0$ at non-zero polarization P. If the temperature is reduced this minimum drops in energy below that of the unpolarized state, and so does the thermodynamically favored configuration. This temperature is defined as the Curie temperature T_C, which, however, now exceeds T_0. Between T_0 and T_C the unpolarized phase exists as a local minimum of the free energy. The most important aspect of a first-order transition is that the order parameter jumps discontinuously to zero at T_C. Solid-liquid transitions are common examples of a discontinuous transition.

In figure 6.2 d), e), f) the free energy, the order parameter P and the susceptibility is schematically plotted for first order transitions.

Finally it is important to note that the Landau-Devonshire theory is a mean field theory. It is assumed that every ion in a double well in the crystal interacts with every other such ion equally, independent how far away it is. Even though this may be a somewhat crude and unphysical approximation, it allows us to replace all ions except one with an average or mean field, making the very complicated mathematics solvable. Since for ferroelectrics the interactions are mainly coulombic, dropping off slowly as $1/r$, the interactions are very long range, and the nature of these system are indeed mean field. Also, since the Landau theory is strictly a macroscopic approach, it cannot predict any microscopic physics like atomic displacements etc. The coefficients in the expansion equation 6.18 can either be determined experimentally, for example, by measuring the dielectric function as a function of temperature, or by first principle calculations.

6.1.3 Coupling between Tetragonal Strain and Polarization

The coupling between strain and polarization is particularly pronounced in the ferroelectric material $PbTiO_3$. It has been shown by fist principle calculation that the hybridization of lead and oxygen causes a large strain that stabilizes the tetragonal phase [212]. If a cubic crystal (for example, $PbTiO_3$) undergoes a ferroelectric phase transition with the polarization pointing along the 3-direction, the symmetry is broken and we expect a tetragonal distortion $\eta_3 = \eta = c/a$ along the same direction. Due to the symmetry of the transition the lowest order coupling is of of order ηP^2 (rather than ηP or $\eta^2 P$), such that the free energy is of the following form:

$$\mathcal{F}_\eta = \frac{1}{2} K \eta^2 + Q \eta P^2 - \eta \sigma. \tag{6.22}$$

The first term simply represents Hooke's law, or that the elastic energy stored in a solid is quadratically dependent on the distortion, K is the elastic constant. Here Q denotes some proportionality constant [1]. The total free energy consists of the terms 6.18 and 6.22:

$$\mathcal{F} = \mathcal{F}_\mathrm{P} + \mathcal{F}_\eta = \frac{1}{2} a P^2 + \frac{1}{4} b P^4 + \frac{1}{2} K \eta^2 + Q \eta P^2 - \eta \sigma \tag{6.23}$$

[1] Please compare the references [213, 214] for more details on the appropriate proportionality constants

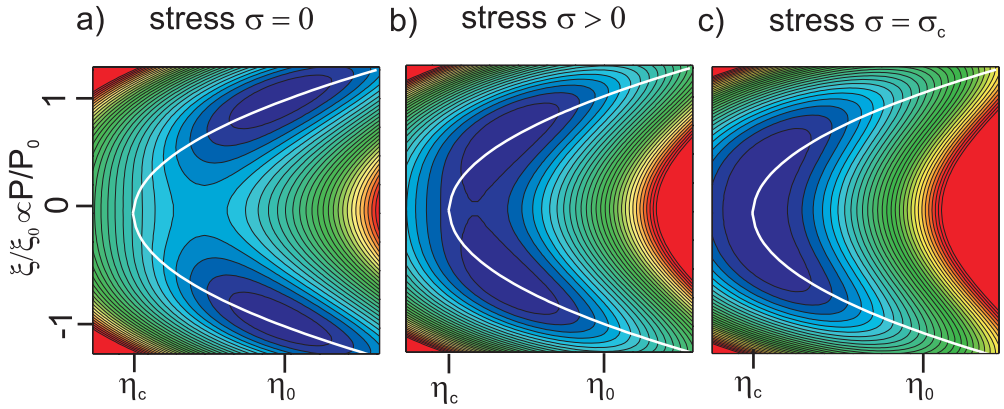

Figure 6.3: The anharmonic potential surface as a function of tetragonal distortion η and polarization P/P_0. The equilibrium positions of the minima for different external stresses lie on the white line. **a**) No external stress defines the starting value η_0 and $P = \pm P_0$. **b**) Reduced values of η and P for a finite stress. **c**) For a critical stress σ_c we can define a critical distortion η_c where the polarization vanishes.

This defines the equilibrium free energy surface as a function of both strain η and polarization P. The equilibrium is again obtained by minimizing $\mathcal{F}$ with respect to both P and η, that is,

$$\frac{\partial \mathcal{F}(P,\eta)}{\partial P} = \frac{\partial \mathcal{F}(P,\eta)}{\partial \eta} = 0. \tag{6.24}$$

In figure 6.3 the energy surface equation 6.23 is plotted for three different external stresses σ. For no stress the minima are found at η_0 and $P/P_0 = \pm 1$. For increasing stress the minima move along the white line and finally in figure 6.3 c) a critical stress corresponds to a critical strain η_c where the polarization vanishes. Please note that the white line is calculated with condition 6.24 and yields a square-root dependence of polarization as a function of strain. Also note that the effect of external stress corresponds to adding a tilted plane $-\eta\sigma$ to the potential surface $\mathcal{F}$. With equation 6.16 we can relate the relative polarization change P/P_0 to a shift of the ion position ξ/ξ_0 within the unit cell, such that the properties of the ferroelectric system are now characterized by the two phonon modes η and ξ. Or in other words, the function of a ferroelectric system, that is, the polarization, is linked to the atomic structure, which is directly accessible by X-ray diffraction.

6.1.4 Ferroelectricity in Thin Layers and Heterostructures

The physical properties of ferroelectric thin films can be substantially different from those of bulk ferroelectrics. The most important aspects which need to be considered in thin layers of ferroelectric materials are mechanical (strain) and electrical (screening or depolarization fields) boundary conditions, apart from practical issues concerned with sample quality. In the framework of the phenomenological theory by Ginzburg-Landau-Devonshire size effects are expected due to a disturbed balance between short- and long-range forces in very small volumes (or compare Cochran equation 6.12). This chapter starts with a discussion of how epitaxial in-plane strain and ferroelectricity are coupled and alter the thermodynamic potential. Further we will introduce the effect of screening and comment on recent developments in the field of nano-layered ferroelectric oxides.

Misfit Epitaxial Strain

Let us consider a thin film grown epitaxially on a thick substrate (compare figure 2.3: the in-plane strain are constant throughout the film and are completely controlled by the substrate-film lattice mismatch. The associated stresses are finite, by contrast there are no constraints on the film surface such that stress along the growth direction is zero. In the present work the special case of a (001) ferroelectric film grown on top of a cubic paraelectric substrate is studied. This implies $\bar{\eta} = a - a_0/a$, where a and a_0 are the constrained (substrate) and the free film in plane lattice constants, respectively. The sought thermodynamic potential F is given by the following Legendre transformation [215, 216]:

$$\tilde{\mathcal{F}} = \mathcal{F} + \sum_{\text{in-plane } \sigma} \bar{\eta}\sigma. \tag{6.25}$$

For the 2-D clamping case with $\sum_{\text{in-plane } \sigma} \partial\tilde{\mathcal{F}}/\partial\sigma = 0$ we can show that both the quadratic and quartic polarization are renormalized [213, 214]. Whether the transition temperature is increased or decreased depends on the sign (and magnitude) of the elastic and electrostrictive coefficients.

Recent work showed that the transition temperature of $BaTiO_3$ can be raised from 120 to above 700 degree Celsius by strain engineering [128]. The biaxial strain of up to 1.7% was set by using different substrates for the growth of the thin ferroelectric $BaTiO_3$ layers. A combination of X-ray, second-harmonic generation and hysteresis measurements unambiguously showed a significantly increase of the transition temperature. In the

same year it was reported that ferroelectricity can be induced in strained $SrTiO_3$ layers, a material which is not ferroelectric at any temperature [217]. Apparently strain, induced by thin film growth, alters the thermodynamic potential such that care has to be taken when defining, for example, the Curie temperature.

Depolarization Effects

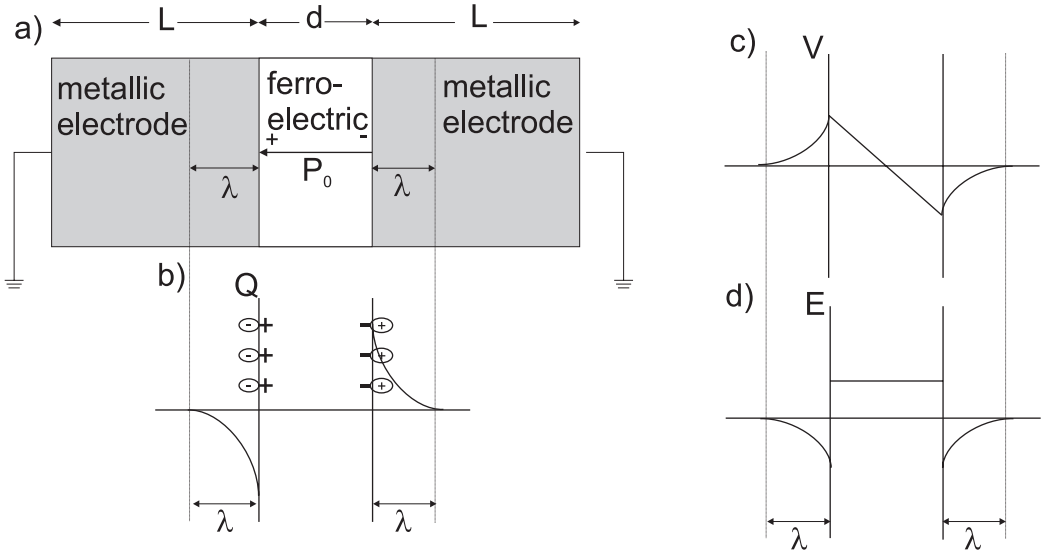

Figure 6.4: **a**) A thin ferroelectric film with polarization P_0 sandwiched between two metallic electrodes with screening length λ. **b**) Associated charges Q: a perfect electrode with screening charges at the surfaces and for an realistic electrode with screening charges displaced from the interface over the length λ. **c**) Corresponding voltage and **d**) depolarization field E_d for a realistic electrode [218].

The predominant role of electrostatic boundary conditions in controlling ferroelectricity in very thin films has recently been demonstrated from first principles [219–221]; even though the idea of imperfect screening has been put forward as early as 1973 in the framework of Ginzburg-Landau-Devonshire theory [222, 223]. In a geometry where the polarization is normal to the boundary, one expects a build-up of free surface charge that, if uncompensated, results in a depolarizing field E_d. If we sandwich the thin ferroelectric layer between two metal electrodes, they can provide charge compensation and the effect of depolarization can be significantly reduced. However, in realistic electrodes the screening charges are distributed over a small but fi-

nite region as shown in figure 6.4. This results in screening charges in the metal plates which are displaced from the interfaces. For a short-circuited ferroelectric capacitor, this spatial charge distribution creates finite dipoles at the interfaces and leads to an associated voltage drop

$$\Delta V = \frac{\lambda_{\text{eff}}}{\varepsilon_0} P \tag{6.26}$$

at each interface [figure 6.4]. To ensure that the whole structure is equipotential a compensating depolarization potential is necessary [222], leading to an associated finite depolarization field in the film, as shown in figure 6.4

$$E_{\text{d}} = -2\frac{\Delta V}{d} = -2\frac{\lambda_{\text{eff}}}{d\varepsilon_0} P, \tag{6.27}$$

where d is the thickness of the film. The parameter λ_{eff} has the dimensions of a length and is referred to as the *effective screening length of the system*. A smaller screening length implies better surface charges screening and a more stable ferroelectric phase. Also the depolarization field increases with decreasing film thickness and eventually suppresses ferroelectricity. This metal-ferroelectric-metal geometry may also try to avoid the depolarization field by forming a ferroelectric domain structure [224]. It should be emphasized that this model of the ferroelectric electrode is highly idealized. Surface molecules and the nature of the bonding at the interface are important factors in how well a ferroelectric can retain its properties as its size is reduced [225]. Nonetheless this simple electro static model is helpful and leads to a modification of the expression for the free energy (equation 6.18) by including the term $-E_{\text{d}}P$ which yields with equation 6.27 [226]:

$$\mathcal{F} = \mathcal{F}_{\text{bulk}} + \mathcal{F}_{\text{depolarization}} = \mathcal{F}_{\text{bulk}} - \frac{2\lambda_{\text{eff}}}{d\varepsilon_0} P^2. \tag{6.28}$$

As expected the quadratic term of the free energy is renormalized, resulting in a reduced critical temperature and suppression of ferroelectricity. It is illustrative to discuss the depolarization effects envisaging the potential surface $\mathcal{F}(P, \eta)$ 6.23, introduced in the previous chapter. The double minimum of the potential surface eventually vanishes with increasing λ_{eff} or decreasing thickness d. Comparing with figure 6.3, we note that differently the effect of the depolarization field is now a smaller contribution of the negative parabola $\propto P^2$. It results in a direct relationship between the re-normalized negative parameter $a \propto T, \lambda_{\text{eff}}, \eta \ldots$ and the polarization P. This together with the established *static* connection between P and η is plotted in figure 6.5. With these simple arguments from thermodynamical theory we can understand

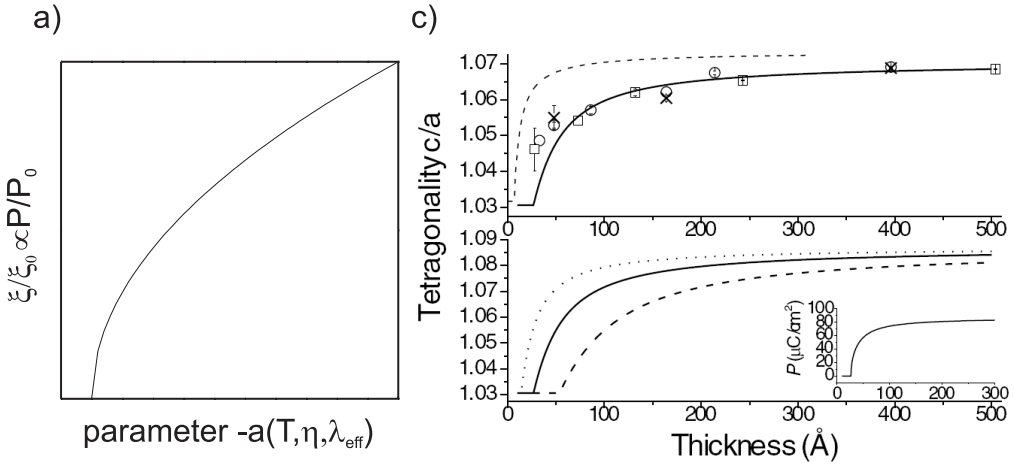

Figure 6.5: The evolution of P/P_0 as a function of the **a**) parameter a, for example, depolarization field, and **b**) as a function of strain, compare white line in figure 6.3. **c**) Evolution of the c/a ratio with the film thickness. Experimental data and model calculation for different screening length λ_{eff}. Inset: thickness dependence of polarization P from model Hamiltonian. From [226].

that the measurement of $\eta = c/a$ may serve as a probe for the polarization. Note that this is a relation which holds in equilibrium, whether this is still true on ultrafast time-scales will be explored in the following. The results of such measurements for $PbTiO_3/SrRuO_3$ systems with different film thicknesses are shown in figure 6.5 c), [226]. The findings show a decrease of the c-axis with decreasing $PbTiO_3$ thickness, suggesting a decrease of the polarization due to depolarization fields. A pronounced drop of the tetragonality η is found for thicknesses below ≈ 100 Å. The best fit to the experimental data revealed an effective screening length of $\lambda_{\text{eff}} = 0.12$ Å for $SrRuO_3$. This in combination with piezoelectric response measurements proved that films with thickness below 50 Å remain ferroelectric at room temperature. Another accurate and element specific method to probe the tetragonal distortion and ion displacement in very thin films is X-ray photoelectron diffraction. This was successfully used to show that films as thin as three unit cells still preserve a ferroelectric polar distortion [227].

Ferroelectricity in Superlattices

Apart from beneficial properties concerning X-ray diffraction (compare chapter 2.5) growing superlattices is an interesting way to create artificial materials with novel electronic and structural properties. Examples of studies where superlattices showed unusual properties include layers of $BaCuO_3$ and

$SrCuO_3$ exhibiting superconductivity, even though neither of these oxides is superconducting itself [228], or thin layers of $SrZrO_3$ and $SrTiO_3$ exhibiting ferroelectricity, even though neither of these two oxides is ferroelectric by itself [229]. Inspired by theoretical calculations [230] that tricolor superlattices should exhibit enhanced ferroelectric properties, in particular, an asymmetric double well potential due to the loss of inversion symmetry, it was demonstrated recently that it is possible to assemble an atomically sharp superlattice consisting of three different building blocks [231, 232]. This tricolor superlattice showed a 50 percent increase of polarization and showed that a single unit cell of $BaTiO_3$ remains ferroelectric in a dielectric environment. First principle studies [233] suggests that in $BaTiO_3/SrTiO_3$ superlattices both layers are polarized such that the polarization is approximately uniform throughout the whole structure. This may be understood in terms of a large electrostatic energy penalty for a build-up of charge at the interfaces in case of discontinuous polarization. This was experimentally verified in $PbTiO_3/SrTiO_3$ superlattices [234]. Additionally they found an unexpected recovery of the tetragonal distortion and polarization for layer thicknesses below 3 unit cells of $PbTiO_3$, which may be related to the precise nature of the substrate-superlattice interface or some degree of intermixing at the superlattice interfaces.

6.2 Characterization of the PZT/SRO Superlattice Sample

The $PbZr_{0.2}Ti_{0.8}O_3/SrRuO_3$ (PZT/SRO) superlattice (SL) sample studied here was fabricated in the Max-Planck-Institute for the Physics of Microstructures, Halle, by pulsed-laser deposition employing a KrF excimer laser ($\lambda =$ 248 nm) [235]. A $SrRuO_3$ layer was deposited on single crystalline $SrTiO_3$ (001) (STO) substrate (miscut angle 0.25°) at a temperature of $T = 980$ K in a background atmosphere of $P = 100$ mTorr oxygen. Subsequently $N = 15$ alternating layers of $d_{PZT} \approx 5$ nm thick PZT and $d_{SRO} \approx 6$ nm thick SRO layer were grown on top with their c axis parallel to the SL stacking axis (T = 850 K, $P = 200$ mTorr oxygen and $T = 980$ K, $P = 100$ mTorr, respectively). The ratio of Zr vs. Ti ions was chosen to match the in-plane lattice constant of PZT with SRO.

The measured stationary X-ray reflectivity (green line) and a simulation based on dynamical X-ray diffraction theory (black line, compare chapter 2.7.3) are shown in figure 6.6 a). The dotted lines are the calculated envelope functions of PZT and SRO and the dashed line is the envelope function

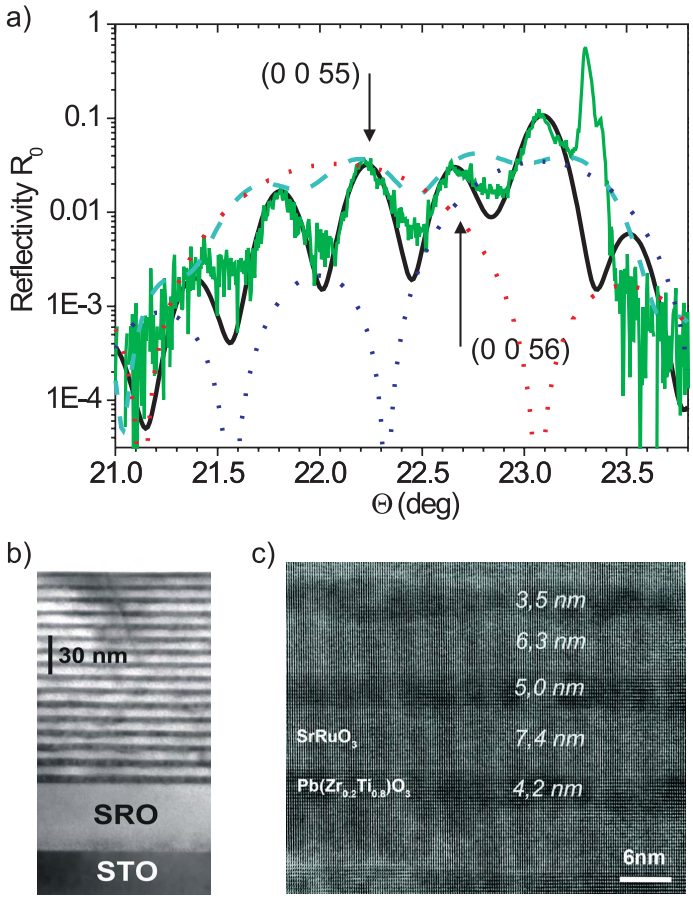

Figure 6.6: **a**) Measured (green line) and simulated (black line) stationary x-ray reflectivity of the PZT/SRO superlattice as a function of the Bragg angle θ. Also shown are the envelope function of PZT (dotted, red line), SRO (dotted, blue line) and of one double layer PZT/SRO (dashed, cyan line). The STO substrate peak is at 23.3° and the peak of the SRO bottom electrode is at 23.1°. Low **b**) and **c**) high resolution TEM image of a thinned PZT/SRO SL

of the double layer PZT/SRO. Note that this is the sum of the scattered amplitudes of the single layers and not the sum of their intensities. One can clearly identify the strong reflection from the $SrTiO_3$ substrate at 23.3° and the broad reflection at lower angles (23.1°) from the bottom $SrRuO_3$ electrode. The four to five peaks at smaller angles are due to the superlattice periodicity. Following the detailed explanation in section 2.5 we can derive the structural parameters averaged over the equilibrium SL structure from

the angular positions and intensities of the SL Bragg peaks. Additionally we assume that the lattice constants of the SRO layers $c_{SRO} = 3.93$Å in the SL agree with the value for a pseudocubic thin film [236]. The superlattice periodicity d_{SL} is derived from the precisely known Bragg angles. The other parameters are gained from the best fit of the theory to the data. As the oxygen atoms make a minor contribution to the diffraction pattern, similar to other structure studies [237], we assume $\xi_{Pb-Ti/Zr} \propto \xi_{Pb-O} \propto \xi_{Ti/Zr-O}$ and use $\xi_{Pb-Ti/Zr} = \xi_{Pb-O} - \xi_{Ti/Zr-O}$ as the soft mode elongation. In Table 6.1 the structural equilibrium parameters are summarized. Without going through more intricate analysis we can already make the following important observations: First, due to the relatively large tetragonal distortion of PZT the two single layer envelope functions are fairly well separated, which implies that the intensity of the (0055) reflection of the SL is mainly governed by the properties of PZT (changes within its unit-cell). Secondly, the (0056) reflection is positioned at the slope of both envelope functions and its intensity depends very sensitively on their position or in other words on changes of the c-axis, i.e on their respective tetragonal strains.

parameter	value (nm)
d_{SL}	11.21
d_{SRO}	6.29
d_{PZT}	4.92
c_{SRO}	0.393
c_{PZT}	0.410
$\xi_{Ti/Zr-O}$	0.024
ξ_{Pb-O}	0.038
a_{SRO}=a_{PZT}	0.393
η_0=c_{PZT}/a_{PZT}	1.024

Table 6.1: Parameters describing the equilibrium structure of the PZT/SRO superlattice

6.3 Time Resolved X-Ray Data

Even though the first successful experiments where performed without an X-ray mirror, the data which are presented in the following have been measured with the Osmic multilayer X-ray optic, in a setup schematically shown in figure 3.2 a). The excitation wavelength was chosen to be 800 nm, with a photon energy low enough to ensure that it exclusively interacts with the

metallic SRO layers. Due to the fairly large mosaicity of the superlattice sample the diffracting area is minimized either by covering part of the sample with a thin copper foil or by putting the sample close to the X-ray mirror focus. This avoids an additional reduction of the temporal resolution due to the non-collinear pump and probe beams. For small time delays we use the strong Bragg reflection of the STO substrate for normalization, for longer time delays a part of the SL reflection unaffected by the pump pulse is used for normalization. All measurements are an average of at least two scan in the forward and backward direction. The average integration time per delay point was between 60 and 120 seconds. This ensures that the error due to the counting statistic remains below 1%, corresponding to about 10.000 photons, reflected off the excited part of the sample. Time-delay zero is accurately determined by comparison with optical data (compare chapter 3.3.1 and chapter 5.3.1).

Figure 6.7 a)- d) shows the transient change of the (0 0 56) reflection after photoexcitation at $t = 0$ for 4 different excitation fluences. The signal shows a oscillatory behavior with a period of 2 ps. The very small difference in oscillation period is due to sample inhomogeneities. Consecutive measurements on the exact same spot of the sample show a constant period, independent of the pump intensity. The first maximum of the positive reflectivity change is reached after 1.5 ps and reaches up to 300% for the highest excitation fluence. Figure 6.7 e) shows the fluence dependence of the peak reflectivity change of the (0 0 56) reflection around t $\approx$ 1.5 ps. The red points correspond to the transients plotted in the same figure. The time-dependent reflectivity curves for the additional black points are not shown. The two lower plots [figure 6.7 f) and g)] compare the optically induced reflectivity changes of the SL reflections (0 0 55) and (0 0 56). One observes distinctly different behavior for the same excitation densities. While the (0 0 56) reflectivity increases, as already discussed, the (0 0 55) reflectivity decreases. The amplitude of the change is significantly smaller and after the first oscillation the sign of the reflectivity reaches positive values. We can also see that the first minimum is reached slightly earlier than the corresponding maximum of the (0 0 56) reflection. Utmost care has been taken not to induce any temporal shift when changing the Bragg angles to Bragg match the two reflections. Also the two curves have been measured in direct succession. The same observations are true for a repeated measurement with higher excitation density shown in figure 6.7 g). Figure 6.8 shows the shift of the angular position of the (0 0 56) reflection as a function of time. After approximately 30 ps it reaches the maximal shift of $\Delta\theta/\theta_{\mathrm{Bragg}} = 2.5 \times 10^{-3}$. Note that the angular position of the SL-Bragg peak is constant for approximately the first 4 ps.

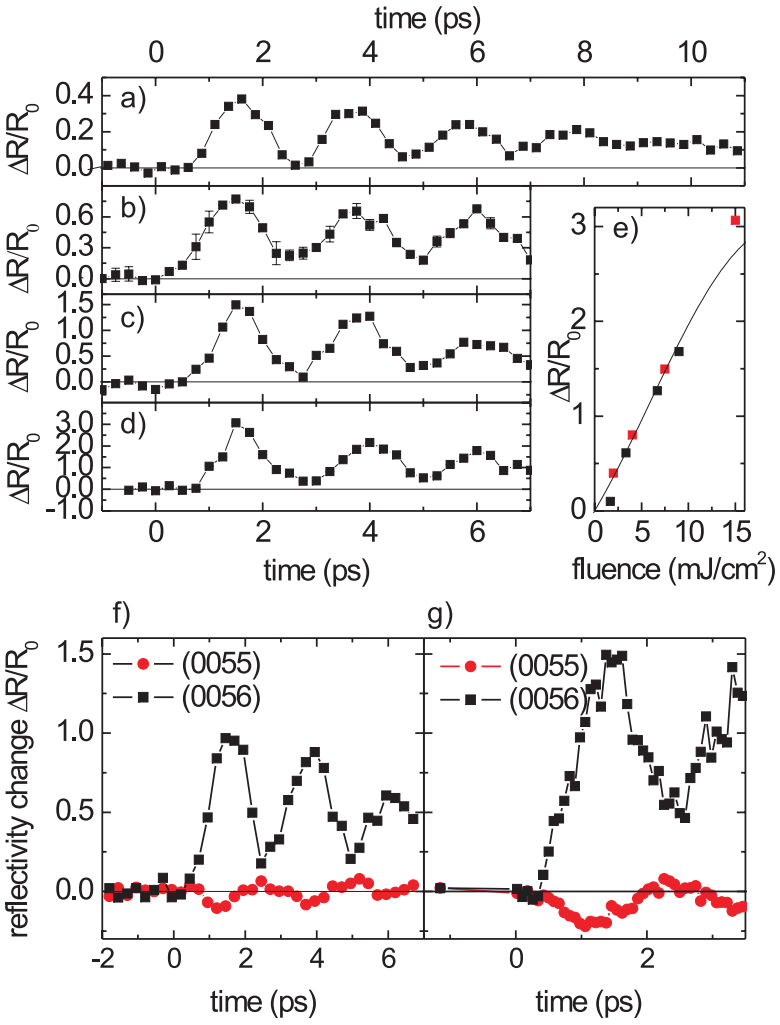

Figure 6.7: Measured X-ray reflectivity change of the (0056) reflection as a function of time for excitation fluences of **a**) 2 mJ/cm^2, **b**) 4 mJ/cm^2, **c**) 7.5 mJ/cm^2 and **d**) 15 mJ/cm^2. **e**) Fluence dependence of the peak reflectivity change of the (0 0 56) reflection around t $\approx$ 1.5 ps. The solid line indicates the calculated reflectivity change according to a linear fluence dependence of the tetragonal distortion. The red points correspond to the measured transients shown in the left panels. **f**) and **g**) Comparison of the time dependent X-ray reflectivity change of the (0 0 55) (red circles) and (0 0 56) (black squares) for two different excitation fluences.

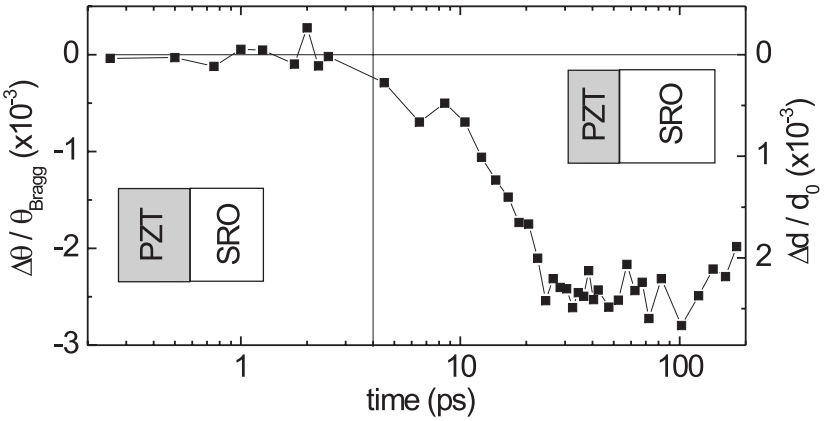

Figure 6.8: Relative angular shift of the (0 0 56) Bragg reflection for an excitation fluence of 5 mJ/cm^2. Right ordinate scale: corresponding change of the SL-period d_{SL}.

6.4 Discussion: Ultrafast Time-Resolved X-Ray Structure Analysis

Superlattice Phonon Motion

We now discuss the structural dynamics of the SL sample giving rise to the X-ray reflectivity changes shown in figures 6.7 and 6.8. The 50 fs pump pulse interacts primarily with the electrons in the metallic SRO layers and generates an electronic excitation spatially modulated with the SL periodicity d_{SL}. The excited electrons lead to an build-up of an (incoherent) phonon population, the predominant source of stress at room temperature. (Refer to the detailed discussion of the stress generation in SRO in chapter 5). This creates uniaxial stress spatially modulated with the same periodicity. Such stress drives a SL phonon mode, that is, a strain wave, with a wave vector g_{SL}, corresponding to the wave vector k = 0 in the folded Brillouin zone ([11, 62], also compare chapter 2.9.1). Stress is generated on a time scale short compared to the vibrational period $T = 2$ ps of the SL phonon mode and thus launches a coherent superposition of acoustic phonon states corresponding to a standing wave in the SL. This results in a modulation of the SRO and PZT layer thicknesses and - with the c axis of the layers and the SL stack axis being parallel - of the tetragonal distortions d_{SRO} and d_{PZT} with a period T. Such lattice motions manifest the oscillations of X-ray reflectivity. With help of figure 6.9 we may appreciate why the SL diffraction

peaks, in particular peak (0 0 56), show such a strong intensity modulation. The expansion of the SRO layer shifts its envelope to smaller angles (blue, shaded area) and the concomitant compression of PZT shifts its envelope to larger angles (red, shaded area). Since the SL peak (0 0 56) is positioned almost exactly at the steepest slope of these two functions, its reflectivity experiences a strong reflectivity increase. The series of figure 6.9 demonstrate how the SL phonon causes an overlap of the single envelope functions of SRO and PZT, which evidently results in an increase of the relevant double STO/PZT double envelope function (cyan, dashed line). This explains the large sensitivity of this particular SL-reflection to uniaxial strain. Note that the SL-reflection (0 0 55) is slightly reduced in intensity. To infer the exact dependence of the reflectivity change of different SL-Bragg peaks on η and ξ, we resort to a full calculation by dynamical X-ray diffraction theory [compare figure 6.10].

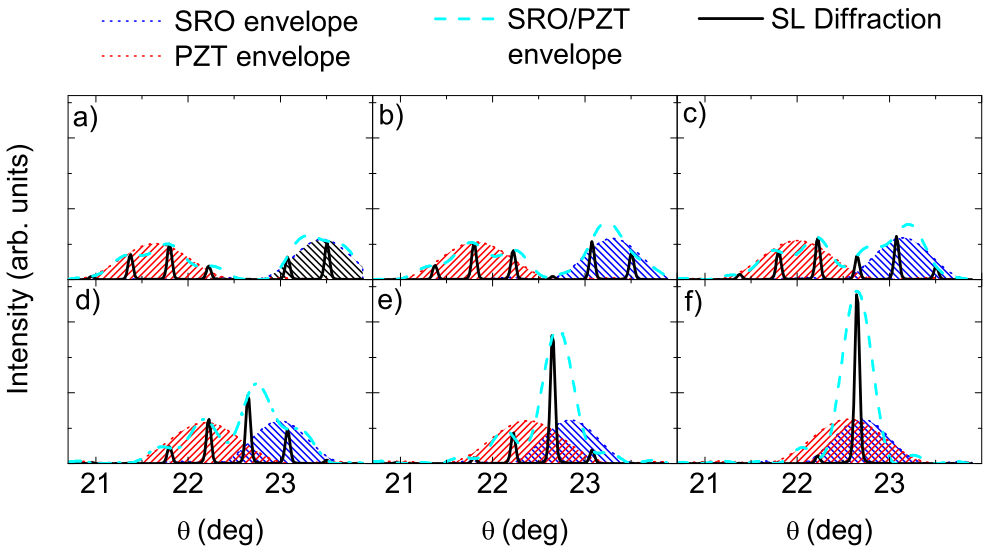

Figure 6.9: Calculated X-ray reflectivity change of the SL Bragg Peaks (black, solid line) together with the PZT envelope (red, filled area), SRO envelope (blue, filled area), SRO/PZT double layer envelope (cyan, dashed line). **a-f**) Starting from zero strain $\eta_0/\eta_0 = 1$ to maximal strain $\eta_{\max}/\eta_0 = 0.022$

The SL Bragg peaks occur at angular positions determined by the reciprocal lattice vectors $G = lg_{\mathrm{SL}}$. The data in figure 6.8 shows that these positions and, because of Bragg's law, d_{SL} remains unchanged during the first

4 ps after excitation. Thus, the SL oscillations during this time occur with a transient expansion (compression) of the SRO layers being compensated by a compression (expansion) of the adjacent PZT layers: $\Delta\eta_{\mathrm{PZT}} = \eta_{\mathrm{PZT}} - \eta_0 = -\Delta\eta_{\mathrm{SRO}} d_{\mathrm{SRO}} d_{\mathrm{PZT}}$. After this initial period, we observe the expansion of the entire SL structure by 0.24%. This expansion of the entire structure originates from strain fronts starting from the interfaces of the SL to air and to the substrate, where the stress is not balanced (compare chapter 4). Such strain fronts propagate with the sound velocities $\mathrm{v_{PZT,SRO}}$, leading to an expansion time of the entire SL (N = 15 periods) of $T_{\mathrm{exp}} = N d_{\mathrm{SL}} = v_{\mathrm{PZT,SRO}} \approx 30$ ps. As a result, the $\mathrm{d_{SL}}$ of most SL periods and, thus, the SL Bragg peak positions remain unchanged during the first 4 ps.

Coupled Lattice and Polarization Dynamics

The measurements of the two different Bragg peaks allow for a quantitative analysis of the microscopic lattice dynamics. To extract the momentary elongations along the two coordinates η_{PZT} and $\xi_{\mathrm{Pb-Ti}}$ from the time-resolved data, we first calculate the intensity change of the (0 0 56) and (0 0 55) SL peaks as a function of η_{PZT} and $\xi_{\mathrm{Pb-Ti}}/\xi_0$ [figures 6.10 a) and b)] for constant $\mathrm{d_{SL}}$ as observed up to delay times of 4 ps. Closer inspection of figure 6.10 a) supports the earlier more qualitative arguments, that the (0 0 56) reflection is mainly sensitive to changes in η. Especially for small strains the contour lines are almost perpendicular along the η direction, while changes of ξ have a negligible influence on the reflected intensity. For very large strains this changes and only with changes of ξ it becomes possible to explain the very large induced reflectivity changes. The intensity dependence of the SL reflection (0 0 55) on the two modes η and ξ is shown in figure 6.10 b) and evidently behaves differently. In particular around $\eta_{\mathrm{PZT}} = \eta_0$ and $\xi_{\mathrm{Pb-Ti}}/\xi_0$=1 its contour lines are nearly orthogonal such that changes in ξ influence its intensity. The analysis of the time-resolved reflectivity data to infer the structural dynamics of the two relevant modes may now be easily comprehended. A specific value of $\Delta R^{56}(t) = R_0^{56}$ measured in the time-resolved experiments corresponds to a calculated contour in figure 6.10 a), and $\Delta R^{55}(t) = R_0^{55}$ corresponds to a contour in figure 6.10 b). The intersection of the two contour lines gives the values of $\eta_{\mathrm{PZT}}(t)$ and $\xi_{\mathrm{Pb-Ti}}(t)/\xi_0$ for the time t, in this way defining a trajectory in $\eta - \xi$ space [black solid line in figures 6.10 a), b) and c)]. The time-dependence of η_{PZT} and $\xi_{\mathrm{Pb-Ti}}/\xi_0$ derived in this way is plotted in figure 6.11 b). The error bars are derived from the intensity fluctuations of the Bragg peaks taking into account the nonlinear transformation into η_{PZT} and $\xi_{\mathrm{Pb-Ti}}/\xi_0$. The anharmonic coupling of the directly driven tetragonal distortion η_{PZT} and the soft mode coordinate $\xi_{\mathrm{Pb-Ti}}$ results in a simultane-

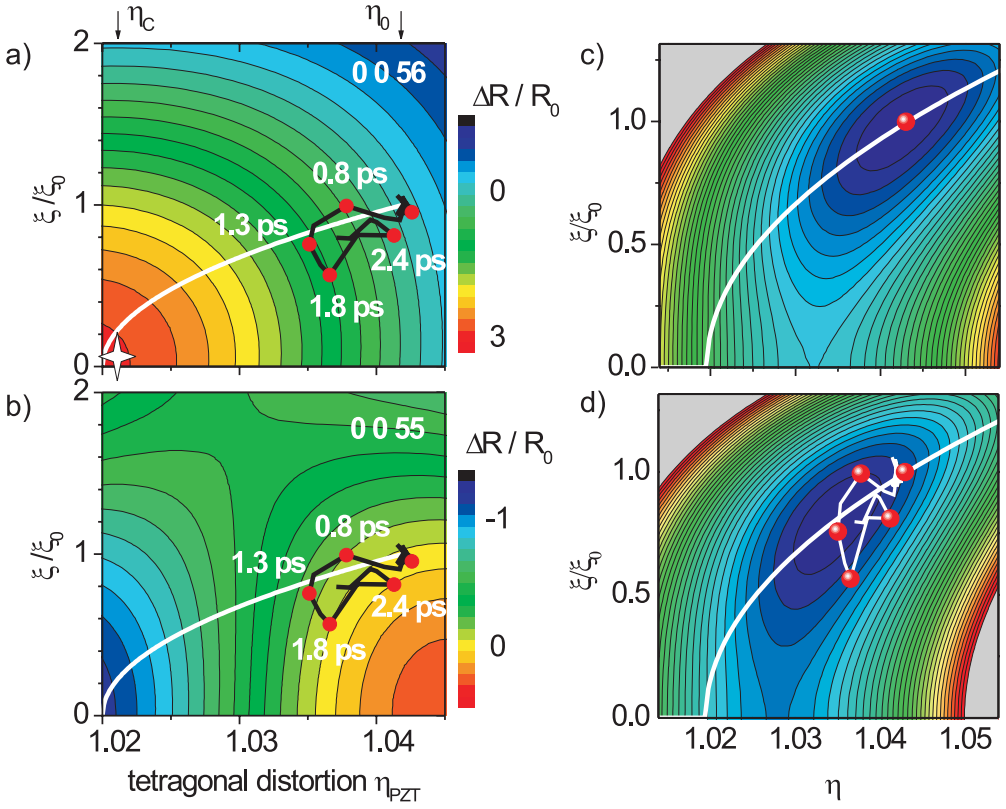

Figure 6.10: **a**) Contour plot of the calculated change of the (0 0 56) reflectivity as a function of the tetragonality η and the relative ion displacement ξ/ξ_0. Black line: trajectory derived from figure 6.11 b) with red dots indicating selected time delays. White star in lower left hand corner marks the largest measured reflectivity change of 300% and corresponds to a complete switch-off the polarization. **b**) Calculated reflectivity change of (0 0 55) as a function of η and ξ. **c**) Qualitative potential surface of the equilibrium structure as a function of the tetragonal distortion η and ion displacement ξ/ξ_0. **d**) Potential surface after ultrafast generation of stress with new potential minimum. Trajectory as shown in **a**) and **b**)

ous elongation of the latter and a change of the polarization P $\propto \xi_{\mathrm{Pb-Ti}}$. Inspection of Fig 6.11 b) shows that the tetragonal distortion η_{PZT} generates a 50 percent decrease of the soft mode elongation $\xi_{\mathrm{Pb-Ti}}/\xi_0$ and, thus, the ferroelectric polarization P on an ultrafast timescale. As mentioned earlier we consider only the two phonon modes η and ξ and assume that other polar-optical modes occurring at frequencies higher than 400 cm^{-1} [238] are not driven by the gradual build-up of stress in our experiment. Thus, the cor-

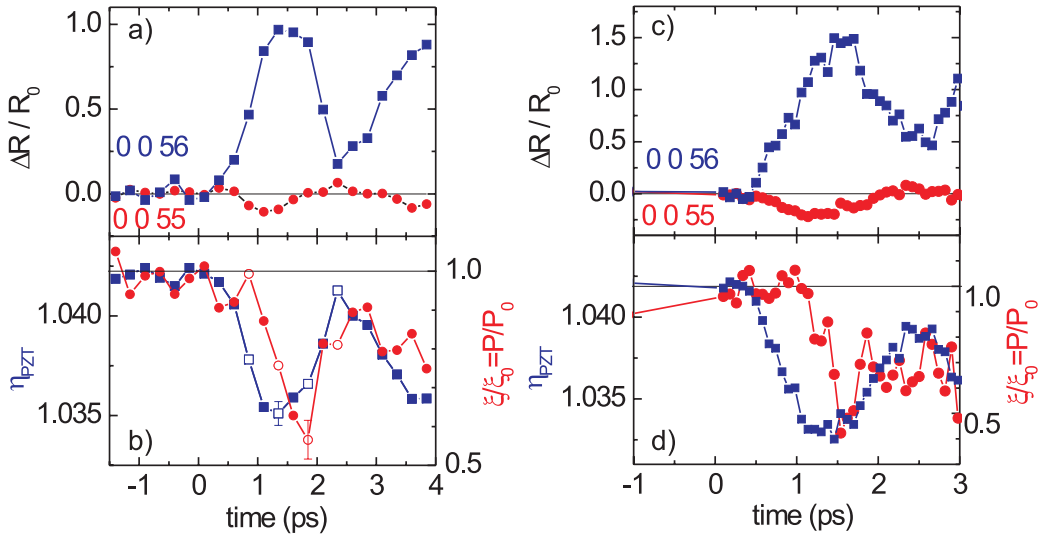

Figure 6.11: **a**) and **c**) as in figure 6.7. **b**) Derived transient change of the tetragonal distortion η(t) (blue squares) and soft mode elongation $\xi_{\mathrm{Pb-Ti}}$ (red circles) equivalent to trajectories in figure 6.10. Solid symbols are reproduced as as dots in figures 6.10 **a**) and **b**). **d**) Equivalent analysis for higher excitation density.

responding contributions to the *e*lectric polarization are absent. Note that this trajectory starts close to the white line (adiabatic application of stress, equation 6.23), with significant deviations after 1.3 ps due to the dynamic coupling of the two modes. For the highest excitation densities, and largest reflectivity changes we can immediately read off the values of η and ξ in the contour plot 6.10 a) for the SL Bragg peak (0 0 56). The white star in the lower left corner of figure 6.10 a) indicates the highest measured reflectivity change $\Delta R_{max}/R_0 = 3$ according to figure 6.7 d) (pump fluence 15 mJ/cm^2), and corresponds to a complete switch-off of the polarization $P \approx 0$. This defines the critical tetragonal distortion $\eta_{\mathrm{C}} = 1.02$, corresponding to a peak strain $\Delta\eta/\eta_0 = 0.022$ which is achieved by a stress of approximately 1 GPa, as estimated with the elastic constants $C_{11} = \rho \cdot v^2$ of PZT and SRO (ρ: mass densities). (Please compare discussion and references in chapter 4.)

Detailed inspection of figure 6.11 a) demonstrates that ξ/ξ_0 reaches its maximum change approximately $\tau_{\mathrm{P}} = 500$ fs after the maximum change of η_{PZT}, a behavior consistent with the shape of the potential energy surface [figure 6.10 c) and d)] of the two coupled modes: Around $\eta \simeq \eta_0$ where vi-

brational motion starts, the narrow potential well along ξ allows for small changes of $\xi_{\mathrm{Pb-Ti}}$ with a comparably high frequency only. During the compression η reaches larger values and the potential along ξ widens and softens, now allowing for a stronger changes in this coordinate with a lower frequency. The additional delay in $\xi_{\mathrm{Pb-Ti}}$ represents the fraction of the soft mode period required to reach the maximum change.

Note that the potential surface shown in figure 6.10 c) and d) is only a qualitative approximation. Only scarce quantitative data is available, one example is the work for bulk $PbTiO_3$ [212]: the presented ab initio calculations determined the depth of the double well potential of the high temperature phase (70 meV) and the large stabilizing strain of the tetragonal structure ($\eta = 1.06$) with a well depth of approximately 200 meV. But note that $PbTiO_3$ undergoes a continuous, second order phase transition under (hydrostatic) pressure at room temperature [201, 239]: here the double well structure vanishes. In the superlattice structure one has to consider biaxial strain due to the growth condition, reduction of polarization due to the finite screening length of $SrRuO_3$ and that twenty percent of the Ti-atoms are replaced by Zr-atoms. As discussed in detail in the introductory section 6.1.3 and 6.1.4 these have a significant impact on the absolute value of polarization. To construct a quantitative potential as a function of the two coordinates remains a challenge for future work [2]

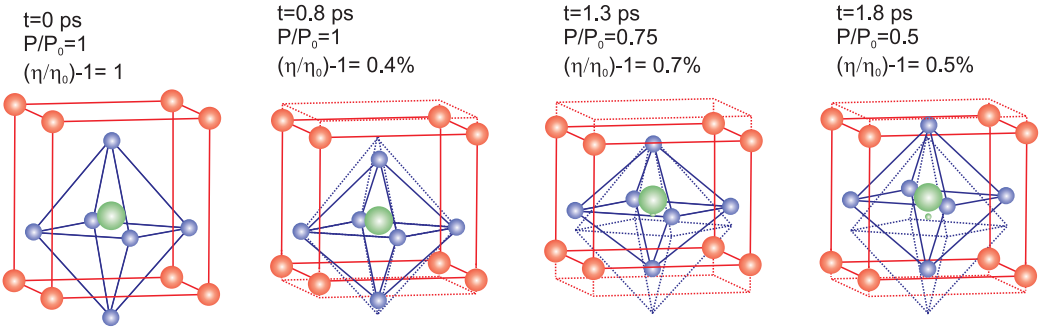

Figure 6.12: Schematic of the coupled dynamics of PZT after launching a lattice excitation in SRO. Atomic displacements are exaggerated. Importantly, the positions of the oxygen atoms have not been determined by the experiment.

Figure 6.12 schematically shows the evolution of one PZT unit cell af-

[2] After the completion of this work, a first-principle-based calculation directly addressed the experimental results presented in this chapter [240]. All our experimental findings could be successfully explained by a 'slow breathing' of dipolar inhomogeneities in highly inhomogeneous dipole patterns.

ter optical excitation at $t = 0$. The tetragonal distortion η is reduced towards a more cubic structure, followed by a delayed movement of the titanium/zirconium ion. The numbers for P/P_0 and $\eta/\eta_0 - 1$ are taken from the measurement shown in figure 6.11 a), but for clarity the plotted atomic displacements have been greatly exaggerated. Importantly, even though the oxygen atoms are shown in the schematic, their time dependent positions have not been measured in the diffraction experiment.

In conclusion, we have presented an ultrafast structural characterization of lattice and polarization dynamics in ferroelectric nanolayers, where a pair of Bragg reflections was chosen to derive the trajectory of the two coupled modes (η and ξ) that are relevant for the ferroelectric polarization P. Optical excitation generates stress of 1 GPa leading to a strong suppression of the ferroelectric polarization, which can even be completely switched off. This work shows the feasibility of active ultrafast manipulation of spatial charge arrangements and electric fields in nanostructures by optically generated mechanical stress, a concept that is highly relevant for unraveling the structure-function relationship in correlated materials.

Chapter 7

Ultrafast Changes of Molecular Crystal Structure Induced by Dipole Solvation

Electron transfer reactions play a dominant role in chemistry and biochemistry. In particular, electron transfer forms the foundation of electrochemistry, underlies the mechanism of many chemical processes and is crucial to the primary steps of essential biological processes such as photosynthesis. The formation of a charge transfer state in an electron transfer reaction involves changes in the nuclear configuration of the reactants and/or a spatial rearrangement of charges in the polar environment.

Several techniques of optical spectroscopy have been developed to gain insight into the solvation process on a molecular level, for example, measurements of the transient spectral shifts of the electronic absorption and/or emission spectra [241], or in a different approach, femtosecond third-order nonlinear response of the coupled system as measured in photon echo studies [242]. Very few studies have pursued the transient structure of the molecular ensemble undergoing a solvation process, after a photoinduced change of a local dipole moment. In solution, transient vibrational spectra of an excited chromophore in the fingerprint range have revealed changes of local, that is, hydrogen bond interactions with the first solvent shell [243]. The lattice response of solid para-H_2 to an impulsive electronic excitation of a NO impurity was studied using femtosecond pump-probe spectroscopy [244]. Also time-resolved Raman studies have addressed the collective response of the solvent by following the intermolecular low-frequency modes during solvation [245]. While such Raman transients clearly demonstrate changes in the frequency spectrum of solvent fluctuations, they leave the transient molecular structure mainly unresolved. This lack of structural information calls for other, in

particular, ultrafast structure-resolving X-ray methods to image changes in molecular separations and orientations directly. Some prominent examples include a picosecond time-resolved X-ray absorption study of an iron complex in an aqueous solution where its structural relaxation from the high spin to low spin state could be determined [246, 247]. Furthermore, at the synchrotron in Grenoble several liquid phase X-ray diffraction experiments were carried out with a temporal resolution of approximately 100 ps: the photodissociation reaction of $C_2H_4I_2$ in methanol revealed a rather complicated reaction pathway [36]. The presented analysis included a decomposition of changes of the solute and changes of the solvent. Similar studies focused on the heating of the solvent [37] and on laser-dissociated iodine dissolved in CCl_4, where atom-atom pair correlation functions of the solute and solvent could be revealed for the first time [35]. However, structural changes due to dipole solvation have mostly remained unexplored, with subpicosecond temporal and atomic spatial resolution in any event.

In the following chapter a time-resolved X-ray study on the model molecular crystal DIABN is demonstrated. The ultrafast molecular rearrangements in response to a local dipole change is mapped directly and in real time. We find structural changes which consist of an angular reorientation of molecules leaving the spacing of lattice planes unchanged. Visible-pump mid-infrared probe studies confirm the occurrence of an intramolecular CT in the studied DIABN crystals. Ultrafast X-ray diffraction and transmission experiments give direct evidence that the X-ray signals are dominated by solvation-related geometrical changes of the crystal lattice, i.e, a collective response of many molecules, rather than local geometrical changes of excited chromophores. The dipole solvation occurs with a 10 ps rise time which is identical to the CT time. Under the conditions of weak femtosecond excitation applied here, a giant modulation of X-ray extinction around low order reflections is found. The extinction is due to elastic scattering and seems to be an effect which has been overlooked in many studies, but may be present in crystals made up of a complex unit cell and consisting of light elements ($Z<10$). In particular our results may be relevant for the growing field of protein crystallography, both stationary and time-resolved.

7.1 Dipole Solvation

Solvation generally refers to any stabilizing interaction of a solute (or solute moiety) and the solvent or a similar interaction of solvent with groups of an insoluble material. In our case the solute and solvent are polar and the solute is a chromophore, that is, it absorbs light at a specific frequency.

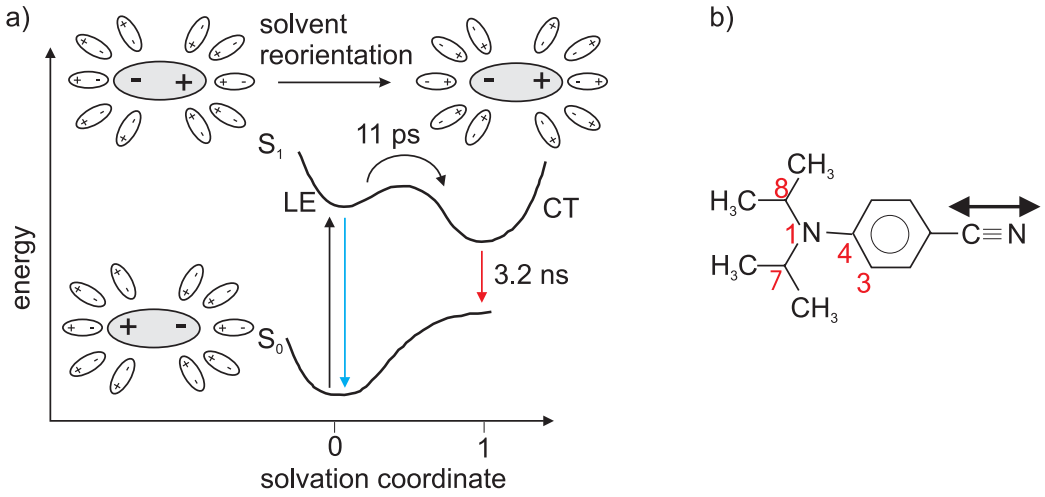

Figure 7.1: **a**) Schematic illustration of nonequilibrium energies in the ground and excited electronic states vs. the solvation coordinate. Absorption (black line) and prompt fluorescence (blue line) to/from the LE are illustrated, as is relaxed fluorescence (red line) from the CT state. Also shown a schematic of the reorientation of the solvent after a dipole flip. **b**) Molecular Structure of DIABN

For a qualitative discussion of the solvation process one often uses the free energy diagram depicted in figure 7.1 a). In initial light absorption by an equilibrated ground electronic state S_0, in which the permanent dipole moment is μ_0, the Franck-Condon principle requires that the nuclear solvent coordinates are 'frozen' at the instant of transition to the (locally) excited state LE with its different dipole moment μ_{LE} [coordinate 0 in figure 7.1 a) illustrated for a dipole flip]. Subsequently, the combined system evolves along the solvation coordinate, in this way lowering the excited state free energy towards a minimum (coordinate 1). I.e. a reorientation of the solvent molecules, which in the case of DIABN goes along with intramolecular conformation changes of the excited chromophore and a further increase of the dipole moment μ_{CT}. Despite the popularity of these diagrams the microscopic nature of the solvation coordinate is often unknown. To what extent time-resolved X-ray diffraction can shed light on this question by following the corresponding atomic motions is addressed in this chapter.

To describe the dipole solvation process after a laser-induced dipole change of the solute in the simplest approximation the solvent is treated as a dielectric continuum. A simplified equation based on Onsager's reaction field theory [248], assumes that the fluorophore is a point dipole residing in the center of a spherical cavity with radius ϱ in a homogeneous and isotropic

dielectric with the solvent static dielectric constant ε_s. It was first developed by Lippert [249, 250] and Mataga [251, 252] and reads for the *Stokes shift*, that is, the gap between the maximum of the absorption and fluorescence band:

$$\Delta\tilde{\nu} = \tilde{\nu}_a - \tilde{\nu}_f = \frac{1}{4\pi\varepsilon_0}\frac{2(\mu_{CT} - \mu_0)^2}{hc\varrho^3}\Delta f + const, \tag{7.1}$$

where

$$\Delta f = \frac{\varepsilon_s - 1}{2\varepsilon_s + 1} - \frac{n^2 - 1}{2n^2 + 1} \tag{7.2}$$

represents the solvent's orientation polarization. If the excited-state dipole is larger, the spectra are red-shifted with increasing solvent polarity Δf, which is referred to as positive solvatochromism. Conversely, if the ground state dipole is larger, the spectrum becomes blue shifted (negative solvatochromism). For further details please refer to ,for example, Reichardt [253].

7.2 DIABN

4-(diisopropylamino)benzonitrile (DIABN) exhibits dual fluorescence in polar solvents [254], thermal vapor [255] and in crystalline form [256] [compare figure 7.2], which serves as evidence for the occurrence of an intramolecular charge transfer state (CT). On a molecular level, CT may be connected with changes in geometry of the charge donating (amino group) and accepting groups as well as with polar solvation, a stabilization of the CT state by a rearrangement of the surrounding. Figure 7.1 a) shows a schematic energy diagram, which gives a qualitative explanation of the red shifted second emission band from the CT state. Optical excitation populates the locally excited state (LE) and subsequently the CT state is formed with a time constant of 11 ps. The CT state decays with a much longer time constant of 2.92 ns. Insight into CT induced changes of the molecular structure has remained limited and the physical meaning of the reaction coordinate is subject of ongoing scientific discussion (see the extensive review by Grabowski et al. [257] and references within). The two main competing hypothesis of the structural rearrangement are the so called planar ICT (PICT) and twist ICT (TICT) model. According to the TICT model, the amino group in the CT state has a perpendicular conformation with respect to the benzene plane. The amino group is decoupled from the benzonitrile moiety and thus the phenyl-amino bond is expected to expand leading to a lower vibrational frequency. The PICT model, on the other hand, assumes that the ICT state is largely planar. The phenyl-amino bond gains partial double bond character entailing an increased vibrational frequency. The transient structure of aminobenzonitriles

such as DIABN has been investigated by ultrafast vibrational spectroscopy in solution [258, 259] in combination with detailed calculations [260], but could not rule out either of the two models. X-ray diffraction experiments on the molecular crystals DIABN and DMABN tried to directly measure the conformation changes of the molecules after photo-excitation [261, 262]. These diffraction experiments with powdered samples were carried out with a very high excitation density and a time resolution of 100 ps. The authors claim that the CT state of DIABN and DMABN has a slightly twisted amino group of 4 and 10 degrees, respectively. The results have remained controversial though, inter alia because the same group [263] ruled out the existence of the CT state in crystalline DMABN in fluorescence measurements. The torsional angle of 10 degrees was then attributed to the LE state. These findings may also be considered to be in possible disagreement with the results presented here. In particular the authors did not give a detailed analysis on the influence of collective intermolecular motion on X-ray diffraction peaks.

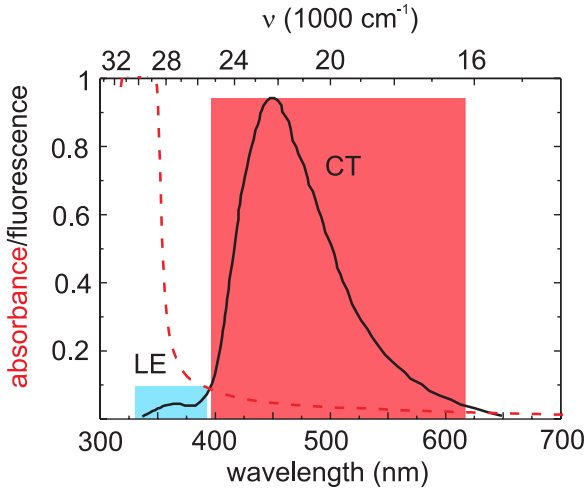

Figure 7.2: Fluorescence of crystalline DIABN (black line, taken from [262]). The fluorescence of the LE state is marked with a blue box, the fluorescence of the CT state with a red box. The red, dashed line is the measured absorption edge of a DIABN crystal.

The molecular and the static crystal structure of DIABN ($C_{13}H_{18}N_2$) is shown in the inset of figure 7.3 a) and figure 7.5 a). The diisopropylamino group of DIABN (plane through C(7), N(1) and C(8)) is twisted by an angle of around 20° relative to the plane of the phenyl ring. The dihedral angle C(3)C(4)N(1)C(7) equals 24.3°, whereas an angle C(3)C(4)N(1)C(8) of

174.6° is found. The structure of DIABN is monoclinic [C12/c1 (no. 15)] with 16 molecules in one unit cell. The lattice constants are a=16.657 Å, b=14.714 Å, c=20.725 Å and the angle $\angle(a,c) = \beta = 92.73°$ [264]. Basically, the crystal forms 4 layers of molecules per unit cell perpendicular to the c-axis which in turn contain pairwise molecules of parallel or anti-parallel orientation. Single crystals of DIABN were grown by sublimation of crystalline powder in a quartz tube [265]. The colorless plates were characterized by a good optical quality and a size of approximately 2×2 mm^2. Their thickness of typically 50 μm was cross checked by multiple reflections in a spectrometer.

7.3 Experimental Methods and Results

In contrast to liquid samples, DIABN crystals show a broad long-wavelength absorption tail [figure 7.1 b)] allowing for a spatially homogeneous optical excitation at 400 nm. This does not only help to avoid light induced damage, but, equally important, ensures that the entire volume which is probed by the X-rays is uniformly excited. For all time-resolved experiments we used 50 fs optical pulses centered around 400 nm for excitation. The CT kinetics in the crystal were studied using a visible-pump IR-probe set-up [266] with probe pulses in the mid-IR spectral range between 2060 and 2160 cm^{-1}. The polarization of the probe pulses lay in the plane defined by the crystallographic a- and b-axis to eliminate artifacts from birefringence. The transient absorbance change at 2104 cm^{-1} is plotted in figure 7.3 a) and rises with a characteristic time constant of 11 ps. The perturbed free induction decay for $t < 1$ ps is not shown.

Figure 7.3 d) shows the stationary Cu K_α X-ray transmission (solid line) as a function of the incident angle θ. The calculated (isotropic) X-ray absorption (dashed line) shows a significantly smaller extinction. The Bragg angles of the (004) and (006) reflections are marked for comparison. Clearly the Bragg reflected intensities at these angles are to small to show up as reduction in the transmitted beam. This measurement was taken for several DIABN samples and while we observed slight variations, the transmission always remained around/below 50% for the two Bragg angles θ_{004} and θ_{006} and a crystal thickness of $d = 50$ μm.

In the time-resolved X-ray diffraction experiments we studied the (004) and (006) Bragg peaks. For a typical crystal thickness of $d = 50$ μm, the steady-state peak reflectivity has values of $R(004) \approx 0.005$ (width $\Delta\theta_{\text{crystal}} \approx 0.15°$) and $R(006) \approx 0.001$. The time-resolved X-ray diffraction/transmission experiments were carried out with very low excitation fluences of approxi-

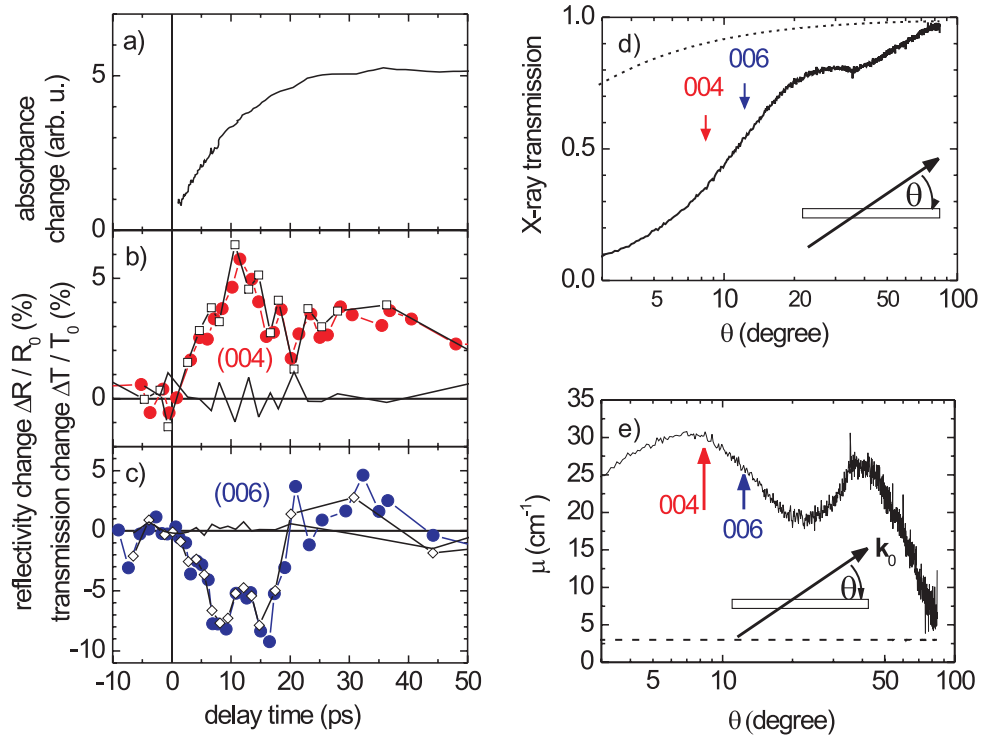

Figure 7.3: **a**) Transient rise (time constant: 11 ps) of the CN stretching absorption of molecules in the ICT state at 2104 cm^{-1} (perturbed free induction decay for $\tau < 1$ ps not shown). **b,c**) Time-resolved change of the X-ray reflectivity $\Delta R/R_0$ measured on the (004) (red circles) and (006) Bragg reflections (blue circles). The respective transmission change $\Delta T/T_0$ (open symbols) is identical to the reflectivity change, that is, $\Delta T/T_0 = \Delta R/R_0$. The thin black line is the difference signal $\Delta T/T_0 - \Delta R/R_0 = 0$. **d**) Measured X-ray transmission (solid line, $\lambda = 0.154$ nm) of a single (50 μm thick) DIABN crystal as a function of the angle θ explained in the inset. The calculated X-ray absorption contribution (dotted line) to the entire beam extinction plays a minor role. **e**) Attenuation coefficient $\mu(\theta)$ calculated with data from **d**) for a thickness of 50 μm. Note that the calculated absorption is constant, that is, isotropic (dotted line), while $\mu(\theta)$ shows a pronounced dependence on the angle of the incoming wave vector k_0

mately 0.15 mJ/cm^2, yielding an excitation density of 10^{-4} molecules. The first X-ray experiments on DIABN crystals were performed without an X-ray mirror and the reflectivity change was normalized to the reflection of a

second, unpumped crystal. In later experiments the ultrashort X-ray pulses were focused onto the sample by a multilayer mirror (No. 1, compare Tab. 3.3) and both, the X-ray reflection and transmission were recorded with the same CCD camera. This was possible due to the relatively small Bragg angles of $\theta_{004} = 8.56°$ and $\theta_{006} = 12.90°$. Only after we realized that also the transmitted X-ray beam is modulated by the optical excitation, instead of using a normalization signal, we decided to reduce the integration time per delay point to a few seconds, limit the number of delay points and minimize the readout time of the CCD chip by pixel-binning and thus acquired one temporal scan in a minimal time (< 30 seconds). The noise level was then reduced by averaging over up to a few thousand scans.

The result of these time-resolved measurements is shown in figure 7.3 b) and c). The filled red symbols show the reflected intensity of the divergent X-ray beam ($\Delta\theta_{\text{mirror}} \simeq \Delta\theta_{\text{crystal}}$) integrated over the (004) Bragg peak as a function of time. The reflectivity increases by approximately 5% within 10 ps, shows some oscillatory features for longer time scales and remains raised by a about 2% after 50 fs. In the lower panel of the same figure the reflectivity change of the (006) reflection are displayed as filled blue dots. It decreases by 10% with approximately the equivalent time constant of 10 ps, increases again and reaches $\Delta R/R_0 \approx 0$ after 20 ps. For even longer times one observes oscillations around zero reflectivity change. In the same figures the transmission change $\Delta T/T_0$ is plotted as hollow symbols. They were recorded simultaneously with the respective reflected signals, that is, for the incident angles θ_{004} and θ_{006}. Strikingly the change in transmission and reflection is identical! The difference signal $\Delta T/T_0 - \Delta R/R_0 = 0$ is plotted in both figures as a thin black line and shows very small fluctuation around zero. Note that also more subtle features are identical in the transmission and reflection measurements. Since the presented data is a result of very many different measurements, taken on different days and with different samples also the oscillatory features are expected to have a physical origin, rather than being simply due to noise.

7.4 Discussion

Charge Transfer in DIABN

Excitation with 50 fs optical pulses centered at 400 nm populates the so-called locally excited state from which the intramolecular CT state is formed. The latter process leads to a shift of the CN stretching mode to lower frequency and a change of its absorption strength [258, 259]. Hence, the observed

absorbance change at 2104 cm^{-1} is attributed to the CN stretching mode, rising with a characteristic time constant of 11 ps. This gives direct evidence, that the CT state is formed in the studied DIABN crystals and also determines its formation time [figure 7.3 a)]. The same characteristic time was also observed in previous measurements on crystalline DIABN [256, 262] and slightly larger (12 ps) in solution [254]. This suggest that the observed rise time of the X-ray signals is induced by intramolecular CT state. However, the reflectivity and transmission changes are of the order of $\Delta R/R_0 \approx 0.1$ and hence orders of magnitude larger than a potential reflectivity change stemming from *local* changes in geometry of the small fraction (10^{-4}) of excited molecules. Instead, both reflection and transmission changes are caused by a major fraction of molecules, that is, a collective response of the crystal to the local photoinduced dipole changes.

Diffuse Scattering

Both stationary and time-resolved X-ray data show very surprising results, which cannot be readily explained with existing concepts of X-ray scattering. This calls for a detailed discussion of the underlying mechanisms, which is presented in the following:

Let us first concentrate on the stationary transmission measurement shown in figure 7.3 d) and e). The solid line in the upper graph shows the measured X-ray transmission ($\lambda = 0.154$ nm) through a 50 μm thick DIABN crystal as a function of the incident angle θ. The transmission drops to approximately 50% for θ around 10°. The dotted line shows the calculated transmission for the absorption coefficient $\mu_{abs} \approx 3$ cm^{-1} of a DIABN crystal of the same thickness. Note that it predicts significantly higher values for the X-ray transmission. The lower figure 7.3 e) displays the attenuation coefficient $\mu(\theta)$ calculated with the measured transmission values shown above as a function of the direction of the incoming X-ray beam $\vec{k}_0$. It shows a pronounced anisotropy, while the attenuation solely due to absorbtion is of course isotropic hence constant in figure 7.3 e) (dotted line). The attenuation coefficient amounts to $\mu \approx 30$ cm^{-1} for $\theta \approx 8°$. This measurement also reveals that attenuation due to Bragg diffraction plays a negligible role, as no drop of transmission is observed around the strongest reflections (004) and (006). Let us draw a comparison with a diamond crystal, a simple structure with a high degree of perfection: in a transmission measurement as presented in figure 7.3 e) one would expect to see a low constant attenuation (dashed line) and depending on the alignment of the crystal a narrow region of zero transmission at the corresponding angular position of a Bragg reflection.

The low reflectivity of the (strongest) (004) and (006) Bragg reflections

point to an ideally imperfect crystal structure. The average DIABN crystal has what is called a mosaic structure (compare chapter 2.7.4). Apparently the individual blocks are so small, that primary extinction plays no role, and the diffraction can be satisfactorily described by kinematic X-ray theory. However the strong (anisotropic) attenuation of the transmitted beam can only stem from scattering effects [1]. In other words, in DIABN we have the peculiar situation, where the cross-section due to incoherent scattering $\sigma_{\text{incoherent}}$ greatly exceeds the cross-section for coherent scattering or Bragg diffraction σ_{Bragg}. Even though this is an exceptional situation it has been observed before. E.g. it has been pointed our that in protein crystals and for a mean temperature factor $B \approx 20$ Å^2 the integrated diffuse intensity will exceed that of the Bragg peaks beyond a momentum transfer of 1/3.8 Å^{-1} and, at the resolution required to locate atoms in protein crystals, more X-rays are diffusely scattered than are diffracted into Bragg reflections [267]. A further example is an experiment where radiation damage in BeO was induced by neutron bombardment and resulted in $\sigma_{\text{Bragg}} < \sigma_{\text{incoherent}}$ [268]. Here the strong diffuse background was attributed to formed clusters with approximately 70 Å diameter tilted with respect to maximum reflectivity.

Before proceeding let us consider a qualitative line of reasoning why DIABN crystal may be expected to exhibit a pronounced and special diffuse scattering. In this context a few earlier publications are mentioned which deal with diffuse scattering of molecular crystals. DIABN crystals are made up of only light elements (Z≤7), such that absorption plays a negligible role and attenuation due to scattering can in principle dominate. Generally diffuse scattering in molecular crystals may have different origins. Very early it was shown by Debye that thermal vibration of atoms gives rise to diffuse scattering, apparently very sensitive on temperature and anisotropy, due to the anisotropy of the elastic constants of the crystal. A second contribution to diffuse scattering was found in molecular crystals which was attributed to translation and librational oscillation of molecules as rigid bodies. Lonsdale et al. [269, 270] was the first to show that certain features in diffuse scattering are due to the shape of the molecule and, therefore, that it was possible to determine the orientation of the molecule in the unit cell by diffuse scattering. The concept to assign a form factor to whole molecules and treat them as a rigid body is mainly inspired by the generally weak intermolecular Van-der-Waals forces compared to the stronger, high frequency intramolecular forces. Pioneering work on diffuse scattering in complex protein crystals revealed pronounced intermolecular motion of molecules within the lattice

[1] Anomalous absorption like present in the Borrmann effect is known to occur only in crystals with a high degree of perfection.

[32–34]. Comprehensive reviews on diffuse scattering in molecular crystals include Amorós and Amorós [45]and Welberry and Butler [44].

The occurrence of diffuse scattering may not be surprising since DIABN has a large and complex unit cell and exhibits almost 500 diffraction peaks with appreciable intensity for Miller indices $(000) < (hkl) < (999)$ and $(0° < \theta_{\mathrm{Bragg}} < 90°)$. (For diamond one finds 13!) Diffuse backgrounds around Bragg reflections will therefore enforcedly overlap and will lead to large values for diffuse X-ray scattering.

The time-resolved X-ray data revealed $\Delta T/T_0 = \Delta R/R_0 \neq 0$, which points to a modulation of the attenuation coefficient $\mu(t)$, rather than changes of the structure factor, or reflectivity. This may be most easily appreciated in the following way. For the primary X-ray beam incident on the crystal with thickness L and an extension larger than the diameter of the beam, we may write for the time-dependent X-ray transmission (Warren [41]):

$$T(t) = e^{-\mu(t)L}. \tag{7.3}$$

For the X-ray reflection of this 'ideally imperfect' crystal, in the sense that primary extinction is negligible, we can write:

$$R(t) = \frac{\delta R}{2\mu(t)} \left[1 - e^{-2\mu(t)L}\right] \tag{7.4}$$

Here δR denotes the reflectivity per unit crystal thickness. The factor 2 in the exponential is due to the doubled X-ray path for reflected rays. (Strictly this is not correct for an anisotropic μ.) The experimental finding that $\Delta T/T_0 = \Delta R/R_0$ for $\tau < 50$ ps demonstrates that both transmission and reflectivity changes are dominated by the transient X-ray attenuation coefficient $\mu(t)$. This holds for the assumption that $\mu d < 1$. Then the transient change of the Bragg reflectivity $\delta R(t)$ of the small mosaic blocks plays a minor role. A strong modulation of the latter would result in $\Delta T/T_0 \neq \Delta R/R_0$. As pointed out earlier by far the dominant term in $\mu(t)$ is diffuse scattering [figure 7.3 e)]. The differences in signal sign and temporal evolution of the (004) and (006) curves again point to a pronounced anisotropy of diffuse X-ray scattering.

At this point emphasize the limited sensitivity of low-index Bragg reflections for small changes within a complex unit-cell. With four layers per DIABN unit-cell, the (004) reflection mainly probes the relative layer distances, while the (006) reflection is more sensitive to the asymmetry of the layer arrangement. In any case both Bragg peaks are not particularly sensitive to subtle intramolecular conformation changes. However, the unchanged reflectivity of the (004) and (006) reflection suggests that the layer distances remain unchanged after optical excitation.

Mathematical Model of Diffuse Scattering

In the following the mathematical description of elastic X-ray scattering in DIABN crystals is presented. Let us begin the discussion with the basic theoretical formula for the total elastic X-ray scattering cross-section. It is valid for the approximation of free electrons, applicable here, since the binding energies of the constituent atoms of DIABN, H,N,C are much smaller than the energy of the keV X-ray photons. Then the attenuation coefficient as a function of the direction of the incoming beam is given by the average electron density times the total cross-section for one electron (compare section 2.4 and Chapter 14.8 in [38]):

$$\mu(\vec{k_0}) = N_e \int d\Omega_S \frac{d\sigma_e(\vec{k_0})}{d\Omega_S} \qquad \text{with} \tag{7.5}$$

$$\frac{d\sigma_e(\vec{k_0})}{d\Omega_S} = \frac{r_e^2}{Z} \left\langle \left| \sum_{j=0}^{Z} \exp\left(i(\vec{k_0} - \vec{k_S})\vec{x_j}\right) \right|^2 \right\rangle |\vec{n} \times (\vec{n} \times \vec{\epsilon})|^2 \tag{7.6}$$

$\vec{k_0} = (2\pi/\lambda, \theta_0, \phi_0)$ and $\vec{k_S} = (2\pi/\lambda, \theta_S, \phi_S) = (2\pi/\lambda, \Omega_S)$ with $\vec{k_0} - k_S = \vec{q}$ are the wave vectors of the incoming and scattered X-ray photons. N_e is the average electron density of the crystal ($N_e \approx 3.4 \times 10^{23}$ cm^{-3}) and $d\sigma_e(\vec{k_0})/d\Omega_S$ is the differential cross-section per electron which depends on the positions $\vec{x_j}$ of all electrons. r_0 is the classical electron radius and $|\vec{n}\times(\vec{n}\times\vec{\epsilon})|^2$ accounts for polarization averaging and amounts to $1/2\cdot[1+\cos^2(\theta)]$ for an unpolarized X-ray beam. The angle brackets $\langle\rangle$ stand for ensemble averaging of the electron positions within the atoms and molecules as well as the spatial and rotational disorder of the molecules themselves. Z is the number of electrons scattering coherently, which can belong to the same atom, the same molecule or even a well ordered fraction of the crystal [45]. Equation 7.5 will show a very different behavior, depending on the value of $(\vec{q}\vec{x})$, or in other words whether the scattering is incoherent or coherent. For the case of Z electrons with identical positions, for example well approximated by Z electrons belonging to a heavy atom ($\vec{q}\vec{x} \ll 1$), we can approximate the exponential factors by unity and calculate the extinction coefficient as follows:

$$\mu = N_e \int_0^{2\pi} d\phi \int_0^{\pi} d\theta \cdot \frac{r_e^2}{Z} \cdot Z^2 \cdot \frac{1}{2}[1 + \cos^2(\theta)] \sin(\theta) \tag{7.7}$$

$$= (N_e/Z)(\frac{8}{3}\pi r_e^2 Z^2) \tag{7.8}$$

$$= (N_e/Z)(\sigma_{\text{Thomson}} Z^2). \tag{7.9}$$

This shows the coherent effect of all the electrons, giving an intensity corresponding to the square of the number of electrons times the intensity for

a single electron. It is also interesting to consider the opposite case of incoherent scattering. For ($\vec{q}\vec{x} \gg 1$) the arguments of the exponents are large and widely different in value. Consequently the cross terms in the square of the sums will average to zero. Only the absolute squared terms will survive. Thus the intensity for incoherent scattering is only the number of scattering electrons times the intensity of a single electron.

The significance of equation 7.5 may be more easily appreciated when we show its relation to the density-density correlation function:

$$n(\vec{x}) = \sum_{i=1}^{Z} \delta(\vec{x} - \vec{x}_{\mathrm{i}}) \tag{7.10}$$

$$\int d^3\vec{x} \quad n(\vec{x}) = Z \tag{7.11}$$

$$\frac{1}{Z}\left\langle \left| \sum_{i=1}^{Z} \exp\left(i(\vec{k}_0 - \vec{k}_{\mathrm{S}})\vec{x}_{\mathrm{i}}\right) \right|^2 \right\rangle = \left\langle \int d^3\Delta\vec{x} \quad \mathrm{AC}(\Delta\vec{x}) \exp(i\vec{q}\Delta\vec{x}) \right\rangle \tag{7.12}$$

$$\mathrm{AC}(\Delta\vec{x}) = \frac{\int d^3\vec{x} \quad n(\vec{x})n(\vec{x} + \Delta\vec{x})}{\int d^3\vec{x} \quad n(\vec{x})} \tag{7.13}$$

where $\Delta\vec{x} = \vec{x}_{\mathrm{i}} - \vec{x}_{\mathrm{j}}$. Hence, the extinction coefficient $\mu(\vec{k}_0)$ in equation 7.5 is the Fourier transform of the density-density autocorrelation integrated over the solid angle of the scattered photons. The autocorrelation function $\mathrm{AC}(\Delta\vec{x})$ is also known as the Patterson function and plays an important role in solving the problem of the unknown phase in crystal structure determination. The Patterson function is a correlation function giving the position of every electron relative to every other electron, but not relative to a fixed origin. Peaks in the Patterson function therefore do not represent the position of the scatters; the peaks are the terminal points of a set of vectors, each vector representing the displacement of some electron from some other electron. It is important to realize that such density-density correlations may exist on different length scale. Electrons are bound in atoms, and the correlation is described by the atomic form factors. The next level of complexity one can imagine is to consider a group of atoms organized in a molecule [45]. Evidently for a perfect static molecular crystal the Patterson function would repeat itself for every unit-cell. However, intramolecular vibrations and more importantly intermolecular motion will eventually wash out correlation effects. On even larger length scales the arrangement of molecules in nano-crystallites and low q phonons may exhibit further correlation effects. In general these will also depend on the direction of the incoming wave vector, first of all because of the shape of the molecule and secondly because of the layered arrangement of molecules within the unit-cell. Note that the ensemble averaging $\langle\rangle$ in equation 7.5 can be mimicked

by truncating the Patterson function. The diffuse intensity is modeled by $I_{\text{diffuse}} \propto \mathcal{FT}(AC(\Delta\vec{x})\exp(-(1/2)(r/\gamma)^2))$, where AC is multiplied with a monotonically decreasing function that smoothly truncates the Patterson function. The parameter γ specifies the range over which couplings of the atomic motions occurs [32]. In our calculation simply the size of the cluster itself (number of electrons Z) will determine the range of couplings such that instead of using a smoothly varying functions the Patterson function is abruptly truncated.

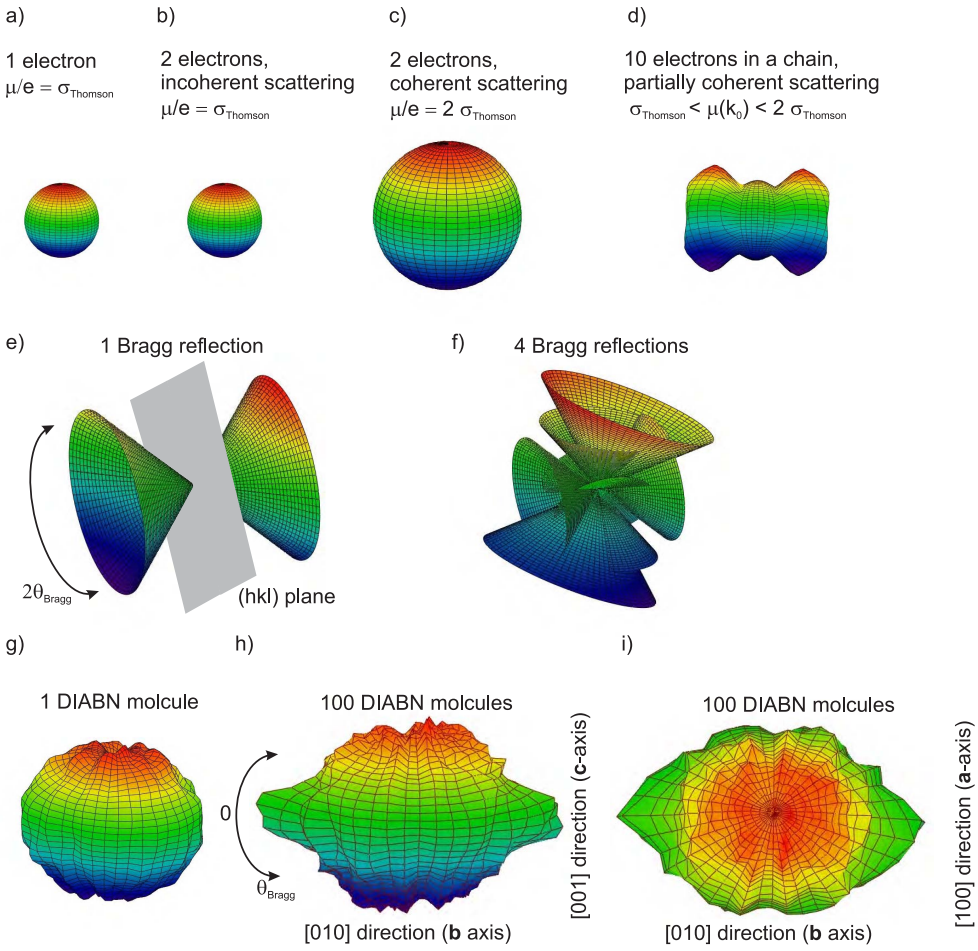

Figure 7.4: Extinction μ_e due to elastic scattering as a function of the incoming wave vector $\vec{k}_0$ for different electron configurations

To elucidate the situation further we have performed simulations for different electron configuration which are shown in figure 7.4 and show an attenuation sphere in units of σ_{Thomson} per electron for all possible incoming X-ray vectors $\vec{k}_0 = (2\pi/\lambda, \theta_0, \phi_0)$. With equation 7.5 one can calculate the

differential cross-section for each electron pair and subsequently sum over all pairs to get the total extinction as a function of incoming wave vector $\vec{k}_0$. This only requires two parameters, namely the distance between the electrons $|\vec{x}|$ forming a pair, derived from their spatial positions, and the angle between the connecting line between the electrons and $\vec{k}_0$. Further details of the calculations can be found in Appendix C. Figure 7.4 a) shows the simplest case for one electron. Of course the total scattering cross-section is isotropic and yields a value of σ_{Thomson}. Figure 7.4 b) depicts the calculated extinction for two electrons which scatter incoherently (realized by $|\vec{x}| \gg 1$) to yield the same result, namely σ_{Thomson}/electron. Differently in c) the distance between the electrons is shrunk to zero, or $|\vec{x}| \to 0$ to produce the coherent result predicted by equation 7.7, namely μ_{e}/electron$\propto Z$. The extinction yields $2 \cdot \sigma_{\text{Thomson}}$/electron. On the right hand side of the first row a chain of 10 electrons is calculated, which now results in an strongly anisotropic attenuation as a function of $\vec{k}_0$ and due to only partial coherent addition of the scattering amplitudes the extinction varies between $\sigma_{\text{Thomson}} \lessapprox \mu_{\text{e}} \lessapprox 2 \cdot \sigma_{\text{Thomson}}$. Hence, the coherent enhancement of $d\sigma_e(\vec{k_0})/d\Omega_S$ is weaker for an ensemble of electrons more separated in space like present in molecules or in small cluster of the latter. These example calculations suggest that depending on the number of electrons and their spatial arrangement the attenuation sphere will change both, its size and its form. This is important to keep in mind.

In the second row of figure 7.4 the opposite limiting case is sketched, namely for the coherent superposition of very many electrons, which lead to Bragg reflections. Of course these have not be calculated with equation 7.5. They are merely schematics. Figure 7.4 e) displays the extinction due to one single Bragg reflection, which yields a double cone. The tilt of the cone depends on the position of the scattering planes in space. The cone angle is $2\theta_{\text{Bragg}}$. Accordingly only for $\vec{k}_0 = \vec{k}_{\text{Bragg}}$ we get an appreciable attenuation, namely primary extinction. The thickness of the walls of the cone will depend on the quality of the sample (here absolute perfection has been assumed) and its size will depend on the number of coherently scattered electrons. Note, that this is the regime where equation 7.5 loses its validity, namely if the attenuation due to coherent scattering is so large, that an appreciable amount of the incoming beam is lost and primary extinction has to be accounted for, that is, multiple scattering. This case must be addressed with dynamical X-ray diffraction theory, according to equation. 2.3. Figure 7.4 f) shows four overlapping double-cones with different orientations, different Bragg angles and different sizes. Such a figure may be measured for a (perfect) diamond crystal, where the extinction sphere is expected to be completely dominated by Bragg reflections. Since diamond has in fact only a one more double cone,

namely 5, it represents a system, where diffuse scattering in comparison with Bragg scattering is negligible.

After these introductory remarks let us now turn to the problem of DIABN. First of all a few simplifications have to be made to allow to calculate the extinction sphere in an reasonable amount of time. We only consider the 2 core electrons (1s orbital) of carbon (C) and nitrogen (N) atoms of DIABN. They are assumed to be localized exactly at the position of the atoms, a reasonable assumption considering their atomic form factor is nearly 1. All other electrons are delocalized and play a minor role in determining the anisotropy of the elastic scattering. Forward scattering of course does not contribute to the attenuation, but has not been subtracted from the total scattering cross-section. A test calculation for a single DIABN molecule is shown in figure 7.4 g). The first signs of anisotropy due to the geometry of the molecule are already noticeable. Figures 7.4 h) and i) shows the calculation for a cluster of 100 DIABN molecules. (Unfortunately this calculation already requires close to 30 hours on a PC, the calculation time is proportional to the number of electrons squared.) Again, it shows the total elastic scattering cross-section integrated over all scattering directions $\vec{k_S}$ as a function of the incoming X-ray beam $\vec{k_0}$. The extinction is largest for the incident wave vector $\vec{k_0}$ parallel to $\vec{b}$. The extinction for $\vec{k_0}$ parallel to $\vec{a}$ is somewhat smaller and for the wave vector parallel to $\vec{c}$ shows a pronounced minimum. Exactly along $\vec{c}$ it even shows a remarkable indentation. Figure 7.5 a) shows the crystal structure of DIABN for a cluster of 72 molecules along the two directions [001] and [011]. The attenuation sphere $\mu(2\pi/\lambda, \theta_0, \phi_0)$ is plotted below the crystal structure and this comparison makes it evident that the pronounced anisotropy is due to the alignment of the molecules in the lattice planes of the crystal. The polar coordinate system θ_0, ϕ_0 is aligned to the crystal axes $\vec{a}, \vec{b}, \vec{c}$ as shown in figure 7.5. The black dots in figure 7.6 show a cut through the anisotropic distribution for $\phi_0 = 150°$ around small values of $\theta_{Bragg} = 90° - \theta_0$. The dashed line in figure 7.6 is the cross-section per electron for a perfectly isotropic scattering of a cluster containing 100 molecules and yields approximately 16 σ_{Thomson} per electron. The position of $\vec{k_0}$ for the (004) and (006) reflection is marked with a red and blue arrow, respectively. Recall that the stationary transmission measurement shown in figure 7.3 e) determined an extinction due to elastic scattering of $\mu \approx 30$ cm^{-1}. This value is reproduced for the coherent case (equation 7.7) and $Z = 130$. In other words the average cross-section per electron must be at least 130 σ_{Thomson}. For the real arrangement of DIABN molecules a cluster of 100 molecules is apparently still to small to explain the large value of μ_e as observed experimentally. Because calculations of even larger DIABN

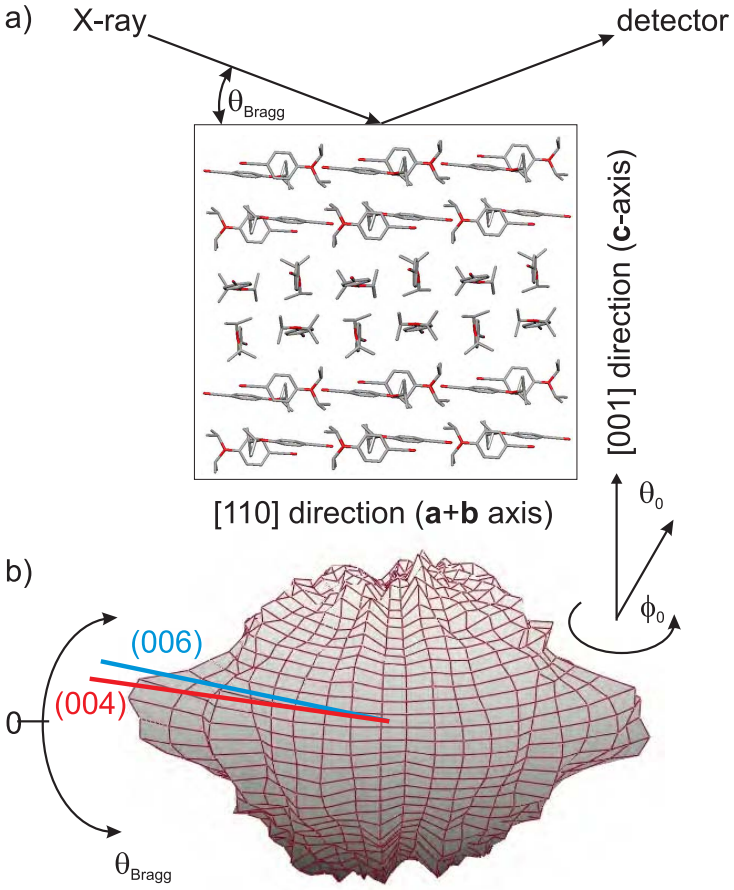

Figure 7.5: **a**) Crystal structure of DIABN showing a cluster of 72 molecules. The crystal alignment during the experiment is indicated.**b**) The attenuation sphere (orientation as molecules in a)) shows the strongly anisotropic result along the axis of the aligned molecules.

clusters go beyond the scope of available computer power we extrapolate the result. The total cross-section around Bragg reflections in the kinematic approximation increases very slowly and calculations for different cluster sizes show that it is approximately proportional to $V^{4/3}$. Accordingly, we extrapolate the result for the small cluster and find that at least 10.000 DIABN molecules must scatter coherently, corresponding to a crystallite with an extension of approximately 20 nm. Of course the correlations may exist on different length scales and may have a more complex spatial arrangement. Also any kind of disorder has been disregarded. As noted earlier this could be incorporated in a more complicated function describing the truncation of

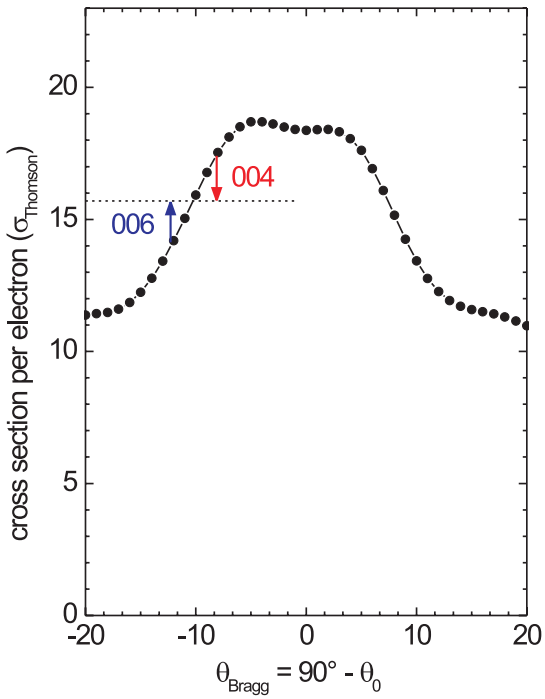

Figure 7.6: The calculated total elastic X-ray scattering cross-section per electron of a nano-crystal containing 100 DIABN molecules as a function of the direction of the incident X-ray beam. Circles: detailed anisotropy for directions of the incident beam around the (004) and (006) Bragg reflections.

the Patterson function, but of course would require knowledge about the real (disordered) crystal structure.

Dipole Solvation in DIABN Crystals

A change of the molecular alignment by a dipole-induced angular reorientation changes the ensemble average of the anisotropic total cross-section [circles in figure 7.6] towards an isotropic one (dashed line), thereby modulating the X-ray extinction. For the Bragg angle of the (004) reflection [figure 7.3 b)], the extinction of the incoming beam due to diffuse scattering is decreased and therefore both the Bragg reflection and the transmission increase, whereas a decrease occurs for the (006) reflection [figure 7.3 c)]. Additionally the number of coherent scatters may be changed after photo excitation, resulting in a reduction of the cross-section per electron.

In the molecular crystal DIABN molecules are coupled through their (static) dipole moment which has a value of $\mu_0 = 6.78$ Debye in the electronic ground state [271]. Femtosecond excitation and the subsequent population of the CT state increase the dipole moment of the excited molecules to $\mu_{CT} \approx 16 - 18$ Debye [254]. The increased dipole moment is the source of additional electric fields. Neighboring molecules experience the largest fields, which – for a distance of ≈ 4 Å and $\Delta\mu \approx 10$ Debye – reach values of 10^{10} V/m. To gain further insight into the distribution and magnitudes of the additional fields due to induced dipole moments, we performed the following simulation. Dipoles with a density of 10^{-4} are statistically distributed and aligned and the sum of their dipolar fields in z-direction E_z on a test molecule is calculated. We limit the approach to the z-direction since the DIABN molecules are aligned along the $\vec{a}/\vec{b}$ directions and thus the field E_z will exert the greatest torque on the individual molecules. To reach a statistical distribution this calculation is repeated 10.000 times. The result is shown in figure 7.7. The diagram shows the histogram of 10.000 events in

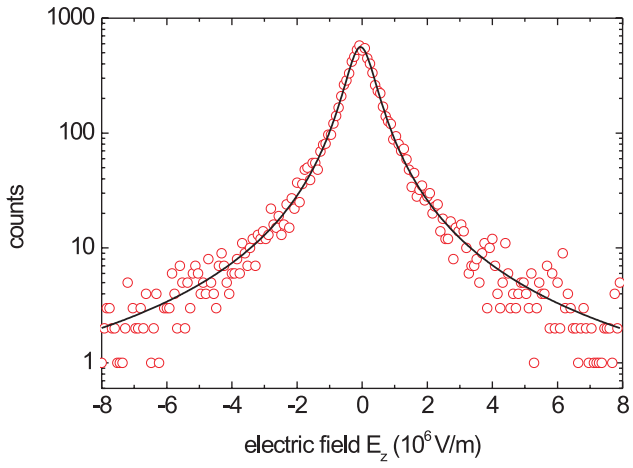

Figure 7.7: Electric field E_z for a statistical distribution of dipoles ($\Delta\mu = 10$ Debye) with a density of 10^{-4}. The black line is a fit according to a Lorentz curve with a width of 10^6 V/m

0.1×10^6 V/m intervals as a function of the electric field E_z. The distribution is well described by a Lorentz curve with a width of 10^6 V/m. In the wings the additional dipolar fields increase, corresponding to a decrease of the distance to the CT dipoles. Most of the molecules will be far away from the excited molecule, hence the largest number of molecules experience no

additional electric fields. These inhomogeneous electric fields generate the torque on the unexcited molecules which drives their angular re-orientation. The increase of the dipole moment of the excited molecule happens on the time-scale set by intramolecular charge transfer, that is, 11 ps [figure 7.3 a)]. The resulting changes of the local electric field at the position of the unexcited molecules occur quasi-instantaneous. With the measured rise time of the X-ray signals in the order of 10 ps, we can conclude that the kinetics of the intermolecular rearrangement is ultimately determined by the dynamics of the charge transfer itself. Note that the dipolar forces and torques can also excite phonons which might be the origin of oscillatory features observed after $\sim$ 10 ps.

Finally, we estimate the expected rotational disorder from the solvation point of view. To determine the solvation energy one has to distinguish between energy shifts due to intramolecular rearrangement of the molecule in the ICT process and the contributions of the solvent itself. This has been done by systematically changing the solvents (that is, Δf) and follow the fluorescence maxima shifts $\Delta\tilde{\nu}$ of the chromophore DIABN [254]. If we assume that the values obtained for liquid solvents are conferrable to the crystalline environment, a linear plot of equation 7.1 as a function of the solvents polarity Δf gives for $\Delta\tilde{\nu} = 22.300$ cm^{-1} a solvation energy of $\Delta E_{solv} \approx 2000$ cm^{-1}. This also determines the value of $\Delta f \approx 0.2$ and with the measured index of refraction $n = 1.8$ allows an estimate of the static dielectric function of the crystal $\epsilon(\omega \to 0) \approx 100$. The polarizability may be calculated with the Clausius-Mossotti relation and with the change of the dipole moment $\Delta\mu \approx 10$ Debye and the known density we estimate the corresponding elastic torque constant to be $D_{rot} \approx 10\,000$ cm^{-1}. The torque is given by $\vec{M} = \vec{\Delta\mu} \times \vec{E}_{\mathrm{loc}}$. Hence, for electric fields between 10^6 and 10^{10} V/m this yields molecular rotation angles $\alpha = M/D_{\mathrm{rot}}$ from 0.01° up to 10° (upper limit due to steric hindering). This simple approximation estimates a sufficient rotational disorder to break the calculated anisotropy.

Figure 7.8 shows a schematic illustration of the observed dipole solvation in the DIABN crystals. For $t < 0$ the DIABN molecules are aligned in the crystal structure. At $t = 0$ the laser pulse excites a small fraction of DIABN molecules which is followed by the formation of the CT state within $t = 10$ ps and accompanied by a change of the dipole moment. Simultaneously this results in a change of its electric field $\vec{E}_{\mathrm{loc}}$, exerting a torque $\vec{M}$ on the (ground state) dipoles of the surrounding unexcited molecules. As the long-range dipole field of the chromophore is of radial symmetry, it induces a spherical rearrangement of molecules in the crystal lattice, leading to a more isotropic scattering cross-section. The time-resolved X-ray data demonstrates that the solvation process in the crystal lattice happens on a time-scale set by the

dynamics of the intramolecular CT.

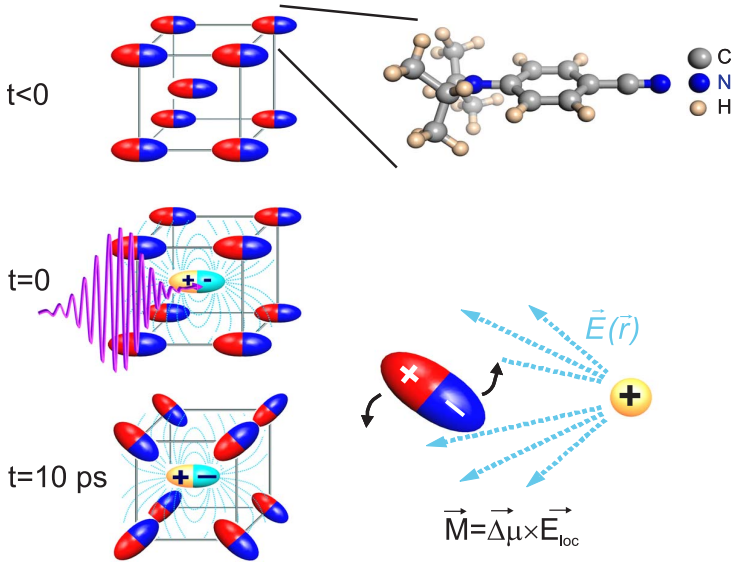

Figure 7.8: Schematic of the solvation dynamics of crystalline DIABN. At $t = 0$ a small fraction of the DIABN molecules are optically excited and form the CT state, accompanied by an increase of the dipole moment. The electric field will exert a torque on the surrounding (polar) molecules and will align them, changing the structure of the molecular ensemble.

In conclusion, structural changes underlying a polar solvation process were directly observed by ultrafast X-ray diffraction/transmission experiments. The photoinduced CT of a small fraction of chromophores in a molecular crystal causes angular reorientation of the unexcited polar environment and determines the transient X-ray response of the system whereas local changes of the chromophore geometry play a negligible role. Monitoring local changes of molecular structure by X-ray diffraction requires a suppression of such solvation processes, for example, by dissolving the system of interest in a nonpolar crystalline environment. On the other hand knowledge of the transient total elastic cross-section contains valuable information on the structural dynamics of the molecular ensemble surrounding the excited chromophore during the solvation process. The high photon count in transmission experiments makes this technique particularly appealing for laser-driven X-ray plasma sources. I envision anisotropic X-ray transmission experiments to develop into a beneficial supplementary structural sensitive technique.

Chapter 8

Conclusion

For the first time femtosecond X-ray pulses have been used to study the structure-function relationship in oxide thin films, a class of materials which has emerged as fertile ground for new physical phenomena and devices. Additionally, femtosecond X-ray scattering is applied to a prototype molecular crystal to study the ultrafast coupling between excited chromophores and their polar surroundings. These studies of fully *reversible* lattice dynamics on systems beyond semi-conductors and bismuth crystals demonstrate the enormous potential of time-resolved X-ray diffraction.

The conclusion gives a brief summary of the main results and an outlook for further experiments on selected aspects:

Summary

Optical excitation of condensed matter modifies its electronic structure and leads to changes of the lattice geometry on a sub-picosecond time scale, ultimately determined by translational, rotational or vibrational motions on an atomic length scale.

Ultrafast optical excitation in a ferroelectric/metallic $Pb(ZrTi)O_3$/ $SrRuO_3$ thin film launches strain waves into a highly perfect $SrTiO_3$ substrate crystal, which are imaged in real time by femtosecond X-ray diffraction. The main results are:

- Due to the very small extinction length in $SrTiO_3$, additional X-ray scattering from strained parts of the sample leads to an increase of the time-dependent angle integrated reflectivity.

- Interference of X-rays scattered from strained and unstrained parts of the sample lead to a double-step behavior of the time-dependent,

angle-integrated X-ray reflectivity. This feature allows to calibrate the underlying strain amplitudes by dynamical X-ray diffraction theory.

- This allows to quantitatively determine strain amplitudes as small as 10 femtometers or a hundred thousandth part of the lattice constant.

Electronic-structural couplings of ferroelectric or ferromagnetic Perovskite oxides assembled in epitaxial nanolayered superlattices have been studied by femtosecond X-ray diffraction. Changes in the diffracted intensity are accurately mapped to changes of lattice parameters. The essential findings are:

- Optical excitation of metallic $SrRuO_3$ leads to a build-up of stress by electron-phonon coupling with a finite rise time of 500 femtoseconds. The amplitude of stress scales linearly with the total amount of deposited energy and is independent of the excitation wavelength. The resulting strain is due to anharmonic phonon-phonon interaction and can be satisfactorily described by the Grüneisen concept. Its amplitude is in the order of one percent, corresponding to a pressure of approximately one gigapascal.

- Optical excitation of ferromagnetic $SrRuO_3$ for $T<T_C$ leads to an ultrafast demagnetization and a magnetic component of stress. This magnetostrictive component is of similar amplitude as the phonon mediated stress, but has a different sign. The amplitude of the magnetovolume effect reveals a pronounced excitation spectrum, consistent with calculations of the electronic band structure and suggesting direct, instantaneous, optical spin-flip transitions, or electron-magnon scattering during thermalization of hot carriers. The magnetostrictive stress shows a rise time of approximately 200 to 700 femtoseconds. The delay is attributed to a finite demagnetization time and/or to elongations of oxygen octahedra oscillations, which are known to stabilize the ferromagnetic ordering.

- A time-resolved X-ray structure analysis of ferroelectric nano-layers measures the atomic amplitudes of the two modes which are known to essentially determine and control ferroelectricity directly. That is, the tetragonal distortion driven by expansion of neighboring optically excited $SrRuO_3$ layers and the ion displacement within the unit-cell or soft mode, which is directly proportional to the macroscopic polarization. These two modes are coupled by a third-order term in Hamiltonian of the crystal, such that the changes of the tetragonal distortion cause an

elongation of the soft mode and a reduction of the macroscopic polarization. The presented experiment demonstrated that the polarization can be reduced to zero within 2 picoseconds, while the time-scale and an additional observed delay of 500 femtoseconds is set by the oscillation frequency of the soft mode shaped by the anharmonic potential surface of these two coupled modes.

Femtosecond X-ray reflectivity and transmission experiments on a polar molecular DIABN crystal reveal collective structural rearrangements after photoinduced dipole changes of single molecules. This presents a further example where changes in electronic properties cause structural rearrangement, and concomitantly, shows how the electronic system is stabilized by its modified surrounding. That is, dipole solvation in a crystalline environment. The experimental results establish:

- X-ray attenuation in DIABN crystals is dominated by anisotropic coherent scattering from crystal clusters containing approximately 10,000 molecules, that is, by diffuse scattering.
- The additional electric fields due to the optically changed dipole moments exert a torque on the surrounding molecules. The resulting angular reorientation lowers the dipole-dipole interaction energy and stabilizes the charge transfer state. This process changes the ensemble averaged anisotropic X-ray attenuation coefficient towards an isotropic one, resulting in the reflection and transmission changes measured in the experiments. Changes of the layer spacing within a unit cell play a negligible role.
- The dynamics of the optically triggered charge transfer reaction in DIABN are mimicked by the collective inter-molecular changes in geometry, which happen on a 10 picosecond time scale.
- Local conformational changes of the diluted chromophores play a negligible role in the X-ray signal changes.

Future Prospects

Femtosecond time-resolved X-ray diffraction is still a young field of science and promises to make significant contributions to a deeper understanding of microscopic processes by unraveling conformational changes on ultrafast time scales. With the constantly growing expertise in X-ray sources delivering ever shorter and brighter pulses, in particular, with the commission of the Free Electron Laser in Stanford, the range of systems that can be investigated

in the future will comprise more complex solids, and will allow to address questions in chemical and biological physics.

More specifically, the experiment presented in chapter 6 on lattice and polarization dynamics could be complemented by directly manipulating the macroscopic polarization and studying the resulting lattice response. Creation of additional hot electrons by photoexcitation in a ferroelectric material is expected to screen the electric fields and reduce the macroscopic polarization. Interesting questions include how the positively charged ion will move in the changed potential landscape and how its displacement will modify the tetragonal distortion. The time scales of these lattice changes will again reveal information about the coupling of these modes.

While the experiment in section 5.4.2 unambiguously demonstrated magnetostrictive effects in $SrRuO_3$ on a sub-picosecond time-scale, the role of oxygen octahedra rotations could not be determined directly. X-ray absorption spectroscopy or EXAFS (extended X-ray absorption fine structure) in the single scattering regime resolves radial atomic positions in the vicinity of the absorbing atom. XANES (X-ray absorption near edge structure) is governed by multiple scattering and contains information about both the electronic and molecular structure and, hence, may have the potential to measure the oxygen bond angles. Also, resonant X-ray scattering can probe charge ordering and local lattice distortion with high precession [272]. For example, this was demonstrated by measuring the intensity of the forbidden (003) X-ray reflection of a manganite at the La L_{II} edge, stemming from the asphericity of the atomic electron density and, hence, connected to oxygen octahedral tilts directly [273]. However, the ultrafast dynamics of such electronic/structural orderings have remained mostly unexplored and only very few structural sensitive experiments on a subpicosecond timescale have been carried out. A femtosecond X-ray absorption experiment at the soft X-ray slicing source at BESSY, Berlin, used a combination of X-ray magnetic circular dichroism and X-ray absorption measurements to reveal the demagnetization dynamics in nickel with a time resolution of 100 femtoseconds [274]. A further promising femtosecond X-ray absorption experiments on the iron(II)-complex has been carried out in the group of Chergui, at the Swiss Light Source [275].

Further experiments on $SrRuO_3$ are desirable to gain more insight into the ultrafast demagnetization process. Magnetic optical Kerr effect experiments, time-resolved X-ray magnetic dichroism [274, 276] and time-resolved photoemission spectroscopy [199, 277, 278] offer a more direct access to the magnetization and may corroborate the hypothesis for demagnetization proposed in section 5.4.5. Also, a wavelength dependent study in the infrared spectrum promises further interesting insight into the nature of ferromag-

netism in $SrRuO_3$.

The method of time-delay zero determination presented in section 3.3.1 reliably allowed to the set time-delay zero with an accuracy of 100 femtoseconds. Yet, it still requires a calibration by all optical means, which is time consuming and, additionally, only viable in plasma sources. To find an instantaneous X-ray signal exclusively stemming from electronic contributions has not been demonstrated. The forbidden reflection (2 2 2) of diamond or silicon crystals owes its origin to 'lobes' of charge density along the bond directions. Ultrafast optically induced bond-breaking should result in a corresponding modified X-ray Bragg reflectivity. Promising preliminary experiments have been carried out, however, no unambiguous data presently exists. Heterodyne amplification of changes in the (2 2 2) reflection by 'Umweganregung' [279] may present an auspicious approach, in particular for shorter probe X-ray wavelengths. This experiment would not only establish a method of ultrafast cross correlation for time-resoled X-ray science, but would also promise new interesting physics.

The experiment on the molecular crystal DIABN discussed in chapter 7 showed that X-ray signal changes of intramolecular origin are completely masked by a collective response of the polar surrounding. Experiments on powdered samples will only evade this problem for extremely small grain sizes well below 20 nm, such that dissolving the chromophore in a non-polar matrix seems to be the most promising approach. Either doping non-polar crystals with DIABN molecules as impurities, or (partially) aligning DIABN molecules in a (non-polar) stretched polymer should reduce solvation related, collective X-ray signals. Additionally, such complicated systems ultimately require to detect many, high indexed Bragg reflections. This calls for different X-ray scattering geometries, such as the Debye-Scherrer powder method.

Bibliography

[1] P. Corkum, D. Jonas, D. Miller, and A.M. (Eds.) Weiner. *Ultrafast Phenomena XV Proceedings of the 15th International Conference, Pacific Grove, USA, July 30 - August 4, 2006*. Springer, Berlin, 2006.

[2] R. F. Service. Battle to become the next-generation X-ray source. *Science*, 298(5597):1356–1358, 2002.

[3] C. Rischel, A. Rousse, I. Uschmann, P. A. Albouy, J. P. Geindre, P. Audebert, J. C. Gauthier, E. Forster, J. L. Martin, and A. Antonetti. Femtosecond time-resolved X-ray diffraction from laser-heated organic films. *Nature*, 390(6659):490–492, 1997.

[4] C. W. Siders, A. Cavalleri, K. Sokolowski-Tinten, C. Toth, T. Guo, M. Kammler, M. H. von Hoegen, K. R. Wilson, D. von der Linde, and C. P. J. Barty. Detection of nonthermal melting by ultrafast X-ray diffraction. *Science*, 286(5443):1340–1342, 1999.

[5] A. Cavalleri, C. Toth, C. W. Siders, J. A. Squier, F. Raksi, P. Forget, and J. C. Kieffer. Femtosecond structural dynamics in VO2 during an ultrafast solid-solid phase transition. *Physical Review Letters*, 87(23): 237401, 2001.

[6] A. Cavalleri, C. W. Siders, C. Rose-Petruck, R. Jimenez, C. Toth, J. A. Squier, C. P. J. Barty, K. R. Wilson, K. Sokolowski-Tinten, M. H. von Hoegen, and D. von der Linde. Ultrafast X-ray measurement of laser heating in semiconductors: Parameters determining the melting threshold. *Physical Review B*, 6319(193306), 2001.

[7] A. Rousse, C. Rischel, S. Fourmaux, I. Uschmann, S. Sebban, G. Grillon, P. Balcou, E. Foster, J. P. Geindre, P. Audebert, J. C. Gauthier, and D. Hulin. Non-thermal melting in semiconductors measured at femtosecond resolution. *Nature*, 410(6824):65–68, 2001.

[8] K. Sokolowski-Tinten, C. Blome, C. Dietrich, A. Tarasevitch, M. H. von Hoegen, D. von der Linde, A. Cavalleri, J. Squier, and M. Kammler. Femtosecond X-ray measurement of ultrafast melting and large acoustic transients. *Physical Review Letters*, 87(225701), 2001.

[9] K. Sokolowski-Tinten, C. Blome, J. Blums, A. Cavalleri, C. Dietrich, A. Tarasevitch, I. Uschmann, E. Forster, M. Kammler, M. Horn-von Hoegen, and D. von der Linde. Femtosecond X-ray measurement of coherent lattice vibrations near the lindemann stability limit. *Nature*, 422(6929):287–289, 2003.

[10] E. Collet, M. H. Lemee-Cailleau, M. Buron-Le Cointe, H. Cailleau, M. Wulff, T. Luty, S. Y. Koshihara, M. Meyer, L. Toupet, P. Rabiller, and S. Techert. Laser-induced ferroelectric structural order in an organic charge-transfer crystal. *Science*, 300(5619):612–615, 2003.

[11] M. Bargheer, N. Zhavoronkov, Y. Gritsai, J. C. Woo, D. S. Kim, M. Woerner, and T. Elsaesser. Coherent atomic motions in a nanostructure studied by femtosecond X-ray diffraction. *Science*, 306(5702): 1771–1773, 2004.

[12] K. Sokolowski-Tinten and D. von der Linde. Ultrafast phase transitions and lattice dynamics probed using laser-produced X-ray pulses. *Journal of Physics-Condensed Matter*, 16(49):R1517–R1536, 2004.

[13] K. J. Gaffney, A. M. Lindenberg, J. Larsson, K. Sokolowski-Tinten, C. Blome, O. Synnergren, J. Sheppard, C. Caleman, A. G. MacPhee, D. Weinstein, D. P. Lowney, T. Allison, T. Matthews, R. W. Falcone, A. L. Cavalieri, D. M. Fritz, S. H. Lee, P. H. Bucksbaum, D. A. Reis, J. Rudati, A. T. Macrander, P. H. Fuoss, C. C. Kao, D. P. Siddons, R. Pahl, K. Moffat, J. Als-Nielsen, S. Duesterer, R. Ischebeck, H. Schlarb, H. Schulte-Schrepping, J. Schneider, D. von der Linde, O. Hignette, F. Sette, H. N. Chapman, R. W. Lee, T. N. Hansen, J. S. Wark, M. Bergh, G. Huldt, D. van der Spoel, N. Timneanu, J. Hajdu, R. A. Akre, E. Bong, P. Krejcik, J. Arthur, S. Brennan, K. Luening, and J. B. Hastings. Observation of structural anisotropy and the onset of liquidlike motion during the nonthermal melting of InSb. *Physical Review Letters*, 95(125701), 2005.

[14] A. M. Lindenberg, J. Larsson, K. Sokolowski-Tinten, K. J. Gaffney, C. Blome, O. Synnergren, J. Sheppard, C. Caleman, A. G. MacPhee, D. Weinstein, D. P. Lowney, T. K. Allison, T. Matthews, R. W. Falcone, A. L. Cavalieri, D. M. Fritz, S. H. Lee, P. H. Bucksbaum, D. A.

Reis, J. Rudati, P. H. Fuoss, C. C. Kao, D. P. Siddons, R. Pahl, J. Als-Nielsen, S. Duesterer, R. Ischebeck, H. Schlarb, H. Schulte-Schrepping, T. Tschentscher, J. Schneider, D. von der Linde, O. Hignette, F. Sette, H. N. Chapman, R. W. Lee, T. N. Hansen, S. Techert, J. S. Wark, M. Bergh, G. Huldt, D. van der Spoel, N. Timneanu, J. Hajdu, R. A. Akre, E. Bong, P. Krejcik, J. Arthur, S. Brennan, K. Luening, and J. B. Hastings. Atomic-scale visualization of inertial dynamics. *Science*, 308 (5720):392–395, 2005.

[15] A. Cavalleri, S. Wall, C. Simpson, E. Statz, D. W. Ward, K. A. Nelson, M. Rini, and R. W. Schoenlein. Tracking the motion of charges in a terahertz light field by femtosecond X-ray diffraction. *Nature*, 442 (7103):664–666, 2006.

[16] D. M. Fritz, D. A. Reis, B. Adams, R. A. Akre, J. Arthur, C. Blome, P. H. Bucksbaum, A. L. Cavalieri, S. Engemann, S. Fahy, R. W. Falcone, P. H. Fuoss, K. J. Gaffney, M. J. George, J. Hajdu, M. P. Hertlein, P. B. Hillyard, M. H. V. Hoegen, M. Kammler, J. Kaspar, R. Kienberger, P. Krejcik, S. H. Lee, A. M. Lindenberg, B. McFarland, D. Meyer, T. Montagne, E. D. Murray, A. J. Nelson, M. Nicoul, R. Pahl, J. Rudati, H. Schlarb, D. P. Siddons, K. Sokolowski-Tinten, T. Tschentscher, D. von der Linde, and J. B. Hastings. Ultrafast bond softening in bismuth: Mapping a solid's interatomic potential with X-rays. *Science*, 315(5812):633–636, 2007.

[17] H. Enquist, H. Navirian, T. N. Hansen, A. M. Lindenberg, P. Sondhauss, O. Synnergren, J. S. Wark, and J. Larsson. Large acoustic transients induced by nonthermal melting of InSb. *Physical Review Letters*, 98(225502), 2007.

[18] P. B. Hillyard, K. J. Gaffney, A. M. Lindenberg, S. Engemann, R. A. Akre, J. Arthur, C. Blome, P. H. Bucksbaum, A. L. Cavalieri, A. Deb, R. W. Falcone, D. M. Fritz, P. H. Fuoss, J. Hajdu, P. Krejcik, J. Larsson, S. H. Lee, D. A. Meyer, R. Pahl, D. A. Reis, J. Rudati, D. P. Siddons, K. Sokolowski-Tinten, D. von der Linde, and J. B. Hastings. Carrier-density-dependent lattice stability in InSb. *Physical Review Letters*, 98(125501), 2007.

[19] P. Beaud, S. L. Johnson, A. Streun, R. Abela, D. Abramsohn, D. Grolimund, F. Krasniqi, T. Schmidt, V. Schlott, and G. Ingold. Spatiotemporal stability of a femtosecond hard-X-ray undulator source studied by control of coherent optical phonons. *Physical Review Letters*, 99(174801), 2007.

[20] S. L. Johnson, P. Beaud, C. J. Milne, F. S. Krasniqi, E. S. Zijlstra, M. E. Garcia, M. Kaiser, D. Grolimund, R. Abela, and G. Ingold. Nanoscale depth-resolved coherent femtosecond motion in laser-excited bismuth. *Physical Review Letters*, 100(155501), 2008.

[21] A. M. Lindenberg, S. Engemann, K. J. Gaffney, K. Sokolowski-Tinten, J. Larsson, P. B. Hillyard, D. A. Reis, D. M. Fritz, J. Arthur, R. A. Akre, M. J. George, A. Deb, P. H. Bucksbaum, J. Hajdu, D. A. Meyer, M. Nicoul, C. Blome, Th. Tschentscher, A. L. Cavalieri, R. W. Falcone, S. H. Lee, R. Pahl, J. Rudati, P. H. Fuoss, A. J. Nelson, P. Krejcik, D. P. Siddons, P. Lorazo, and J. B. Hastings. X-ray diffuse scattering measurements of nucleation dynamics at femtosecond resolution. *Physical Review Letters*, 100(135502), 2008.

[22] A. Cavalleri, M. Rini, H. H. W. Chong, S. Fourmaux, T. E. Glover, P. A. Heimann, J. C. Kieffer, and R. W. Schoenlein. Band-selective measurements of electron dynamics in VO2 using femtosecond near-edge X-ray absorption. *Physical Review Letters*, 95(067405), 2005.

[23] M. Rini, R. Tobey, N. Dean, J. Itatani, Y. Tomioka, Y. Tokura, R. W. Schoenlein, and A. Cavalleri. Control of the electronic phase of a manganite by mode-selective vibrational excitation. *Nature*, 449(7158):72–74, 2007.

[24] A. Melnikov, I. Radu, U. Bovensiepen, O. Krupin, K. Starke, E. Matthias, and M. Wolf. Coherent optical phonons and parametrically coupled magnons induced by femtosecond laser excitation of the gd(0001) surface. *Physical Review Letters*, 91(227403), 2003.

[25] A. Melnikov, A. Povolotskiy, and U. Bovensiepen. Magnon-enhanced phonon damping at Gd(0001) and Tb(0001) surfaces using femtosecond time-resolved optical second-harmonic generation. *Physical Review Letters*, 100(247401), 2008.

[26] C. Rose-Petruck, R. Jimenez, T. Guo, A. Cavalleri, C. W. Siders, F. Raksi, J. A. Squier, B. C. Walker, K. R. Wilson, and C. P. J. Barty. Picosecond-milliangstrom lattice dynamics measured by ultrafast X-ray diffraction. *Nature*, 398(6725):310–312, 1999.

[27] A. M. Lindenberg, I. Kang, S. L. Johnson, T. Missalla, P. A. Heimann, Z. Chang, J. Larsson, P. H. Bucksbaum, H. C. Kapteyn, H. A. Padmore, R. W. Lee, J. S. Wark, and R. W. Falcone. Time-resolved X-ray

diffraction from coherent phonons during a laser-induced phase transition. *Physical Review Letters*, 84(1):111–114, 2000.

[28] A. Cavalleri, C. W. Siders, F. L. H. Brown, D. M. Leitner, C. Toth, J. A. Squier, C. P. J. Barty, K. R. Wilson, K. Sokolowski-Tinten, M. H. von Hoegen, D. von der Linde, and M. Kammler. Anharmonic lattice dynamics in germanium measured with ultrafast X-ray diffraction. *Physical Review Letters*, 85(3):586–589, 2000.

[29] D. A. Reis, M. F. DeCamp, P. H. Bucksbaum, R. Clarke, E. Dufresne, M. Hertlein, R. Merlin, R. Falcone, H. Kapteyn, M. M. Murnane, J. Larsson, T. Missalla, and J. S. Wark. Probing impulsive strain propagation with X-ray pulses. *Physical Review Letters*, 86(14):3072–3075, 2001.

[30] H. J. Lee, J. Workman, J. S. Wark, R. D. Averitt, A. J. Taylor, J. Roberts, Q. McCulloch, D. E. Hof, N. Hur, S. W. Cheong, and D. J. Funk. Optically induced lattice dynamics probed with ultrafast x-ray diffraction. *Physical Review B*, 77(132301), 2008.

[31] A. H. Chin, R. W. Schoenlein, T. E. Glover, P. Balling, W. P. Leemans, and C. V. Shank. Ultrafast structural dynamics in InSb probed by time-resolved X-ray diffraction. *Physical Review Letters*, 83(2):336–339, 1999.

[32] D. L. D. Caspar, J. Clarage, D. M. Salunke, and M. Clarage. Liquid-like movements in crystalline insulin. *Nature*, 332(6165):659–662, 1988.

[33] J. Doucet and J. P. Benoit. Molecular-dynamics studied by analysis of the X-ray diffuse-scattering from lysozyme crystals. *Nature*, 325(6105): 643–646, 1987.

[34] G. U. Nienhaus, J. Heinzl, E. Huenges, and F. Parak. Protein crystal dynamics studied by time-resolved analysis of X-ray diffuse-scattering. *Nature*, 338(6217):665–666, 1989.

[35] A. Plech, M. Wulff, S. Bratos, F. Mirloup, R. Vuilleumier, F. Schotte, and P. A. Anfinrud. Visualizing chemical reactions in solution by picosecond X-ray diffraction. *Physical Review Letters*, 92(125505), 2004.

[36] H. Ihee, M. Lorenc, T. K. Kim, Q. Y. Kong, M. Cammarata, J. H. Lee, S. Bratos, and M. Wulff. Ultrafast X-ray diffraction of transient molecular structures in solution. *Science*, 309(5738):1223–1227, 2005.

[37] M. Cammarata, M. Lorenc, T. K. Kim, J. H. Lee, Q. Y. Kong, E. Pontecorvo, M. Lo Russo, G. Schiro, A. Cupane, M. Wulff, and H. Ihee. Impulsive solvent heating probed by picosecond X-ray diffraction. *Journal of Chemical Physics*, 124(12), 2006.

[38] John D Jackson. *Classical Electrodynamics*. Wiley, New York, 2. ed. edition, 1975.

[39] E. Prince Ed. *International Tables of Crystallography, Vol.C*. Springer, Berlin, 2004.

[40] B. L. Henke, E. M. Gullikson, and J. C. Davis. X-ray interactions - photoabsorption, scattering, transmission, and reflection at E=50-30,000 eV, Z=1-92. *Atomic Data and Nuclear Data Tables*, 54(2):181–342, 1993.

[41] B. E. Warren. *X-Ray Diffraction*. Addison-Wesley, Reading, Massachusetts, 1969.

[42] Des McMorrow Jens Als-Nielsen. *Elements of Modern X-ray Physics*. John Wiley and Sons Ltd, New York, 2001.

[43] L.D. Landau and E.M. Lifschitz. *Lehrbuch der theoretischen Physik*, volume II, Feldtheorie. Akademie Verlag, Berlin, 1963.

[44] T. R. Welberry and B. D. Butler. Diffuse-X-ray scattering from disordered crystals. *Chemical Reviews*, 95(7):2369–2403, 1995.

[45] José Luis Amorós and Marisa Amorós. *Molecular Crystals: Their Transforms and Diffuse Scattering*. John Wiley and Sons Ltd, New York, 1968.

[46] Wolfgang Hrsg. v. Bauer, Günther / Richter. *Optical Characterization of Epitaxial Semiconductor Layers*. Springer, Berlin, 1995.

[47] P. F. Fewster. X-ray-diffraction from low-dimensional structures. *Semiconductor Science and Technology*, 8(11):1915–1934, 1993.

[48] P. F. Fewster. High-resolution diffraction-space mapping and topography. *Applied Physics a-Materials Science & Processing*, 58(3):121–127, 1994.

[49] P. Vandersluis, J. J. M. Binsma, and T. Vandongen. High-resolution X-ray-diffraction of periodic surface gratings. *Applied Physics Letters*, 62(24):3186–3188, 1993.

[50] Mario Birkholz. *Thin Film Analysis by X-Ray Scattering*. Wiley-VCH, Weinheim, 2005.

[51] C. G. Darwin. The theory of x-ray reflexion. part ii. *Phil. Mag.*, 27: 675, 1914.

[52] M Fiebig. Revival of the magnetoelectric effect. *JOURNAL OF PHYSICS D-APPLIED PHYSICS*, 38(8):R123–R152, APR 21 2005. ISSN 0022-3727.

[53] G. Shirane, R. Pepinsky, and B. C. Frazer. X-ray and neutron diffraction study of ferroelectric $PbTiO_3$. *Acta Crystallographica*, 9(2):131–140, 1956.

[54] S. Yamanaka, T. Maekawa, H. Muta, T. Matsuda, S. Kobayashi, and K. Kurosaki. Thermophysical properties of $SrHfO_3$ and $SrRuO_3$. *Journal of Solid State Chemistry*, 177(10):3484–3489, 2004.

[55] C. B. Eom, R. B. Vandover, J. M. Phillips, D. J. Werder, J. H. Marshall, C. H. Chen, R. J. Cava, R. M. Fleming, and D. K. Fork. Fabrication and properties of epitaxial ferroelectric heterostructures with ($SrRuO_3$) isotropic metallic oxide electrodes. *Applied Physics Letters*, 63(18): 2570–2572, 1993.

[56] Q. Gan, R. A. Rao, C. B. Eom, L. Wu, and F. Tsui. Lattice distortion and uniaxial magnetic anisotropy in single domain epitaxial (110) films of $SrRuO_3$. *Journal of Applied Physics*, 85(8):5297–5299, 1999.

[57] K. A. Muller and H. Burkard. $SrTiO_3$ - intrinsic quantum para-electric below 4-k. *Physical Review B*, 19(7):3593–3602, 1979.

[58] P. A. Fleury, J. F. Scott, and J. M. Worlock. Soft phonon modes and 110 degrees k phase transition in $SrTiO_3$. *Physical Review Letters*, 21 (1):16–19, 1968.

[59] Kittel. *Solid state physics*. John Wiley and Sons, New York, 1977.

[60] Neil W. Ashcroft and N. David Mermin. *Festkörperphysik*. Oldenburg Verlag, Munich, 2001.

[61] A. S. Barker, J. L. Merz, and A. C. Gossard. Study of zone-folding effects on phonons in alternating monolayers of gaas-alas. *Physical Review B*, 17(8):3181–3196, 1978.

[62] C. Colvard, T. A. Gant, M. V. Klein, R. Merlin, R. Fischer, H. Morkoc, and A. C. Gossard. Folded acoustic and quantized optic phonons in (GaAl)As superlattices. *Physical Review B*, 31(4):2080–2091, 1985.

[63] M. Bargheer, N. Zhavoronkov, M. Woerner, and T. Elsaesser. Recent progress in ultrafast X-ray diffraction. *Chemphyschem*, 7(4):783–792, 2006.

[64] A. Rousse, C. Rischel, and J. C. Gauthier. Colloquium: Femtosecond X-ray crystallography. *Reviews of Modern Physics*, 73(1):17–31, 2001.

[65] M. F. DeCamp, D. A. Reis, P. H. Bucksbaum, B. Adams, J. M. Caraher, R. Clarke, C. W. S. Conover, E. M. Dufresne, R. Merlin, V. Stoica, and J. K. Wahlstrand. Coherent control of pulsed X-ray beams. *Nature*, 413(6858):825–828, 2001.

[66] J. Larsson, A. Allen, P. H. Bucksbaum, R. W. Falcone, A. Lindenberg, G. Naylor, T. Missalla, D. A. Reis, K. Scheidt, A. Sjogren, P. Sondhauss, M. Wulff, and J. S. Wark. Picosecond X-ray diffraction studies of laser-excited acoustic phonons in InSb. *Applied Physics a-Materials Science & Processing*, 75(4):467–478, 2002.

[67] A. M. Lindenberg, I. Kang, S. L. Johnson, R. W. Falcone, P. A. Heimann, Z. Chang, R. W. Lee, and J. S. Wark. Coherent control of phonons probed by time-resolved X-ray diffraction. *Optics Letters*, 27(10):869–871, 2002.

[68] O. Synnergren, M. Harbst, T. Missalla, J. Larsson, G. Katona, R. Neutze, and R. Wouts. Projecting picosecond lattice dynamics through X-ray topography. *Applied Physics Letters*, 80(20):3727–3729, 2002.

[69] M. F. DeCamp, D. A. Reis, A. Cavalieri, P. H. Bucksbaum, R. Clarke, R. Merlin, E. M. Dufresne, D. A. Arms, A. M. Lindenberg, A. G. MacPhee, Z. Chang, B. Lings, J. S. Wark, and S. Fahy. Transient strain driven by a dense electron-hole plasma. *Physical Review Letters*, 91(165502), 2003.

[70] O. Synnergren, T. N. Hansen, S. Canton, H. Enquist, P. Sondhauss, A. Srivastava, and J. Larsson. Coherent phonon control. *Applied Physics Letters*, 90(17):3, 2007.

[71] F. Schotte, M. H. Lim, T. A. Jackson, A. V. Smirnov, J. Soman, J. S. Olson, G. N. Phillips, M. Wulff, and P. A. Anfinrud. Watching a

protein as it functions with 150-ps time-resolved X-ray crystallography. *Science*, 300(5627):1944–1947, 2003.

[72] R. W. Schoenlein, W. P. Leemans, A. H. Chin, P. Volfbeyn, T. E. Glover, P. Balling, M. Zolotorev, K. J. Kim, S. Chattopadhyay, and C. V. Shank. Femtosecond X-ray pulses at 0.4 Angstrom generated by 90 degrees Thomson scattering: A tool for probing the structural dynamics of materials. *Science*, 274(5285):236–238, 1996.

[73] R. W. Schoenlein, S. Chattopadhyay, H. H. W. Chong, T. E. Glover, P. A. Heimann, C. V. Shank, A. A. Zholents, and M. S. Zolotorev. Generation of femtosecond pulses of synchrotron radiation. *Science*, 287(5461):2237–2240, 2000.

[74] G. Ingold, M. Boege, W. Bulgheroni, A. Keller, J. Krempaski, C. Schulze-Briese, L. Schulz, T. Schmidt, D. Zimoch, T. Hara, T. Tanaka, and H. Kitamura. Performance of small-gap undulators at the SLS intermediate energy storage ring. *AIP Conference Proceedings*, 879(1):388–391, 2007.

[75] S. Khan, K. Holldack, T. Kachel, R. Mitzner, and T. Quast. Femtosecond undulator radiation from sliced electron bunches. *Physical Review Letters*, 97(074801), 2006.

[76] K. Holldack, S. Khan, R. Mitzner, and T. Quast. Femtosecond terahertz radiation from femtoslicing at BESSY. *Physical Review Letters*, 96(054801), 2006.

[77] A. L. Cavalieri, D. M. Fritz, S. H. Lee, P. H. Bucksbaum, D. A. Reis, J. Rudati, D. M. Mills, P. H. Fuoss, G. B. Stephenson, C. C. Kao, D. P. Siddons, D. P. Lowney, A. G. MacPhee, D. Weinstein, R. W. Falcone, R. Pahl, J. Als-Nielsen, C. Blome, S. Dusterer, R. Ischebeck, H. Schlarb, H. Schulte-Schrepping, T. Tschentscher, J. Schneider, O. Hignette, F. Sette, K. Sokolowski-Tinten, H. N. Chapman, R. W. Lee, T. N. Hansen, O. Synnergren, J. Larsson, S. Techert, J. Sheppard, J. S. Wark, M. Bergh, C. Caleman, G. Huldt, D. van der Spoel, N. Timneanu, J. Hajdu, R. A. Akre, E. Bong, P. Emma, P. Krejcik, J. Arthur, S. Brennan, K. J. Gaffney, A. M. Lindenberg, K. Luening, and J. B. Hastings. Clocking femtosecond X-rays. *Physical Review Letters*, 94(114801), 2005.

[78] M. Ferray, A. Lhuillier, X. F. Li, L. A. Lompre, G. Mainfray, and C. Manus. Multiple-harmonic conversion of 1064-nm radiation in rare-

gases. *Journal of Physics B-Atomic Molecular and Optical Physics*, 21 (3):L31–L35, 1988.

[79] Z. H. Chang, A. Rundquist, H. W. Wang, M. M. Murnane, and H. C. Kapteyn. Generation of coherent soft X rays at 2.7 nm using high harmonics. *Physical Review Letters*, 79(16):2967–2970, 1997.

[80] M. Drescher, M. Hentschel, R. Kienberger, G. Tempea, C. Spielmann, G. A. Reider, P. B. Corkum, and F. Krausz. X-ray pulses approaching the attosecond frontier. *Science*, 291(5510):1923–1927, 2001.

[81] C. Winterfeldt, C. Spielmann, and G. Gerber. Colloquium: Optimal control of high-harmonic generation. *Reviews of Modern Physics*, 80 (1):117–140, 2008.

[82] J. Seres, P. Wobrauschek, C. Streli, V. S. Yakovlev, E. Seres, F. Krausz, and C. Spielmann. Generation of coherent keV X-rays with intense femtosecond laser pulses. *New Journal of Physics*, 8, 2006.

[83] M. M. Murnane, H. C. Kapteyn, M. D. Rosen, and R. W. Falcone. Ultrafast X-ray pulses from laser-produced plasmas. *Science*, 251(4993): 531–536, 1991.

[84] A. Rousse, P. Audebert, J. P. Geindre, F. Fallies, J. C. Gauthier, A. Mysyrowicz, G. Grillon, and A. Antonetti. Efficient K-alpha-X-ray source from femtosecond laser-produced plasmas. *Physical Review E*, 50(3):2200–2207, 1994.

[85] G. Korn, A. Thoss, H. Stiel, U. Vogt, M. Richardson, T. Elsaesser, and M. Faubel. Ultrashort 1-kHz laser plasma hard X-ray source. *Optics Letters*, 27(10):866–868, 2002.

[86] Y. Jiang, T. W. Lee, W. Li, G. Ketwaroo, and C. G. Rose-Petruck. High-average-power 2-kHz laser for generation of ultrashort X-ray pulses. *Optics Letters*, 27(11):963–965, 2002.

[87] C. Reich, C. M. Laperle, X. D. Li, B. Ahr, F. Benesch, and C. G. Rose-Petruck. Ultrafast X-ray pulses emitted from a liquid mercury laser target. *Optics Letters*, 32(4):427–429, 2007.

[88] W. Fullagar, M. Harbst, S. Canton, J. Uhlig, M. Walczak, C. G. Wahlstrom, and V. Sundstrom. A broadband laser plasma X-ray source for application in ultrafast chemical structure dynamics. *Review of Scientific Instruments*, 78(11), 2007.

[89] H.-P. Schlenvoigt, K. Haupt, A. Debus, F. Budde, O. Jackel, S. Pfotenhauer, H. Schwoerer, E. Rohwer, J. G. Gallacher, E. Brunetti, R. P. Shanks, S. M. Wiggins, and D. A. Jaroszynski. A compact synchrotron radiation source driven by a laser-plasma wakefield accelerator. *Nature Physics*, 4:745–2473, 2008.

[90] N. Zhavoronkov, Y. Gritsai, G. Korn, and T. Elsaesser. Ultra-short efficient laser-driven hard X-ray source operated at a kHz repetition rate. *Applied Physics B-Lasers and Optics*, 79(6):663–667, 2004.

[91] N. Zhavoronkov and G. Korn. Regenerative amplification of femtosecond laser pulses in Ti:sapphire at multikilohertz repetition rates. *Optics Letters*, 29(2):198–200, 2004.

[92] R. A. Kaindl, M. Wurm, K. Reimann, P. Hamm, A. M. Weiner, and M. Woerner. Generation, shaping, and characterization of intense femtosecond pulses tunable from 3 to 20 μm. *Journal of the Optical Society of America B-Optical Physics*, 17(12):2086–2094, 2000.

[93] Vitalij L Ginzburg. *Propagation of electromagnetic waves in plasma*. Gordon & Breach, New York, 1961.

[94] R. P. Godwin. Optical mechanism for enhanced absorption of laser energy incident on solid targets. *Physical Review Letters*, 28(2):85–87, 1972.

[95] U. Teubner, J. Bergmann, B. Vanwonterghem, F. P. Schafer, and R. Sauerbrey. Angle-dependent X-ray-emission and resonance-absorption in a laser-produced plasma generated by a high-intensity ultrashort pulse. *Physical Review Letters*, 70(6):794–797, 1993.

[96] S. Bastiani, A. Rousse, J. P. Geindre, P. Audebert, C. Quoix, G. Hamoniaux, A. Antonetti, and J. C. Gauthier. Experimental study of the interaction of subpicosecond laser pulses with solid targets of varying initial scale lengths. *Physical Review E*, 56(6):7179–7185, 1997.

[97] D. C. Eder, G. Pretzler, E. Fill, K. Eidmann, and A. Saemann. Spatial characteristics of K-alpha radiation from weakly relativistic laser plasmas. *Applied Physics B-Lasers and Optics*, 70(2):211–217, 2000.

[98] F. Brunel. Not-so-resonant, resonant absorption. *Physical Review Letters*, 59(1):52–55, 1987.

[99] H. Schwoerer, P. Gibbon, S. Dusterer, R. Behrens, C. Ziener, C. Reich, and R. Sauerbrey. Mev X-rays and photoneutrons from femtosecond laser-produced plasmas. *Physical Review Letters*, 86(11):2317–2320, 2001.

[100] G. Malka and J. L. Miquel. Experimental confirmation of ponderomotive-force electrons produced by an ultrarelativistic laser pulse on a solid target. *Physical Review Letters*, 77(1):75–78, 1996.

[101] M. Hagedorn, J. Kutzner, G. Tsilimis, and H. Zacharias. High-repetition-rate hard X-ray generation with sub-millijoule femtosecond laser pulses. *Applied Physics B-Lasers and Optics*, 77(1):49–57, 2003.

[102] V. M. Gordienko, I. M. Lachko, P. M. Mikheev, A. B. Savel'ev, D. S. Uryupina, and R. V. Volkov. Experimental characterization of hot electron production under femtosecond laser plasma interaction at moderate intensities. *Plasma Physics and Controlled Fusion*, 44(12):2555–2568, 2002.

[103] S. C. Wilks, W. L. Kruer, M. Tabak, and A. B. Langdon. Absorption of ultra-intense laser-pulses. *Physical Review Letters*, 69(9):1383–1386, 1992.

[104] C. Reich, P. Gibbon, I. Uschmann, and E. Forster. Yield optimization and time structure of femtosecond laser plasma K alpha sources. *Physical Review Letters*, 84(21):4846–4849, 2000.

[105] F. N. Beg, A. R. Bell, A. E. Dangor, C. N. Danson, A. P. Fews, M. E. Glinsky, B. A. Hammel, P. Lee, P. A. Norreys, and M. Tatarakis. A study of picosecond laser-solid interactions up to 10^{19} W/cm^{-2}. *Physics of Plasmas*, 4(2):447–457, 1997.

[106] N. Zhavoronkov, Y. Gritsai, M. Bargheer, M. Woerner, T. Elsaesser, F. Zamponi, I. Uschmann, and E. Forster. Microfocus Cu K-alpha source for femtosecond x-ray science. *Optics Letters*, 30(13):1737–1739, 2005.

[107] N. Zhavoronkov, Y. Gritsai, M. Bargheer, M. Woerner, and T. Elsaesser. Generation of ultrashort K-alpha radiation from quasipoint interaction area of femtosecond pulses with thin foils. *Applied Physics Letters*, 86(244107), 2005.

[108] N. Zhavoronkov, C. von Korff Schmising, M. Bargheer, M. Woerner, T. Elsaesser, O. Klimo, and J. Limpouch. High repetition rate ultrafast

X-ray source from the fs-laser-produced-plasma. *Journal De Physique Iv*, 133:1201–1203, 2006.

[109] P. Rez. Electron ionization cross-sections for K-shell, L-shell and M-shell. *X-Ray Spectrometry*, 13(2):55–59, 1984.

[110] M. T. Liu, Z. An, C. H. Tang, Z. M. Luo, X. F. Peng, and X. G. Long. Experimental electron-impact K-shell ionization cross sections. *Atomic Data and Nuclear Data Tables*, 76(2):213–234, 2000.

[111] F. Ewald, H. Schwoerer, and R. Sauerbrey. K-alpha-radiation from relativistic laser-produced plasmas. *Europhysics Letters*, 60(5):710–716, 2002.

[112] Y. Kobayashi, T. Ohno, T. Sekikawa, Y. Nabekawa, and S. Watanabe. Pulse width measurement of high-order harmonics by autocorrelation. *Applied Physics B-Lasers and Optics*, 70(3):389–394, 2000.

[113] T. Sekikawa, T. Katsura, S. Miura, and S. Watanabe. Measurement of the intensity-dependent atomic dipole phase of a high harmonic by frequency-resolved optical gating. *Physical Review Letters*, 88(193902), 2002.

[114] J. M. Schins, P. Breger, P. Agostini, R. C. Constantinescu, H. G. Muller, G. Grillon, A. Antonetti, and A. Mysyrowicz. Observation of laser-assisted auger decay in argon. *Physical Review Letters*, 73(16): 2180–2183, 1994.

[115] J. M. Schins, P. Breger, P. Agostini, R. C. Constantinescu, H. G. Muller, A. Bouhal, G. Grillon, A. Antonetti, and A. Mysyrowicz. Cross-correlation measurements of femtosecond extreme-ultraviolet high-order harmonics. *Journal of the Optical Society of America B-Optical Physics*, 13(1):197–200, 1996.

[116] A. Bouhal, R. Evans, G. Grillon, A. Mysyrowicz, P. Breger, P. Agostini, R. C. Constantinescu, H. G. Muller, and D. vonderLinde. Cross-correlation measurement of femtosecond noncollinear high-order harmonics. *Journal of the Optical Society of America B-Optical Physics*, 14(4):950–956, 1997.

[117] T. E. Glover, R. W. Schoenlein, A. H. Chin, and C. V. Shank. Observation of laser assisted photoelectric effect and femtosecond high order harmonic radiation. *Physical Review Letters*, 76(14):2468–2471, 1996.

[118] E. S. Toma, H. G. Muller, P. M. Paul, P. Breger, M. Cheret, P. Agostini, C. Le Blanc, G. Mullot, and G. Cheriaux. Ponderomotive streaking of the ionization potential as a method for measuring pulse durations in the XUV domain with fs resolution. *Physical Review A*, 6206(061801), 2000.

[119] M. Drescher, M. Hentschel, R. Kienberger, M. Uiberacker, V. Yakovlev, A. Scrinizi, T. Westerwalbesloh, U. Kleineberg, U. Heinzmann, and F. Krausz. Time-resolved atomic inner-shell spectroscopy. *Nature*, 419 (6909):803–807, 2002.

[120] P. H. Citrin, Eisenber.Pm, W. C. Marra, T. Aberg, Utriaine.J, and E. Kallne. Linewidths in X-ray photoemission and X-ray-emission spectroscopies - what do they measure. *Physical Review B*, 10(4):1762–1765, 1974.

[121] Cornelius Gahl, Armin Azima, Martin Beye, Martin Deppe, Kristian Doebrich, Urs Hasslinger, Franz Hennies, Alexej Melnikov, Mitsuru Nagasono, Annette Pietzsch, Martin Wolf, Wilfried Wurth, and Alexander Foehlisch. A femtosecond X-ray/optical cross-correlator. *NATURE PHOTONICS*, 2(3):165–169, MAR 2008.

[122] H. Navirian, H. Enquist, T. N. Hansen, A. Mikkelsen, P. Sondhauss, A. Srivastava, A. A. Zakharov, and J. Larsson. Repetitive ultrafast melting of InSb as an X-ray timing diagnostic. *Journal of Applied Physics*, 103(10), 2008.

[123] C. von Korff Schmising, M. Bargheer, M. Kiel, N. Zhavoronkov, M. Woerner, T. Elsaesser, I. Vrejoiu, D. Hesse, and M. Alexe. Accurate time delay determination for femtosecond X-ray diffraction experiments. *Applied Physics B-Lasers and Optics*, 88(1):1–4, 2007.

[124] M. Braun, C. von Korff Schmising, M. Kiel, N. Zhavoronkov, J. Dreyer, M. Bargheer, T. Elsaesser, C. Root, T. E. Schrader, P. Gilch, W. Zinth, and M. Woerner. Ultrafast changes of molecular crystal structure induced by dipole solvation. *Physical Review Letters*, 98(248301), 2007.

[125] M. Bargheer, N. Zhavoronkov, R. Bruch, H. Legall, H. Stiel, M. Woerner, and T. Elsaesser. Comparison of focusing optics for femtosecond x-ray diffraction. *Applied Physics B-Lasers and Optics*, 80(6):715–719, 2005.

[126] P. Kirkpatrick and A. V. Baez. Formation of optical images by x-rays. *Journal of the Optical Society of America*, 38(9):766–774, 1948.

[127] J.-M. Triscone (Eds.) K. Rabe, Ch. H. Ahn. *Physics of Ferroelectrics: A Modern Perspective (105 Topics in Applied Physics)*. Springer, Berlin, 2007.

[128] K. J. Choi, M. Biegalski, Y. L. Li, A. Sharan, J. Schubert, R. Uecker, P. Reiche, Y. B. Chen, X. Q. Pan, V. Gopalan, L. Q. Chen, D. G. Schlom, and C. B. Eom. Enhancement of ferroelectricity in strained $BaTiO_3$ thin films. *Science*, 306(5698):1005–1009, 2004.

[129] L. Pintilie, M. Lisca, and M. Alexe. Polarization reversal and capacitance-voltage characteristic of epitaxial $Pb(Zr,Ti)O_3$ layers. *Applied Physics Letters*, 86(192902):3, 2005.

[130] M. Tanaka and G. Honjo. Electron optical studies of barium titanate single crystal films. *Journal of the Physical Society of Japan*, 19(6): 954–970, 1964.

[131] S. Takenaka and H. Kozuka. Sol-gel preparation of single-layer, 0.75 mu m thick lead zirconate titanate films from lead nitrate-titanium and zirconium alkoxide solutions containing polyvinylpyrrolidone. *Applied Physics Letters*, 79(21):3485–3487, 2001.

[132] P. Kostic, Y. Okada, N. C. Collins, Z. Schlesinger, J. W. Reiner, L. Klein, A. Kapitulnik, T. H. Geballe, and M. R. Beasley. Non-fermi-liquid behavior of $SrRuO_3$: Evidence from infrared conductivity. *Physical Review Letters*, 81(12):2498–2501, 1998.

[133] M. I. Cohen and R. F. Blunt. Optical properties of $SrTiO_3$ in region of absorption edge. *Physical Review*, 168(3):929–933, 1968.

[134] C. Thomsen, H. T. Grahn, H. J. Maris, and J. Tauc. Surface generation and detection of phonons by picosecond light-pulses. *Physical Review B*, 34(6):4129–4138, 1986.

[135] R. O. Bell and G. Rupprecht. Elastic constants of strontium titanate. *Physical Review*, 1(1):90–94, 1963.

[136] M. Kahn. Acoustic and elastic properties of PZT ceramics with anisotropic pores. *Journal of the American Ceramic Society*, 68(11): 623–628, 1985.

[137] Z. Li, M. Grimsditch, C. M. Foster, and S. K. Chan. Dielectric and elastic properties of ferroelectric materials at elevated temperature. *Journal of Physics and Chemistry of Solids*, 57(10):1433–1438, 1996.

[138] A. G. Kalinichev, J. D. Bass, B. N. Sun, and D. A. Payne. Elastic properties of tetragonal $PbTiO_3$ single crystals by Brillouin scattering. *Journal of Materials Research*, 12(10):2623–2627, 1997.

[139] P. Kuzel, C. Dugautier, P. Moch, F. Le Marrec, and M. G. Karkut. Phase transition in lead titanate thin films: a Brillouin study. *Journal of Physics-Condensed Matter*, 14(47):12287–12300, 2002.

[140] A Bruchhausen, N. D. Lanzillotti-Kimura, A. Fainstein, A. Soukiassian, D. A. Tenne, D. Schlom, X. X. Xi, and A. Cantarero. Acoustic properties of nanoscale oxide heterostructures probed by UV Raman spectroscopy. *Journal of Physics: Conference series (IOP)*, 92(December): 012160, 2007.

[141] Y. A. Abramov, V. G. Tsirelson, V. E. Zavodnik, S. A. Ivanov, and I. D. Brown. The chemical bond and atomic displacements in $SrTiO_3$ from x-ray diffraction analysis. *Acta Crystallographica Section B-Structural Science*, 51:942–951, 1995.

[142] M. I. Kaganov, I. M. Lifshitz, and L. V. Tanatarov. Relaxation between electrons and the crystalline lattice. *Soviet Physics Jetp-Ussr*, 4(2): 173–178, 1957.

[143] T. H. K. Barron, J. G. Collins, and G. K. White. Thermal-expansion of solids at low-temperatures. *Advances in Physics*, 29(4):609–730, 1980.

[144] M. Born. *Dynamical Theory of Crystal Lattices*. Clarendon Press, Oxford, 1954.

[145] D. N. Talwar and M. Vandevyver. Pressure-dependent phonon properties of iii-v compound semiconductors. *Physical Review B*, 41(17): 12129–12139, 1990.

[146] H. Park, X. Wang, S. Nie, R. Clinite, and J. Cao. Mechanism of coherent acoustic phonon generation under nonequilibrium conditions. *Physical Review B*, 72(100301):4, 2005.

[147] S. H. Nie, X. Wang, H. Park, R. Clinite, and J. M. Cao. Measurement of the electronic Grüneisen constant using femtosecond electron diffraction. *Physical Review Letters*, 96(025901), 2006.

[148] G. L. Eesley. Observation of non-equilibrium electron heating in copper. *Physical Review Letters*, 51(23):2140–2143, 1983.

[149] J. G. Fujimoto, J. M. Liu, E. P. Ippen, and N. Bloembergen. Femtosecond laser interaction with metallic tungsten and nonequilibrium electron and lattice temperatures. *Physical Review Letters*, 53(19): 1837–1840, 1984.

[150] R. W. Schoenlein, W. Z. Lin, J. G. Fujimoto, and G. L. Eesley. Femtosecond studies of nonequilibrium electronic processes in metals. *Physical Review Letters*, 58(16):1680–1683, 1987.

[151] P. B. Corkum, F. Brunel, N. K. Sherman, and T. Srinivasanrao. Thermal response of metals to ultrashort-pulse laser excitation. *Physical Review Letters*, 61(25):2886–2889, 1988.

[152] P. B. Allen. Theory of thermal relaxation of electrons in metals. *Physical Review Letters*, 59(13):1460–1463, 1987.

[153] S. D. Brorson, J. G. Fujimoto, and E. P. Ippen. Femtosecond electronic heat-transport dynamics in thin gold-films. *Physical Review Letters*, 59 (17):1962–1965, 1987.

[154] G. Tas and H. J. Maris. Electron-diffusion in metals studied by picosecond ultrasonics. *Physical Review B*, 49(21):15046–15054, 1994.

[155] M. Woerner, W. Frey, M. T. Portella, C. Ludwig, T. Elsaesser, and W. Kaiser. Ultrafast thermalization of nonequilibrium holes in p-type germanium studied by femtosecond infrared-spectroscopy. *Physical Review B*, 49(24):17007–17010, 1994.

[156] M. Woerner and T. Elsaesser. Ultrafast thermalization of nonequilibrium holes in p-type tetrahedral semiconductors. *Physical Review B*, 51(24):17490–17498, 1995.

[157] M. Bargheer, N. Zhavoronkov, J. C. Woo, D. S. Kim, M. Woerner, and T. Elsaesser. Excitation mechanisms of coherent phonons unravelled by femtosecond X-ray diffraction. *Physica Status Solidi B-Basic Solid State Physics*, 243(10):2389–2396, 2006.

[158] W. Hong, H. N. Lee, M. Yoon, H. M. Christen, D. H. Lowndes, Z. G. Suo, and Z. Y. Zhang. Persistent step-flow growth of strained films on vicinal substrates. *Physical Review Letters*, 95(095501), 2005.

[159] C.B. Carter D.B. Williams. *Transmission Electron Microscopy: A Textbook in Materials Science.* Plenum Press, New York, 1996.

[160] B. Alefeld. Change of lattice parameters of $SrTiO_3$ near phase transition at 108 degrees K. *Zeitschrift Fur Physik*, 222(2):155–164, 1969.

[161] F. W. Lytle. X-ray diffractometry of low-temperature phase transformations in strontium titanate. *Journal of Applied Physics*, 35(7): 2212–2215, 1964.

[162] A. Heideman and H. Wettenge. Change of lattice-parameters of $SrTiO_3$. *Zeitschrift Fur Physik*, 258(5):429–438, 1973.

[163] T. Kiyama, K. Yoshimura, K. Kosuge, Y. Ikeda, and Y. Bando. Invar effect of $SrRuO_3$: Itinerant electron magnetism of Ru 4d electrons. *Physical Review B*, 54(2):R756–R759, 1996.

[164] D. Kirillov, Y. Suzuki, L. Antognazza, K. Char, I. Bozovic, and T. H. Geballe. Phonon anomalies at the magnetic phase-transition in $SrRuO_3$. *Physical Review B*, 51(18):12825–12828, 1995.

[165] M. N. Iliev, A. P. Litvinchuk, H. G. Lee, C. L. Chen, M. L. Dezaneti, C. W. Chu, V. G. Ivanov, M. V. Abrashev, and V. N. Popov. Raman spectroscopy of $SrRuO_3$ near the paramagnetic-to-ferromagnetic phase transition. *Physical Review B*, 59(1):364–368, 1999.

[166] E. Beaurepaire, J. C. Merle, A. Daunois, and J. Y. Bigot. Ultrafast spin dynamics in ferromagnetic nickel. *Physical Review Letters*, 76(22): 4250–4253, 1996.

[167] G. P. Zhang, W. Hubner, E. Beaurepaire, and J. Y. Bigot. Laser-induced ultrafast demagnetization: Femtomagnetism, a new frontier? In *Spin Dynamics in Confined Magnetic Structures I*, volume 83 of *Topics in Applied Physics*, pages 245–288. Springer-Verlag Berlin, Berlin, 2002.

[168] B. Koopmans. Laser-induced magnetization dynamics. In *Spin Dynamics in Confined Magnetic Structures II*, volume 87 of *Topics in Applied Physics*, pages 253–316. Springer-Verlag Berlin, Berlin, 2003.

[169] J. Hohlfeld, E. Matthias, R. Knorren, and K. H. Bennemann. Nonequilibrium magnetization dynamics of nickel. *Physical Review Letters*, 78 (25):4861–4864, 1997.

[170] A. Scholl, L. Baumgarten, R. Jacquemin, and W. Eberhardt. Ultrafast spin dynamics of ferromagnetic thin films observed by fs spin-resolved two-photon photoemission. *Physical Review Letters*, 79(25):5146–5149, 1997.

[171] G. P. Zhang and W. Hubner. Laser-induced ultrafast demagnetization in ferromagnetic metals. *Physical Review Letters*, 85(14):3025–3028, 2000.

[172] T. Ogasawara, K. Ohgushi, Y. Tomioka, K. S. Takahashi, H. Okamoto, M. Kawasaki, and Y. Tokura. General features of photoinduced spin dynamics in ferromagnetic and ferrimagnetic compounds. *Physical Review Letters*, 94(8):4, 2005.

[173] Klaus Elk and Wilmut Gasser. *Die Methode der Greenschen Funktionen in der Festkörperphysik*. Akademie-Verlag, Berlin, 1979.

[174] E. C. Stoner. Collective electron ferromagnetism. *Proceedings of the Royal Society of London Series a-Mathematical and Physical Sciences*, 165(A922):0372–0414, 1938.

[175] E. C. Stoner. Collective electron ferromagnetism ii. energy and specific heat. *Proceedings of the Royal Society of London Series a-Mathematical and Physical Sciences*, 169(A938):0339–0371, 1939.

[176] M. Itoh, M. Shikano, and T. Shimura. High-spin and low-spin transition of Ru^{4+} in the perovskite-related layered system $Sr_{N+1}Ru_NO_{3N+1}$ (n=1, 2, and infinity) with the change in n. *Physical Review B*, 51(22): 16432–16435, 1995.

[177] A. Callagha, C. W. Moeller, and R. Ward. Magnetic interactions in ternary ruthenium oxides. *Inorganic Chemistry*, 5(9):1572–&, 1966.

[178] J. M. Longo, P. M. Raccah, and J. B. Goodenou. Magnetic properties of $SrRuO_3$ and $CaRuO_3$. *Journal of Applied Physics*, 39(2P2):1327–&, 1968.

[179] S. N. Bushmeleva, V. Y. Pomjakushin, E. V. Pomjakushina, D. V. Sheptyakov, and A. M. Balagurov. Evidence for the band ferromagnetism in $SrRuO_3$ from neutron diffraction. *Journal of Magnetism and Magnetic Materials*, 305(2):491–496, 2006.

[180] G. Cao, S. McCall, M. Shepard, J. E. Crow, and R. P. Guertin. Thermal, magnetic, and transport properties of single-crystal $Sr_{1-x}Ca_xRuO_3$ (0<=x<=1.0). *Physical Review B*, 56(1):321–329, 1997.

[181] P. B. Allen, H. Berger, O. Chauvet, L. Forro, T. Jarlborg, A. Junod, B. Revaz, and G. Santi. Transport properties, thermodynamic properties, and electronic structure of $SrRuO_3$. *Physical Review B*, 53(8): 4393–4398, 1996.

[182] II Mazin and D. J. Singh. Electronic structure and magnetism in Ru-based perovskites. *Physical Review B*, 56(5):2556–2571, 1997.

[183] D. J. Singh. Electronic and magnetic properties of the 4d itinerant ferromagnet $SrRuO_3$. *Journal of Applied Physics*, 79(8):4818–4820, 1996.

[184] A. Kanbayasi. Magnetocrystalline anisotropy of $SrRuO_3$. *Journal of the Physical Society of Japan*, 41(6):1879–1883, 1976.

[185] J. S. Lee, Y. S. Lee, T. W. Noh, S. Nakatsuji, H. Fukazawa, R. S. Perry, Y. Maeno, Y. Yoshida, S. I. Ikeda, J. J. Yu, and C. B. Eom. Bond-length dependence of charge-transfer excitations and stretch phonon modes in perovskite ruthenates: Evidence of strong p-d hybridization effects. *Physical Review B*, 70(085103):6, 2004.

[186] K. Fujioka, J. Okamoto, T. Mizokawa, A. Fujimori, I. Hase, M. Abbate, H. J. Lin, C. T. Chen, Y. Takeda, and M. Takano. Electronic structure of $SrRuO_3$. *Physical Review B*, 56(11):6380–6383, 1997.

[187] B. Dabrowski, M. Avdeev, O. Chmaissem, S. Kolesnik, P. W. Klamut, M. Maxwell, and J. D. Jorgensen. Freezing of octahedral tilts below the curie temperature in $SrRu_{1-v}O_3$ perovskites. *Physical Review B*, 71(104411):5, 2005.

[188] G. M. Leitus, S. Reich, and F. Frolow. Structural rearrangement in $SrRuO_3$ near the magnetic critical point. *Journal of Magnetism and Magnetic Materials*, 206(1-2):27–36, 1999.

[189] T. Moriya and K. Usami. Magnetovolume effect and invar phenomena in ferromagnetic metals (reprinted from solid-state commun, vol 34, pg 95-99, 1980). *Solid State Communications*, 88(11-12):911–915, 1993.

[190] Q. Gan, R. A. Rao, C. B. Eom, J. L. Garrett, and M. Lee. Direct measurement of strain effects on magnetic and electrical properties of epitaxial $SrRuO_3$ thin films. *Applied Physics Letters*, 72(8):978–980, 1998.

[191] K. Terai, T. Ohnishi, M. Lippmaa, H. Koinuma, and M. Kawasaki. Magnetic properties of strain-controlled $SrRuO_3$ thin films. *Japanese Journal of Applied Physics Part 2-Letters*, 43(2A):L227–L229, 2004.

[192] S. Kolesnik, Y. Z. Yoo, O. Chmaissem, B. Dabrowski, T. Maxwell, C. W. Kimball, and A. P. Genis. Effect of crystalline quality and

substitution on magnetic anisotropy of $SrRuO_3$ thin films. *Journal of Applied Physics*, 99(8):3, 2006.

[193] F. Castelpoggi, L. Morelli, H. R. Salva, S. L. Cuffini, R. Carbonio, and R. D. Sanchez. Specific heat measurement of the magnetoresistant perovskite $SrRuO_3$. *Solid State Communications*, 101(8):597–599, 1997.

[194] J. J. Neumeier, A. L. Cornelius, and K. Andres. Thermodynamic investigation of the magnetic phase transitions of $CaMnO_3$ and $SrRuO_3$. *Physical Review B*, 6417(172406):3, 2001.

[195] N. Menyuk, J. A. Kafalas, K. Dwight, and Goodenou J. B. Pressure-effect measurements using a vibrating-coil magnetometer. *Journal of Applied Physics*, 40(3):1324–&, 1969.

[196] M. Shikano, T. K. Huang, Y. Inaguma, M. Itoh, and T. Nakamura. Pressure-dependence of the magnetic transition-temperature for ferromagnetic $SrRuO_3$. *Solid State Communications*, 90(2):115–119, 1994.

[197] J. J. Hamlin, S. Deemyad, J. S. Schilling, M. K. Jacobsen, R. S. Kumar, A. L. Cornelius, G. Cao, and J. J. Neumeier. Ac susceptibility studies of the weak itinerant ferromagnet $SrRuO_3$ under high pressure to 34 GPa. *Physical Review B*, 76(014432):7, 2007.

[198] F. Le Marrec, A. Demuer, D. Jaccard, J. M. Triscone, M. K. Lee, and C. B. Eom. Magnetic behavior of epitaxial $SrRuO_3$ thin films under pressure up to 23 GPa. *Applied Physics Letters*, 80(13):2338–2340, 2002.

[199] H. S. Rhie, H. A. Durr, and W. Eberhardt. Femtosecond electron and spin dynamics in ni/w(110) films. *Physical Review Letters*, 90(247201), 2003.

[200] E. O. Kane. Band structure of indium antimonide. *Journal of Physics and Chemistry of Solids*, 1(4):249–261, 1957.

[201] J. A. Sanjurjo, E. Lopezcruz, and G. Burns. High-pressure raman-study of zone-center phonons in $PbTiO_3$. *Physical Review B*, 28(12): 7260–7268, 1983.

[202] Y. W. So, D. J. Kim, T. W. Noh, J. G. Yoon, and T. K. Song. Polarization switching kinetics of epitaxial $Pb(Zr_{0.4}Ti_{0.6})O_3$ thin films. *Applied Physics Letters*, 86(092905), 2005.

[203] W. Cochran. Crystal stability and the theory of ferroelectricity. *Advances in Physics*, 9(36):387–423, 1960.

[204] A. S. Sonin and B. A Strukow. *Einführung in die Ferroelektrizität*. Akademie Verlag, Berlin, 1974.

[205] K. Kopizki. *Einführung in die Festkörperphysik*. Teubner Studienbücher, Stuttgard, 1993.

[206] L. D. Landau. . *Phys. Z. Sowjun.*, 11:545, 1937.

[207] L. D. Landau. . *Zh. Eksp. Teor. Fiz.*, 7:627, 1937.

[208] D. ter Haar (Ed.). *Collected Papers of L.D. Landau*. Pergamon, Oxford, 1965.

[209] A. F. Devonshire. Theory of barium titanate 1. *Philosophical Magazine*, 40(309):1040–1063, 1949.

[210] A. F. Devonshire. Theory of barium titanate 2. *Philosophical Magazine*, 42(333):1065–1079, 1951.

[211] A. F. Devonshire. Theory of ferroelectrics. *Advances in Physics*, 3(10): 85–130, 1954.

[212] R. E. Cohen. Origin of ferroelectricity in perovskite oxides. *Nature*, 358(6382):136–138, 1992.

[213] M. J. Haun, E. Furman, S. J. Jang, H. A. McKinstry, and L. E. Cross. Thermodynamic theory of $PbTiO_3$. *Journal of Applied Physics*, 62(8): 3331–3338, 1987.

[214] G. A. Rossetti, L. E. Cross, and K. Kushida. Stress-induced shift of the curie-point in epitaxial $PbTiO_3$ thin-films. *Applied Physics Letters*, 59(20):2524–2526, 1991.

[215] P. W. Jr. Forsbergh. Effect of a 2-dimensional pressure on the curie point of barium titanate. *Physical Review*, 93(4):686–692, 1954.

[216] N. A. Pertsev, A. G. Zembilgotov, and A. K. Tagantsev. Effect of mechanical boundary conditions on phase diagrams of epitaxial ferroelectric thin films. *Physical Review Letters*, 80(9):1988–1991, 1998.

[217] J. H. Haeni, P. Irvin, W. Chang, R. Uecker, P. Reiche, Y. L. Li, S. Choudhury, W. Tian, M. E. Hawley, B. Craigo, A. K. Tagantsev, X. Q. Pan, S. K. Streiffer, L. Q. Chen, S. W. Kirchoefer, J. Levy, and D. G. Schlom. Room-temperature ferroelectricity in strained $SrTiO_3$. *Nature*, 430(7001):758–761, 2004.

[218] M. Dawber, P. Chandra, P. B. Littlewood, and J. F. Scott. Depolarization corrections to the coercive field in thin-film ferroelectrics. *Journal of Physics-Condensed Matter*, 15(24):L393–L398, 2003.

[219] P. Ghosez and K. M. Rabe. Microscopic model of ferroelectricity in stress-free $PbTiO_3$ ultrathin films. *Applied Physics Letters*, 76(19): 2767–2769, 2000.

[220] B. Meyer and D. Vanderbilt. Ab initio study of $BaTiO_3$ and $PbTiO_3$ surfaces in external electric fields. *Physical Review B*, 63(205426), 2001.

[221] J. Junquera and P. Ghosez. Critical thickness for ferroelectricity in perovskite ultrathin films. *Nature*, 422(6931):506–509, 2003.

[222] R. R. Mehta, Silverma.Bd, and J. T. Jacobs. Depolarization fields in thin ferroelectric films. *Journal of Applied Physics*, 44(8):3379–3385, 1973.

[223] I. P. Batra, P. Wurfel, and Silverma.Bd. Depolarization field and stability considerations in thin ferroelectric films. *Journal of Vacuum Science & Technology*, 10(5):687–692, 1973.

[224] V. Nagarajan, J. Junquera, J. Q. He, C. L. Jia, R. Waser, K. Lee, Y. K. Kim, S. Baik, T. Zhao, R. Ramesh, P. Ghosez, and K. M. Rabe. Scaling of structure and electrical properties in ultrathin epitaxial ferroelectric heterostructures. *Journal of Applied Physics*, 100(5):051609, 2006.

[225] D. D. Fong, A. M. Kolpak, J. A. Eastman, S. K. Streiffer, P. H. Fuoss, G. B. Stephenson, C. Thompson, D. M. Kim, K. J. Choi, C. B. Eom, I. Grinberg, and A. M. Rappe. Stabilization of monodomain polarization in ultrathin $PbTiO_3$ films. *Physical Review Letters*, 96(127601), 2006.

[226] C. Lichtensteiger, J. M. Triscone, J. Junquera, and P. Ghosez. Ferroelectricity and tetragonality in ultrathin $PbTiO_3$ films. *Physical Review Letters*, 94(047603), 2005.

[227] L. Despont, C. Koitzsch, F. Clerc, M. G. Garnier, P. Aebi, C. Lichtensteiger, J. M. Triscone, F. J. Garcia de Abajo, E. Bousquet, and P. Ghosez. Direct evidence for ferroelectric polar distortion in ultrathin lead titanate perovskite films. *Physical Review B*, 73(094110), 2006.

[228] D. P. Norton, B. C. Chakoumakos, J. D. Budai, D. H. Lowndes, B. C. Sales, J. R. Thompson, and D. K. Christen. Superconductivity in $SrCuO_2$-bacuo2 superlattices - formation of artificially layered superconducting materials. *Science*, 265(5181):2074–2077, 1994.

[229] T. Tsurumi, T. Harigai, D. Tanaka, S. M. Nam, H. Kakemoto, S. Wada, and K. Saito. Artificial ferroelectricity in perovskite superlattices. *Applied Physics Letters*, 85(21):5016–5018, 2004.

[230] N. Sai, B. Meyer, and D. Vanderbilt. Compositional inversion symmetry breaking in ferroelectric perovskites. *Physical Review Letters*, 84 (24):5636–5639, 2000.

[231] M. P. Warusawithana, E. V. Colla, J. N. Eckstein, and M. B. Weissman. Artificial dielectric superlattices with broken inversion symmetry. *Physical Review Letters*, 90(036802):4, 2003.

[232] H. N. Lee, H. M. Christen, M. F. Chisholm, C. M. Rouleau, and D. H. Lowndes. Strong polarization enhancement in asymmetric three-component ferroelectric superlattices. *Nature*, 433(7024):395–399, 2005.

[233] J. B. Neaton and K. M. Rabe. Theory of polarization enhancement in epitaxial $BaTiO_3/SrTiO_3$ superlattices. *Applied Physics Letters*, 82 (10):1586–1588, 2003.

[234] M. Dawber, C. Lichtensteiger, M. Cantoni, M. Veithen, P. Ghosez, K. Johnston, K. M. Rabe, and J. M. Triscone. Unusual behavior of the ferroelectric polarization in $PbTiO_3/SrTiO_3$ superlattices. *Physical Review Letters*, 95(177601), 2005.

[235] I. Vrejoiu, G. Le Rhun, L. Pintilie, D. Hesse, M. Alexe, and U. Goesele. Intrinsic ferroelectric properties of strained tetragonal $PbZr_{0.2}Ti_{0.8}O_3$ obtained on layer-by-layer grown, defect-free single-crystalline films. *Advanced Materials*, 18(13):1657, 2006.

[236] N. D. Zakharov, K. M. Satyalakshmi, G. Koren, and D. Hesse. Substrate temperature dependence of structure and resistivity of $SrRuO_3$

thin films grown by pulsed laser deposition on (100) $SrTiO_3$. *Journal of Materials Research*, 14(11):4385–4394, 1999.

[237] C. L. Jia, V. Nagarajan, J. Q. He, L. Houben, T. Zhao, R. Ramesh, K. Urban, and R. Waser. Unit-cell scale mapping of ferroelectricity and tetragonality in epitaxial ultrathin ferroelectric films. *Nature Materials*, 6(1):64–69, 2007.

[238] P. Ghosez, E. Cockayne, U. V. Waghmare, and K. M. Rabe. Lattice dynamics of $BaTiO_3$, $PbTiO_3$, and $PbZrO_3$: A comparative first-principles study. *Physical Review B*, 60(2):836–843, 1999.

[239] R. Ramirez, M. F. Lapena, and J. A. Gonzalo. Pressure-dependence of free-energy expansion coefficients in $PbTiO_3$ and $BaTiO_3$ and tricritical-point behavior. *Physical Review B*, 42(4):2604–2606, 1990.

[240] I. Ponomareva and L. Bellaiche. Nature of dynamical coupling between polarization and strain in nanoscale ferroelectrics from first principles. *Physical Review Letters*, 101(19):197602, 2008.

[241] M. L. Horng, J. A. Gardecki, A. Papazyan, and M. Maroncelli. Subpicosecond measurements of polar solvation dynamics - coumarin-153 revisited. *Journal of Physical Chemistry*, 99(48):17311–17337, 1995.

[242] S. A. Passino, Y. Nagasawa, T. Joo, and G. R. Fleming. Three-pulse echo peak shift studies of polar solvation dynamics. *Journal of Physical Chemistry A*, 101(4):725–731, 1997.

[243] C. Chudoba, E. T. J. Nibbering, and T. Elsaesser. Site-specific excited-state solute-solvent interactions probed by femtosecond vibrational spectroscopy. *Physical Review Letters*, 81(14):3010–3013, 1998.

[244] L. Bonacina, P. Larregaray, F. van Mourik, and M. Chergui. Lattice response of quantum solids to an impulsive local perturbation. *Physical Review Letters*, 95(015301), 2005.

[245] D. F. Underwood and D. A. Blank. Measuring the change in the intermolecular raman spectrum during dipolar solvation. *Journal of Physical Chemistry A*, 109(15):3295–3306, 2005.

[246] M. Khalil, M. A. Marcus, A. L. Smeigh, J. K. McCusker, H. H. W. Chong, and R. W. Schoenlein. Picosecond X-ray absorption spectroscopy of a photoinduced iron(ii) spin crossover reaction in solution. *Journal of Physical Chemistry A*, 110(1):38–44, 2006.

[247] W. Gawelda, V. T. Pham, M. Benfatto, Y. Zaushitsyn, M. Kaiser, D. Grolimund, S. L. Johnson, R. Abela, A. Hauser, C. Bressler, and M. Chergui. Structural determination of a short-lived excited iron(ii) complex by picosecond X-ray absorption spectroscopy. *Physical Review Letters*, 98(057401), 2007.

[248] L. Onsager. Electric moments of molecules in liquids. *Journal of the American Chemical Society*, 58:1486–1493, 1936.

[249] E. Lippert. Dipolmoment und Elektronenstruktur von angeregten Molekulen. *Zeitschrift Fur Naturforschung Part a-Astrophysik Physik Und Physikalische Chemie*, 10(7):541–545, 1955.

[250] E. Lippert. Habilitationsschrift zur Erlangung der Lehrberichtigung (venia legendi) fur das Fach physikalische Chemie an der Technischen-Hochschule-Stuttgart - spektroskopische Bestimmung des Dipolmomentes aromatischer Verbindungen im ersten angeregten Singulettzustand. *Zeitschrift Fur Elektrochemie*, 61(8):962–975, 1957.

[251] N. Mataga, Y. Kaifu, and M. Koizumi. Solvent effects upon fluorescence spectra and the dipolemoments of excited molecules. *Bulletin of the Chemical Society of Japan*, 29(4):465–470, 1956.

[252] N. Mataga and Kubota T. *Molecular interactions and electronic spectra.* Dekker, New York, 1970.

[253] Ch. Reichardt. *Solvents and Solvent Effects in Organic Chemistry.* Wiley-VCH, Weinheim, 2002.

[254] A. Demeter, S. Druzhinin, M. George, E. Haselbach, J. L. Roulin, and K. A. Zachariasse. Dual fluorescence and fast intramolecular charge transfer with 4-(diisopropylamino) benzonitrile in alkane solvents. *Chemical Physics Letters*, 323(3-4):351–360, 2000.

[255] R. Daum, S. Druzhinin, D. Ernst, L. Rupp, J. Schroeder, and K. A. Zachariasse. Fluorescence excitation spectra of jet-cooled 4-(diisopropylamino)benzonitrile and related compounds. *Chemical Physics Letters*, 341(3-4):272–278, 2001.

[256] S. I. Druzhinin, A. Demeter, and K. A. Zachariasse. Dual fluorescence and intramolecular charge transfer with crystalline 4-(diisopropylamino)benzonitrile. *Chemical Physics Letters*, 347(4-6): 421–428, 2001.

[257] Z. R. Grabowski, K. Rotkiewicz, and W. Rettig. Structural changes accompanying intramolecular electron transfer: Focus on twisted intramolecular charge-transfer states and structures. *Chemical Reviews*, 103(10):3899–4031, 2003.

[258] C. Chudoba, A. Kummrow, J. Dreyer, J. Stenger, E. T. J. Nibbering, T. Elsaesser, and K. A. Zachariasse. Excited state structure of 4-(dimethylamino)benzonitrile studied by femtosecond mid-infrared spectroscopy and ab initio calculations. *Chemical Physics Letters*, 309 (5-6):357–363, 1999.

[259] W. M. Kwok, C. Ma, D. Phillips, P. Matousek, A. W. Parker, and M. Towrie. Picosecond time-resolved study of 4-dimethylaminobenzonitrile in polar and nonpolar solvents. *Journal of Physical Chemistry A*, 104(18):4188–4197, 2000.

[260] J. Dreyer and A. Kummrow. Shedding light on excited-state structures by theoretical analysis of femtosecond transient infrared spectra: Intramolecular charge transfer in 4-(dimethylamino)benzonitrile. *Journal of the American Chemical Society*, 122(11):2577–2585, 2000.

[261] S. Techert, F. Schotte, and M. Wulff. Picosecond X-ray diffraction probed transient structural changes in organic solids. *Physical Review Letters*, 86(10):2030–2033, 2001.

[262] S. Techert and K. A. Zachariasse. Structure determination of the intramolecular charge transfer state in crystalline 4-(diisopropylamino)benzonitrile from picosecond x-ray diffraction. *Journal of the American Chemical Society*, 126(17):5593–5600, 2004.

[263] A. Demeter and K. A. Zachariasse. Fluorescence of crystalline 4-(dimethylamino)benzonitrile. absence of dual fluorescence and observation of single-exponential fluorescence decays. *Chemical Physics Letters*, 380(5-6):699–703, 2003.

[264] W. Frey, C. Root, P. Gilch, and M. Braun. Crystal structure of 4-(diisopropylamino)benzonitrile,$C_{13}H_{18}N_2$. *Zeitschrift Fur Kristallographie-New Crystal Structures*, 219(3):291–292, 2004.

[265] C. Root. Röntgenbeugung und transiente Absorption an organischen Molekülkristallen im sub-Pikosekunden Zeitbereich. *PhD thesis, Ludwig-Maximilian Universität München*, 2006.

[266] T. Schrader, A. Sieg, F. Koller, W. Schreier, Q. An, W. Zinth, and P. Gilch. Vibrational relaxation following ultrafast internal conversion: comparing IR and Raman probing. *Chemical Physics Letters*, 392(4-6): 358–364, 2004.

[267] J. B. Clarage and G. N. Phillips. Cross-validation tests of time-averaged molecular-dynamics refinements for determination of protein structures by X-ray crystallography. *Acta Crystallographica Section D-Biological Crystallography*, 50:24–36, 1994.

[268] Sb Austerman and K. T. Miller. Dimensional and X-ray diffraction changes in irradiated single crystal BeO. *Physica Status Solidi*, 11(1): 241–253, 1965.

[269] K. Lonsdale, J. M. Robertson, and I. Woodward. Structure and molecular anisotropy of sorbic acid, $CH_3{\cdot}CH{:}CH{\cdot}CH{:}CH{\cdot}COOH$. *Proceedings of the Royal Society of London Series a-Mathematical and Physical Sciences*, 178(A972):0043–0052, 1941.

[270] K. Lonsdale. X-ray study of crystal dynamics : An historical and critical survey of experiment and theory. *Proceedings of the Physical Society*, 54:314–353, 1942.

[271] V. A. Galievsky, S. I. Druzhinin, A. Demeter, Y. B. Jiang, S. A. Kovalenko, L. P. Lustres, K. Venugopal, N. P. Ernsting, X. Allonas, M. Noltemeyer, R. Machinek, and K. A. Zachariasse. Ultrafast intramolecular charge transfer and internal conversion with tetrafluoroaminobenzonitriles. *Chemphyschem*, 6(11):2307–2323, 2005.

[272] Y. Murakami, J. P. Hill, D. Gibbs, M. Blume, I. Koyama, M. Tanaka, H. Kawata, T. Arima, Y. Tokura, K. Hirota, and Y. Endoh. Resonant X-ray scattering from orbital ordering in $LaMnO_3$. *Physical Review Letters*, 81(3):582–585, 1998.

[273] J. Geck, P. Wochner, S. Kiele, P. Reutler, A. Revcolevschi, and B. Buchner. Octahedral tilts and electronic correlations in $La_{7/8}Sr_{1/8}MnO_3$. *Physical Review B*, 75(014405), 2007.

[274] C. Stamm, T. Kachel, N. Pontius, R. Mitzner, T. Quast, K. Holldack, S. Khan, C. Lupulescu, E. F. Aziz, M. Wietstruk, H. A. Durr, and W. Eberhardt. Femtosecond modification of electron localization and transfer of angular momentum in nickel. *Nature Materials*, 6(10):740–743, 2007.

[275] C. Bressler, C. Milne, V.T. Pham, A El Nahhas, R. van der Veen, W. Gawelda, S. P. Johnson, Beaud, D. Grolimund, M. Kaiser, C. N. Borca, G. Ingold, R. Abela, , and M. Chergui. Femtosecond XANES of the light-induced spin cross-over in an iron(II)-complex. *Nature, submitted*, 2008.

[276] A. Melnikov, H. Prima-Garcia, M. Lisowski, T. Giessel, R. Weber, R. Schmidt, C. Gahl, N. M. Bulgakova, U. Bovensiepen, and M. Weinelt. Nonequilibrium magnetization dynamics of gadolinium studied by magnetic linear dichroism in time-resolved 4f core-level photoemission. *Physical Review Letters*, 100(107202), 2008.

[277] M. Aeschlimann, M. Bauer, S. Pawlik, W. Weber, R. Burgermeister, D. Oberli, and H. C. Siegmann. Ultrafast spin-dependent electron dynamics in fcc Co. *Physical Review Letters*, 79(25):5158–5161, 1997.

[278] M. Lisowski, P. A. Loukakos, A. Melnikov, I. Radu, L. Ungureanu, M. Wolf, and U. Bovensiepen. Femtosecond electron and spin dynamics in Gd(0001) studied by time-resolved photoemission and magneto-optics. *Physical Review Letters*, 95(137402), 2005.

[279] M Renninger. Umweganregung, eine bisher unbeachtete Wechselwirkungserscheinung bei Raumgitterinterferenzen. *Zeitschrift für Physik A Hadrons and Nuclei*, 106(3-4):141–176, 1937.

[280] L.D. Landau and E.M. Lifschitz. *Lehrbuch der theoretischen Physik*, volume I, Mechanik. Akademie Verlag, Berlin, 1990.

[281] Franz Schwabl. *Quantenmechanik*. Springer, Berlin, 1998.

Appendix A

Darwin Formalism for Heterostructures

I will briefly discuss further details concerning the X-ray reflectivity calculations for different Perovskite crystal structures and how to incorporate strain in the matrix framework:

Along the c-axis, or for symmetric Bragg reflections (00l), one can write for the scattering matrix for one cubic $SrTiO_3$ unit cell:

$$HL_{STO} = H(O)\cdot H(Sr)\cdot L(\frac{1}{2}\, c_{\mathrm{STO}}\delta)\cdot H(O)\cdot H(O)\cdot H(Ti)\cdot L(\frac{1}{2}\, c_{\mathrm{STO}}\delta), \quad \text{(A.1)}$$

where H and L denote the scattering and propagation matrices, respectively. The matrices $L(\frac{1}{2}\, c_{\mathrm{STO}}\delta)$ depend on the angle θ of the incident X-rays and on strain δ, both of which determine the distance between scattering planes. In the X-ray diffraction calculation for propagating strain waves in a STO substrate (compare chapter 4), we must multiply HL matrices, where the propagation matrices L are modified according to the penetration of the strain front:

$$HL_{STO}(\theta,\delta) = \prod_{\delta(d)}^{\mathrm{N}} HL_{STO}(\theta,\delta(d)) \quad \text{(A.2)}$$

where N is the number of unit-cells contributing to the diffraction signal. This yields X-ray reflectivity curves of STO which depend on the penetration depth $d = N \cdot c_{\mathrm{STO}}$ of the strain front, and, since the strain fronts propagate with the velocity of sound, reflectivity curves as a function of time.

The (pseudo-cubic) $SrRuO_3$ is described with a corresponding formula.

For ferroelectric $Pb(Zr_{0.2}Ti_{0.8})O_3$ we must write:

$$HL_{\mathrm{PZT}} = H(O) \cdot L(\xi_{\mathrm{Pb-O}}\delta_\xi) \cdot H(Pb) \cdot L(\frac{1}{2}\, c_{\mathrm{PZT}}\delta - \xi_{\mathrm{Pb-O}}\delta_\xi) \cdot H(O) \cdot H(O) \cdot L(\xi_{\mathrm{Ti-O}}\delta_\xi) \cdot H(Ti_{0.8}Sr_{0.2}) \cdot L(\frac{1}{2}\, c_{\mathrm{PZT}}\delta + \xi_{\mathrm{Ti-O}}\delta_\xi). \tag{A.3}$$

Note that we can account for tetragonal distortion ($c_{PZT}\delta$) and ion displacement ($\xi_{\mathrm{Ti-O}}\delta_\xi$) and ($\xi_{\mathrm{Pb-O}}\delta_\xi$) separately. Additionally in the case of superlattices where an expansion of SRO is fully compensated by a compression of PZT we have to consider the thickness of the individual layers as follows:

$$\delta_{\mathrm{expan.}} = -[(\delta_{\mathrm{compr.}} - 1)\frac{c_{\mathrm{PZT}} \cdot n_{\mathrm{PZT}}}{c_{\mathrm{SRO}} \cdot n_{\mathrm{SRO}}}] + 1, \tag{A.4}$$

where $n_{\mathrm{SRO/PZT}}$ is the number of unit cells of SRO and PZT, respectively.

Appendix B

Lattice Dynamics Calculation

To calculate small atomic displacements x_i in a linear chain model with N atoms with mass m_i, connected with spring with elastic constants κ_i and subject to stress $\Delta(t)$, we have to solve a system of N ($i = 1, 2, \ldots N$) linear inhomogeneous differential equations:

$$m_\mathrm{i}\ddot{x}_\mathrm{i} + \sum_\mathrm{n} \kappa_\mathrm{i,n} x_\mathrm{n} = \Delta_\mathrm{i}(t). \tag{B.1}$$

The solution of an inhomogeneous differential equation is the sum of the general solution to the homogeneous equation and a particular solution to the inhomogeneous equation. Accordingly, we first of all look for N unknown equations of the form $x_\mathrm{i} \propto \exp(i\omega t)$. The calculation is performed in a matrix formalism, such that the eigenfrequencies can be determined by solving the eigenvalue equation:

$$\sum_\mathrm{k} (\kappa \cdot M)_\mathrm{i,k} S_\mathrm{k} = \omega_\mathrm{i}^2 S_\mathrm{i} \tag{B.2}$$

with

$$\kappa = \begin{pmatrix} \kappa_1 & -\kappa_1 & 0 & & \ldots & & & 0 \\ -\kappa_1 & 2\kappa_1 & -\kappa_1 & & & & & \\ 0 & \ddots & \ddots & \ddots & & & & \\ \vdots & & \ddots & \ddots & \ddots & & & \\ & & 0 & -\kappa_\mathrm{i} & 2\kappa_\mathrm{i} & -\kappa_\mathrm{i} & 0 & \\ & & & & & \ddots & & \\ & & & & & -\kappa_\mathrm{N} & 2\kappa_\mathrm{N} & -\kappa_\mathrm{N} \\ 0 & & & & & & -\kappa_\mathrm{N} & \kappa_\mathrm{N} \end{pmatrix} \tag{B.3}$$

The matrix M is a matrix with only diagonal elements with $M_\mathrm{i,i} = m_\mathrm{i}^{-1}$. The form of matrix κ ensures that only nearest neighbor coupling is taken

into a account. The symbol '$\cdot$' stands for matrix multiplication. S denotes an orthogonal matrix containing the eigenvectors as rows of the homogenous equation with eigenvalues ω_{i}^2, that is $(S^{\mathrm{T}}(\kappa M)S = \Omega)$, where $\Omega_{\mathrm{i,i}} = \omega_{\mathrm{i}}^2$. The general solution is then [280]:

$$X_{\mathrm{i}}(t) = \sum_{\mathrm{k}} C_{\mathrm{k}} e^{i\omega_{\mathrm{k}} t}(M^{1/2} \cdot S)_{\mathrm{i,k}} + \sum_{\mathrm{k}}(M^{1/2} \cdot (\kappa \cdot M)^{-1} \cdot M^{1/2})_{\mathrm{i,k}}\Delta_{\mathrm{k}} \tag{B.4}$$

$$= \sum_{\mathrm{k}} C_{\mathrm{k}} e^{i\omega_{\mathrm{k}} t}(M^{1/2} \cdot S)_{\mathrm{i,k}} + \sum_{\mathrm{k}}(M^{1/2} \cdot (S \cdot \Omega^{-1} \cdot S^{\mathrm{T}}) \cdot M^{1/2})_{\mathrm{i,k}}\Delta_{\mathrm{k}} \tag{B.5}$$

The stress Δ_{k} is a vector containing the derivative of the excitation pattern, that is, of the potential energy stored in the compressed springs. The constants C_{i} are determined for the initial condition $X_{\mathrm{i}}(0) = 0$ and are given by $C_{\mathrm{i}} = -\sum_{\mathrm{k}}(\Omega^{-1} \cdot S^{\mathrm{T}} \cdot M^{1/2})_{\mathrm{i,k}}\Delta_{\mathrm{k}}$.

For the strain pattern of the PZT/SRO/STO heterostructure discussed in chapter 4, the indices $0 < i < 249\ \mathrm{nm}/c_{\mathrm{PZT}} \approx 605$ stand for the number of unit cells of material PZT with mass m_{PZT} and spring constant κ_{PZT}, indices $605 < i < 350\ \mathrm{nm}/c_{\mathrm{SRO}} \approx 859$ for SRO and for $i > 859$ for the substrate STO. For a homogeneous elastic potential energy in the PZT and SRO layers Δ is given by $\Delta_0 = -1$ and $\Delta_{859} = 1$ and all other entries identical 0. The strain pattern is then computed with $X_{\mathrm{i}}(t) - X_{\mathrm{i+1}}(t)$. This ensures that an expansion wave starts from the air/PZT interface, an expansion wave into the SRO layer and a compression wave into the substrate, while the latter two have half the amplitude of the first strain front.

Appendix C

Total Extinction of DIABN

In the following more details about the calculation leading to the total extinction as a function of the incoming wave vector k_0 is presented.
The absolute square of equation 7.5 can be rewritten with the following identity:

$$\left|\sum_{i=1}^{Z} e^{i\vec{q}\vec{x_i}}\right|^2 = \sum_{i,j=1}^{Z} e^{i\vec{q}\vec{x_i}} e^{-i\vec{q}\vec{x_j}} = \sum_{\mathrm{i,j}=1}^{Z} \cos[\vec{q}(\vec{x}_\mathrm{i} - \vec{x}_\mathrm{j})]. \tag{C.1}$$

It turns out that is easiest to rewrite the formulas in spherical coordinates. The parametrization is shown in figure C.1. In particular, the $\cos(\Theta)$ term in the polarization factor P yields (see also chapter 5.3 in Schwabl [281]):

$$\begin{aligned}&\cos(\Theta) = \cos(\theta_0, \theta_\mathrm{S}, \phi_0, \phi_\mathrm{S}) = \\ &\cos(\theta_0)\cos(\theta_\mathrm{S}) + \sin(\theta_0)\sin(\theta_\mathrm{S})\cos(\phi_0 - \phi_\mathrm{S})\end{aligned} \tag{C.2}$$

One sets $k = qz$, with $q = 2\pi/\lambda$ and z the distance between the electrons. Here the electrons are positioned along the z-axis as shown in figure C.1 b). The cross-section for one electron pair in units of $\sigma_{\mathrm{Thomsen}}$ yields:

$$\begin{aligned}&\sigma_{\mathrm{pair}}(\theta_0, \phi_0, k)/\sigma_{\mathrm{Thomsen}} = \\ &\frac{3}{8\pi}\int_0^{2\pi}\int_0^{\pi} \frac{1 + \cos(\theta_0, \theta_\mathrm{S}, \phi_0, \phi_\mathrm{S})^2}{2} \cos[\cos(\theta_0) - \cos(\theta_\mathrm{S})k] d\theta_\mathrm{S} d\phi_\mathrm{S}\end{aligned} \tag{C.3}$$

When performing the integration the dependence on ϕ_0 drops out and the resulting analytic expression gives:

$$\begin{aligned}&\sigma_{\mathrm{pair}}(a, k)/\sigma_{\mathrm{Thomsen}} = \\ &\frac{3}{8}\frac{\cos(ka)(ka(1 + 3(2a^2 - 1) + (-1 + 3k^2) + (-3 + k^2)(2a^2 - 1))\sin(k))}{k^3},\end{aligned} \tag{C.4}$$

where the abbreviation $a = \cos(\theta_0)$ is introduced. Note that the angle θ_0 is between the incoming X-ray beam and the connecting line of the electron pair as shown in figure C.1 b). To get the total cross-section of a cluster of electrons, one has to some up over all possible electron pairs l, k.

$$\mu(\vec{k_0})/\sigma_{\text{Thomsen}} = \sum_l \sum_k \sigma_{\text{pair}}(a_{lk}, k_{lk}))/\sigma_{\text{Thomsen}}. \tag{C.5}$$

The incoming wave vector k_0 is calculated in a grid of $(0 < \theta_0 < \pi, 0 < \phi_0 < 2\pi)$ and the coordinates of the N and C atoms of the DIABN molecules are used to determine the value of $a_{lk} = \cos(\theta_0)_{lk}$ and z_{lk} for every pair. Only the two 1s electrons are considered and since their atomic form factors are close to one, we simply multiply the final result by two. This will then yield the 3-dimensional plots shown in figure 7.4. Note that the calculation time depends on the density of the grid θ and ϕ and increases with $Z(Z-1)$, where Z is the number of electrons.

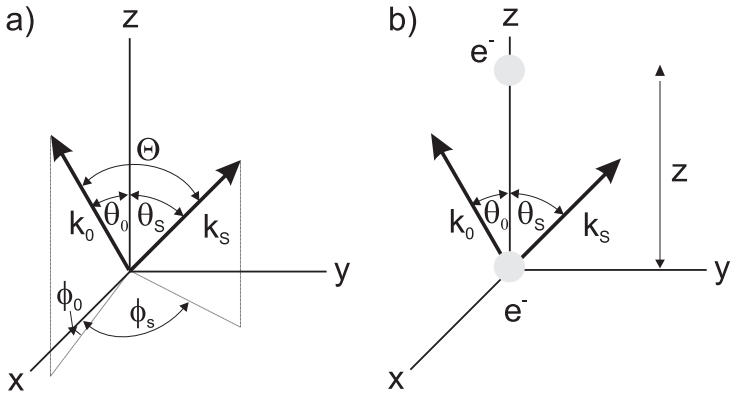

Figure C.1: **a**) Illustration of parametrization in terms of the angles $\theta_0, \theta_S, \phi_0, \phi_S$ **b**) Geometry of the incoming X-ray beam and the electron pair.

Appendix D

Abbreviations

a, b	in-plane lattice constant
B	Debye Waller factor
c	out-of-plane lattice constant
d_{hkl}	distance between lattice planes (hkl)
d_{SL}	superlattice periodicity
E	electric field
$f_0(\vec{Q}, E)$	atomic form factor
g_{SL}	reciprocal SL vector $2\pi/d_{\mathrm{SL}}$
$\vec{G}$	reciprocal lattice vector
$\vec{k}_{0,\mathrm{S}}$	incoming/scattered wave vector
M	Debye Waller mean temperature factor
$\vec{Q}$	wave vector transfer $\vec{k}_0 - \vec{k}_{\mathrm{S}}$
$q(f_0, \theta)$	amplitude of scattered X-ray of an atomic plane
p	polarization factor
$P, \mathfrak{P}$	macroscopic polarization
r_0	Thomson scattering length
T	temperature
T_{c}	critical/Curie Temperature
V	volume
Z^*	Born effective charge
α	thermal expansion coefficient
α_{e}	electronic polarizability
β	compressibility
$\gamma_{\mathrm{e,l,m}}$	electronic, lattice, magnetic Grüneisenparameter
$\varepsilon_{s,e}$	static, optical-frequency dielectric constant
η	tetragonal distortion c/a
λ	optical *or* X-ray wavelength

λ_{eff}	screening length
θ	diffracting angle
θ_{Bragg}	Bragg angle
χ	dielectric susceptibility
σ	stress
σ_{Thomson}	Thomson scattering cross-section
ξ	ion displacement in unit cell
ω	circular frequency *or*
	angle between crystal surface and X-ray beam

Table D.1: List of most common abbreviations

Appendix E

Publications

Journal Articles

- Ultrafast magnetostriction and phonon-mediated stress in a photoexcited ferromagnet. C. von Korff Schmising, A. Harpoeth, N. Zhavoronkov, Z. Ansari, M. Woerner, T. Elsaesser, M. Bargheer, M. Schmidbauer, I. Vrejoiu, D. Hesse, M. Alexe. *Physical Review B*, 78, 060404(R) (2008)

- Real-time studies of reversible lattice dynamics by femtosecond X-ray diffraction. C. von Korff Schmising, M. Bargheer, M. Woerner, T. Elsaesser. *Zeitschrift für Kristallographie*, 223, 04-05, (2008)

- Coupled ultrafast lattice and polarization dynamics in ferroelectric nanolayers. C. von Korff Schmising, M. Bargheer, M. Kiel, N. Zhavoronkov, M. Woerner, T. Elsaesser, I Vrejoiu, D. Hesse, and M Alexe. *Physical Review Letters*, 98, 257601 (2007)

- Accurate time delay determination for femtosecond X-ray diffraction experiments. C. von Korff Schmising, M. Bargheer, M. Kiel, N. Zhavoronkov, M. Woerner, T. Elsaesser, I. Vrejoiu, D. Hesse, and M. Alexe. *Applied Physics B*, 88, 1 (2007)

- Ultrafast changes of molecular crystal structure induced by dipole solvation M. Braun, C. von Korff Schmising, M. Kiel, N. Zhavoronkov, J. Dreyer, M. Bargheer, T. Elsaesser, C. Root, T.E. Schrader, P. Gilch, W. Zinth, and M. Woerner. *Physical Review Letters*, 98, 248301 (2007)

- Schwingende Nanoschichten im Röntgen-Stroboskop. M. Bargheer, C. von Korff Schmising, M. Woerner, and T. Elsaesser. *Physik in unserer Zeit*, 38, 60 (2007)

- High repetition rate ultrafast X-ray source from the femtosecond laser produced plasma. N. Zhavoronkov, C. von Korff Schmising, M. Bargheer, M. Woerner, T. Elsaesser, O. Klimo, and J. Limpouch *Journal de Physique*, 133, 1201 (2006)

- Strain propagation in nanolayered perovskites probed by ultrafast X-ray diffraction. C. von Korff Schmising, M. Bargheer, M. Kiel, N. Zhavoronkov, M. Woerner, T. Elsaesser, I, Vrejoiu, D. Hesse, and M. Alexe. *Physical Review B*, 73, 212202 (2006)

- Rectangular-core microstructured polymer optical fibre for interconnect. M. van Eijkelenborg, N. Issa, M. Hiscocks, C. von Korff Schmising, R. Lwin. *Electronic Letters*, 42, 201-202 (2006)

- Long-living currents induced by nanosecond light pulses in LiNbO3 Crystals. O. Beyer, C. von Korff Schmising, M. Luennemann, K. Buse, B. Sturman. *Optics Express*, 14, 1533-1540 (2006)

- Femtosecond holography in lithium niobate crystals. H.T. Hsieh, D. Psaltis, O. Beyer, D. Maxein, C. von Korff Schmising, K. Buse, B. Sturmann. *Optics Letters*, 30, 2233-2235 (2005)

Conference proceedings:

- Probing strain propagation in nanolayered perovskites by diffraction of femtosecond X-ray pulses. C. von Korff Schmising, M. Bargheer, M. Kiel, N. Zhavoronkov, M. Woerner, T. Elsaesser, I. Vrejoiu, D. Hesse, and M. Alexe. *Ultrafast Phenomena XV*, P. Corkum, D. Jonas, R. J. D. Miller, A. M. Weiner (Eds.), Springer Berlin 2007, p. 713

- Femtosecond X-ray diffraction of DIABN single crystals. M. Braun, C. Root, T.E. Schrader, P. Gilch, W. Zinth, M. Bargheer, C. von Korff Schmising, M. Kiel, N. Zhavoronkov, M. Woerner, and T. Elsaesser. *Ultrafast Phenomena XV*, P. Corkum, D. Jonas, R. J. D. Miller, A. M. Weiner (Eds.), Springer Berlin 2007, p. 725

- Ultrafast structure and polarization dynamics in nanolayered perovskites studied by femtosecond X-ray diffraction. C. von Korff Schmising, M. Bargheer, M. Kiel, N. Zhavoronkov, M. Woerner, T. Elsaesser, I. Vrejoiu, D. Hesse, and M. Alexe. *Journal of Physics Conference Series*, 92, 012177 (2007)

- High numerical aperture in large-core microstructured polymer optical fibres. N. A. Issa, C. von Korff Schmising, W. E. Padden and M. A. van Eijkelenborg, *Proceedings of the international Plastic Optical Fiber (POF) conference*, Nürnberg, Germany, pp. 436-43 (2004)

Appendix F

Danksagung

Mein besonderer Dank gilt Professor Thomas Elsässer, der es mir ermöglicht hat, mich im Rahmen meine Doktorarbeit mit einem so spannendem Thema zu beschäftigen. Die herausragenden experimentellen Möglichkeiten am Max Born Institut und die Teilnahme an zahlreichen internationalen Konferenzen habe ich sehr zu schätzen gewusst.

Professor Oliver Benson und Professor Martin Wolf danke ich für die Bereitschaft die Gutachten zu verfassen.

Matias Bargheer verdanke ich mein ganzes Wissen über nichtlineare Spektroskopie, Röntgenbeugung und Phononenpropagation; seine klaren physikalischen Bilder haben mir den Einstieg in die Festkörperphysik sehr erleichtert. Ich möchte mich für seine immer freundliche, unkomplizierte und geduldige Hilfsbereitschaft bedanken. Außerdem habe ich ihm die Auswahl der untersuchten Übergitterproben zu verdanken, die sich als ideales System für die zeitaufgelöste Röntgenbeugung erwiesen haben.

Ich danke Michael Wörner, der mit seiner unbegrenzten physikalischen Kreativität wesentlich zum Gelingen dieser Arbeit beigetragen hat. Die freundliche Atmosphäre in seiner Abteilung, sein geduldiges Erläutern physikalischer Modelle und seine Begeisterung für Physik haben mir sehr gut gefallen.

Ohne ein so fabelhaft funktionierendes Lasersystem hätte diese Arbeit nicht durchgeführt werden können. Dafür möchte ich meinen ganz besonderen Dank Nikolai Zhavoronkov aussprechen, der mir immer zuvorkommend und schnell bei Problemen geholfen hat.

Des Weiteren gilt mein Dank Mareike Kiel, für die erfolgreiche Zeit, in der wir im Labor zusammengearbeitet haben, Anders Harpøth, der mir unermüdlich und hilfsbereit bei den zeitaufwändigen Experimenten an den ferromagnetischen Strukturen geholfen hat, Zunaira Ansari, für viele gute Ideen und die Hilfe bei der Justage verschiedener Lichtquellen und Cynthia Aku-Leh, für die Fertigstellung der optischen Anrege-Abfrage Experimente.

Für interessante physikalische Diskussionen und Hilfe bei experimentellen Schwierigkeiten gilt mein Dank ganz besonders Klaus Reimann, Peter Gaal, Wilhelm Kühn, Flavio Zamponi, Claus Ropers, Valeri Kozich, Jens Dreyer und Philip Rothhardt. Außerdem möchte ich mich bei Markus Breusing bedanken, der sich spontan bereiterklärt hat das Fortgeschrittenenpaktikum zu übernehmen. Bei Gabriele Kordaß bedanke ich mich für eine freundliche Büronachbarschaft und für tatkräftige Hilfe bei Bestellungen und vielen kleinen Problemen. Mein Dank gilt auch den Werkstätten, insbesondere Peter Stolz, Jörg Schulze und Roman Penslin, denen es immer gelungen ist, meine Wünsche schnell und ohne bürokratische Hürden zu erfüllen.

Ich bedanke mich bei Ionela Vrejoui, Dietrich Hesse und Marin Alexe vom Max-Planck-Insitut für Mikrostrukturphysik in Halle für die Herstellung der hervorragenden Oxid-Heterostrukturen und die konstruktiven Diskussionen über Ferroelektrizität in dünnen Filmen.

Bei Martin Schmidbauer vom Leibniz Institut für Kristallzüchtung, Berlin, bedanke ich mich herzlich für die Hilfe bei den hochauflösenden Röntgendiffraktionsmessungen.

Auch den Mitgliedern der Arbeitsgruppe von Professor Zinth in der Ludwig-Maximilians-Universität München sei für die erfolgreiche Zusammenarbeit bei den DIABN Experimenten mein herzlicher Dank ausgesprochen. Insbesondere bedanke ich mich bei Christoph Root, Tobias Schrader und Markus Braun für die Herstellung der Proben, die Hilfe bei den zeitaufgelösten Röntgenexperimenten in Berlin und für die optische Charakterisierung der Proben.

Selbständigkeitserklärung

Hiermit erkläre ich, dass ich die vorliegende Dissertation, „Femtosecond X-Ray Scattering in Condensed Matter“, selbstständig erarbeitet und verfasst habe und alle Hilfsmittel und Hilfen angegeben habe.
Ich erkläre, dass ich mich nicht für einen Doktorgrad anderwärts beworben habe und auch einen dementsprechenden Doktorgrad nicht besitze.
Des weiteren erkläre ich, dass ich von der zugrunde liegenden Promotionsordnung Kenntnis genommen habe.

Clemens von Korff Schmising